

# BULGARIAN CHEMICAL COMMUNICATIONS

2024 Volume 56 / Number 3

*Journal of the Chemical Institutes  
of the Bulgarian Academy of Sciences  
and of the Union of Chemists in Bulgaria*



Selected papers presented at the 10<sup>th</sup> International Conference on New Trends in  
Chemistry, April 19-21, 2024, Budapest



# Continuous flow chromium (VI) adsorption onto peach stone- and acrylonitrile-divinylbenzene copolymer-based activated carbons

D. Duranoğlu\*, I. Küçük, Ü. Beker

Department of Chemical Engineering, Faculty of Chemical and Metallurgical Engineering, Yildiz Technical University, Davutpasa Campus, 34220, Esenler, Istanbul, Turkey

Received May 24, 2024; Accepted: June 14, 2024

Peach stone-based activated carbon (PS-AC) and acrylonitrile divinyl benzene copolymer-based activated carbon (ANDVB-AC) were evaluated in fixed-bed continuous flow Cr(VI) adsorption studies. The results were compared with those for the commercial activated carbon (CPG-LF). Continuous flow adsorption studies were carried out in a fixed-bed column with various concentrations of a Cr(VI) solution of pH 2. The effect of flow rate on the breakthrough capacity was investigated *via* breakthrough curves. Although total Cr(VI) adsorption capacities were obtained as 122, 58, and 103 mg/g for PS-AC, ANDVB-AC and CPG-LF, respectively, the breakthrough capacities were determined to be 25.0, 35.2, and 30.0 mg/g. When polymer-based AC was used, 61% of the capacity was effectively utilized while with peach stone-based AC, only 21% of the capacity was effectively utilized at a flow rate of 5 mL/min. This difference was attributed to the shorter contact time of the solution in the column and the slower adsorption kinetics of PS-AC. At a lower flow rate (0.96 mL/min) peach stone-AC can be utilized with higher (47%) efficiency. Both peach stone- and polymer-based activated carbons can be effectively utilized in a fixed column under continuous flow with high Cr(VI) adsorption capacities.

**Keywords:** Chromium; activated carbon; continuous flow adsorption; peach stone; acrylonitrile divinyl benzene

## INTRODUCTION

Water sources contaminated with Cr(VI) compounds which are toxic and of carcinogenic nature, should be treated. Due to the superior properties like high specific surface area, porous structure and oxygen-containing surface functional groups, activated carbon (AC) can be effectively used for removal of contaminants from aqueous solutions. Any carbonaceous materials available at low cost, both naturally occurring like agricultural wastes and synthetic like polymers, can be utilized as precursors in the production of activated carbons [1, 2]. Commercial activated carbons are mainly produced from wood, coal and coconut shells. Due to their adsorptive properties, low cost and sustainability, activated carbons prepared from agricultural by-products could be superior compared to conventional activated carbons [3].

Various kinds of biomass have been utilized as activated carbons for Cr(VI) adsorption in a fixed bed column [4-8]. Availability and abundance of precursor are crucial. Peach stone is one of the most abundant agricultural wastes of juice factories. Turkey is the fifth peach manufacturer in the world with a production of 485,000 tons [9]. On the other hand, polymer-derived carbons can be better controlled by the choice of precursor material, including its own porosity, chemical composition, and pore size distribution, as well as by carbonization and activation conditions. Polymer-

based activated carbons are more stable and mechanically resistant compared to other biomass-based activated carbons. Moreover, owing to the shape of the beads of the polymer precursor, activated carbon shows good hydrodynamic properties in fixed-bed applications.

The aim of the current study is to investigate Cr(VI) adsorption onto peach stone-based (PS-AC) and acrylonitrile-divinylbenzene copolymer-based activated carbon (ANDVB-AC) in a fixed bed column. Cr(VI) adsorption on different activated carbons was compared *via* breakthrough curves obtained.

## EXPERIMENTAL

### *Fixed bed column studies*

Continuous flow adsorption studies were carried out in a fixed-bed column of 13 mm diameter. Different concentrations of a Cr(VI) solution prepared at pH 2 were fed into the fixed-bed polyethylene column using a peristaltic pump until all adsorbent was saturated. In the column experiments, activated carbons dried overnight at 378 K were used. The solution at the column outlet was collected into tubes using a timed fractionated sample collector, then Cr(VI) concentrations were determined at 540 nm wavelength by using Analytic Jena Specord 40 spectrometer after complexing with diphenylcarbazide in acidic medium [10]. Experiments were continued until the concentration

\* To whom all correspondence should be sent:  
E-mail: [dduran@yildiz.edu.tr](mailto:dduran@yildiz.edu.tr)

of the collected outlet solution was equal to the concentration of the inlet solution.

Breakthrough curves were obtained by plotting relative concentration of inlet and outlet values against the amount of the outlet solution or bed volume. The bed volume was calculated using Equation 1:

$$\text{Bed volume} = \frac{V}{(\pi \cdot D^2 \cdot h)/4} \quad (1)$$

V, D and h values given in Equation 1 show the outlet solution volume (mL), column diameter (cm) and the height of the activated carbon in the column (cm), respectively.

*Studies conducted with peach stone-based activated carbon (PS-AC):* The PS-AC sample with a particle size of 0.14-0.56 mm was filled into the ion exchange column. The height of activated carbon in the column was 14 mm (0.8 g of PS-AC). The adsorption experiments were carried with four different Cr(VI) concentrations (5 ppm, 15 ppm, 30 ppm and 60 ppm) and a feeding flow rate of 5 mL/min until the column reached saturation. In order to examine the effect of flow rate on the breakthrough point capacity, separate experiments were conducted with a concentration of 30 ppm and a flow rate of 0.96 mL/min.

*Studies conducted with polymer-based activated carbon (ANDVB-AC):* The activated carbon with a particle size of 0.075-0.29 mm was filled into the ion exchange column. The height of activated carbon in the column was 27.5 mm. The adsorption experiment was carried with a Cr(VI) solution at a concentration of 30 ppm at a feeding flow rate of 5 mL/min until the column reached saturation.

*Studies with commercial activated carbon (CPG-LF):* The CPG-LF sample with a particle size of 0.14-0.56 mm was filled into the ion exchange column. The height of activated carbon in the column was 14 mm. The adsorption experiment was carried with a 30 ppm Cr(VI) solution at a feeding flow rate of 5 mL/min until the column reached

saturation.

## MATERIALS

Peach stones (PS) were obtained from a fruit juice factory in Bursa, Turkey. They were converted into activated carbon (PS-AC) *via* steam activation at 1073 K as described in our previous study [11]. Acrylonitrile-divinylbenzene copolymer beads (ANDVB) were prepared by a suspension polymerization method with hexadecane and toluene (1:9 w/w) as diluents. The level of crosslinker was set at 40 wt%. Full details of the polymerization are given in ref. [12]. The activation of ANDVB beads was performed in three successive stages; air oxidation at 573K, then carbonization at 673 K for 4 h and finally at 1123 K for 1 h under nitrogen flow. Detailed production conditions of polymer-based activated carbon (ANDVB-AC) were previously reported [11]. Commercial activated carbon (Chemviron Carbon, CPG-LF) was used for the comparison of the adsorption results. Some characteristics of polymer-based ACs are given in Table 1. N<sub>2</sub> adsorption measurements were performed using Quantachrome Autosorb-1-C surface analyser. Nitrogen adsorption-desorption isotherms of the AC samples produced within the scope of the study are given in Figure 1. Visual inspection of adsorption isotherms provides useful information about adsorption and pore structure of the adsorbent. When the figures are examined, it is seen that the nitrogen adsorption of all carbon samples obeys a Type I isotherm. Microporous adsorbents demonstrate a Type I isotherm [13]. At small values of P/P<sub>0</sub>, the micropores are filled with adsorbed gas and then the curve flattens. This indicates that adsorption does not continue after the micropores are filled. SEM images obtained from JEOL JSM-633SF model field emission scanning electron microscope, are also shown in Figure 1. The porous structure of produced carbons is clearly seen from the figure.

**Table 1.** Characteristics of activated carbons

Properties	PS-AC	ANDVB-AC	CPG-LF
BET surface area (m <sup>2</sup> /g)	608	579	693
Pore volume (cm <sup>3</sup> /g)	0.341	0.300	0.351
Micropore volume (cm <sup>3</sup> /g)	0.331	0.234	0.318
Composition (Kjeldahl %N; %N; %C; %H; %O)	0.15; 0.22; 93.18; 0.94; 5.67	4.69; 4.49; 82.29; 1.38; 11.85	0.50; 0.86; 91.37; 0.73; 7.04

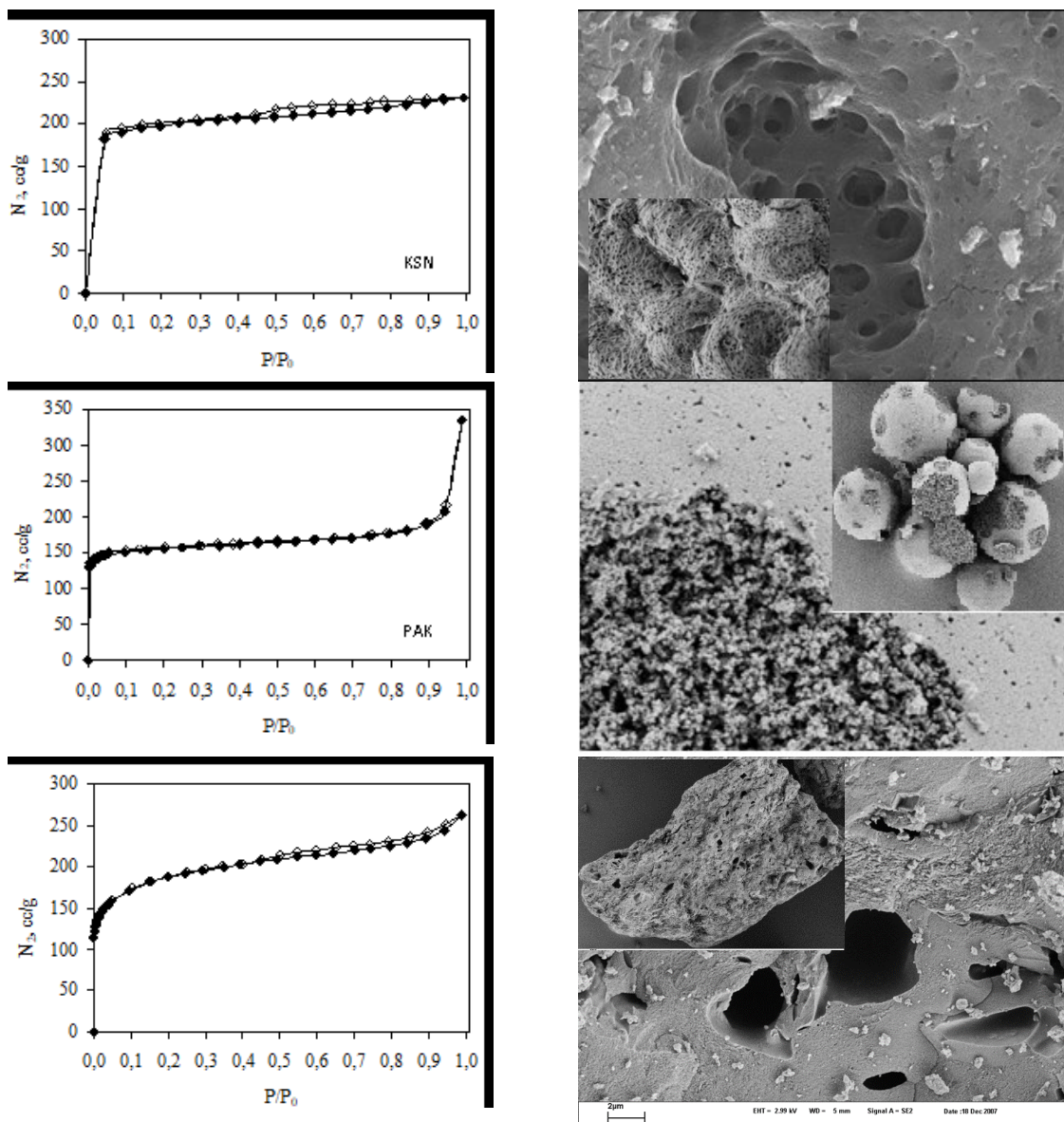


Figure 1. Nitrogen adsorption-desorption isotherms and SEM images of the AC samples

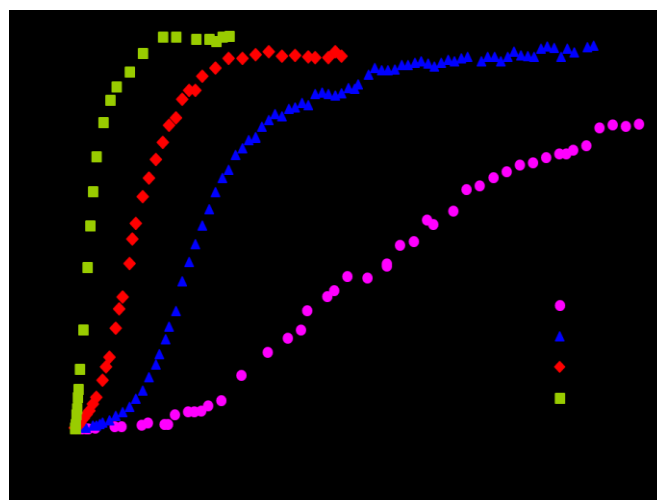


Figure 2. Breakthrough curves obtained with PS-AC activated carbon (PS-AC: 0.8 g; bed volume: 3.4 mL; flow rate: 5 mL/min)

## RESULTS AND DISCUSSION

## Sorption studies with PS-AC

In order to determine the dynamic behaviour of the adsorption column, the time at which the breakthrough point appears and the shape of the breakthrough curves are very important parameters. Breakthrough curves are usually created by plotting the relative concentration ( $C/C_0$ ), the ratio of column outlet concentration to inlet concentration, as a function of time or bed volume [14].

The breakthrough curves obtained as a result of adsorption experiments performed with PS-AC at different inlet Cr(VI) concentrations are shown in Figure 2. As seen, the relative concentration of outlet solution is initially very close to zero, then, it increases by further solution passing through the column, i.e. the column reaches a saturation point. The first break points seen in the figure are called breakthrough points. When the inlet Cr(VI) concentration was increased, breakthrough points began to appear earlier. Breakthrough point is seen after approximately 5.3 L of solution (~2800 bed volumes) passes through the column with 5 ppm inlet concentration, while the breakthrough points are 2.2 L, 660 mL and 100 mL (~1200, ~360 and ~55 bed volumes) for the inlet concentrations of 15 ppm, 30 ppm and 60 ppm, respectively. In addition, as can be seen in Figure 2, a much steeper curve was obtained at higher inlet concentrations. The PS-AC column was completely saturated after 4 L of Cr(VI) solution passed through the column when working with an initial concentration of 60 ppm. On the other hand, approximately 40 L of Cr(VI) solution was required to saturate the column for 5 ppm inlet concentration. In order to examine the effect of flow rate on adsorption, the breakthrough point curves obtained at 30 ppm inlet concentration with different flow rates (0.96 mL/min and 5 mL/min) for PS-AC are given in Figure 3. The breakthrough point, which was seen at 660 mL (~360 bed volumes) when the flow rate was 5 mL/min, was observed after 1250 mL (~670 bed volumes) of solution passed through the column at a flow rate of 0.96 mL/min. The breakthrough point curve obtained at a lower flow rate was much steeper, and the column quickly reached saturation. This situation can be explained by the contact time between the solution and activated carbon. While the contact time in the column is 22 seconds at a high flow rate (5 mL/min), this time is 116 seconds at a low flow rate (0.96 mL/min). By 5-fold increasing of the contact time between the activated carbon and the solution, the PS-AC in the column was much more effectively utilized.

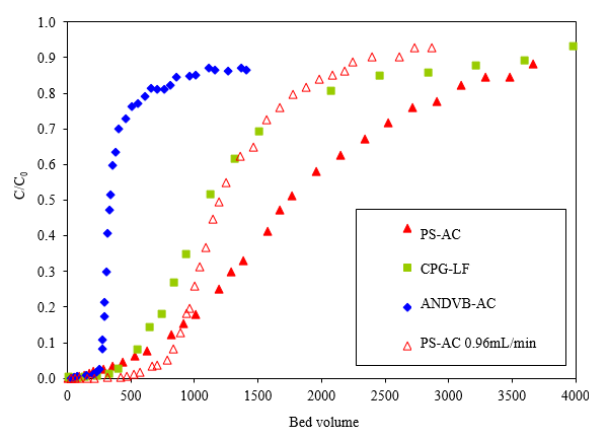


**Figure 3.** Breakthrough curves obtained with different activated carbons (flow rates: 5 mL/min; Cr(VI) inlet conc: 30 ppm; PS-AC bed volume: 1.84 mL; ANDVB-AC bed volume: 3.94 mL; CPG-LF bed volume: 1.86 mL)

The breakthrough curves obtained as a result of the column sorption study performed with three different activated carbons (PS-AC, ANDVB-AC and commercial CPG-LF) can be seen in Figure 3. When studied under the same conditions, the breakthrough point of the commercial activated carbon occurred when about 430 bed volumes of solution were passed, while the breakthrough points of PS-AC and ANDVB-AC were observed at 360 and 250 bed volumes, respectively. Breakthrough capacity of PS-AC is very close to that of the commercial one whereas ANDVB-AC shows the lowest capacity with a much steeper curve compared to the others. This steeper curve resulted in lower exhaustion capacity, however, higher utility of the capacity.

The amount of substance per unit adsorbent amount at the breakthrough point is called breakthrough point capacity, and this value is lower than the total capacity value. Breakthrough capacity depends on process conditions and is meaningless when these conditions are given without being specified. Total capacity refers to the total amount of substance adsorbed by the column until it reaches saturation and depends on the amount of adsorbent [15]. The total and breakthrough capacities given in Table 2 were calculated from the breakthrough curve graphs. The most suitable profile for the specified operating conditions (30 ppm inlet concentration and 5 mL/min flow rate) was provided by ANDVB-AC. Compared to PS-AC and CPG-LF, although the total capacity of the ANDVB-AC sample is very low, the breakthrough point capacity is high. While 60% of the capacity could be effectively utilized when polymer-based activated carbon (ANDVB-AC) was used, only 21% of the total capacity could be effectively utilized when peach stone-based activated carbon (PS-AC) was used (Table 2).

**Table 2.** Breakthrough and total capacities, capacity utilizations

AC	Flow rate (mL/min)	Residence time <sup>a</sup> (s)	Breakthrough capacity <sup>b</sup> (mg/mL)	Total capacity <sup>b</sup> (mg/mL)	Breakthrough capacity <sup>c</sup> (mg/g)	Total capacity <sup>c</sup> (mg/g)	Effective capacity utilization <sup>d</sup> (%)
PS-AC	5	22	10.8	52.5	25.0	122	21
ANDVB-AC	5	47	7.1	11.8	35.2	58	60
CPG-LF	5	22	12.9	44.3	30.0	103	30
PS-AC	0.96	116	19.2	41.2	44.6	96	47

<sup>a</sup> Residence time = Bed volume/Flow rate; <sup>b</sup> based on the volume of activated carbon; <sup>c</sup> based on the mass of activated carbon; <sup>d</sup> Effective capacity utilization = (Breakthrough capacity/Total capacity) × 100

This is closely related to the residence time of the solution in the column. The residence time of the solution in ANDVB-AC the column is 47 sec, while when PS-AC and CPG-LF are used, this residence time is about 22 sec. By increasing the residence time in PS-AC from 22 sec to 116 sec via decreasing the flow rate, the breakthrough point capacity could be increased by 80% and the effective capacity utilization rate could be increased to 47%. In commercial applications of ion exchangers, the breakthrough point capacity is generally 50% of the total capacity for strongly acidic and strongly basic resins and 80% or more for weakly acidic and weakly basic resins. Accordingly, ANDVB-AC and PS-AC (at low flow rate conditions) can be effectively utilized as Cr(VI) adsorbents in fixed-bed columns. In ion exchangers, the ion exchange capacity is usually given per unit resin volume [16]. Adsorption capacity values given in Table 2 are on the basis of both volume and mass. Although ANDVB-AC is superior to PS-AC considering breakthrough point capacities calculated on mass basis, if breakthrough point capacities calculated on volumetric basis are examined, it is seen that PS-AC is more efficient.

### CONCLUSION

According to our findings it may be concluded that:

- Peach stone-based AC showed higher Cr(VI) adsorption capacity compared to the others, however, its capacity utilization is low due to the low kinetics in nature. On the other hand, peach stone-based activated carbon can be effectively used with low flow rates.

- Even though polymer-based AC has the lowest total capacity, its capacity utilization is significantly high.

Hence, both peach stone- and polymer-based activated carbons are promising adsorbents for

Cr(VI) removal from aqueous solutions in a continuous flow process.

### REFERENCES

1. A. A. Attia, B. S. Girgis, N. A. Fathy, *Dyes and Pigments*, **76**, 282 (2008).
2. B. S. Girgis, A. A. Attia, N. A. Fathy, *Colloids and Surfaces A: Physicochemical Engineering Aspects*, **299**, 79 (2007).
3. P. Galiatsatou, M. Metaxas, V. Kasselouri-Rigopoulou, *Mikrochimica Acta*, **136**, 147 (2001).
4. S. Yüksel, R. Orhan, *Arabian Journal for Science and Engineering*, **44**, 5345 (2019).
5. S. M. Yakout, M. R. Hassan, H. A. Omar, *Desalination and Water Treatment*, **170**, 128 (2019).
6. H. Haroon, J. A. Shah, M. S. Khan, T. Alam, R. Khan, S. A. Asad, M. A. Ali, G. Farooq, M. Iqbal, M. Bilal, *J. Water Process Eng.*, **38**, 101577 (2020).
7. A. Ajmani, C. Patra, S. Subbiah, S. Narayanasamy, *J. Environ. Chem. Eng.*, **8**, 103825 (2020).
8. S. Mohanta, M. K. Sahu, P. C. Mishra, A. K. Giri, *Water Science & Technology*, **84**, 55 (2021).
9. Z. G. Göktolga, B. Gözener, O. Karkacier, *G.O.Ü. Ziraat Fakültesi Dergisi*, **23**, 39 (2006).
10. APHA (American Public Health Association), *Standard Methods for Examination of Water and Wastewater*, Baltimore, 2005.
11. D. Duranoğlu, A. W. Trochimczuk, U. Beker, *Chem. Eng. J.*, **165**, 56 (2010).
12. A. W. Trochimczuk, M. Streat, B. N. Kolarz, *React. Funct. Polym.*, **46**, 259 (2001).
13. International Union of Pure and Applied Chemistry (IUPAC), *Reporting Physisorption Data for Gas/Solid Systems with Special Reference to the Determination of Surface Area and Porosity*, **57**, 603, 1985.
14. E. Malkoc, Y. Nuhoglu, M. Dunder, *Journal of Hazardous Materials*, **138**, 142 (2006).
15. F. Helfferich, *Ion Exchange*, Dover Publications, New York, 1995.
16. F. C. Nachad, J. Schubert, *Ion Exchange Technology*, Academic Press, New York, J., 1965.

## Modeling of continuous-flow phenol adsorption onto acrylonitrile-divinylbenzene copolymer

E. Neziri, D. Duranoğlu\*

Yildiz Technical University, Chemical Engineering Department, 34220, Esenler, İstanbul, Turkey

Received June 3, 2024; Accepted: August 17, 2024

Phenol, a highly toxic organic compound, is commonly found in industrial effluents of pharmaceuticals, paper, plastics, and petrochemicals production processes. Effective treatment techniques should be enhanced to reduce the negative effects of phenol contamination in water sources, which poses serious environmental risks. An efficient option for treating water sources polluted with phenol is the continuous adsorption technique. Due to high mechanical strength, large surface area, ease of regeneration, and cost-effectiveness, polymeric structures are promising adsorbents. In this study, continuous-flow phenol adsorption onto acrylonitrile-divinylbenzene (AN-DVB) copolymer was investigated. Phenol adsorption was modeled in order to characterize the adsorption process, and the predictive accuracy of the models under continuous flow conditions was evaluated. A phenol aqueous solution was passed through a fixed column packed with AN-DVB copolymer beads at room temperature. Longer breakthrough and exhaustion periods were obtained by increasing the amount of adsorbent in the column; however, shorter breakthrough and exhaustion times and lower adsorption capacity were obtained by increasing the flow rate without altering the amount of adsorbent. The experimental breakthrough curves were modeled with Adams & Bohart, Thomas, Yoon & Nelson, Clark and modified dose-response column models *via* non-linear regression analysis. For every condition under investigation, the modified dose-response model provided a good fit with the experimental data. Isopropanol was found to successfully regenerate polymer beads through adsorption-desorption cycles.

**Keywords:** Adsorption; Modeling; Phenol; Acrylonitrile-divinylbenzene copolymer; Continuous process.

### INTRODUCTION

Phenol ( $C_6H_5OH$ ) is a widely used aromatic compound that can be found in the wastewater of manufacturing processes, such as pharmaceuticals, petroleum refineries, etc. [1, 2]. It is toxic to humans, plants and aquatic organisms at small dosage; therefore, it was classified as a priority pollutant by the United States Environmental Protection Agency. Phenol concentration was limited to  $1 \mu\text{g/L}$  by World Health Organization [1]. Although in order to remove phenol from water resources, different methods such as adsorption, distillation, advanced oxidation processes, etc. have been studied [3], the most favorable is the highly effective low-cost adsorption process [4]. The usage of polymers as adsorbents is promising due to their low cost, easy regeneration, controllable pore structure and high mechanical strength [5].

Since most plants are operated in continuous process, studying under continuous flow is very important for the industrial applications. Studies on phenol removal in a fixed-bed column using activated carbon [6] and polymeric structures [7] have been conducted. Fixed-bed columns have easy

industrial application, offering data on the concentration of pollutants in the effluent as a function of time [8].

The aim of this study is to investigate and model the adsorption of phenol onto acrylonitrile-divinylbenzene copolymer (AN-DVB) in a continuous process. Breakthrough curve data obtained at different column bed heights and flow rates were modeled using Adams & Bohart, Thomas, Yoon & Nelson, Clark and modified-dose response models. Regeneration of AN-DVB polymers using isopropanol was also studied.

### EXPERIMENTAL

#### *Fixed-bed adsorption studies*

A specified amount of AN-DVB was placed in a glass column with glass filter to prevent particle loss. Peristaltic pump was used to constantly feed a  $25 \text{ mg/L}$  phenol solution to the column at room temperature. Samples were gathered at different time intervals and the phenol concentration was measured using UV spectrophotometry at 270 nm. Conditions for the experiments are given in Table 1.

\* To whom all correspondence should be sent:  
E-mail: dilekdur@gmail.com, dduran@yildiz.edu.tr

**Table 1.** Experimental conditions of fixed-bed column studies

Exp. no	C <sub>0</sub> (mg/L)	Weight of adsorbent (g)	Q (mL/min)	Bed height (mm)	D (mm)
1	25.0	0.1722	1	13.73	10.4
2	25.0	0.6888	1	42.51	10.4
3	25.0	0.6888	5	42.51	10.4

• *Analysis of column data*

Column data was analyzed using the equations given below [9]. Effluent volume was calculated using Equation (1):

$$V_{\text{eff}} \text{ (mL)} = Q \cdot t_{\text{total}} \quad (1)$$

where Q is the volumetric flow rate (mL/min) and t<sub>total</sub> is total flow time (min). The amount of phenol adsorbed throughout the column is notated as q<sub>total</sub> and it was calculated using Equation (2) where A is the area under the curve of adsorbed phenol concentration (C<sub>ad</sub> = C<sub>0</sub> - C<sub>t</sub>) against time, and Q is the volumetric flow rate (mL/min).

$$q_{\text{total}} \text{ (mg)} = \frac{Q \cdot A}{1000} \quad (2)$$

Amount of phenol that passed through column was found using Equation (3):

$$m_{\text{total}} \text{ (mg)} = \frac{C_0 \cdot Q \cdot t_{\text{total}}}{1000} \quad (3)$$

Unadsorbed phenol concentration at equilibrium C<sub>eq</sub> (mg/L) was found using Equation (4):

$$C_{\text{eq}} \text{ (mg/L)} = \frac{m_{\text{total}} - q_{\text{total}}}{V_{\text{eff}} 1000} \quad (4)$$

where V<sub>eff</sub> is the effluent solution volume in mL. Total phenol removal was calculated by Equation (5):

$$\text{Total removal of phenol (\%)} = \frac{q_{\text{total}}}{m_{\text{total}}} \cdot 100 \quad (5)$$

The maximum adsorption capacity of the column (q<sub>eq</sub>) was calculated using Equation (6):

$$q_{\text{eq}} \text{ (mg/g)} = \frac{q_{\text{total}}}{X} \quad (6)$$

where X is amount (g) of adsorbent in the column.

Breakthrough capacity was calculated by following the same steps at the breakthrough point.

Effective capacity utilization (%) was calculated using Equation (7):

$$\text{Effective capacity utilization (\%)} = \frac{\text{Breakthrough capacity}}{\text{Total capacity}} \cdot 100 \quad (7)$$

• *Modeling of fixed-bed adsorption data*

Five different models (Adams & Bohart, Thomas, Yoon & Nelson, Clark and modified dose-response) were employed for modeling experimental data. The parameters of the given models were

obtained using a curve fitting toolbox in MATLAB 2022b software.

*Adams & Bohart model.* This model is based on the theory of surface reaction, indicating that the reaction is not immediate. This model assumes that adsorption is related to flow rate, flow concentration and amount of adsorbent. However, this model is more accurate in the initial part of the breakthrough curve (C<sub>t</sub> < 0.5 C<sub>0</sub>) [10, 11]. It is expressed in Equation (8):

$$\frac{C_t}{C_0} = \frac{1}{e^{(k_{AB} \cdot N_0 \cdot \frac{Z}{U} - k_{AB} \cdot C_0 \cdot t)} + 1} \quad (8)$$

where k<sub>AB</sub> (L/mg min) is the Adam & Bohart model's kinetic constant, N<sub>0</sub>(mg/L) is the capacity per volume in fixed bed, Z (mm) is the bed depth of column, U (mm/min) is the linear velocity and C<sub>0</sub> and C<sub>t</sub>(mg/L) are the inlet concentration and outlet concentration, respectively.

*Thomas model.* Thomas model assumes that adsorption is based on a second-order reversible reaction rather than mass transfer, which can be a drawback since interphase mass transfer can have significant control on column adsorption [12]. The Thomas model is expressed in Equation (9):

$$\frac{C_t}{C_0} = \frac{1}{e^{(k_{Th} \cdot q_0 \cdot \frac{X}{Q} - k_{Th} \cdot C_0 \cdot t)} + 1} \quad (9)$$

where k<sub>Th</sub> (mL/min·mg) is Thomas kinetic coefficient, q<sub>0</sub> (mg/g) maximum adsorption capacity, Q (mL/min) volumetric flow rate and X (g) is mass of adsorbent in the column.

*Modified dose-response model.* Modified dose-response model is a regulation of the Thomas model. It reduces the errors of the Thomas model especially in the lower and higher breakthrough curve times [13]. The modified dose-response model is expressed in Equation (10):

$$\frac{C_t}{C_0} = 1 - \frac{1}{\left(\frac{C_0 \cdot Q \cdot t}{q_0 \cdot X}\right)^a + 1} \quad (10)$$

where a is a modified dose-response model's parameter.

*Yoon & Nelson model.* It is based on the assumption that the probability of adsorption for each sorbate molecule is inversely proportional to the probability of sorbate sorption and sorbate breakthrough on the sorbent [12]. Yoon & Nelson model is shown in Equation (11):

$$\frac{C_t}{C_0} = \frac{1}{e^{k_{YN}(\tau-t)} + 1} \quad (11)$$

where  $k_{YN}$  ( $\text{min}^{-1}$ ) is the Yoon–Nelson rate constant and  $t$  (min) is the required time for  $C_t/C_0=0.5$ .

*Clark model.* It was developed on the assumption that mass transfer is present in the entire column and that adsorption occurs according to the Freundlich isotherm [14]. It is expressed in Equation (12).

$$\frac{C_t}{C_0} = \frac{1}{(1+A \cdot e^{(-r \cdot t)})^{\frac{1}{n-1}}} \quad (12)$$

where  $A$  and  $r$  are the Clark model constants and  $n$  is the Freundlich constant.

### Regeneration

The AN-DVB polymers' reusability was evaluated using adsorption-desorption cycles. The used beads were regenerated using isopropanol in a continuous flow column system once each cycle was finished. The polymers were then reintroduced for the following cycle after being thoroughly cleaned with distilled water.

## MATERIALS

Suspension polymerization method was used in the preparation of acrylonitrile-divinylbenzene copolymer (AN-DVB), with hexadecane and toluene (1:9 w/w) as diluents. One-third of the mixture was made up of monomers, and the other two-thirds were made up of inert diluents; the crosslinker level was set as 40%. Full details of the polymerization are given in Duranoğlu *et al.* [15]. Characteristics of AN-DVB are given in Table 2. The porous structure of the polymer was examined by nitrogen adsorption method using the Quantachrome Autosorb-1-C

surface characterization device. The surface area was calculated using the BET (Brunauer, Emet and Teller) method, and the pore volumes were calculated using the DFT (Density Functional Theory) method and nitrogen adsorption isotherms. These calculations were performed automatically using the Autosorb1 software program. Carbon, nitrogen and hydrogen contents were determined by VarioEL III CHNS elemental analyzer.

Nitrogen adsorption-desorption isotherm of AN-DVB is given in Figure 1A. Nitrogen adsorption of AN-DVB copolymer fits type II isotherm according to IUPAC classification, indicating non-porous or macroporous adsorbent. As seen in Table 2, the micropore volume is very low compared to the total pore volume. In addition, AN-DVB contains mostly acidic functional groups. The relatively low porous structure of AN-DVB copolymer beads can be seen on the SEM images given in Figures 1B and 1C.

**Table 2.** Characteristics of AN-DVB

Properties	AN-DVB	Ref.
Product yield (%)	82	
BET surface area ( $\text{m}^2/\text{g}$ )	70	[15]
Pore volume ( $\text{cm}^3/\text{g}$ )	0.1430	[15]
Micropore volume ( $\text{cm}^3/\text{g}$ )	0.0260	[15]
Acidic groups ( $\text{meq/g}$ ) <sup>1</sup>	0.5499	
Basic groups ( $\text{meq/g}$ ) <sup>1</sup>	-	

<sup>1</sup>Measured by Boehm method [16]

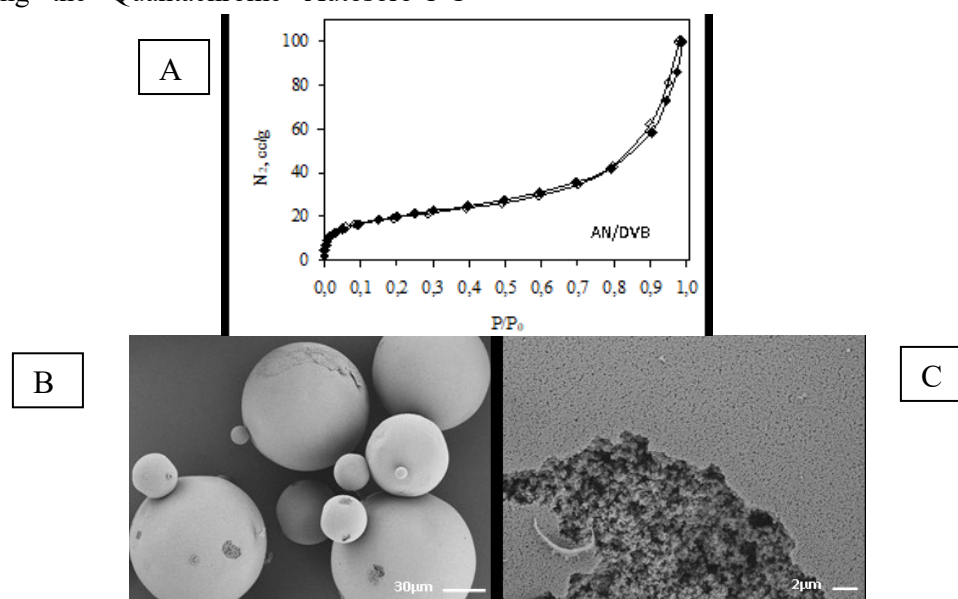


**Figure 1.** A: Nitrogen adsorption-desorption isotherm (♦: adsorption; ◇: desorption); B, C: SEM images

RESULTS AND DISCUSSION

Results of fixed-bed column studies

Breakthrough curves for each experiment are given in Figure 2.  $C_t/C_0$  increased rapidly and linearly and reached the exhaustion point at around 0.82. After exhaustion point, where the adsorbent capacity reached the maximum,  $C_t/C_0$  showed a slower increase.  $C_t/C_0$  data were also plotted against the bed volume (Figure 3), which was calculated using Equation 13:

$$\text{Bed volume} = \frac{V}{\pi \frac{D^2}{4} h} \tag{13}$$

where V is effluent solution volume (mL), D is diameter of column (cm), and h is the height of polymer bed (cm).

The column data analysis results are given in Table 3. The effect of bed height was observed by increasing the amount of AN-DVB from Exp. 1 to Exp. 2. Comparing the breakthrough curves (Figure 3) it can be seen that increasing adsorbent amount increased breakthrough and exhaustion times. The amount of adsorbed phenol ( $q_{\text{total}}$ ), as well as total removal % increased with increase in bed height (Table 3). The effect of flow rate was observed without changing the bed height from Exp. 2 to Exp. 3. Increasing flow rate resulted in decreased breakthrough and exhaustion time and lower adsorption capacity and total removal (Table 3). The breakthrough capacities were calculated for the threshold breakthrough point of 0.20. Effective capacity utilization was calculated (Table 4). Despite

having a shorter residence time and lower total capacity, Exp. 1 showed a higher breakthrough capacity and effective capacity utilization.

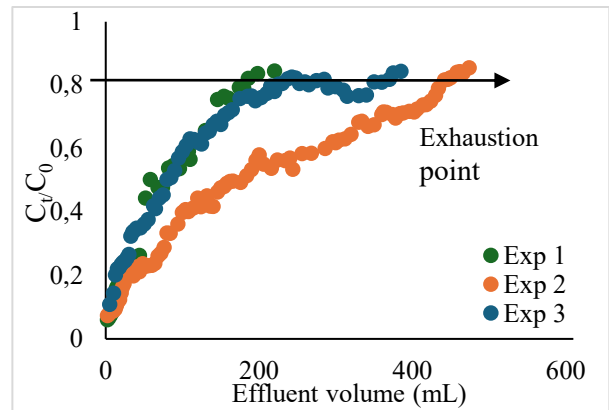


Figure 2. Breakthrough curves for Exps. 1, 2 and 3

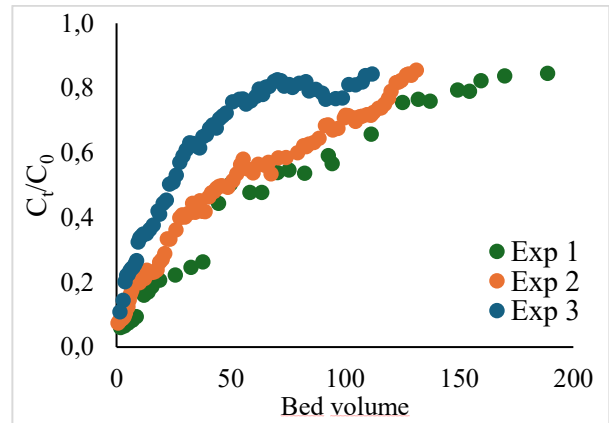


Figure 3. Breakthrough curves with respect to bed volume

Table 3. Results of column data analysis

Exp. no	Bed height (mm)	Adsorbent mass (g)	Q (mL/min)	$V_{\text{eff}}$ (mL)	$q_{\text{total}}$ (mg)	$q_{\text{eq}}$ (mg/g)	Total removal (%)
1	13.73	0.1722	1	186	2.30	13.37	48.74
2	42.51	0.6888	1	442	6.09	8.84	56.69
3	42.51	0.6888	5	238	2.48	3.60	42.97

Table 4. Breakthrough and total capacities

Exp. no	Flow rate Q (mL/min)	Residence time <sup>a</sup> (min)	Breakthrough capacity (mg/g)	Total capacity (mg/g)	Effective capacity utilization (%)
1	1	1.17	2.85	13.37	21.33
2	1	3.61	0.87	8.84	9.84
3	5	0.72	0.39	3.60	10.91

<sup>a</sup> Residence time = Bed volume/Flow rate

*Fixed-bed adsorption modeling*

The obtained Adams & Bohart model constants are given in Table 5. Adams & Bohart rate constant ( $k_{AB}$ ) decreased with the increase in bed height (Exp. 1 to Exp. 2) and increased with increase of flow rate (Exp. 2 to Exp. 3.) while the saturation concentration ( $N_0$ ) decreased with increase of both bed height and flow rate. Correlation coefficient ( $R^2$ ) values show a relatively good fit between the model and the experimental data.

The maximum adsorption capacity,  $q_0$ , and the rate constant,  $k_{th}$ , were calculated for Thomas model. The  $q_0$  values decreased with the increase of flowrate and increase of bed height. The theoretical  $q_0$  values are very close to the experimental values. Relatively

high  $R^2$  values indicate good fitness between the model and the experimental data, however, they are lower compared to the  $R^2$  values of modified dose-response and Clark models. Modified dose-response model parameters were also estimated and given in Table 5. The found  $q_0$  values were not as close as the Thomas model calculated values. However, modified dose-response model was successful in explaining the breakthrough curve as it can be observed in Figure 4, resulting in higher  $R^2$  values. Compared to other models, obtained  $R^2$  values for each experiment were higher, making it the best fitting model. It can be concluded that the modified dose-response model is the most appropriate model to represent phenol continuous adsorption onto AN-DVB.

**Table 5.** Fixed-bed adsorption models' parameters

	Exp. 1	Exp. 2	Exp. 3
<i>Adams &amp; Bohart model</i>			
$k_{AB}$ (L/mg·min)	7.60E-04	2.73E-04	0.0021
$N_0$ (mg/L)	1958.60	1430.70	687.395
$R^2$	0.944	0.938	0.889
<i>Thomas model</i>			
$k_{th}$ (mL/min·mg)	0.76	0.2725	2.1479
$q_{0,theo}$ (mg/g)	13.26	7.50	3.43
$q_{0,exp}$ (mg/g)	13.37	8.84	3.60
$R^2$	0.944	0.938	0.889
<i>Modified dose-response model</i>			
a	1.286	1.0294	1.036
$q_{0,theo}$ (mg/g)	10.442	5.629	2.550
$q_{0,exp}$ (mg/g)	13.372	8.839	3.600
$R^2$	0.976	0.973	0.979
<i>Yoon &amp; Nelson model</i>			
$k_{YN}$ (min <sup>-1</sup> )	0.019	0.007	0.052
$t_{%50,theo}$ (min)	89.87	212.65	19.47
$t_{%50,exp}$ (min)	76.91	86.49	16.00
$R^2$	0.944	0.938	0.889
<i>Clark model</i>			
A	0.062	0.051	0.042
r (min <sup>-1</sup> )	0.014	0.005	0.041
$R^2$	0.969	0.961	0.922

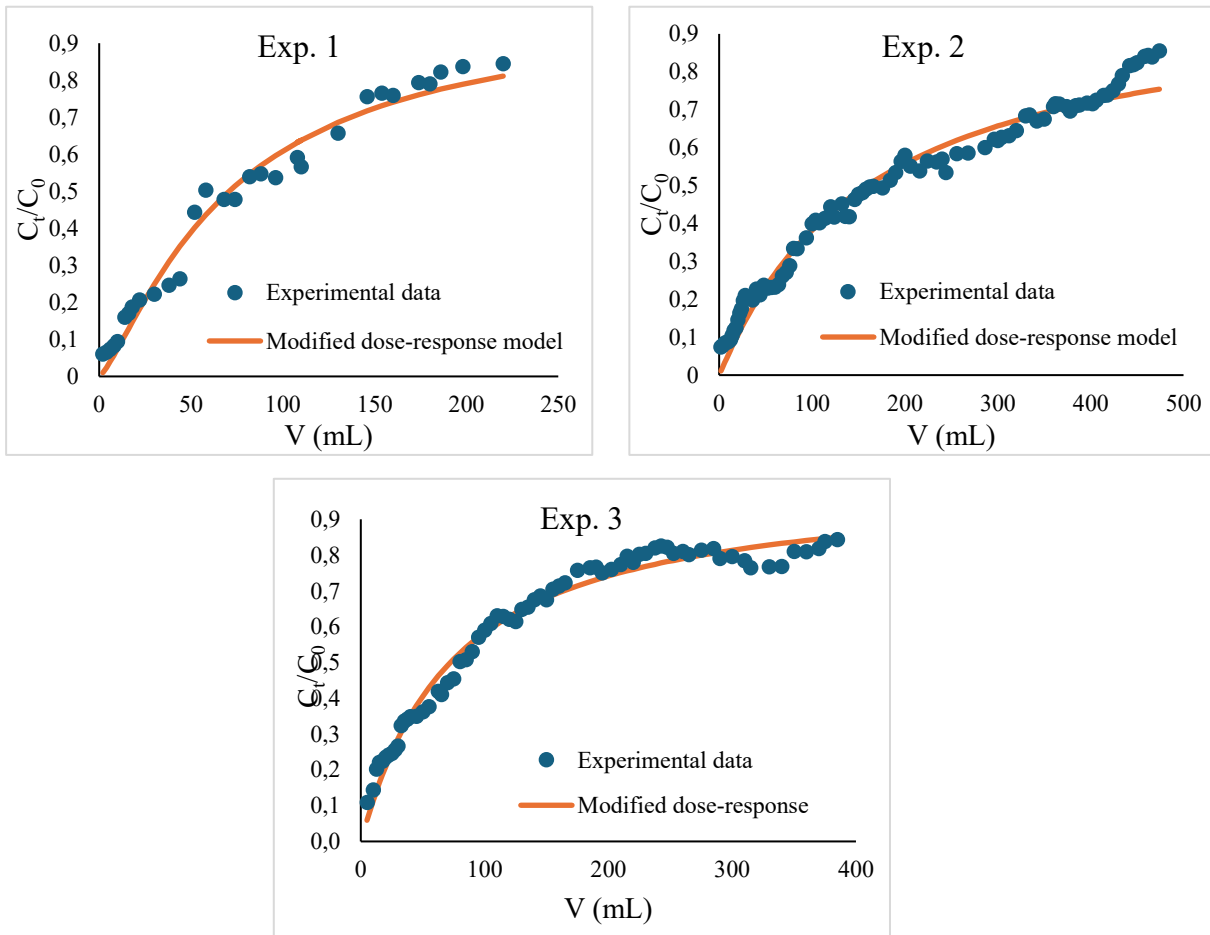


Figure 4. Breakthrough curves of the modified dose-response model

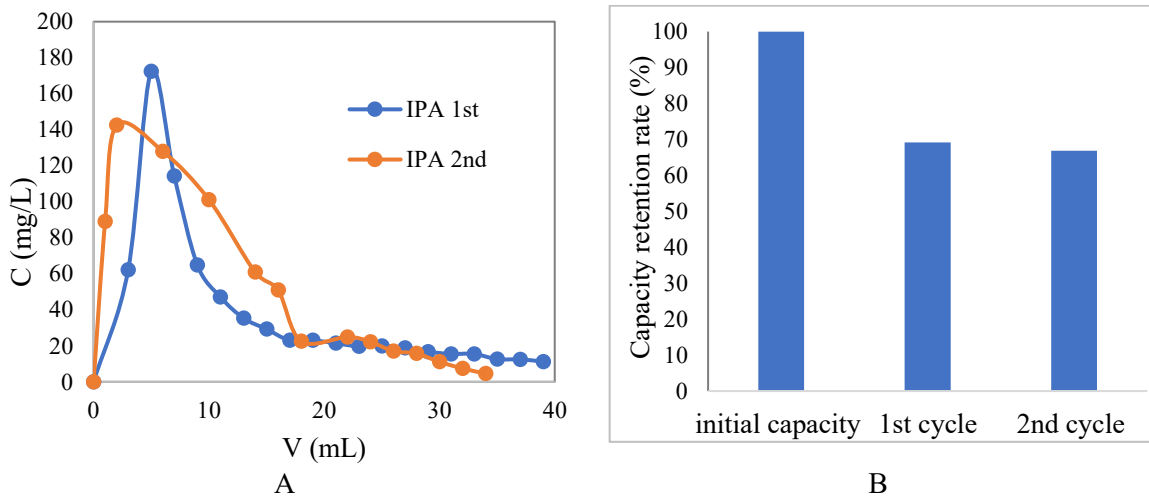


Figure 5. A: Regeneration of AN-DVB beads; B: Adsorption capacity retention rate

Yoon-Nelson model's constants are given in Table 5, where  $k_{YN}$  decreased with increase in the bed height and increased with the increase in the flowrate. Although relatively high  $R^2$  values were obtained like in Thomas and Adams & Bohart models, we cannot describe the adsorption process with Yoon-Nelson model due to the fact that the  $t_{50\%}$  values are not close to the experimental values. Clark model constants were obtained using the Freundlich constant obtained in batch studies. The Clark model

constant A and r decreased as the bed height increased. The  $R^2$  values obtained were higher than for the other models except for the modified dose-response model. As indicated, with Clark model mass transfer plays an important role in the continuous adsorption process. It can be concluded that Clark model can describe the phenol adsorption kinetics on polymer beads in a fixed-bed column.

### Regeneration of the polymer beads

Isopropanol (IPA) was found to be effective in desorption of phenol (Figure 5A) in a very short time. Although there is a drop on the adsorption capacity after regeneration, the regenerated polymers maintained the adsorption capacities after the first cycle (Figure 5B). This suggests that IPA is effective in desorbing phenol from the polymer beads while also maintaining the adsorbent's performance.

### CONCLUSION

Phenol adsorption onto AN-DVB in a fixed-bed column was studied. Increasing bed height resulted in an increase of the breakthrough and exhaustion times, while increasing the flow rate resulted in a decrease of breakthrough and exhaustion times along with a reduced adsorption capacity. The experimental breakthrough curves fitted very well the modified dose-response model. As the modified dose-response model indicates heterogeneous surfaces and variable adsorption energies, it can be concluded that different interactions with different energy levels like hydrogen bonding, dipole-dipole interactions, and  $\pi$ - $\pi$  stacking interactions could be responsible for phenol adsorption onto AN-DVB. On the other hand, Clark model was good in describing the kinetics of the adsorption while Thomas model - in estimation of the maximum adsorption capacity. Due to the Thomas model's simplicity and ease of use, it can be used for preliminary designing and scale-up purposes for industrial applications. Clark model kinetic parameters can also be used to determine the size of the adsorption column and the operating conditions. Isopropanol was found to successfully regenerate

polymer beads through adsorption-desorption cycles.

### REFERENCES

1. Y. Dehmani, D. Dridi, T. Lamhasni, S. Abouarnadasse, R. Chtourou, E. C. Lima, *J. Water Process. Eng.*, **49**, 102965 (2022).
2. K. A. Mohamad Said, A. F. Ismail, Z. Abdul Karim, M. S. Abdullah, A. Hafeez, *Process. Saf. Environ. Prot.*, **151**, 257 (2021).
3. L. G. C. Villegas, N. Mashhadi, M. Chen, D. Mukherjee, K. E. Taylor, N. Biswas, *Curr. Pollu. Rep.*, **2** (3), 157 (2016).
4. J. Zhang, N. Liu, H. Gong, Q. Chen, and H. Liu, *Microporous Mesoporous Mater.*, **336**, 111836 (2022).
5. G. Che-Galicia, J. F. Guayaquil-Sosa, T. Larios-Pachuca, J. A. Galicia-Aguilar, *J. Environ. Chem. Eng.*, **10** (5), 108357 (2022).
6. H. W. Lee, K. J. Kim, A. G. Fane, *Sep. Sci. Technol.*, **32** (11), 1835 (1997).
7. A. Hao, Z. Fu, J. Huang, *Sep. Purif. Technol.*, **311**, 123380 (2023).
8. T. Taweekarn, W. Wongniramaikul, W. Sriprom, W. Limsakul, A. Choodum, *Polym.*, **15**, (19), 3989 (2023).
9. A. P. Lim A. Z. Aris, *Biochem. Eng. J.*, **87**, 50 (2014).
10. R. Han *et al.*, *Chem. Eng. J.*, **149** (1-3), 123 (2009).
11. J. Goel, K. Kadirvelu, C. Rajagopal, V. K. Garg, *J. Hazard Mater.*, **125** (1-3), 211 (Oct. 2005).
12. Z. Aksu F. Gönen, *Process. Biochem.*, **39** (5), 599 (2004).
13. G. Yan, T. Viraraghavan, M. Chen, *Adsorpt. Sci. Technol.*, **19** (1), 25 (2001).
14. R. M. Clark, *Environ. Sci. Technol.*, **21** (1), 573 (1987).
15. D. Duranoğlu, A. W. Trochimczuk, Ü. Beker, *Chem. Eng. J.*, **165** (1), 56 (2010).
16. H. P. Boehm, *Carbon*, **40** (1), 145 (2002).

# Kinetic investigation of methyl violet dye adsorption on agar-agar impregnated activated carbon

B. Hazar, D. Şakar\*

Yildiz Technical University, Chemistry Department, 34220, Esenler, Istanbul, Turkey

Received June 1, 2024; Accepted: August 15, 2024

Agar-agar-impregnated activated carbon (AA-AC) which is a biopolymer-based adsorbent was prepared, characterized *via* FTIR-ATR and used for the adsorption of methyl violet (MV) dye from synthetic waste water. The effects of different reaction parameters such as initial MV concentration, contact time and solution temperature on the adsorption of MV onto AA-AC at constant adsorbent dose were investigated. To determine the best adsorption equilibrium the Freundlich, Langmuir and Temkin models were applied and to determine the adsorption kinetics the pseudo first-order, pseudo second-order and Webber-Morris intraparticle diffusion models were applied.

**Keywords:** Methyl violet dye; Agar-agar impregnated activated carbon; Dye removal; Adsorption isotherms; Kinetic parameters

## INTRODUCTION

Adsorption technique is widely used to cleaning waste water from dyes on industrial and lab scale as it is simple, cost-effective and easily applicable [1]. Activated carbons in granular or powdered form obtained from waste materials or commercially available are the most widely used sorbents in adsorption technique because of their excellent sorption capability for inorganic pollutants in industry [2, 3]. Especially dyes are a problem of the waste water in the textile industry [4]. Methyl violet (MV) dye, a harmful basic dye, is used in textile industry. *Saba senegalensis* shell residue-based activated carbon [5] and hydrolyzed polyacrylamide nanocomposite grafted onto xanthan gum, or incorporated in nanosilica [6] were successfully used to remove MV from waste water. Agar-agar is a porous galactose polymer. Agar-agar-impregnated activated carbon (AA-AC) is a biopolymer-based adsorbent which has been successfully used to remove  $Pb^{+2}$  from water [7].

In the present study, the preparation of agar-agar-embedded activated carbon adsorbent obtained by

physical mixing of activated carbon with an agar-agar solution is reported. FTIR-ATR spectral analysis was used to confirm the presence of agar-agar on the activated carbon. The AA-AC adsorbent was used to remove MV from synthetic waste water solutions. Three kinetic and isotherm models were applied.

## EXPERIMENTAL

Activated carbon, methyl violet ( $C_{24}H_{27}N_3ClH$ ) and agar-agar were purchased from Fluka, Merck and Sigma-Aldrich, respectively (Fig. 1). Activated carbon powder (5 g) was impregnated by mixing with 3.75 g of agar-agar in 50 ml of hot water at 85 °C for 24 h. After impregnation, AA-AC was washed three times with cold water to remove non-adsorbed agar-agar from the medium and was dried in a vacuum oven at 100 °C. Thermo Fischer brand Nicolet 10 model FTIR-ATR spectrophotometer, Sigma brand 3-18K model ultracentrifuge device, Shimadzu brand Uvmini-1240 UV-Visible spectrophotometer and Daihan Scientific multi-heat mixer were used.

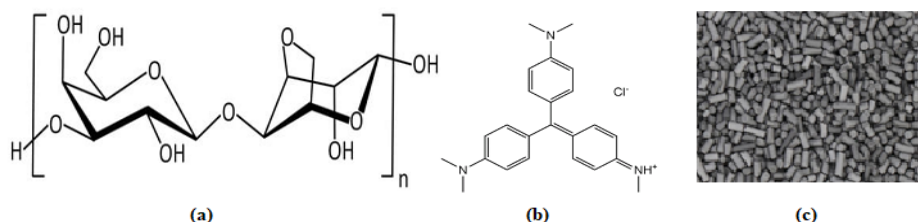


**Figure 1.** Chemical structures of agar-agar (a), methyl violet dye (b) and image of granulated activated carbon (c)

\* To whom all correspondence should be sent:  
E-mail: dsakar@yildiz.edu.tr

The concentrations of methyl violet in synthetic waste water solution and in an aqueous solution were determined using a double-beam visible spectrophotometer at a wavelength of 578 nm (Figure 2).

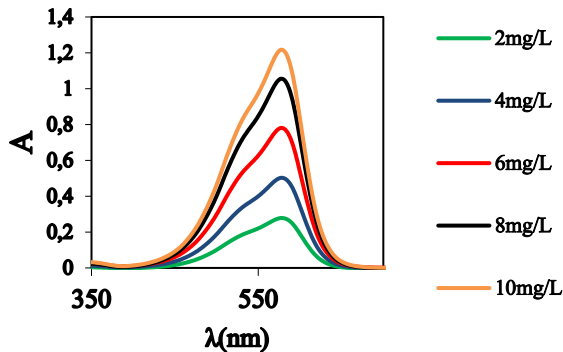


Figure 2. Absorbance changes of different concentrations of MV in pure water

A calibration curve ( $A=0.1215C+0.0379$ ,  $R^2 = 0.993$ ) (Figure 3) was constructed from the absorbance values of 2-4-6-8-10 mg/l of MV dye solutions prepared by dilution from 1000 mg/l stock solution in water.

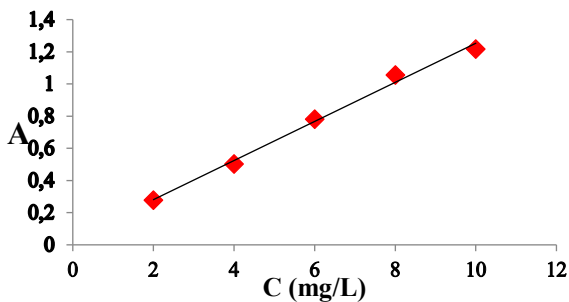


Figure 3. Calibration curve for MV in pure water

Methyl violet removal was carried out from synthetic wastewater solutions by adsorption on AC and AA-AC. In all measurements, the amount of adsorbent was kept constant at 80 mg and the mixing speed was kept constant at 300 rpm. In the adsorption experiments, the effects of time (30-60-90-120-150-180-210-240 min at room temperature in 50 mg/L MV solution), temperature (20-25-30-35-40-45-50 °C in 50 mg/L MV solution for 150 min) and initial concentration (50-100-150-200-250-300-350-400-450-500 mg/L for 150 min at room temperature) were examined.

The dye removal yield percentage (RY, %) of MV was calculated by using Eq.1 [8]:

$$\%RY = \frac{(C_0 - C_e)}{C_0} \cdot 100 \quad (1)$$

The adsorption capacity of AC and AA-AC, the amount of MV adsorbed at equilibrium, was calculated by using Eq. 2:

$$q_e = \frac{(C_0 - C_e) \cdot V}{w} \quad (2)$$

where  $q_e$  (mg/g) is the adsorbed amount of MV per gram adsorbent,  $C_0$  (mg/L) and  $C_e$  (mg/L) are MV dye solution concentration at the initial and equilibrium stages, respectively.  $V$  (L) is the volume of the MV solution, and  $w$  (g) is the amount of the AC and AA-AC adsorbents.

## RESULTS AND DISCUSSION

To determine the chemical composition of the agar-agar-impregnated activated carbon adsorbent, FTIR-ATR analysis was conducted and the FTIR-ATR spectra of AC and AA-AC are given in Figure 4.

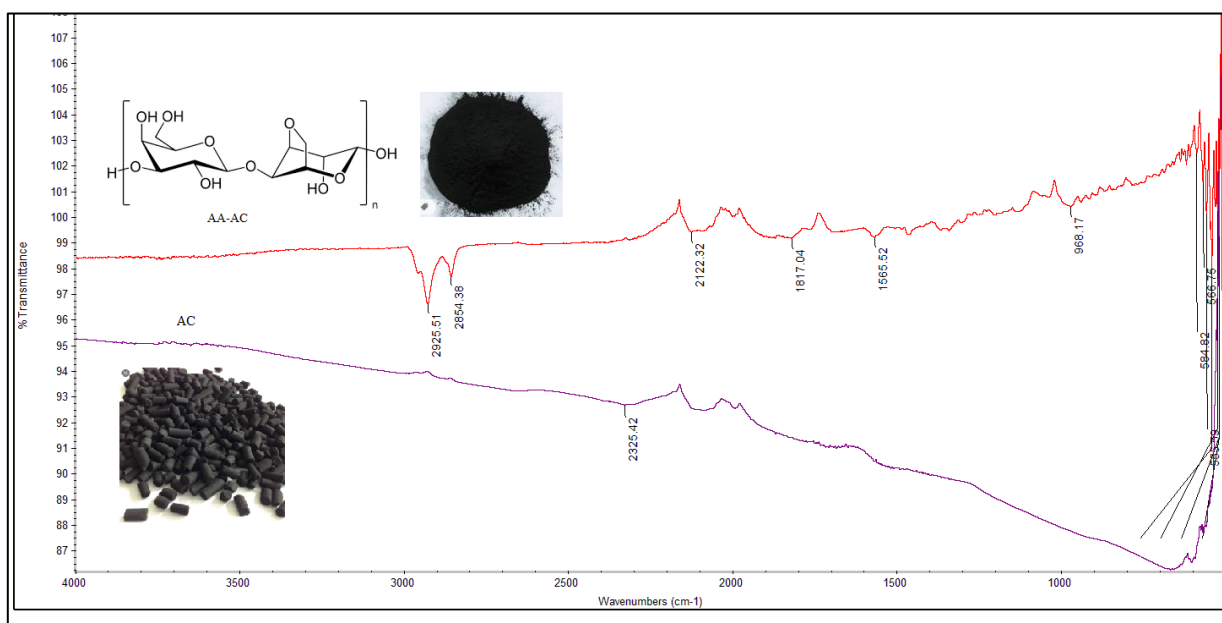


Figure 4. FTIR-ATR spectra of AC and AA-AC

The new peaks observed are: the absorption peak of agar-agar at 2925 cm<sup>-1</sup> (O–H stretching vibration of hydroxyl group), and at 968 cm<sup>-1</sup> (C–O stretching vibration of pyranose ring). In order to investigate the effect of contact time on dye adsorption and to determine the optimum retention time for the adsorption capacity, the adsorption removal efficiencies of AC and AA-AC were examined for 30-60-90-120-150-180-210-240 min from a solution containing 50 mg/L of dye. After the corresponding

time passed, the batches were centrifuged for 10 min, the adsorption values of the solutions were taken on a UV-VIS spectrophotometer, C<sub>e</sub> values were found from the calibration curve according to their absorbance at 578 nm, and dye removal yield percentage (RY, %) and adsorption capacity, q<sub>e</sub> of AC and AA-AC adsorbents were calculated according to Eqs. 1 and 2, respectively. The results are given in Table 1.

**Table 1.** Contact time effect: MV dye solution concentration at the equilibrium stage, dye removal yield percentage and adsorption capacity of AC and AA-AC adsorbents

t (min)	AC				AA-AC			
	A	C <sub>e</sub> (mg/L)	RY (%)	q <sub>e</sub> (mg/g)	A	C <sub>e</sub> (mg/L)	RY (%)	q <sub>e</sub> (mg/g)
30	3.84	31.3	37.4	29.2	2.84	23.1	53.9	42.1
60	4.87	39.8	20.5	15.9	3.24	26.4	47.2	36.9
90	4.77	38.9	22.0	17.2	2.95	23.9	52.1	40.7
120	4.27	34.9	30.2	23.6	2.97	24.1	51.7	40.4
150	3.25	26.5	47.0	36.8	3.01	24.5	50.9	39.8
180	4.34	35.4	29.2	22.8	2.76	22.4	55.1	43.1
210	5.06	41.4	17.2	13.4	2.90	23.5	52.9	41.3
240	5.09	41.6	16.8	13.1	3.08	25.0	49.9	38.9

**Table 2.** Effect of temperature on adsorption of MV by AC and AA-AC

T (°C)	AC				AA-AC			
	A	C <sub>e</sub> (mg/L)	RY (%)	q <sub>e</sub> (mg/g)	A	C <sub>e</sub> (mg/L)	RY (%)	q <sub>e</sub> (mg/g)
20	3.85	31.4	37.2	29.1	3.78	30.8	38.5	30.0
25	3.82	31.2	37.6	29.4	3.70	30.6	38.7	30.0
30	3.83	31.3	37.4	29.2	3.77	30.8	38.5	30.1
35	3.81	31.1	37.7	29.5	3.79	30.9	38.1	29.8
40	3.78	30.9	38.3	29.9	3.78	30.8	38.5	30.0
45	3.80	30.9	38.0	29.7	3.70	30.6	38.7	30.3
50	3.80	31.0	38.0	29.7	3.70	30.6	38.7	30.4

The optimum removal efficiency was determined at 150 min for AC and at 180 min for AA-AC.

The rate of MV adsorption on AA and AA-AC adsorbents was investigated at temperatures of 20-25-30-35-40-45-50 °C in a 50 mg/L MV solution for 150 min. As seen in Table 2, dye removal yield percentage and adsorption capacity of adsorbents at equilibrium did not significantly change with increased temperature.

#### Adsorption isotherms

The adsorption isotherm expresses the relationship between the amount of substance adsorbed at constant temperature and the equilibrium pressure or equilibrium concentration. In this study, the Freundlich and Temkin adsorption isotherms were applied. The non-linear Freundlich equation is given according to Eq. 3[9]:

$$q_e = K_F C_e^{1/n} \quad (3)$$

where K<sub>F</sub>(L/mg) is the Freundlich constant. The linear Freundlich equation is given in Eq. 4 and applied for MV dye adsorption (initial MV concentrations: 50-100-150-200-250-300-350-400-450-500 mg/L for 150 min at room temperature) on AC and AA-AC adsorbents.

$$\log q_e = \log K_F + \left(\frac{1}{n}\right) \log C_e \quad (4)$$

For the Freundlich adsorption isotherm, the linear log q<sub>e</sub> versus log C<sub>e</sub> plot was drawn and the kinetic parameters, n and K<sub>F</sub>, were obtained from the slope and the intersection point of the linear plot, respectively, and are given in Table 3.

The Freundlich isotherms for AC and AA-AC are given in Figs. 5 and 6.

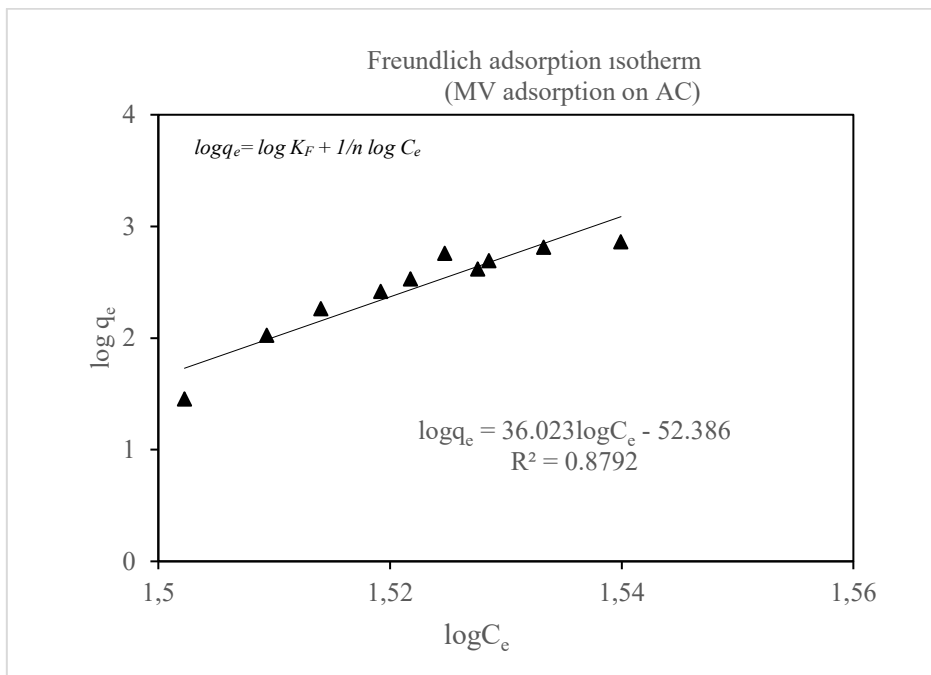


Figure 5. Freundlich isotherm for MV dye adsorption on AC

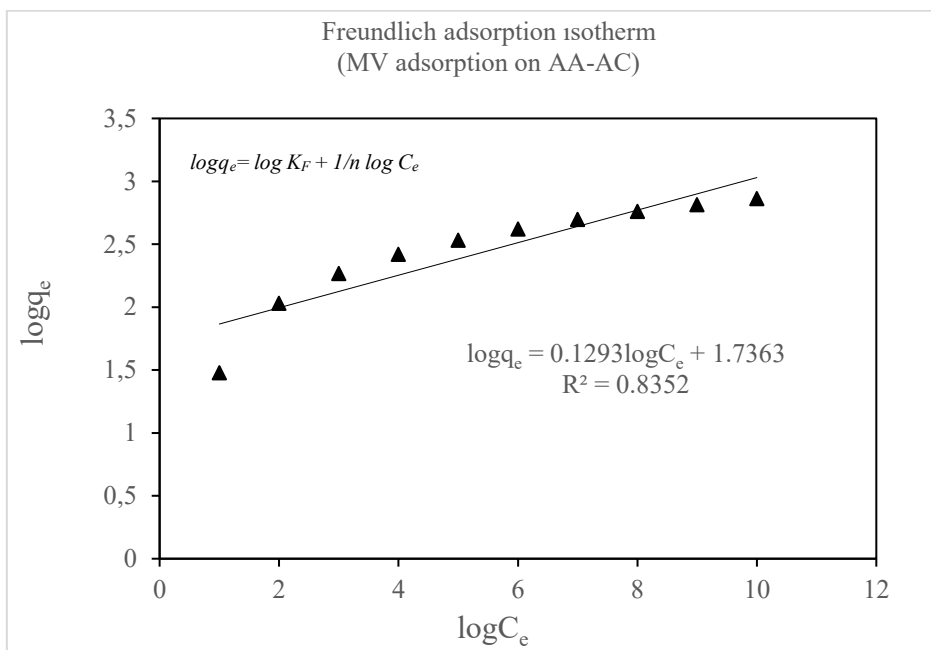


Figure 6. Freundlich isotherm for MV dye adsorption on AA-AC

The linear Temkin equation is given in Eq. 5 [10]:

$$q_e = \frac{RT}{b} \ln A + \frac{RT}{b} \ln C_e \quad (5)$$

where R is the universal gas constant ( $J \text{ mol}^{-1} \text{ K}^{-1}$ ), T is temperature (K), A is Temkin isotherm equilibrium binding constant ( $L \cdot g^{-1}$ ), b is Temkin isotherm constant.

For the Temkin adsorption isotherm, the linear  $q_e$  versus  $\ln C_e$  plot was drawn and the Temkin adsorption isotherm parameters, A and b were obtained from the slope and the intersection point of this linear plot, respectively, and the results were given in Table 3.

The Temkin isotherms for AC and AA-AC are shown in Figs. 7 and 8.

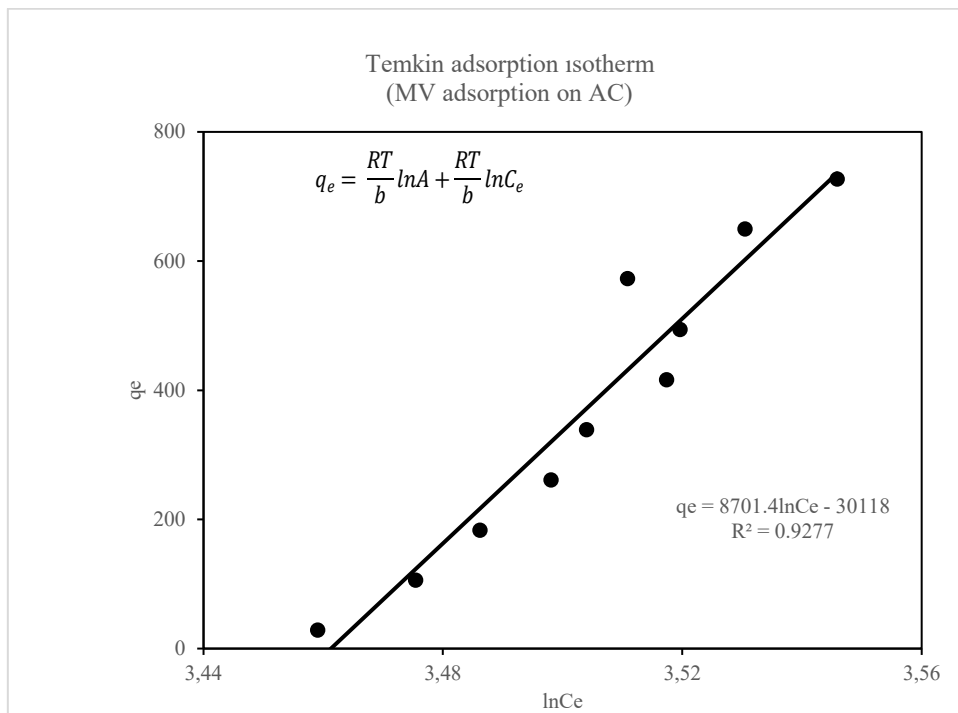


Figure 7. Temkin isotherm for MV dye adsorption on AC

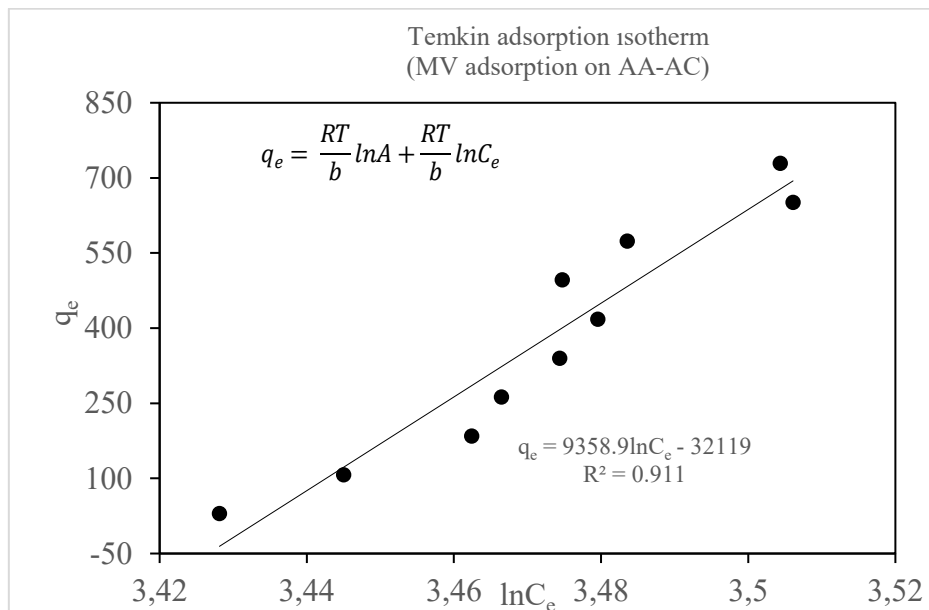


Figure 8. Temkin isotherm for MV dye adsorption on AA-AC

Table 3. Graphically determined parameters for Freundlich and Temkin isotherm models based on experimental studies

Isotherm		AC	AA-AC
Freundlich	logK <sub>F</sub> (L.mg <sup>-1</sup> )	-52.4	1.7
	n	0.028	7.74
	R <sup>2</sup>	0.879	0.835
Temkin	lnA	-3.46	-3.43
	b	0.28	0.26
	R <sup>2</sup>	0.928	0.911

**Table 4.** Adsorption kinetics parameters for MV adsorption on AC and AA-AC

Kinetic Model	Parameters	AC	AA-AC
Pseudo 1 <sup>st</sup>	$k_1$	0.0012	0.0002
	$R^2$	0.068	0.008
Pseudo 2 <sup>nd</sup>	$k_2$	0.0023	0.0448
	$R^2$	0.798	0.993
WM ID	$k_3$	0.746	0.0539
	C	29.852	39.812
	$R^2$	0.0958	0.0093

According to the regression coefficients of these two isotherms, it was concluded that the experimental adsorption data fit well the Temkin isotherm model (Table 3).

#### Adsorption kinetics studies

Adsorption kinetics is used to show what kind of mechanism plays a role during the adsorption of the adsorbed substance onto the adsorbent surface. To determine the kinetics of MV removal from synthetic waste water solutions *via* AC and AA-AC, the pseudo-first [11], pseudo second order [12] and Webber-Morris intraparticle diffusion models (WM ID) [13] were tested by fitting the experimental data as shown in Eqs. 5, 6 and 7, respectively.

$$\ln(q_e - q_t) = \ln q_e - k_1 t \quad (5)$$

$$\frac{t}{q_t} = \frac{1}{k_2 q_e^2} + \frac{1}{q_e} t \quad (6)$$

$$q_t = k_3 t^{\frac{1}{2}} + C \quad (7)$$

In the equations,  $q_t$  and  $q_e$  (mg. g<sup>-1</sup>) are the amounts of MV adsorbed at various  $t$  times and equilibrium,  $k_1$  (min<sup>-1</sup>),  $k_2$  (g.mg<sup>-1</sup>. min<sup>-1</sup>) and  $k_3$  (mg.g<sup>-1</sup>. min<sup>-1/2</sup>) are the pseudo-first-order, pseudo-second-order and intraparticle diffusion model rate constants, respectively.  $C$  in Eq. 7 is the intercept related to the thickness of the boundary layer. The kinetic parameters for the adsorption of MV on AC and AA-AC adsorbents are given in Table 4.

Comparing the correlation coefficients of the three kinetic models, it is seen that the kinetics of MV adsorption onto AC and AA-AC followed the pseudo-second-order model.

#### CONCLUSION

The aim of this study was to develop a biopolymer-impregnated activated carbon adsorbent for the treatment of synthetic waste water containing

methyl violet dye by the adsorption technique. The plot of the adsorption isotherms showed that the Temkin model better represents the adsorption of methyl violet on AA-AC adsorbent. The kinetic studies proved that the adsorption of MV on AA-AC adsorbent fits the pseudo-second-order kinetic model with good correlation. The maximum MV removal yield with AA-AC adsorbent was obtained at 180 min as 55%.

#### REFERENCES

1. R. J. Ganaie, S. Rafiq, A. Sharma, *IOP Conf. Series: Earth and Environmental Science*, 1110 012040, (2023).
2. P. K. Malik, *Journal of Hazardous Materials*, **113** (1-3) (2004).
3. S. Ho, *Journal of Geoscience and Environment Protection*, **8** (5) (2020).
4. T. Robinson, G. McMullan, R. Marchant, P. Nigam, *Bioresource Technology*, **77**(3), 247 (2001).
5. M. Ndoye, M. Faye, C. Kane, A. Diop, M. Diop, *Journal of Geoscience and Environment Protection*, **11**, 197 (2023).
6. S. Ghorai, A. Sarkar, M. Raoufi, A. B. Panda, H. Schönherr, S. Pal, *ACS Applied Materials & Interfaces*, **6**(7) (2014).
7. S. Saidi, F. Boudrahem, I. Yahiaoui, F. Aissani-Benissad, *Water Science and Technology*, **79** (7), 1316 (2019).
8. M. Vanderborght, E. Van Grieken, *Anal. Chem.*, **49**(2), 311 (1977).
9. N. D. Hutson, R. T. Yang, *J. Colloid Interf. Sci.*, 189 (2000).
10. M. Temkin, V. Pyzhev, *Acta Physicochimica U.R.S.S.*, **12**, 327 (1940).
11. S. Lagergren, *Kungliga Svenska Vetenskapsakademiens Handlingar*, **24** (4), 1 (1898).
12. Y. S. Ho, G. McKay, *Process Safety and Environmental Protection*, **76** (2), 183 (1998).
13. W. J. Weber, J. C. Morris, *Journal of the Sanitary Engineering Division*, **89** (2), 31 (1963).

## Drying kinetics, mathematical modeling and color analysis of *Solen marginatus*: A comparative study of oven, infrared, and microwave drying methods

Z. O. Ozyalcin, A. S. Kipcak\*

Department of Chemical Engineering, Faculty of Chemistry and Metallurgy Engineering, Yildiz Technical University, Davutpasa Campus, Davutpasa Street No. 127, Esenler, 34220 Istanbul, Türkiye

Received June 11, 2024; Accepted: August 17, 2024

This study investigates the drying kinetics and mathematical modeling of *Solen marginatus*, commonly known as the grooved razor shell. *Solen marginatus* is dried using three different methods: oven drying (OD), infrared drying (IRD), and microwave drying (MWD), each at various temperatures and power levels. The effects of drying equipment, temperatures, and power levels on drying time, drying rate, effective moisture diffusivity, and activation energy are analyzed, with color analysis performed for each method. Fourteen well-known mathematical models are applied, and the three models with the highest coefficient of determination ( $R^2 > 0.999$ ) are selected. Results indicate that drying time decreases with increasing temperature or power of the equipment. The effective moisture diffusivities range from  $2.00 \times 10^{-10} - 3.53 \times 10^{-10} \text{ m}^2/\text{s}$  in OD,  $2.53 \times 10^{-10} - 6.02 \times 10^{-10} \text{ m}^2/\text{s}$  in IRD, and  $4.08 \times 10^{-9} - 9.34 \times 10^{-9} \text{ m}^2/\text{s}$  in MWD. The activation energies for OD, IRD, and MWD are calculated as 27.83 kJ/mol, 42.35 kJ/mol, and 40.98 kJ/kg, respectively. In terms of color retention, IRD was found to be the most effective drying method followed by oven and then MWD.

**Keywords:** clam, drying kinetics, grooved razor shell, mathematical modeling, seafood

### INTRODUCTION

*Solen marginatus* is a bivalve characterized by two long narrow shell valves open at both ends but connected by hinges. They can be found buried in sandy-muddy seashore areas since they can adapt greatly to tides and soft sediments [1, 2]. This species is distributed from Norway to the Mediterranean Sea and North Africa; it is the only species that belongs to *Solenidae* genus in Europe [3]. *Solen marginatus* has high importance in the crustacean industry. It is seen to be sold at high prices at the international market. Since it can be used for various foods, *Solen marginatus* has become one of the competitors among crustaceans [2].

Seafood is highly perishable due to its high water content and the presence of spoilage-causing microorganisms. The spoilage mechanisms in seafood can lead to changes in color, texture, odor, and taste, making it unsafe for consumption [4]. Drying processes are crucial for seafood preservation as they remove moisture, inhibiting the growth of spoilage microorganisms and preventing enzymatic reactions that lead to deterioration [5].

In recent years, there has been a surge in interest in utilizing advanced drying techniques for seafood processing. Various methods such as microwave, infrared, and oven drying have been investigated to improve the quality and efficiency of seafood drying

processes [6]. Infrared drying, for example, has garnered attention for its ability to offer superior heating uniformity, leading to enhanced quality characteristics compared to traditional methods [7]. Additionally, combined infrared and convective drying methods have been recognized for their rapid and effective heat transfer, resulting in seafood products with improved organoleptic properties [8].

Similar to the increasing consumption rates, there are many seafood drying studies in the literature. In the recent past, studies on seafood such as sea cucumber [9, 10], calamari [11], squid [12], clam [13], crab [14], yellow croaker [15], grass carp [16], and sea bass [17] have been carried out using different drying equipment such as oven, hot-air, infra-red, microwave, and lyophilizator. Despite the studies conducted with many seafood products, there is a lack of literature on drying studies with *Solen marginatus*, which has found its place in many exclusive cuisines.

In this study, the drying performance of *Solen marginatus* at different temperatures was investigated to understand the oven, vacuum oven, and microwave drying kinetics. In order to better comprehend the drying mechanism of *Solen marginatus*, the compatibility with fourteen mathematical models was tested. In addition, the effective moisture diffusion coefficient was calculated and the effects of different methods and temperatures on color change were determined by color analysis.

\* To whom all correspondence should be sent:

E-mail: [skipcak@yildiz.edu.tr](mailto:skipcak@yildiz.edu.tr)

## MATERIAL AND METHODS

### *Samples and equipment*

*Solen marginatus* samples were obtained frozen from a local fish market in Enez, Edirne, Turkey, and were kept in a refrigerator (1050T model; Arcelik, Eskisehir, Turkey) at -18 °C until the experiments. Before drying, the samples were thawed at +4 °C and rinsed with deionized water to remove sand and other admixtures. The internal organs of the samples were cleaned, and the remaining excess water was gently drained. The samples prepared with a length of  $9 \pm 0.8$  cm and a thickness of  $0.3 \pm 0.02$  cm were transferred to the drying process (Figure 1).

Initial moisture percentages of the samples were removed by drying at 105 °C in a Nüve EV-18 (Nüve, Ankara, Turkey) oven for 3 h. Oven drying (OD) was carried out in the same model oven, infrared drying (IRD) was carried out in a MA 50.R model infrared moisture analyzer (Radweg Balances and Scales, Radom, Poland) and microwave drying (MWD) was completed in a home-type Delonghi MW205S model microwave (Delonghi, Treviso, Italy).

### *Drying experiments*

OD and IRD temperatures were selected as 60, 70, and 80°C and the samples' weight was noted at intervals of 15 min for each temperature level. In the third method, MWD was used at 140, 210, and 350 W. The samples' weight was recorded for 140 W at intervals of 30 sec and for 210 and 350 W at intervals of 1 min. Drying proceeded until the moisture in the product decreased to 5%. The samples were cooled at room temperature when the drying was finished. Afterwards, dried samples, which are shown in Figure 1, were packed into polyethylene bags and were placed in a desiccator to keep safe from moisture.

### *Mathematical modeling of drying curves*

In drying processes, a diffusion equation is commonly used to explain mass transfer phenomena.

The diffusion coefficient in this equation, which is influenced by moisture content, is crucial for understanding the drying process and is typically determined through experiments. This coefficient can be obtained either by analyzing drying curves or by deriving it from experimental moisture concentration data collected during the drying process [18]. The moisture content and the moisture rate of *Solen marginatus* are calculated using Eqns. (1) and (2) [17].

$$M = \frac{m_w}{m_d} \quad (1)$$

$$MR = \frac{M_t - M_e}{M_i - M_e} \quad (2)$$

As  $M_e$  value is rather small compared to  $M_t$  and  $M_i$ , it is usually neglected in the calculations. Drying rate, which indicates the rate of moisture release from a material's surface, is a crucial parameter in drying processes. It can be mathematically expressed using Eqn (3) to quantify the rate of moisture removal over time [17, 19].

$$DR = \frac{M_{t+\Delta t} - M_t}{\Delta t} \quad (3)$$

Fick's second law of diffusion is commonly used to explain the moisture diffusion process during drying. Effective moisture diffusivity encompasses various mass transfer mechanisms within foods, including liquid diffusion, vapor diffusion, surface diffusion, capillary flow, and hydrodynamic flow. Understanding moisture diffusivity and its variations under different drying conditions is essential for optimizing drying processes and ensuring product quality [20]. Additionally, determining effective moisture diffusivity and activation energy aids in comprehending the drying behavior of specific products [21].

While different geometries require different calculations in the use of Fick's second law, *Solen marginatus* was used as a thin layer in the drying processes and the moisture amount was calculated with Eqn. (4) [17].

$$MR = \frac{8}{\pi^2} \sum_{n=1}^{\infty} \frac{1}{(2n+1)^2} \exp\left(-\frac{(2n+1)^2 \pi^2 D_{eff} \times t}{4L^2}\right) \quad (4)$$

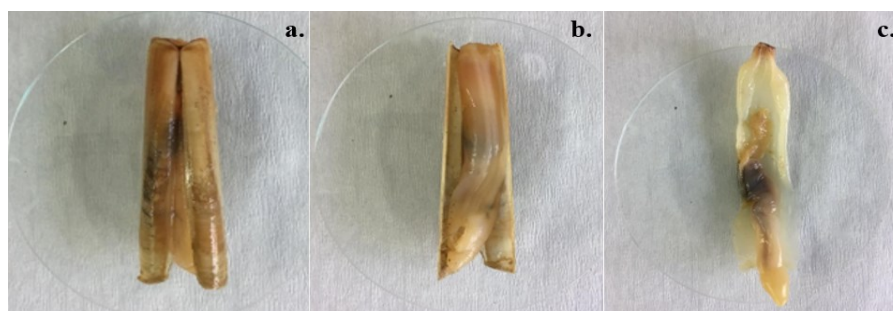


**Fig. 1.** Preparation of *Solen marginatus* sample for drying (a. shell view, b. meat view, c. meat view without the shell)

In the equation,  $t$  is the drying time in sec and  $L$  is the sample half-thickness in m. Since the initial terms have no bearing on the outcome, Eqn. (4) can be simplified to Eqn. (5). The slope of the graph  $\ln(MR)$  vs  $t$ , which is created using the data collected during experiments, can be used to determine  $D_{eff}$  [17].

$$\ln(MR) = \ln\left(\frac{8}{\pi^2}\right) - (\pi^2 \frac{D_{eff} \times t}{4L^2}) \quad (5)$$

While oven and IR dryers are operated with a temperature parameter the MW is operated with a power parameter. Therefore, temperature-based (Eqn. 6) and power-based (Eqn. 7) Arrhenius equations were used when calculating  $E_a$  [17].

$$D_{eff} = D_0 \exp\left(-\frac{E_a}{R(T+273.15)}\right) \quad (6)$$

$$D_{eff} = D_0 \exp\left(-\frac{E_a \times m}{P}\right) \quad (7)$$

Activation energy is determined *via* the slope ( $E_a/R$ ) of the  $D_{eff}$  versus  $1/T$  plot constructed from experimentally obtained data.

To find the most fitted model, coefficient of determination ( $R^2$ ), root-mean-square error (RMSE) and reduced chi-square statistic ( $\chi^2$ ) values were calculated using Eqns. (8) - (10). Drying data were tested for Aghbashlo *et al.*, Alibas, Henderson *et al.*, Jena and Das, Lewis, Logarithmic, Midilli & Kucuk, Page, Parabolic, Peleg, Two-term exponential, Verma *et al.*, Wang *et al.* and Weibull models using nonlinear regression method in Statistica (Statistica, 2016) [22].

$$R^2 = 1 - \frac{\sum_{i=1}^n (MR_{exp,i} - MR_{pre,i})^2}{\sum_{i=1}^n (MR_{exp,i} - \frac{1}{n} \sum_{i=1}^n MR_{exp,i})^2} \quad (8)$$

$$RMSE = \left(\frac{1}{n} \sum_{i=1}^n (MR_{exp,i} - MR_{pre,i})^2\right)^{1/2} \quad (9)$$

$$\chi^2 = \frac{\sum_{i=1}^n (MR_{exp,i} - MR_{pre,i})^2}{n-z} \quad (10)$$

The equations denote the following:  $n$  is the total number of experiments;  $z$  is the number of constants in the proposed model;  $MR_{exp}$  stands for the experimental moisture content values; and  $MR_{pre}$  stands for the predicted moisture content values.

$R^2$  values are intended to be near 1 when choosing the best model for the approaches. Conversely, it is anticipated that RMSE and  $\chi^2$  values will be near zero.

### Color analysis

The color of food products is one of the first aspects noticed by consumers, influencing their initial perception and acceptance of the product [23]. The Hunter Lab color system is extensively used in the food industry for color analysis due to its effectiveness and prevalence. This system measures parameters such as  $L^*$  (lightness/darkness),  $a^*$  (redness/greenness), and  $b^*$  (yellowness/blueness), providing a comprehensive assessment of color changes in food products [24]. Color analysis was performed by PCE-CSM1 colorimeter (PCE Instruments UK Ltd., Southampton Hampshire, United Kingdom). Color parameters of the samples were measured before and after the experiments for each method and equipment and total color change was calculated from Eqn. (11) [22].

$$\Delta E = \sqrt{(L_0 - L)^2 + (a_0 - a)^2 + (b_0 - b)^2} \quad (11)$$

### RESULTS AND DISCUSSION

After conducting a moisture analysis to ascertain the overall moisture content, it was discovered that *Solen marginatus* had an initial moisture content of 77.42% on a wet basis. The samples were dried until their moisture level dropped to under 5%. Figure 2 depicts the appearance of *Solen marginatus* during sample preparation and drying.

The moisture content vs. time and drying rate vs. moisture content graphs shown in Figure 2 were created using the weighing data collected during drying. Looking at the plots in Figure 2, the drying rate increases with increasing temperature and power, as expected, and the drying times varied with the type of dryer. Drying took place for 255, 195 and 150 min at 60°C, 70°C and 80 °C for OD, 210, 135 and 90 min at 60°C, 70°C and 80 °C for IRD and 11, 7 and 5.5 min at 140, 210 and 350 W for MWD.



**Fig. 2.** *Solen marginatus* sample before and after drying (a. meat without the shell, b. cleaned meat, c. oven dried meat)

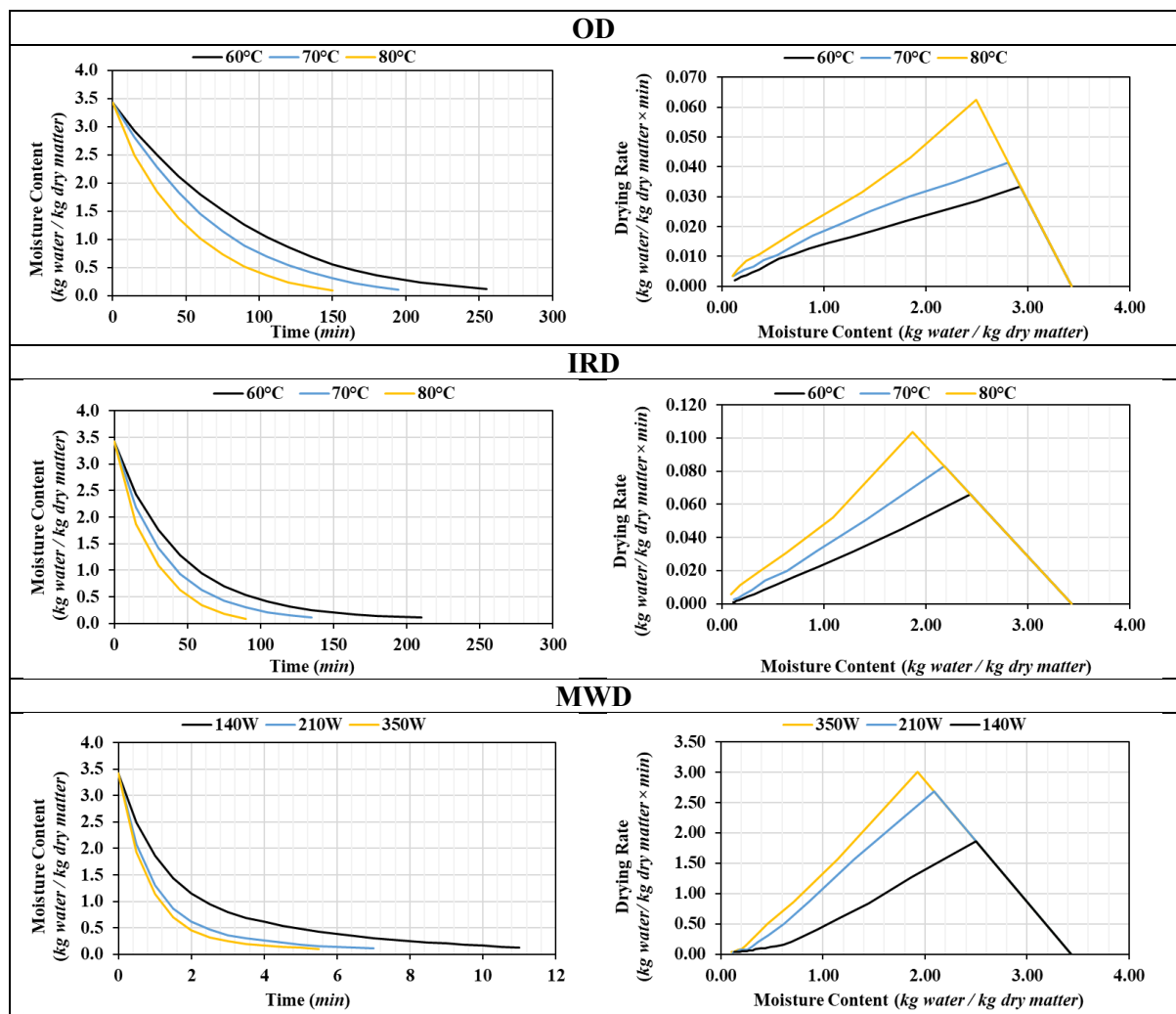


Fig. 3. Graphs of moisture content vs. time (left) and drying rate vs. moisture content (right)

It has been emphasized in the literature that practical drying of biological products mainly takes place in the falling rate period, as the conditions required for constant rate drying are rare [25]. In line with this, it can be seen that drying was carried out in the decreasing rate period for all temperatures and dryers. It can be seen that drying times are longer and final moisture contents are higher for OD compared to IRD and MWD. When evaluated on the basis of drying time, it can be interpreted that the OD process is comparatively inefficient. MWD is highlighted in the literature as the method with the shortest drying time among the drying methods in various food drying studies [26]. However, microwave drying can have limitations, such as non-uniform temperature distribution during heating, which can lead to uneven drying and potential hot and cold spots in the food being dried. This uneven energy distribution, which has also been reported in the literature, can lead to inconsistent drying results [27]. Moisture levels in the MWD samples decreased very rapidly to below 5%. Visual irregularities and regional burns

were observed, particularly in the thicker regions of the samples.

The  $D_{eff}$  value was calculated based on the moisture ratios as  $2.00 \times 10^{-10}$ ,  $2.63 \times 10^{-10}$ , and  $3.53 \times 10^{-10} \text{ m}^2/\text{s}$  for OD at 60, 70 and 80°C, respectively; for IRD,  $2.53 \times 10^{-10}$ ,  $3.78 \times 10^{-10}$ , and  $6.02 \times 10^{-10} \text{ m}^2/\text{s}$  at 60, 70 and 80°C, respectively; and for MWD,  $4.08 \times 10^{-9}$ ,  $6.92 \times 10^{-9}$ , and  $9.34 \times 10^{-9} \text{ m}^2/\text{s}$  at 140, 210 and 350 W, respectively. All values obtained were found to be within the  $D_{eff}$  values given in the studies for food drying processes ( $10^{-12} - 10^{-8} \text{ m}^2/\text{s}$ ) [28]. A dried product with a high  $D_{eff}$  indicates that the product has a greater capacity for moisture to move within its structure during the drying process [29]. It was observed that the MWD  $D_{eff}$  values were much higher compared to OD and ID due to the rapid drying.

Activation energy is a critical parameter that represents the minimum energy required to initiate the mass transfer process from the interior to the surface of the food product during drying [30].

**Table 1.** Modeling coefficients and statistical data of OD, IRD and MWD (avg.  $R^2 > 0.999$ )

Model	Parameter	OD			IRD			MWD		
		60°C	70°C	80°C	60°C	70°C	80°C	140W	210W	350W
Alibas	a	1.675636	1.106938	1.328243	0.974354	0.970026	1.207561	0.818547	0.889379	0.931961
	k	0.007328	0.010642	0.020878	0.025420	0.033665	0.047415	0.775551	1.141618	1.238055
	n	0.989727	1.045495	0.914718	0.970261	0.972430	0.868411	0.950897	0.998244	0.981440
	b	0.001680	0.000317	0.001228	-0.000018	-0.000098	0.001336	0.013627	-0.011472	-0.006927
	g	-0.676093	-0.107560	-0.328118	0.025619	0.030005	-0.207549	0.182643	0.110846	0.067924
	R <sup>2</sup>	0.999977	0.999981	0.999991	0.999997	0.999991	0.999998	0.999832	0.999966	0.999981
	χ <sup>2</sup>	0.000003	0.000003	0.000001	0.000001	0.000002	0.000001	0.000012	0.000003	0.000003
	RMSE	0.001387	0.001287	0.000871	0.000412	0.000877	0.000432	0.003086	0.001506	0.001215
Aghbashlo et al.	k <sub>1</sub>	0.010182	0.013172	0.019898	0.023477	0.030986	0.039475	0.686019	1.136747	1.281111
	k <sub>2</sub>	-0.000970	-0.001239	-0.000688	0.001652	0.001682	0.000577	0.138150	0.181083	0.158655
	R <sup>2</sup>	0.999923	0.999972	0.999573	0.999889	0.999982	0.999635	0.999358	0.999486	0.999510
	χ <sup>2</sup>	0.000007	0.000003	0.000047	0.000010	0.000002	0.000054	0.000040	0.000040	0.000046
	RMSE	0.002553	0.001554	0.006199	0.002925	0.001267	0.006191	0.006036	0.005924	0.006197
Midilli & Kucuk	a	0.994935	0.998520	0.999206	1.000402	1.000193	0.999859	1.007722	1.002614	1.000736
	k	0.007669	0.010541	0.022528	0.025986	0.034121	0.048995	0.624669	0.958846	1.110145
	n	1.080425	1.070695	0.967975	0.955883	0.958094	0.922522	0.773483	0.862966	0.909740
	b	-0.000063	-0.000097	-0.000212	0.000096	0.000094	-0.000222	0.002975	0.005524	0.005939
	R <sup>2</sup>	0.999782	0.999968	0.999929	0.999988	0.999986	0.999972	0.997977	0.999023	0.999765
	χ <sup>2</sup>	0.000024	0.000004	0.000010	0.000001	0.000002	0.000007	0.000139	0.000091	0.000028
	RMSE	0.004296	0.001669	0.002517	0.000947	0.001108	0.001716	0.010715	0.008172	0.004290

Activation energy values for drying food can be given in different ranges in the literature.  $E_a$  values calculated based on the Arrhenius equation were found to be 27.83 kJ/mol, 42.35 kJ/mol, and 40.98 kJ/kg for OD, IR and MWD, respectively, and OD and IRD  $E_a$  values were found in the range of 14.42 to 43.26 kJ/mol reported in the literature [31].

Statistical constants and coefficients calculated for the 3 models that show the highest compatibility with all drying systems among the 14 tested models are given in Table 1. According to the evaluations, the best fit was obtained in the Alibas model for OD, IRD and MWD with  $R^2$  values between 0.999977 – 0.999991, 0.999991 – 0.999998, and 0.999832 – 0.999981, respectively;  $\chi^2$  values between 0.000001 – 0.000003, 0.000001 – 0.000002, and 0.000003 – 0.000012, respectively; RMSE values between 0.000871 – 0.001387, 0.000412 – 0.000877, and 0.001215 – 0.003086, respectively. Following Alibas, Aghbashlo *et al.* model was the second most suitable for OD, IRD and MWD with  $R^2$  values

between 0.999573 – 0.999972, 0.999635 – 0.999982, and 0.999358 – 0.999510, respectively;  $\chi^2$  values between 0.000003 – 0.000047, 0.000002 – 0.000054, and 0.000040 – 0.000046, respectively; RMSE values between 0.001554 – 0.006199, 0.001267 – 0.006191, and 0.005924 – 0.006197, respectively. The Midilli & Kucuk model was the third most compatible model for OD, IRD and MWD with  $R^2$  values between 0.999782 – 0.999968, 0.999972 – 0.999988, and 0.997977 – 0.999765, respectively;  $\chi^2$  values between 0.000004 – 0.000024, 0.000001 – 0.000007, and 0.000028 – 0.000139, respectively; RMSE values between 0.001669 – 0.004296, 0.000947 – 0.001716, and 0.004290 – 0.010715, respectively.

#### Color analysis results

It was noted that one of the main evaluation criteria for the customer regarding drying is the color change. For this reason, it is expected that the  $\Delta E$  values will be as minimal as possible. Looking at the

L\* values in Figure 4, it can be seen that the darkness of the dried material is highest at the lowest temperature/power for each equipment. This is because the drying time increases at the lowest drying temperature or power. Similarly, it is observed that a\* values decrease with increasing drying time in OD and IRD. However, it is seen that the a\* values are higher than expected due to regional burning caused by sudden drying in MWD samples. b\* values exhibited an inversely proportional distribution with a\* values and increased with the increase in drying time. When ΔE values are analyzed it is seen that the highest values are obtained with MWD. It was interpreted that this situation was directly related to regional burns caused by sudden drying. After MWD, it was interpreted that the reason for the high ΔE values in the OD samples was the long drying time. When all the data were compared, it was found that IRD samples gave the most efficient results in terms of ΔE.

### CONCLUSION

This study investigated the drying behavior of *Solen marginatus* by oven, infrared and microwave irradiation at different temperatures and power levels. Drying data were tested using fourteen common models and total color changes were determined by color analysis. At the end of drying, it was found that oven drying caused color changes in the samples due to the long drying time and the high final moisture content. On the other hand, microwave drying was very fast, the final moisture content decreased rapidly and burnt areas appeared in the samples. Due to the local burning, the final product quality decreased and the color change was reached at the highest value. The drying time of the infrared samples was shorter than that of the oven samples. When color change values were examined, this dryer gave the best color retention. Of the mathematical models studied, the Alibas model gave the best fit for all dryers.

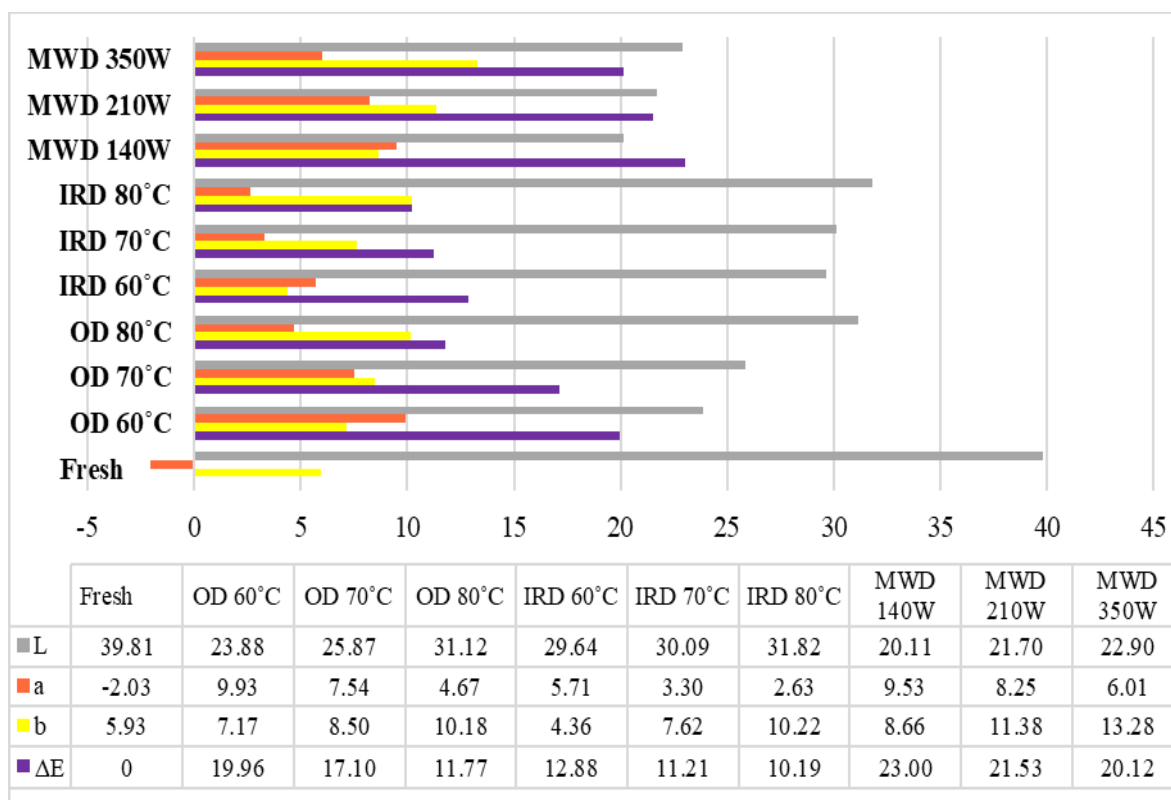


Fig. 4. Color values of *Solen marginatus*

REFERENCES

1. E. Ç. Taş, U. Sunlu, *TURJAF*, **7**(2), 306 (2019).
2. N. Souissi, S. Boughriba, O. Abdelhedi, M. Hamdi, M. Jridi, S. Li, M. Nasri, *RSC advances*, **9**(20), 11538. (2019).
3. M. Esposito, S. Canzanella, A. Danese, A. Pepe, P. Gallo, *Toxics*, **10**(8), 452 (2022).
4. M. Kontominas, A. Badeka, I. Kosma, C. Nathanailides, *Animals*, **11**(1), 92 (2021). <https://doi.org/10.3390/ani11010092>
5. A. Mahmud, B. Abraha, M. Samuel, H. Mohammedidris, W Abraham, E. Mahmud, *MOJ Food Process. Technol*, **6**, 303 (2018).
6. D. Huang, K. Men, X. Tang, W. Li, S. Sherif, *J. Food Process. Eng.*, **44**(1) (2020). <https://doi.org/10.1111/jfpe.13608>
7. S. A. R. Pinheiro, P. C. Corrêa, J. G. Silva, J. S. Zeymer, M. E. V. de Araújo, *J. Food Process Eng.*, **44**(12). (2021). <https://doi.org/10.1111/jfpe.13886>
8. M. H. Alizehi, M. Niakousari, M. Fazaeli, M. Iraj, *J. Food Process Eng.* **43**(12) (2020). <https://doi.org/10.1111/jfpe.13563>
9. P. Jiang, W. Jin, Y. Liu, N. Sun, K. Zhu, Z. Bao, X. Dong, *J. Food Qual.*, **2022**(1), 5147373 (2022).
10. X. He, R. Lin, S. Cheng, S. Wang, L. Yuan, H. Wang, M. Tan, *J. Food Sci.*, **86**(6), 2499 (2021).
11. Z. O. Ozyalcin, A. S. Kipcak, *TrJFAS*, **21**(3), 135 (2021).
12. V. Pankyamma, S. Y. Mokam, J. Debbarma, B. M. Rao, *J. Sci. Food Agric.*, **99**(13), 5778 (2019).
13. D. A. Delfiya, L. Mathai, S. Murali, K. C. Neethu, A. R. Nair, G. Ninan, *Solar Energy*, **274**, 112554 (2024).
14. Z. Ö. Ö. Genç, A. S. Kipçak, *Aquat. Sci. Eng.*, **38**(3), 137 (2023).
15. B. S. Kim, B. J. Oh, J. H. Lee, Y. S. Yoon, H. I. Lee, *Foods*, **9**(2), 196 (2020)..
16. J. Qin, Z. Wang., X. Wang, W. Shi, *Food Sci. Nutr.*, **8**(8), 4159 (2020)..
17. Z. O. Ozyalcin, A. S. Kipcak, N. Tugru, *J. Aquat. Food Prod. Technol*, **32**(4), 384 (2023).
18. S. Phitakwinai, S. Thepa, W. Nilnont, *Food Sci. Amp. Nutr.*, **7**(9), 2921 (2019). <https://doi.org/10.1002/fsn3.1144>
19. Á. Calín-Sánchez, L. Lipán, M. Cano-Lamadrid, A. Kharaghani, K. Masztalerz, Á. A. Carbonell-Barrachina, ... A. Figiel, *Foods*, **9**(9), 1261(2020). <https://doi.org/10.3390/foods9091261>
20. J. Li, Y. Deng, W. Xu, R. Zhao., T. Chen, M. Wang, ... D. Liu, *Trends Food Sci, Technol.*, **131**, 31 (2023).
21. D. Delfiya, K. Prashob, S. Murali, P. Alfia, M. Samuel, R. Pandiselvam, *J. Food Process Eng.* **45**(6) (2021). <https://doi.org/10.1111/jfpe.13810>
22. Z. O. Ozyalcin, A. S. Kipcak, *Aquat Food Prod T.*, **31**(2), 187 (2022).
23. R. A. L. Jutkus, N. Li, L. S. Taylor, L. J. Mauer, *Int. J. Food Prop.*, **18**(4), 862 (2015). <https://doi.org/10.1080/10942912.2013.805770>
24. H. Wang, Y. Zhu, D. Xie, H. Zhang, Y. H. Zhang, P. Jin, ... Du, Q. *Foods*, **11**(16), 2540 (2022). <https://doi.org/10.3390/foods11162540>
25. T. Nguyen, Q. Nguyen, P. Nguyen, *PJFNS*, **27** (2022). <https://doi.org/10.31883/pjfn/144835>
26. P. Jha, M. Meghwal, P. K. Prabhakar, *J Food Process. Preserv.*, **45**(9) (2021). <https://doi.org/10.1111/jfpp.15717>
27. H. Bozkır, Y. Tekgöl, E. S. Erten, *J. Food Process Eng.*, **44**(1) (2020). <https://doi.org/10.1111/jfpe.13611>
28. N. Jiang, J. Ma, R. Ma, Y. Zhang, P. Chen, M. Ren, ... C Wang, *Food Sci. Technol.*, (2023). <https://doi.org/10.1590/fst.100422>
29. A. S. Kipçak, O. İsmail, *Journal of Food Science and Technology*, **58**(1), 281 (2020). <https://doi.org/10.1007/s13197-020-04540-0>
30. O. M. Nkem, A. O. Oladejo, A. F. Alonge, *J Sci Food Agric*, **104**(5), 3047 (2023). <https://doi.org/10.1002/jsfa.13196>
31. F. N. Stephenus, M. A. Z Benjamin, A. Anuar, M. A. Awang, *Foods*, **12**(15), 2859 (2023). <https://doi.org/10.3390/foods12152859>

## Investigation of mass transfer in infrared drying of Ahlat pears: experimental and modelling approaches

O. T. A. Alshamhazi, I. Küçük\*, I. Doymaz

Chemical Engineering Department, Yıldız Technical University, İstanbul, Turkey

Accepted: May 24, 2024

Drying is an essential, energy-intensive process in food preservation that involves combined heat and mass transfer mechanisms to remove moisture from food products and extend their shelf life. This study focuses on the efficacy of infrared (IR) drying of Ahlat pear (*Pyrus elaeagnifolia* L.) which has rich vitamin content and high nutritional value. It can be consumed both fresh and dried under various infrared powers (38, 50, 62, 74, and 88 W). The effects of different power levels on drying kinetics was investigated and a comprehensive analysis was performed to evaluate the drying characteristics and kinetics. Results clearly showed the effect of IR dryer on drying time. The drying curves depicted a falling-rate period during the drying process, while no constant-rate period was observed. By using Fick's second law, the effective moisture diffusivity was determined, revealing a range from  $1.07 \times 10^{-8}$  to  $2.03 \times 10^{-8}$  m<sup>2</sup>/s across the conditions of experiments. Activation energy was calculated by a modified Arrhenius type equation as 1.6382 kW/kg. The variation of moisture content during drying of Ahlat pears was investigated by selecting six mathematical models. Regression analysis results showed that the Alibas model is the most suitable model to describe drying behavior.

**Keywords:** Infrared drying, Ahlat pear, effective diffusivity, modeling

### INTRODUCTION

Ahlat pear, a member of the *Rosaceae* family, is a wild pear species that can grow in dry and harsh conditions across a wide area from Anatolia to Europe. Economically significant since ancient times, this fruit has a pleasant taste and aroma and can be consumed fresh or dried. In addition, various parts of the fruit have anti-inflammatory, antioxidant, analgesic, antimicrobial, antispasmodic, wound-healing and antibacterial properties, allowing it to be used in folk medicine to treat fever, pain, diarrhea, snake bites and other diseases [3, 5].

For the sustenance of human life, it's crucial that foods, including fruits and vegetables, can be preserved without spoiling, making the methods of food preservation extremely important.

Among these methods, drying, which is a traditional and industrial food preservation technique used in the food industry for many years, stands out due to its ease of application and cost advantage.

Decreasing of moisture content through drying plays an important role in extending the shelf life of food products, thus leading to a reduction in transportation, packaging and storage expenses. The food industry has recognized the significance of different drying methods, including spray-drying, freeze-drying, and non-thermal techniques [6-8]. Infrared drying technology is efficient and maintains

product quality in various food processing applications. Infrared radiation reduces drying time and enhances color, rehydration, and antioxidant content [8].

Using mathematical models plays a vital role in comprehending and optimizing the drying process of food products. Theoretical, semi-theoretical, and empirical models are the three categories of mathematical models. Each category considers different aspects of the drying phenomenon [9]. Thin-layer drying models have been extensively utilized to depict the drying process of agricultural products. Effective moisture diffusivity and the kinetics of the drying process can be determined by applying these models [10]. A limited amount of information can be found in the literature regarding mathematical modeling of Ahlat pear drying. The primary objectives of this study were to assess the influence of infrared power on drying duration, to model the experimental data using six drying models, and to determine the effective moisture diffusivity and activation energy.

### EXPERIMENTAL

#### *Materials and methods*

- *Preparation of samples and drying procedures.* High-quality Ahlat pears were obtained from a local market in İstanbul, Turkey. The initial moisture content of the Ahlat pears was determined

\* To whom all correspondence should be sent:  
E-mail: [kucuk@yildiz.edu.tr](mailto:kucuk@yildiz.edu.tr)

by oven-drying at 105°C for 6 h. Triplicate samples were used to measure the moisture content, and the average value was found to be 68.75% on wet basis. Drying experiments were conducted in an infrared dryer (Snijders, Tilburg, Netherlands). 32±0.9 g of Ahlat pear samples were used in the experiments and samples were dried at 38, 50, 62, 74 and 88 W infrared power. Moisture losses were recorded at 15-min intervals throughout the drying process using a digital balance. Once the moisture content reached 20%, the drying process was halted, and the samples were allowed to cool before being packed into polyethylene bags and stored at room temperature. The data from the experiments were gathered and utilized to create the drying curves.

- *Mathematical modeling and data analysis.* The drying kinetics of the Ahlat pear samples was described by evaluating six models (Table 1). The moisture content and moisture ratio of Ahlat pears were denoted as M and MR, respectively and calculated using equations commonly used in the literature [1, 17, 18].

The data collected from the experiments were analyzed utilizing the Statistica 10 software package (StatSoft Inc., USA). Model parameters were determined *via* a nonlinear regression process employing the Levenberg-Marquardt algorithm. The assessment of the alignment between experimental data and all models was conducted using metrics including the coefficient of determination ( $R^2$ ), reduced chi-square ( $\chi^2$ ), and root mean square error (RMSE).  $R^2$ ,  $\chi^2$ , and RMSE were calculated using the formulas presented in Table 2 where  $MR_{exp,i}$  stands for the experimental dimensionless moisture ratio,  $MR_{pre,i}$  denotes the predicted dimensionless moisture ratio, N represents the number of observations, and z signifies the number of constants [17].

**Table 1.** Mathematical models designed for fitting to the drying of Ahlat pear.

Ref.	Model name	Model
[12]	Alibas	$MR = a \exp(-kt^n + bt) + g$
[13]	Aghbashlo et al.	$MR = a \exp(-at/(1 + bt))$
[14]	Henderson&Pabis	$MR = a \exp(-kt)$
[11]	Logarithmic	$MR = a \exp(-kt) + c$
[15]	Page	$MR = a \exp(-kt^n)$
[16]	Logistic	$MR = a/(1 + b \exp(kt))$

**Table 2.** The  $R^2$ ,  $\chi^2$  and RMSE formulas

$$R^2 = 1 - \frac{\sum_{i=1}^N (MR_{pre,i} - MR_{exp,i})^2}{\sum_{i=1}^N (MR_{pre,i} - MR_{exp,i})^2}$$

$$\chi^2 = \frac{\sum_{i=1}^N (MR_{exp,i} - MR_{pre,i})^2}{N - 2}$$

$$RMSE = \frac{1}{N} \sum_{i=1}^N (MR_{pre,i} - MR_{exp,i})$$

### Determination of effective moisture diffusivity and computation of activation energy

The effective moisture diffusivity ( $D_{eff}$ ) values for dried Ahlat pear were determined by applying Fick's second law of diffusion equation. The analytical solution for Fick's second law, considering unsteady-state diffusion in Cartesian coordinates, assumes moisture migration through diffusion with constant effective diffusivity, constant temperature, and negligible shrinkage during the drying process. This solution is then reformulated in logarithmic form (Eq. 1). All equations for determining effective moisture diffusivity and activation energy are given in Table 3. To ascertain the effective moisture diffusivity, the experimental drying data are graphed with  $\ln(MR)$  plotted *versus* time. This representation reveals a linear correlation, where the slope of the line corresponds to the parameter K, as defined in Eq. 2.

The correlation between effective diffusivity and temperature is frequently represented by the Arrhenius equation (Eq. 3). In this context,  $D_0$  stands for the pre-exponential factor in the Arrhenius equation, measured in  $m^2/s$ .  $E_a$  denotes the activation energy in kW/kg, while m represents the mass of dried samples in kilograms, and p signifies the infrared power in W.

**Table 3.** Equations for effective moisture diffusivity and activation energy

$$\ln(MR) = \ln\left(\frac{8}{\pi^2}\right) - \left(\frac{\pi^2 D_{eff}}{4L^2}\right) t \quad (1)$$

$$K = \left(\frac{\pi^2 D_{eff}}{4L^2}\right) \quad (2)$$

$$D_{eff} = D_0 \exp\left(\frac{-E_a m}{p}\right) \quad (3)$$

## RESULTS AND DISCUSSION

### Analysis of drying curves and evaluation of models

The changes in the moisture content over drying time at 38, 50, 62, 74 and 88 W are illustrated in Figure 1(A). Drying time decreased with the increase in the infrared power, as expected. The drying times were recorded as 285, 255, 195, 150 and 135 min at infrared powers of 38, 50, 62, 74 and 88 W, respectively. The moisture content

consistently decreased as the drying time progressed. At 50 W infrared power, the drying time was 1.889 times longer than the drying time at 88 W infrared power. This finding is consistent with the results of

Doymaz and Ismail [18], where the drying time at 50 W was 1.807 times longer than the drying time at 88 W.

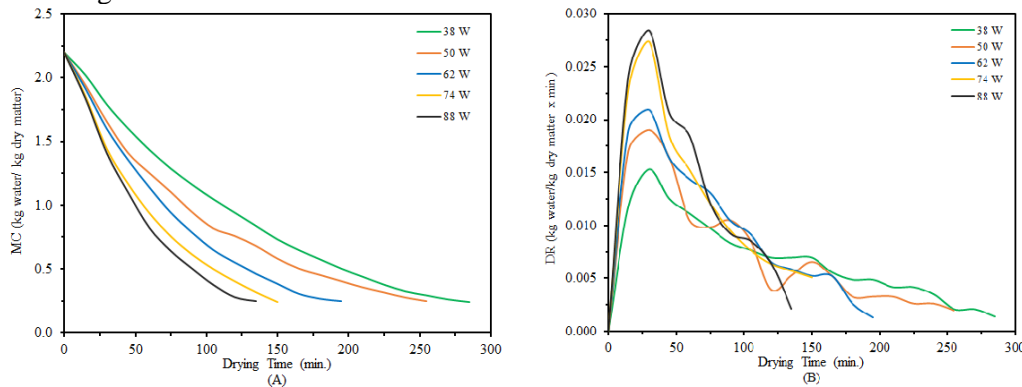


**Fig. 1.** Moisture content *versus* drying time (A), Drying rate *versus* drying time (B) at 38, 50, 62, 74 and 88 W.

**Table 4.** Statistical parameters of models for different infrared powers.

IR Power (W)	Model	R <sup>2</sup>	χ <sup>2</sup>	RMSE
38	Alibas	0.9996	0.000036	0.017902
	Aghbashlo <i>et al.</i>	0.9996	0.000033	0.017787
	Henderson and Pabis	0.9984	0.000134	0.040341
	Logarithmic	0.9996	0.000037	0.019987
	Page	0.9994	0.000046	0.024614
	Logistic	0.9995	0.000042	0.022012
50	Alibas	0.9994	0.000053	0.020612
	Aghbashlo <i>et al.</i>	0.9993	0.000056	0.021064
	Henderson and Pabis	0.9982	0.000142	0.041833
	Logarithmic	0.9992	0.000069	0.024560
	Page	0.9990	0.000073	0.023640
	Logistic	0.9978	0.000185	0.045852
62	Alibas	0.9998	0.000020	0.011198
	Aghbashlo <i>et al.</i>	0.9992	0.000073	0.021254
	Henderson and Pabis	0.9990	0.000095	0.028115
	Logarithmic	0.9992	0.000079	0.024049
	Page	0.9996	0.000034	0.014259
	Logistic	0.9995	0.000047	0.016829
74	Alibas	0.9998	0.000030	0.009844
	Aghbashlo <i>et al.</i>	0.9989	0.000110	0.019765
	Henderson and Pabis	0.9989	0.000106	0.019111
	Logarithmic	0.9990	0.000109	0.020418
	Page	0.9991	0.000084	0.019836
	Logistic	0.9991	0.000101	0.021278
88	Alibas	0.9997	0.000056	0.015138
	Aghbashlo <i>et al.</i>	0.9979	0.000228	0.027170
	Henderson and Pabis	0.9970	0.000328	0.041763
	Logarithmic	0.9978	0.000276	0.034924
	Page	0.9990	0.000103	0.019982
	Logistic	0.9987	0.000158	0.024377

Figure 1(B) illustrates the drying rate curves of Ahlat pear. The drying rate shows a continual decrease over time. At the beginning, there are higher drying rates, which then decrease as the sample's moisture content is reduced. This decrease is due to the samples shrinking, causing a decrease in porosity and an increase in resistance to water movement, ultimately leading to a further reduction in drying rates. The predominance of the falling-rate period indicates that moisture movement in Ahlat

pear slices is mainly controlled by diffusion as the primary physical mechanism [19].

The most suitable model was selected by the highest R<sup>2</sup> and the lowest χ<sup>2</sup> and RMSE values. Statistical computing results are shown in Table 4. The R<sup>2</sup> values for all models are above 0.99. Alibas model provided the highest R<sup>2</sup> values as 0.9996 and the lowest χ<sup>2</sup> values as 0.000036 and RMSE values as 0.017902 which makes it the best model for 38 W. For 50, 62, 74 and 88 W, Alibas model is also the

best model and the  $R^2$  values are 0.9994, 0.9998, 0.9998 and 0.9997,  $\chi^2$  values are 0.000053, 0.000020, 0.000030 and 0.000056 and RMSE values

are 0.020612, 0.011198, 0.009844 and 0.015138 for 50, 62, 74 and 88 W, respectively.

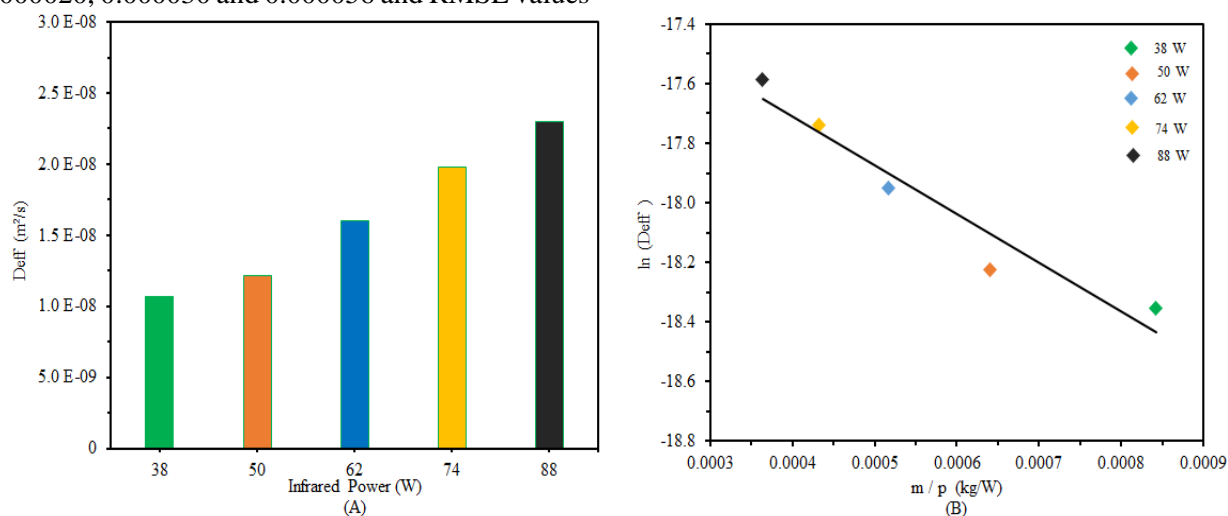


**Fig. 2.** Variation of effective moisture diffusivity with IR powers (A), Arrhenius-type relationship between effective diffusivity and IR powers (B)

#### Effective moisture diffusivity and activation energy

The effective moisture diffusivity was determined by plotting  $\ln(MR)$  versus drying time. The values of effective moisture diffusivity ( $D_{eff}$ ) were calculated according to Eq. (3) and are displayed in Figure 2(A). For the Ahlat pear, the  $D_{eff}$  values ranged from  $1.07 \times 10^{-8}$  to  $2.03 \times 10^{-8}$   $m^2/s$  within the IR power range of 38–88 W. The highest  $D_{eff}$  value was recorded at 88 W, while the lowest was at 38 W. The  $D_{eff}$  values obtained for Ahlat pear slices are like those reported by Doymaz and Ismail [18].

Drawing  $\ln(D_{eff})$  versus  $m/p$  results in a linear relationship with a slope equivalent to  $(-E_a)$ , facilitating the straightforward estimation of  $E_a$  (Figure 2. (B)). Equation (4) shows the impact of infrared power on  $D_{eff}$  for the samples, with the associated coefficients:

$$D_{eff} = 3.9145 \times 10^{-8} \exp\left(\frac{-1638.2 \times m}{p}\right) \quad (R^2 = 0.9315) \quad (4)$$

The calculated activation energy value is 1.6382 kW/kg, exhibiting a close resemblance to the activation energy values reported in the literature for the drying process of pears [18].

#### CONCLUSION

The drying behavior of Ahlat pears was investigated using an infrared dryer at different power levels ranging from 38 to 88 W. According to the results, infrared power has a significant role in the drying process of Ahlat pears and a higher power reduces the drying time. Six drying models were

utilized to analyze the drying kinetics of Ahlat pears, and statistical analysis established that the Alibas model was the most suitable model in predicting the experimental data at all power levels. The effective diffusivity values for Ahlat pear samples ranged from  $1.07 \times 10^{-8}$  to  $2.03 \times 10^{-8}$   $m^2/s$ , while the activation energy was calculated to be 1.6382 kW/kg. These findings offer valuable insights into the drying characteristics of Ahlat pears under different drying conditions.

#### REFERENCES

1. E. Taghinezhad, M., Kaveh, A. Jahanbakhshi, I. Golpour, *J. of Food Process. Eng.*, **43**, 1 (2020).
2. M. Ilhan, E. K. Akkol, H. Taştan, F. T. G. Dereli, I. Tümen, *Open Chemistry*, **17**, 13 (2019)
3. F. U. Yerlitürk, O. Arslan, S. Sinan, N. Gencer, O. Ozensoy, *Journal of Food Biochemistry*, **32**, 368 (2008)
4. R. Anşın, Z. C. Özkan, 1993. Tohumlu Bitkiler (*Spermatophyta*) Odunsu Taksonlar, KTÜ Basımevi, Trabzon, 2006, p. 450.
5. M. Siddiq, J. N. Cash, *Journal of Food Processing and Preservation*, **24**, 353 (2000).
6. D. Witrowa-Rajchert, A. Wiktor, M. Sledz, M. Nowacka, *Drying Technology*, **32**, 1386 (2014).
7. S. Kandasamy, R. Naveen, *J. of Food Process. Eng.*, **45**, e14059 (2022).
8. A. Salarikia, S. Ashtiani, M. Golzarian, *Journal of Food Processing and Preservation*, **41**, e12930 (2016).
9. Z. Wang, J. Sun, X. Liao, F. Chen, G. Zhao, J. Wu, X. Hu, *Food Research International*, **40**, 39 (2007).
10. C. Kara, İ. Doymaz, *Heat and Mass Transfer*, **51**, 983 (2014).
11. T. J. Afolabi, T. Y. Tunde-Akintunde, J. A. Adeyanju, *J. Food Sci. Technol.*, **52**, 2731 (2015).

12. I. Alibas, *Journal of Agricultural Sciences*, **18**, 43 (2012).
13. M. Aghbashlo, M. H. Kianmehr, S. Khani, M. Ghasemi, *International Agrophys.*, **23**, 313 (2009).
14. S. M. Henderson, S. Pabis, *J. Agric. Engng Res.*, **6**, 169 (1961).
15. G. Page, MS Thesis, Purdue University, West Lafayette, USA, 1949.
16. P. K. Chandra, R. P. Singh, *Applied Numerical Methods for Food and Agricultural Engineers*, CRC Press. Boca Raton, FL., 1995, p. 163.
17. V. C. Marianni, C. A. Perussello, A. Cancelier, T. J. Lopes, A. Silva, *J. of Food Process. Eng.*, **37**, 619 (2015).
18. I. Doymaz, *Erwerbs-Obstbau*, **65**, 47 (2023).
19. I. T. Toğrul, R. S. Çelebi, H. Toğrul, *Journal of the Faculty of Engineering and Architecture of Gazi University*, **33**, 1231 (2018).
20. I. Doymaz, I. Küçük, *Bulgarian Chemical Communications*, **49**, 90 (2017).

## The effect of chemical pretreatment on the drying behavior of blueberries

B. Gök, E. Kıpçak\*

Yıldız Technical University, Davutpaşa Campus, Department of Chemical Engineering, Faculty of Chemical and Metallurgical Engineering, No: 127, 34220, Esenler, Istanbul, Turkey

Received June 28, 2024; Accepted: August 17, 2024

Blueberries (*Vaccinium corymbosum*) are small, blue, perishable fruits, which are packed with nutrients, minerals, organic acids and polyphenols. Additionally, blueberries are notable for their antioxidant properties, which can help to reduce the negative effects of diseases such as cancer and diabetes. However, they are seasonally produced and have short shelf life, so drying is an effective preservation method. Drying processes often include physical or chemical pretreatments to improve the quality of the dried fruit and shorten the drying time. While there are many studies on the antioxidant capacity and nutritional content of blueberries, research on their detailed drying behavior and the effects of different pretreatments is still limited. This study explores the impact of chemical pretreatment with  $K_2CO_3$  solutions on the infrared and vacuum oven drying of blueberries. Blueberry samples were treated with these solutions at 30°C and 60°C before drying. Each pretreatment involved immersing the blueberries in the  $K_2CO_3$  solutions for 1 and 3 min. After the pretreatments, drying was conducted at temperatures of 70°C and 80°C using infrared and vacuum oven methods. The drying behavior of the pretreated blueberries was compared to that of untreated samples. Effective moisture diffusivities ( $D_{eff}$ ) were calculated, and the drying curves were modeled using 14 established mathematical equations. The results showed that the use of vacuum oven provided faster drying and  $K_2CO_3$  pretreatments reduced drying time. 1 min dipping of the blueberries in a 30°C  $K_2CO_3$  solution caused the most prominent decrease in the drying time and increase in the  $D_{eff}$  values. However, further contact of the blueberries at the foresaid solution temperature, and increasing the solution temperature at this dipping time did not cause a major change in the drying performance.

**Keywords:** Blueberry; infrared drying; vacuum oven drying;  $K_2CO_3$ ; chemical pretreatment

### INTRODUCTION

Blueberries (*Vaccinium corymbosum*) are small, round, dark purple fruits with a sweet-sour taste [1]. They are mainly grown in America, with the United States being the leading producer, as well as in Europe [2]. Blueberries are rich sources of vitamins, minerals, anthocyanins, phenolic acids, proanthocyanidins, flavonoids and dietary fibers. They are among the fruits highest in vitamin C and antioxidants, giving them protective properties against numerous diseases such as cardiovascular and urinary diseases, Alzheimer's disease, aging, muscular degeneration, vision problems, diabetes and cancer [1-5]. Blueberries are described as the "natural health package" by Li *et al.* [6], due to all of the aforementioned physiological functions and enhancing human immunity. However, blueberries are only available seasonally, are delicate and prone to mechanical damage, and perish quickly [1, 3, 5]. Therefore, various food processing technologies are used to extend their shelf lives and to improve their preservation.

Drying is a commonly used method to preserve food products, by reducing their water content to prevent harmful microbial and physicochemical reactions and inhibit enzymatic activities. This

method is crucial in food science due to its numerous benefits, such as allowing safe storage over an extended period and reducing packaging and transportation costs due to decreased weight and volume [5, 7-10]. Additionally, dried fruits maintain or even enhance their nutritional values, making them excellent alternatives and useful additives in various food products [11]. However, drying is a time and energy intensive process, prompting the exploration of additional measures to optimize its use. Pretreatment processes are one of such measures, as they can decrease the time of drying, lower the consumption of energy, and maintain the quality of food products [8, 12, 13]. Moreover some food products, especially berries, are known to have a waxy outer layer that protects them from withering in ambient conditions. This condition obstructs the application of the drying processes [4, 14, 15]. Physical and chemical pretreatments are commonly used to remove the foresaid waxy outer layer to enhance the drying efficiency. However, chemical pretreatments have a major advantage over the physical ones, as they require a very short contact time to increase the rate of dehydration. Literature studies demonstrate that potassium carbonate ( $K_2CO_3$ ), potassium hydroxide (KOH), potassium

\* To whom all correspondence should be sent:  
E-mail: [eyildir@yildiz.edu.tr](mailto:eyildir@yildiz.edu.tr)

metabisulfite ( $K_2S_2O_5$ ), sodium hydroxide (NaOH), sodium carbonate ( $Na_2CO_3$ ), ethyl oleate ( $C_{20}H_{38}O_2$ ), ascorbic acid ( $C_6H_8O_6$ ) and citric acid ( $C_6H_8O_7$ ) are the most common chemicals that are used in the pretreatment solutions [10, 13-17]. Among the aforementioned chemicals,  $K_2CO_3$  has been reported to successfully enhance the removal of the waxy outer layer and thereby lower the internal resistance for the diffusion of water [18]. Moreover, as a food additive, the use of  $K_2CO_3$  has been approved by the Turkish Food Codex Regulation. Hence, it is accepted as not to pose a risk regarding human health [13].

In the literature there are many articles that examine how drying affects the nutritional contents and the antioxidant capacities of blueberries. However, there is a lack of studies exploring how different pretreatment conditions impact the drying process and its kinetics. To address this gap, this study investigates the effects of  $K_2CO_3$  chemical pretreatment on the infrared drying and vacuum oven drying of blueberries. During the experiments, blueberry samples were subjected to  $K_2CO_3$  solutions at 30°C and 60°C prior to drying. Furthermore, at each pretreatment temperature, the blueberries were contacted with the  $K_2CO_3$  solutions for 1 min and 3 min, respectively. Following the chemical pretreatments, the infrared drying and vacuum oven drying of the samples were carried out at 70°C and 80°C. The effects of the aforementioned pretreatments on the drying behavior of blueberries were compared to those of untreated dried samples, and the effective moisture diffusivities ( $D_{eff}$ ) were determined. Additionally, the experimental drying data was modeled using the 14 most well-known mathematical modeling equations from the literature.

## EXPERIMENTAL

### *Preparation of the samples*

The blueberries used in the experiments were imported from Peru and were obtained from a market in Istanbul. Blueberries of similar size, each with a radius of about 1 cm, were chosen and cut horizontally into two halves to study thin layer diffusion. In every experiment, 5 g of blueberries were dried. Before drying, the initial moisture content ( $M_0$ ) of the blueberries was measured using the AOAC method [19], which involved drying them for 3 hours in a hot air-drying oven at 105°C (KH-45, Kenton, Guangzhou, China). The initial moisture content of the untreated blueberries was found as 4.2632 kg water/kg dry matter, or 81% on a wet basis.

- *Experimental methods.* The vacuum oven drying experiments were carried out at a Nüve EV-018 model oven (Nüve, Ankara, Turkey). Here, the vacuum assistance was supplied through a vacuum pump of KNF N022AN.18 model (KNF, Freiburg, Germany). During the experiments, the oven pressure was measured as 0.3 atm. For the infrared drying experiments, on the other hand, Radwag MA 50.R model infrared dryer that worked with 230 V at 50 MHz was used (Radwag Balances and Scales, Radom, Poland).

For the chemical pretreatments,  $K_2CO_3$  solutions were prepared by adding 25 g of  $K_2CO_3$ , 2.5 g of olive oil and distilled water to reach the desired solution volume of 500 ml. During the experiments, blueberry samples were treated with  $K_2CO_3$  solutions at temperatures of 30°C and 60°C before drying. Additionally, at each temperature, the blueberries were exposed to the  $K_2CO_3$  solutions for 1 min and 3 min, respectively.

To designate the drying kinetic parameters, experiments were conducted at temperatures of 70°C and 80°C. Blueberry samples were weighed every 15 min to measure their moisture contents. A digital balance with a precision of 0.001 g was used for weighing (AS 220.R2, Radwag, Radom, Poland). Two identical experiments were performed for each drying condition, and the drying process was concluded when the weight of the blueberries decreased to approximately 5% of their initial moisture contents.

- *Determination of the drying parameters.* To generate the drying curves, the moisture content (M), drying rate (DR) and moisture ratio (MR) for each experimental condition need to be calculated. These parameters were determined through Eqns. 1, 2 and 3 provided below [16, 20, 21]:

$$M = \frac{m_w}{m_d} \quad (1)$$

In the aforementioned equation M is the moisture content (kg water/kg dry matter). The water content and the dry matter content of the blueberries are represented with  $m_w$  and  $m_d$ , respectively (kg).

$$DR = \frac{M_{t+dt} - M_t}{dt} \quad (2)$$

Eqn. 2 defines DR as the drying rate (kg water/kg dry matter·min), where t is the drying time (min),  $M_t$  and  $M_{t+dt}$  are the moisture contents at times t and t+dt, respectively (kg water/kg dry matter).

$$MR = \frac{M_t - M_e}{M_0 - M_e} \quad (3)$$

In Eqn. 3, MR represents the dimensionless moisture ratio. Here,  $M_t$ ,  $M_e$  and  $M_0$  are the

instantaneous moisture content at time  $t$ , the equilibrium moisture content and the initial moisture content, respectively (kg water/kg dry matter). Due to the low moisture content at equilibrium ( $M_e$ ) compared to the initial and instantaneous values, it is omitted in the calculations [20, 21].

In order to describe moisture diffusion during the drying process of food products, Fick's 2<sup>nd</sup> law of diffusion is applied. In this study, some assumptions were made to solve the equation. Firstly, the shrinkage of the blueberries was ignored. Additionally, it was assumed that symmetrical mass transfer occurred from the center solely through diffusion, with constant diffusivity. Based on these assumptions, Fick's 2<sup>nd</sup> law for a thin layer of thickness  $2L$  is modified to Eqn. 4 [16, 21, 22]:

$$MR = \frac{8}{\pi^2} \sum_{n=1}^{\infty} \frac{1}{(2n+1)^2} \exp\left(-\frac{(2n+1)^2 \pi^2 D_{eff} \times t}{4L^2}\right) \quad (4)$$

In Eqn. 4,  $D_{eff}$  represents the effective moisture diffusivity ( $m^2/s$ ),  $t$  denotes time (s),  $L$  is half the thickness of the blueberry sample (m) and  $n$  is a positive integer. For extended drying durations,  $n$  is typically assumed to be 1 [21, 22]. Thus, Eqn. 4 can be simplified to Eqn. 5. Using Eqn. 5,  $D_{eff}$  can be computed from  $\ln(MR)$  versus  $t$  plot's slope, as described below:

$$\ln(MR) = \ln\left(\frac{8}{\pi^2}\right) - \left(\pi^2 \frac{D_{eff} \times t}{4L^2}\right) \quad (5)$$

- *Mathematical modeling.* During the drying of the blueberries, 14 drying models from the literature were tested for mathematical modeling. The drying models applied to the experimental data, along with their equations, are presented in Table 1.

**Table 1.** Drying models applied to the experimental data [21]

Model Name	Model Equation
Page	$MR = \exp(-kt^n)$
Peleg	$MR = a + t/(k_1 + k_2 t)$
Lewis	$MR = \exp(-kt)$
Alibas	$MR = a \times \exp((-kt^n) + bt) + g$
Weibull	$MR = \exp(-(t/b)^a)$
Parabolic	$MR = a + bt + ct^2$
Jena <i>et al.</i>	$MR = a \times \exp(-kt + b\sqrt{t}) + c$
Verma <i>et al.</i>	$MR = a \times \exp(-kt) + (1-a) \times \exp(-gt)$
Logarithmic	$MR = a \times \exp(-kt) + c$
Aghbaslo <i>et al.</i>	$MR = \exp(-k_1 t / (1 + k_2 t))$
Wang & Singh	$MR = 1 + at + bt^2$
Midilli & Kucuk	$MR = a \times \exp(-kt^n) + bt$
Henderson & Pabis	$MR = a \times \exp(-kt)$
Two-Term Exponential	$MR = a \times \exp(-kt) + (1-a) \times \exp(-kat)$

For the models presented in Table 1,  $t$  represents time (min) and  $a$ ,  $b$ ,  $c$  and  $g$  are coefficients. The drying exponent specific to each equation is represented by  $n$ ; and the drying coefficients are represented by  $k$ ,  $k_1$  and  $k_2$ . Statistica 7.0 software was employed for the nonlinear Levenberg-Marquardt procedure regressions in the modeling process (Statsoft Inc., Tulsa, OK). The fitting of the models to the drying data was evaluated based on the coefficient of determination ( $R^2$ , Eqn. 6), reduced chi-square ( $\chi^2$ , Eqn. 7) and root mean square error (RMSE, Eqn. 8) values [10, 16, 21, 23].

$$R^2 = 1 - \frac{\sum_{i=1}^N (MR_{exp,i} - MR_{pre,i})^2}{\sum_{i=1}^N (MR_{exp,i} - (\frac{1}{N}) \sum_{i=1}^N MR_{exp,i})^2} \quad (6)$$

$$\chi^2 = \frac{\sum_{i=1}^N (MR_{exp,i} - MR_{pre,i})^2}{N-z} \quad (7)$$

$$RMSE = \left(\frac{1}{N} \sum_{i=1}^N (MR_{exp,i} - MR_{pre,i})^2\right)^{\frac{1}{2}} \quad (8)$$

In these equations,  $N$  represents the number of experiments,  $z$  denotes the number of constants in the model equations, and  $MR_{exp}$  and  $MR_{pre}$  indicate the experimental moisture ratios and the predicted moisture ratios, respectively. The model chosen as the most suitable was the one with the highest  $R^2$ , the lowest  $\chi^2$ , and the lowest RMSE values.

## RESULTS AND DISCUSSION

### *Moisture content and effective moisture diffusivity*

The drying curves that demonstrate the moisture content change ( $M$ ) with respect to time for the 70°C and 80°C infrared drying of blueberries at are presented in Fig. 1. Here, Fig. 1a presents the results without any pretreatment; Figs. 1b and 1c present the results for the blueberry samples dipped in 30°C  $K_2CO_3$  solution for 1 min and 3 min, respectively; and Fig. 1d and 1e present the results for the blueberry samples dipped in 60°C  $K_2CO_3$  solution for 1 min and 3 min, respectively, during infrared drying. Considering Fig. 1a, for the drying of blueberries without any pretreatment, the initial moisture content of 4.2632 kg water/kg dry matter was seen to decrease to 0.1871 and 0.0933 at 70°C and 80°C, respectively. For the weight of the blueberry samples to reach approximately 5% of their initial moisture contents, it took 255 min at 70°C and 135 min at 80°C drying conditions. When the samples were dipped in a 30°C  $K_2CO_3$  solution for 1 min (Fig. 1b), the drying durations were found to decrease to 210 and 105 min at 70°C and 80°C, respectively. However, further contact of the blueberry samples with the 30°C  $K_2CO_3$  solution for 3 min did not cause any change in the drying times (Fig. 1c). Accordingly, the drying time remained as

210 min at 70°C and there was a minor increase to 120 min at 80°C. At these conditions, the initial moisture content of 4.2632 kg water/kg dry matter decreased to 0.2022 kg water/kg dry matter at 70°C and to 0.1290 kg water/kg dry matter at 80°C. Increasing the K<sub>2</sub>CO<sub>3</sub> pretreatment solution's temperature to 60°C did not show a distinct change in the drying durations for a 1 min contact time (Fig. 1d), which were 225 min for 70°C and 105 min for

80°C infrared drying temperatures. The initial moisture content of 4.2632 kg water/kg dry matter was seen to reduce to 0.2367 and 0.1734 kg water/kg dry matter at 70°C and 80°C, respectively. However, when the contact time with the K<sub>2</sub>CO<sub>3</sub> pretreatment solution was increased to 3 min, as it can be observed from Fig. 1e, the drying durations reached the shortest values of the infrared experiments (165 min for 70°C and 90 min for 80°C).

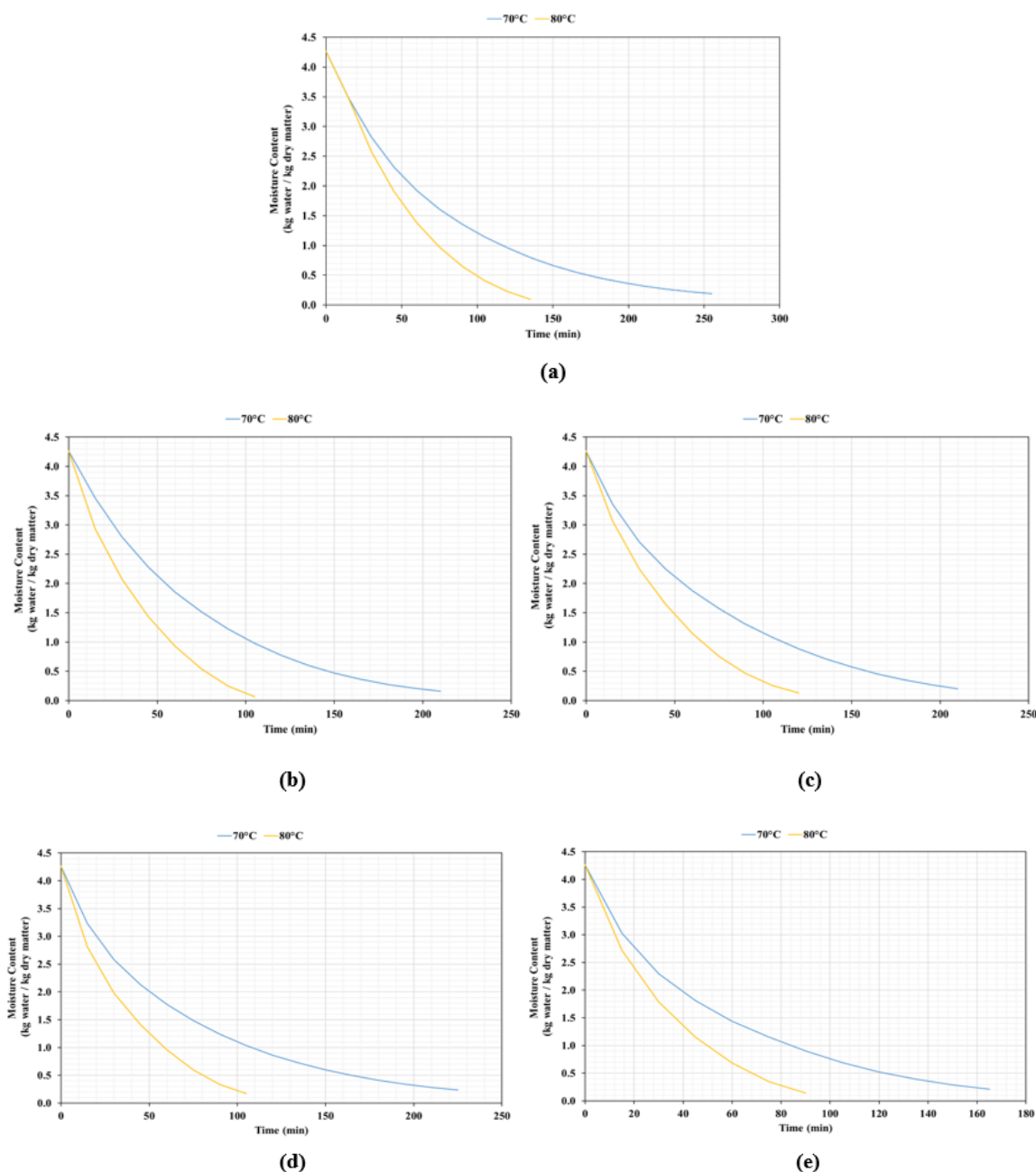


**Fig. 1.** The change in moisture contents of blueberries for infrared drying (a) without any pretreatment, (b) 30°C, 1 min K<sub>2</sub>CO<sub>3</sub> pretreatment, (c) 30°C, 3 min K<sub>2</sub>CO<sub>3</sub> pretreatment, (d) 60°C, 1 min K<sub>2</sub>CO<sub>3</sub> pretreatment (e): 60°C, 3 min K<sub>2</sub>CO<sub>3</sub> pretreatment

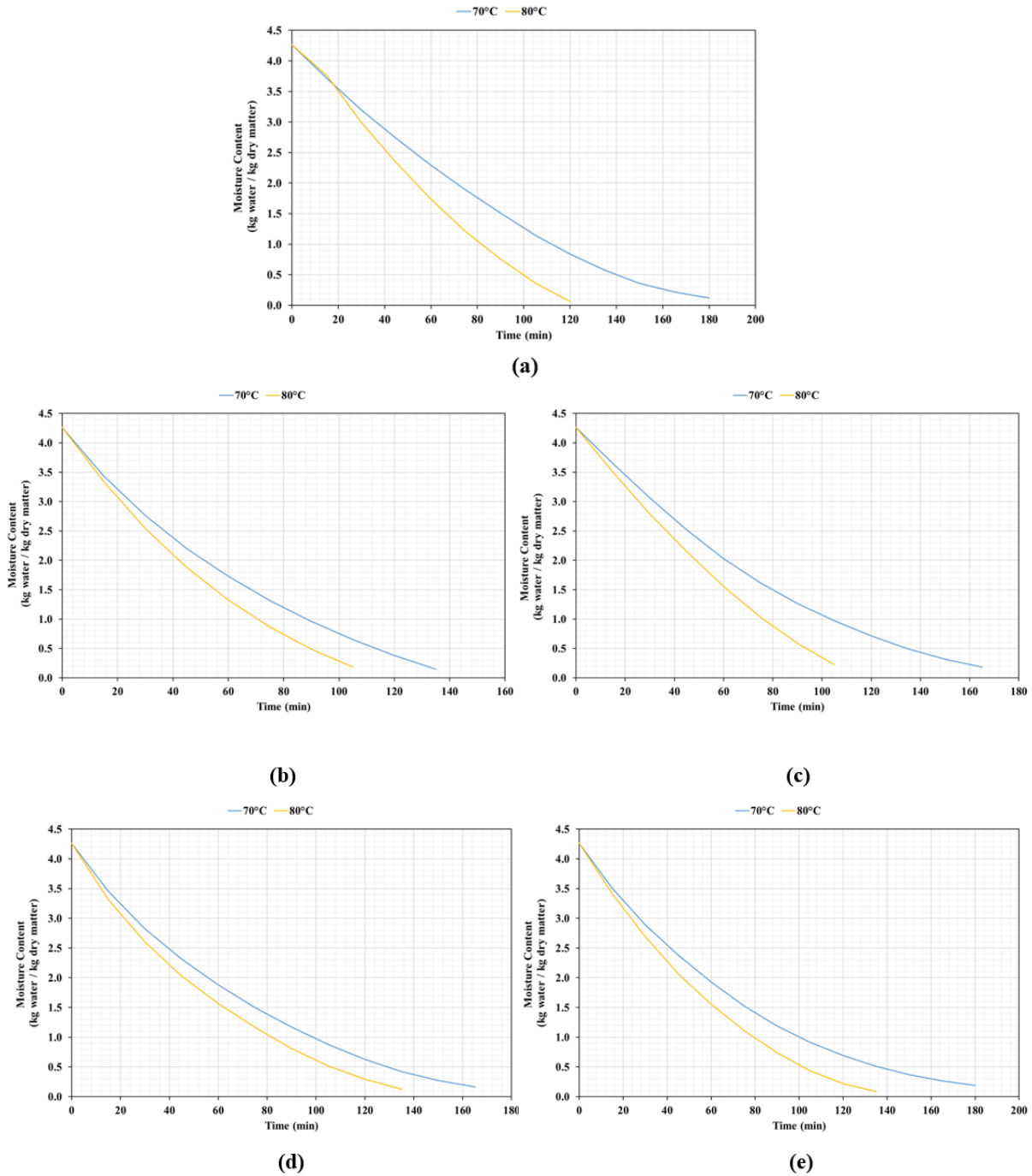


**Fig. 2.** The change in moisture content of blueberries for vacuum oven drying: (a) without any pretreatment, (b) 30°C, 1 min K<sub>2</sub>CO<sub>3</sub> pretreatment, (c) 30°C, 3 min K<sub>2</sub>CO<sub>3</sub> pretreatment, (d) 60°C, 1 min K<sub>2</sub>CO<sub>3</sub> pretreatment, (e) 60°C, 3 min K<sub>2</sub>CO<sub>3</sub> pretreatment

Fig. 2 presents the change of moisture content (M) with time for the 70°C and 80°C vacuum oven drying of blueberries without any pretreatment (Fig. 2a), pretreatment with 30°C K<sub>2</sub>CO<sub>3</sub> solution (Fig. 2b and 2c) and pretreatment with 60°C K<sub>2</sub>CO<sub>3</sub> solution (Fig. 2d and 2e). The results demonstrate that vacuum oven drying yielded much shorter drying times both for the untreated and K<sub>2</sub>CO<sub>3</sub> pretreated blueberry samples. For instance, the drying times of

the untreated blueberries were 180 min and 120 min for 70°C and 80°C drying temperatures respectively, when vacuum oven was employed. Moreover, the initial moisture content of 4.2632 kg water/kg dry matter was seen to decrease to 0.1184 and 0.0637 for the foresaid temperatures. The application of the chemical pretreatment showed a likewise tendency with the infrared drying experiments. When the blueberries were dipped in a 30°C K<sub>2</sub>CO<sub>3</sub> solution

for 1 min (Fig. 2b), the drying times were observed to similarly decrease to 135 and 105 min at 70°C and 80°C, respectively. Just like infrared drying, further contact time with K<sub>2</sub>CO<sub>3</sub> solution did not cause a positive change in the drying times (Fig. 2c). For 30°C and 3 min K<sub>2</sub>CO<sub>3</sub> pretreatment, the initial moisture content of 4.2632 kg water/kg dry matter decreased to 0.2266 at 70°C and to 0.1844 at 80°C. When K<sub>2</sub>CO<sub>3</sub> solution's temperature was increased from 30 to 60°C, again a significant change was not observed. For vacuum oven drying at 70°C, the

drying durations increased from 165 min to 180 min, when the dipping time was raised from 1 min to 3 min. For vacuum oven drying at 80°C, on the other hand, the drying durations were 135 min for both pretreatment times (Figs. 2d and 2e).

As outlined in the Experimental, the effective moisture diffusivity (D<sub>eff</sub>) values were determined according to Eqn. 5, derived from the slopes of ln(MR) versus drying time plots. The resulting D<sub>eff</sub> values, alongside the drying times for all experimental conditions, are compiled in Table 2.

**Table 2.** Drying times and D<sub>eff</sub> values for the drying of blueberries

Pretreatment Type	Drying Parameter	Infrared Drying		Vacuum Oven Drying	
		70°C	80°C	70°C	80°C
Without Pretreatment	Drying Time (min)	255	135	180	120
	D <sub>eff</sub> (m <sup>2</sup> /s)	5.14·10 <sup>-10</sup>	1.13·10 <sup>-9</sup>	7.98·10 <sup>-10</sup>	1.28·10 <sup>-9</sup>
1 min K <sub>2</sub> CO <sub>3</sub> Pretreatment, 30°C	Drying Time (min)	210	105	135	105
	D <sub>eff</sub> (m <sup>2</sup> /s)	6.51·10 <sup>-10</sup>	1.54·10 <sup>-9</sup>	9.47·10 <sup>-10</sup>	1.33·10 <sup>-9</sup>
3 min K <sub>2</sub> CO <sub>3</sub> Pretreatment, 30°C	Drying Time (min)	210	120	165	105
	D <sub>eff</sub> (m <sup>2</sup> /s)	5.90·10 <sup>-10</sup>	1.19·10 <sup>-9</sup>	7.68·10 <sup>-10</sup>	1.10·10 <sup>-9</sup>
1 min K <sub>2</sub> CO <sub>3</sub> Pretreatment, 60°C	Drying Time (min)	225	105	165	135
	D <sub>eff</sub> (m <sup>2</sup> /s)	5.27·10 <sup>-10</sup>	1.24·10 <sup>-9</sup>	7.33·10 <sup>-10</sup>	1.02·10 <sup>-9</sup>
3 min K <sub>2</sub> CO <sub>3</sub> Pretreatment, 60°C	Drying Time (min)	165	90	180	135
	D <sub>eff</sub> (m <sup>2</sup> /s)	7.40·10 <sup>-10</sup>	1.54·10 <sup>-9</sup>	7.30·10 <sup>-10</sup>	1.15·10 <sup>-9</sup>

As demonstrated in Table 2, D<sub>eff</sub> values increased with increasing drying temperature and the use of vacuum oven drying. For infrared drying, K<sub>2</sub>CO<sub>3</sub> pretreatment resulted in a minor increase in the D<sub>eff</sub> values for both drying temperatures. For the chemical pretreatments at 30°C, increasing the contact time with K<sub>2</sub>CO<sub>3</sub> solution decreased the effective moisture diffusivities. On the contrary, 60°C chemical pretreatment experiments showed an opposite trend, in which increasing the dipping duration resulted in an increase in the effective moisture diffusivities. The highest D<sub>eff</sub> value, 1.54·10<sup>-9</sup> m<sup>2</sup>/s, was obtained for the experiment conducted at 60°C K<sub>2</sub>CO<sub>3</sub> pretreatment for 3 min, at 80°C infrared drying. For vacuum oven drying, which proved to yield shorter drying times and higher D<sub>eff</sub> values at low drying temperatures, D<sub>eff</sub> was seen to increase only for the experiments that included K<sub>2</sub>CO<sub>3</sub> pretreatment at 30°C and 1 min dipping time. The highest D<sub>eff</sub> value was encountered at 80°C vacuum oven drying, which was 1.33·10<sup>-9</sup> m<sup>2</sup>/s; and it was obtained for the experiment conducted at 30°C K<sub>2</sub>CO<sub>3</sub> pretreatment for 1 min. As mentioned in the Introduction, the literature studies investigating the effect of K<sub>2</sub>CO<sub>3</sub> chemical pretreatment on the drying performance of food products is still scarce. Bingol *et al.* [24]

studied the convective air drying of Thompson seedless grapes at 60°C, where the grapes were pretreated in a mixture of potassium carbonate and ethyl oleate solution for 1, 2 and 3 min. The authors also investigated the effect of various dipping solution temperatures varying between 30 and 60°C on the drying performance. Accordingly, the drying rate of grapes improved with the use of chemical pretreatment. In accordance with the results obtained in the present study, dipping the grapes at low solution temperatures yielded a faster drying rate than 50°C solution temperature for the same pretreatment time. Moreover, similar to the findings for vacuum oven drying here, at dipping temperatures of 50°C and 60°C, it was observed that various dipping durations had no significant effect on the drying times. This conclusion was obtained in another study, in which the drying of cape gooseberries was investigated by using K<sub>2</sub>CO<sub>3</sub> – olive oil and NaOH – olive oil mixtures with various concentrations as a pretreatment [18]. The samples were dipped in the pretreatment solutions at 28°C for 20 and 60 min. It was seen that chemical pretreatments resulted in higher moisture losses. However, increasing the pretreatment time did not have a major influence neither on the final moisture contents nor on the effective moisture diffusivities of the cape gooseberry samples.

Yılmaz and Uyak [13] studied the effect of 13 different pretreatment solutions involving  $K_2CO_3$  and  $NaHCO_3$  solutions with various oils on the sun drying performance of raisins. The authors stated that dipping the raisins in pretreatment solutions accelerated the drying process. Doymaz [25] used a cabinet dryer for the drying of black grapes at  $60^\circ C$ , by using 5%  $K_2CO_3$  and 0.5% olive oil solution as a chemical pretreatment. The author has stated that the use of  $K_2CO_3$  pretreatment decreased the drying time from 65 h to 28 h; and increased the  $D_{eff}$  value from  $3.82 \cdot 10^{-10} \text{ m}^2/\text{s}$  to  $1.05 \cdot 10^{-9} \text{ m}^2/\text{s}$  when compared to the untreated samples. A similar finding was also reported in another study, in which the cabinet drying of seedless grapes was investigated at 55, 65

and  $75^\circ C$  [26]. The grapes were pretreated with a solution involving 4%  $K_2CO_3$  and 1% olive oil at  $20^\circ C$  for 1 min. The authors reported that the chemically pretreated grape samples dried faster than the untreated ones and had greater effective moisture diffusivities.

- *Mathematical modeling.* The mathematical modeling results that were obtained for the infrared drying of blueberries, both with and without pretreatments, are shown in Table 3; whereas those for vacuum oven drying are demonstrated in Table 4. The tables show the results for the best 3 models having the highest  $R^2$ , the lowest  $\chi^2$  and lowest RMSE values among the 14 models that have been tested.

**Table 3.** Statistical data of the best 3 drying models obtained for infrared drying

Infrared Drying, No Pretreatment					
70°C Drying Temperature			80°C Drying Temperature		
Verma <i>et al.</i>	Alibas	Weibull	Aghbaslo <i>et al.</i>	Page	Weibull
a = 0.093338	a = 0.938908				
k = 0.041708	k = 0.017065	a = 0.944711	$k_1 = 0.014800$	k = 0.006868	a = 1.251728
g = 0.011790	n = 0.952105	b = 77.347850	$k_2 = -0.003359$	n = 1.251731	b = 53.476658
$R^2 = 0.999957$	b = -0.000215	$R^2 = 0.999932$	$R^2 = 0.999640$	$R^2 = 0.999578$	$R^2 = 0.999578$
$\chi^2 = 0.000008$	g = 0.062626	$\chi^2 = 0.000011$	$\chi^2 = 0.000082$	$\chi^2 = 0.000096$	$\chi^2 = 0.000096$
RMSE = 0.002632	$R^2 = 0.999949$	RMSE = 0.003088	RMSE = 0.008179	RMSE = 0.008861	RMSE = 0.008861
	$\chi^2 = 0.000012$				
	RMSE = 0.002868				
Infrared Drying, 30°C and 1 min $K_2CO_3$ Pretreatment					
70°C Drying Temperature			80°C Drying Temperature		
Logarithmic	Aghbaslo <i>et al.</i>	Page	Logarithmic	Aghbaslo <i>et al.</i>	Page
a = 1.024398	$k_1 = 0.013438$	k = 0.012101	a = 1.108394	$k_1 = 0.021623$	k = 0.015880
k = 0.013269	$k_2 = -0.000530$	n = 1.035576	k = 0.020326	$k_2 = -0.003058$	n = 1.126723
c = -0.027156	$R^2 = 0.999908$	$R^2 = 0.999788$	c = -0.114802	$R^2 = 0.999136$	$R^2 = 0.998096$
$R^2 = 0.999968$	$\chi^2 = 0.000015$	$\chi^2 = 0.000035$	$R^2 = 0.999796$	$\chi^2 = 0.000157$	$\chi^2 = 0.000346$
$\chi^2 = 0.000006$	RMSE = 0.003677	RMSE = 0.005586	$\chi^2 = 0.000042$	RMSE = 0.011336	RMSE = 0.016823
RMSE = 0.002174			RMSE = 0.005506		
Infrared Drying, 30°C and 3 min $K_2CO_3$ Pretreatment					
70°C Drying Temperature			80°C Drying Temperature		
Midilli & Kucuk	Verma <i>et al.</i>	Two Term Exp.	Midilli & Kucuk	Logarithmic	Page
a = 1.000284	a = 0.049963	a = 0.047820	a = 0.998779	a = 1.081951	k = 0.015013
k = 0.023122	k = 0.176415	k = 0.270956	k = 0.021765	k = 0.018775	n = 1.103146
n = 0.861844	g = 0.012933	$R^2 = 0.999571$	n = 0.978232	c = -0.086514	$R^2 = 0.998895$
b = -0.000261	$R^2 = 0.999573$	$\chi^2 = 0.000076$	b = -0.000596	$R^2 = 0.999872$	$\chi^2 = 0.000214$
$R^2 = 0.999956$	$\chi^2 = 0.000070$	RMSE = 0.007620	$R^2 = 0.999890$	$\chi^2 = 0.000028$	RMSE = 0.013226
$\chi^2 = 0.000008$	RMSE = 0.007599		$\chi^2 = 0.000028$	RMSE = 0.004507	
RMSE = 0.002452			RMSE = 0.004183		
Infrared Drying, 60°C and 1 min $K_2CO_3$ Pretreatment					
70°C Drying Temperature			80°C Drying Temperature		
Verma <i>et al.</i>	Two Term Exp.	Alibas	Aghbaslo <i>et al.</i>	Two Term Exp.	Henderson&Pabis
		a = 1.184367			
a = 0.142754	a = 0.142377	k = 0.027807	$k_1 = 0.024843$	a = 0.015305	a = 0.996844
k = 0.083827	k = 0.084725	n = 0.794394	$k_2 = -0.000796$	k = 1.669035	k = 0.025856
g = 0.012060	$R^2 = 0.999988$	b = 0.000385	$R^2 = 0.998870$	$R^2 = 0.998747$	$R^2 = 0.998715$
$R^2 = 0.999988$	$\chi^2 = 0.000002$	g = -0.183970	$\chi^2 = 0.000190$	$\chi^2 = 0.000271$	$\chi^2 = 0.000216$
$\chi^2 = 0.000002$	RMSE = 0.001281	$R^2 = 0.999983$	RMSE = 0.012481	RMSE = 0.013142	RMSE = 0.013309
RMSE = 0.001277		$\chi^2 = 0.000003$			
		RMSE = 0.001501			

**Table 3.** Continued

Infrared Drying, 60°C and 3 min K <sub>2</sub> CO <sub>3</sub> Pretreatment					
70°C Drying Temperature			80°C Drying Temperature		
Aghbaslo <i>et al.</i>	Logarithmic	Parabolic	Alibas	Parabolic	Wang & Singh
			a = 0.588739		
k <sub>1</sub> = 0.020717	a = 0.951661	a = 0.914913	k = 0.774614	a = 0.969178	a = -0.022563
k <sub>2</sub> = 0.001650	k = 0.019081	b = -0.011803	n = 0.000002	b = -0.021311	b = 0.000134
R <sup>2</sup> = 0.998654	c = 0.024022	c = 0.000041	b = -0.007907	c = 0.000124	R <sup>2</sup> = 0.996161
χ <sup>2</sup> = 0.000168	R <sup>2</sup> = 0.998339	R <sup>2</sup> = 0.989896	g = 0.411261	R <sup>2</sup> = 0.997028	χ <sup>2</sup> = 0.000614
RMSE = 0.012181	χ <sup>2</sup> = 0.000222	χ <sup>2</sup> = 0.001347	R <sup>2</sup> = 0.989248	χ <sup>2</sup> = 0.000535	RMSE = 0.022419
	RMSE = 0.013533	RMSE = 0.033306	χ <sup>2</sup> = 0.002572	RMSE = 0.019729	
			RMSE = 0.037455		

**Table 4.** Statistical data of the best 3 drying models obtained for vacuum oven drying

Vacuum Oven Drying, No Pretreatment					
70°C Drying Temperature			80°C Drying Temperature		
Aghbaslo <i>et al.</i>	Parabolic	Wang & Singh	Midilli & Kucuk	Aghbaslo <i>et al.</i>	Parabolic
			a = 1.003165		
k <sub>1</sub> = 0.008337	a = 1.005056	a = -0.008974	k = 0.003276	k <sub>1</sub> = 0.009662	a = 1.025114
k <sub>2</sub> = -0.003221	b = -0.009082	b = 0.000019	n = 1.327302	k <sub>2</sub> = -0.005698	b = -0.011921
R <sup>2</sup> = 0.999921	c = 0.000020	R <sup>2</sup> = 0.999812	b = -0.001140	R <sup>2</sup> = 0.999365	c = 0.000029
χ <sup>2</sup> = 0.000013	R <sup>2</sup> = 0.999832	χ <sup>2</sup> = 0.000032	R <sup>2</sup> = 0.999912	χ <sup>2</sup> = 0.000140	R <sup>2</sup> = 0.999053
RMSE = 0.003438	χ <sup>2</sup> = 0.000031	RMSE = 0.005304	χ <sup>2</sup> = 0.000025	RMSE = 0.010688	χ <sup>2</sup> = 0.000234
	RMSE = 0.005022		RMSE = 0.003982		RMSE = 0.013049
Vacuum Oven Drying, 30°C and 1 min K <sub>2</sub> CO <sub>3</sub> Pretreatment					
70°C Drying Temperature			80°C Drying Temperature		
Verma <i>et al.</i>	Logarithmic	Parabolic	Midilli & Kucuk	Verma <i>et al.</i>	Logarithmic
			a = 0.999890		
a = 1.048215	a = 1.255558	a = 0.982561	k = 0.012547	a = -0.935529	a = 1.338851
k = 0.012915	k = 0.010626	b = -0.011741	n = 1.052367	k = 0.003666	k = 0.012065
g = -0.008318	c = -0.260330	c = 0.000036	b = -0.001376	g = 0.009988	c = -0.336694
R <sup>2</sup> = 0.999984	R <sup>2</sup> = 0.999938	R <sup>2</sup> = 0.999400	R <sup>2</sup> = 0.999997	R <sup>2</sup> = 0.999990	R <sup>2</sup> = 0.999983
χ <sup>2</sup> = 0.000002	χ <sup>2</sup> = 0.000008	χ <sup>2</sup> = 0.000079	χ <sup>2</sup> = 0.000001	χ <sup>2</sup> = 0.000002	χ <sup>2</sup> = 0.000003
RMSE = 0.001305	RMSE = 0.002594	RMSE = 0.008082	RMSE = 0.000667	RMSE = 0.001208	RMSE = 0.001579
Vacuum Oven Drying, 30°C and 3 min K <sub>2</sub> CO <sub>3</sub> Pretreatment					
70°C Drying Temperature			80°C Drying Temperature		
Aghbaslo <i>et al.</i>	Parabolic	Wang & Singh	Parabolic	Wang & Singh	Midilli & Kucuk
			a = 1.001804		a = 0.998960
k <sub>1</sub> = 0.010245	a = 0.999894	a = -0.010261	b = -0.012653	a = -0.012589	k = 0.007904
k <sub>2</sub> = -0.002686	b = -0.010258	b = 0.000027	c = 0.000034	b = 0.000034	n = 1.101464
R <sup>2</sup> = 0.999943	c = 0.000027	R <sup>2</sup> = 0.999906	R <sup>2</sup> = 0.999978	R <sup>2</sup> = 0.999975	b = -0.002040
χ <sup>2</sup> = 0.000009	R <sup>2</sup> = 0.999906	χ <sup>2</sup> = 0.000014	χ <sup>2</sup> = 0.000004	χ <sup>2</sup> = 0.000004	R <sup>2</sup> = 0.999958
RMSE = 0.002741	χ <sup>2</sup> = 0.000015	RMSE = 0.003518	RMSE = 0.001764	RMSE = 0.001879	χ <sup>2</sup> = 0.000009
	RMSE = 0.003517				RMSE = 0.002445
Vacuum Oven Drying, 60°C and 1 min K <sub>2</sub> CO <sub>3</sub> Pretreatment					
70°C Drying Temperature			80°C Drying Temperature		
Logarithmic	Aghbaslo <i>et al.</i>	Parabolic	Midilli & Kucuk	Logarithmic	Aghbaslo <i>et al.</i>
			a = 0.999198		
a = 1.140042	k <sub>1</sub> = 0.012230	a = 0.972749	k = 0.017115	a = 1.164516	k <sub>1</sub> = 0.014517
k = 0.011179	k <sub>2</sub> = -0.001967	b = -0.010591	n = 0.958669	k = 0.013054	k <sub>2</sub> = -0.002630
c = -0.146612	R <sup>2</sup> = 0.999434	c = 0.000030	b = -0.000950	c = -0.171182	R <sup>2</sup> = 0.999227
R <sup>2</sup> = 0.999859	χ <sup>2</sup> = 0.000081	R <sup>2</sup> = 0.999066	R <sup>2</sup> = 0.999931	R <sup>2</sup> = 0.999859	χ <sup>2</sup> = 0.000161
χ <sup>2</sup> = 0.000021	RMSE = 0.008436	χ <sup>2</sup> = 0.000143	χ <sup>2</sup> = 0.000019	χ <sup>2</sup> = 0.000033	RMSE = 0.011484
RMSE = 0.004207		RMSE = 0.010837	RMSE = 0.003443	RMSE = 0.004901	
Vacuum Oven Drying, 60°C and 3 min K <sub>2</sub> CO <sub>3</sub> Pretreatment					
70°C Drying Temperature			80°C Drying Temperature		
Midilli & Kucuk	Verma <i>et al.</i>	Two-Term Exp.	Logarithmic	Two-Term Exp.	Midilli & Kucuk
			a = 1.235259		a = 1.000000
a = 1.000000	a = 0.476031	a = 0.003136	k = 0.012256	a = 0.002874	k = 0.215135
k = 0.262958	k = 0.014265	k = 4.521424	c = -0.229720	k = 6.267741	n = 0.000001
n = 0.000001	g = 0.014265	R <sup>2</sup> = 0.996728	R <sup>2</sup> = 0.999790	R <sup>2</sup> = 0.990913	b = -0.006473
b = -0.004603	R <sup>2</sup> = 0.996863	χ <sup>2</sup> = 0.000583	χ <sup>2</sup> = 0.000053	χ <sup>2</sup> = 0.002606	R <sup>2</sup> = 0.986249
R <sup>2</sup> = 0.977569	χ <sup>2</sup> = 0.000519	RMSE = 0.021112	RMSE = 0.006203	RMSE = 0.040722	χ <sup>2</sup> = 0.003934
χ <sup>2</sup> = 0.003958	RMSE = 0.020676				RMSE = 0.050036
RMSE = 0.055016					

## CONCLUSION

This study explored the impact of chemical pretreatment using a  $K_2CO_3$  solution on the infrared and vacuum oven drying of blueberries. The research investigated how various drying methods, temperatures, pretreatment solution temperatures and pretreatment durations influenced the drying efficiency. Additionally, 14 drying models from existing literature were applied to mathematically model the drying process of blueberries. Vacuum oven drying was observed to reduce drying times, and drying rates were found to increase as the drying temperature was raised from 70 to 80°C.  $K_2CO_3$  pretreatment solution's temperature was selected as 30°C and 60°C, and at both temperatures, the blueberry samples were dipped in the pretreatment solution for 1 min and 3 min. Accordingly, for the infrared drying experiments, it was seen that 1 min dipping of the blueberries in a 30°C  $K_2CO_3$  pretreatment solution caused a decrease in the drying time and an increase in the  $D_{eff}$  values. However, further contact of the blueberries at the foresaid solution temperature, and increasing the solution temperature at this dipping time did not cause any significant change in the drying performance. 3 min pretreatment with 60°C  $K_2CO_3$  solution yielded the highest  $D_{eff}$  value and the shortest drying time. The drying duration was between 135 - 255 min for the untreated blueberries, 105 - 210 min for blueberries treated with  $K_2CO_3$  at 30°C, and 90 - 225 min for blueberries treated with  $K_2CO_3$  at 60°C.  $D_{eff}$  values were found between  $1.13 \cdot 10^{-9} - 5.14 \cdot 10^{-10}$  m<sup>2</sup>/s for the untreated blueberries,  $1.54 \cdot 10^{-9} - 6.51 \cdot 10^{-10}$  m<sup>2</sup>/s for blueberries treated with  $K_2CO_3$  at 30°C, and  $1.54 \cdot 10^{-9} - 7.40 \cdot 10^{-10}$  m<sup>2</sup>/s for blueberries treated with  $K_2CO_3$  at 60°C.

When using vacuum oven drying, a comparable reduction in drying time and an increase in  $D_{eff}$  were observed after immersing the blueberries for 1 min in a  $K_2CO_3$  solution at 30°C. However, raising the temperature of the pretreatment solution or extending the contact time with  $K_2CO_3$  did not notably improve the drying efficiency. The drying duration was between 120 - 180 min for the untreated blueberries, 105 - 165 min for blueberries treated with  $K_2CO_3$  at 30°C, and 135 - 180 min for blueberries treated with  $K_2CO_3$  at 60°C.  $D_{eff}$  values, on the other hand, varied between  $1.28 \cdot 10^{-9} - 7.98 \cdot 10^{-10}$  m<sup>2</sup>/s for the untreated blueberries,  $1.33 \cdot 10^{-9} - 9.47 \cdot 10^{-10}$  m<sup>2</sup>/s for blueberries treated with  $K_2CO_3$  at 30°C, and  $1.15 \cdot 10^{-9} - 7.33 \cdot 10^{-10}$  m<sup>2</sup>/s for blueberries treated with  $K_2CO_3$  at 60°C.

## REFERENCES

1. K. S. Ravichandran, K. Krishnaswamy, *Crit. Rev. Food. Sci. Nutr.*, **63** (20), 4235 (2023).
2. M. Zielinska, A. Michalska, *Food Chem.*, **212**, 671 (2016).
3. M. Zielinska, P. Sadowski, W. Blaszczyk, *LWT Food Sci. Technol.*, **62**, 555 (2015).
4. Z. Petrova, K. Slobodianiuk, O. Grakov, *East-Eur. J. Enterp. Technol.*, **2** (11(122)), 83 (2023).
5. A. Akcicek, E. Avci, Z. H. Tekin-Cakmak, M. Z. Kasapoglu, O. Sagdic, S. Karasu, *ACS Omega*, **8**, 41603 (2023).
6. S. Li, Y. Tao, D. Li, G. Wen, J. Zhou, S. Manickam, Y. Han, W. S. Chai, *Chemosphere*, **276**, 130090 (2021).
7. K. J. Mothibe, M. Zhang, J. Nsor-atindana, Y. Wang, *Drying Technol.*, **29** (14), 1611 (2011).
8. L. Deng, A. S. Mujumdar, Q. Zhang, X. Yang, J. Wang, Z. Zheng, Z. Gao, H. Xiao, *Crit. Rev. Food Sci. Nutr.*, **59** (9), 1408 (2017).
9. M. Pateiro, M. Vargas-Ramella, D. Franco, A. Gomes da Cruz, G. Zengin, M. Kumar, K. Dhama, J. M. Lorenzo, *Food Chem., X*, **16**, 100465 (2022).
10. İ. Doymaz, *J. Food Sci. Technol.*, **49** (2), 214 (2012).
11. X. Zhang, M. Li, L. Zhu, Z. Geng, X. Liu, Z. Cheng, M. Zhao, Q. Zhang, X. Yang, *Foods*, **12**, 4255 (2023).
12. F. A. N. Fernandes, M. I. Gallaub, S. Rodrigues, *LWT*, **41**, 604 (2008).
13. S. Yılmaz, C. Uyak, *J. Agric. Sci.*, **30** (2), 229 (2024).
14. C. Cui, D. Zhao, J. Huang, J. Hao, Progress on research and development of goji berry drying: a review, *Int. J. Food Prop.*, **25** (1), 435 (2022).
15. İ. Doymaz, *J. Food Eng.*, **78**, 591 (2007).
16. İ. Doymaz, H. Demir, A. Yildirim, *Chem. Eng. Commun.*, **202** (10), 1271 (2015).
17. A. Boudboud, M. B. Aziz, H. Hajjaj, I. Hajji, B. de Meulenaer, H. Mazouz, *Int. J. Food Sci.*, **2023**, 4438353 (2023).
18. J. E. Vasquez-Parra, C. I. Ochoa-Martinez, M. Bustos-Parra, *J. Food Eng.*, **119**, 648 (2013).
19. AOAC, Association of Official Analytical Chemists, Official Methods of Analysis of AOAC International, 16th edn., AOAC International, Rockville, MD, 1995.
20. A. S. Kıpçak, E. M. Derun, N. Tugrul, I. Doymaz, *Chem. Ind. Chem. Eng. Q.*, **27** (3), 279 (2021).
21. E. Kıpçak, *J. Turk. Chem. Soc. Sect. B: Chem. Eng.*, **6** (1), 1 (2023).
22. İ. Doymaz, A. S. Kıpçak, S. Piskin, *Czech J. Food Sci.*, **33** (4), 367 (2015).
23. M. Ayriksa, A. Bahadir, A. Dağdeviren, K. Roshanaei, T. Coşkun, G. K. Ongun, M. Özkaymak, *J. Polytech.*, **25** (3), 1217 (2022).
24. G. Bingol, J. S. Roberts, M. O. Balaban, Y. O. Devres, *Drying Technol.*, **30**, 597 (2012).
25. İ. Doymaz, *J. Food Eng.*, **76**, 212 (2006).
26. İ. Doymaz, P. Altner, *Food Sci. Biotechnol.*, **21** (1), 43 (2012).

# Theoretical study of possible reaction pathways with the OH radical of the Apranax (AP) molecule with naproxen sodium (NS) as an active ingredient

B. Eren\*, Y. Yalcin Gurkan

<sup>1</sup>Tekirdag Namik Kemal University, Vocational School of Social Sciences, Turkey

<sup>2</sup>Tekirdag Namik Kemal University, Department of Chemistry, Turkey

Received June 11, 2024; Accepted: August 15, 2024

In this study, Apranax (AP) with active ingredient naproxen sodium (NS) was examined. Geometric optimizations of the fragments were made on the DFT/B3LYP/6-31G(d) basic set of the Quantum Mechanical Density Functional Theory to theoretically determine all possible reaction pathways of AP with the OH radical. Since the reaction of the molecule with the OH radical is important for both water purification and atmospheric chemistry, calculations were performed both in the gas phase and in the water phase, modeled with CPCM in the COSMO (conductor-like screening solvation model) solvent model. The degradation mechanism was clarified by examining the energy values for all fragments, the bond lengths of the atoms in the fragments, the bond angles, and the Mulliken charges.

**Keywords:** Apranax, naproxen sodium, DFT, OH radical, Gaussian 09

## INTRODUCTION

In this study, the degradation mechanism and fate of the Apranax (AP) molecule in nature of one of the five molecules we investigated in our current scientific research project entitled. "Examining the theoretical degradation mechanisms of selected pharmaceutical product active ingredients" were examined. It is estimated that, the molecules selected within the scope of the project are either excreted from the body through faeces after being used for treatment purposes or it will be mixed into wastewater through the natural cycle as domestic waste without being used at all. When pharmaceutical products, popularly called medicines, are excreted from the body, or are not used and thrown away as waste, their fate in nature has not been investigated yet. The main purpose of this study is to theoretically elucidate the fate of the AP molecule and its hydroxylated parts during degradation in nature.

Naproxen or naproxen sodium (NS) is available and is safely and effectively used worldwide.

Almost one in every five prescriptions for non-steroidal anti-inflammatory drugs contains this active ingredient, such as Apranax fort and Apranax (AP), which are mainly orally administered. Apranax is one of the drugs widely used for the relief of mild to moderate pain, such as headache, toothache, muscle pain, backache, or cold, as well as for medicinal purpose as a treatment of pain for those who suffer from rheumatic diseases such as strains, sprains, menstrual pain, osteoarthritis, rheumatoid arthritis, or other conditions. AP may cause nausea,

diarrhoea, and vomiting. It has side effects such as abdominal pain and skin rash, and its half-life is short. NA is a white crystalline substance used as an analgesic. It is soluble in water; pH of the aqueous solution is 6 or above [1-6].

AP is a hydroxyl scavenger biomolecule. It is also a detector of hydroxyl radicals due to its hydroxylation ability. Attack of any hydroxyl radical on an aromatic compound results in the formation of a new hydroxylated product which can be much more harmful than the original molecule at the beginning of the process. Knowing the degradation mechanism is very important for monitoring the products [7]. Organic compounds undergo photolysis. They react with the OH radical and this reaction causes decomposition reactions in the atmosphere. The OH radical acts as an electrophile in its reaction with any organic molecule and therefore, it easily binds to unsaturated bonds, whereas the O radical is a nucleophile and therefore cannot interact with bonds. If an aliphatic side chain is attached to an aromatic molecule, the OH radical prefers binding to the aromatic ring [8-14]. This study examines the probability of obtaining more dangerous substances through hydroxylation of the AP molecule on its mixing with nature. Of course, all necessary research experiments are carried out before pharmaceutical products are placed on the market, all possible side effects are determined, after which the product is used for the treatment of people. The issue that is ignored or not given much importance is "What would happen if many pharmaceutical products used for therapeutic purposes mix with nature?".

\* To whom all correspondence should be sent:

E-mail: [beren@nku.edu.tr](mailto:beren@nku.edu.tr)

## MATERIALS

Theoretically, to determine all possible reaction paths of AP, geometric optimizations were made on the DFT/B3LYP/6-31G(d) basis set of the Quantum Mechanical Density Functional Theory (DFT), one of the methods for studying electronic structure. For all fragments, energy values were calculated, and geometric optimizations were made using the Gauss View 5.0.8 molecular representation program and the Gaussian 09 program in orbital calculations. With Gaussian 09 program the energies of atoms and molecules can be calculated, geometric optimizations can be made and vibration frequencies, force constants and dipole moments depending on energy can be calculated. Gauss View 5.0.8 Preparing input files for Gaussian package programs is a graphical interface designed to visualize the outputs. Gaussian views molecules, visualizes them, allowing us to rotate and move them as we wish, and it allows us to make changes. Moreover, even for complex calculations, it can be easily entered to prepare the files. It allows us to examine a graphical display of the results calculated by the Gaussian program [15]. The fragmentation reaction energy is affected by the water molecules in the aqueous environment. In addition, geometry stretching in solutions is induced by H<sub>2</sub>O. In other words, the presence of a dielectric medium such as H<sub>2</sub>O causes relaxation in the geometry of the solute and has a stabilizing effect, reducing the energy for this mechanism [7]. Therefore, in this study, CPCM in the COSMO (conductor-like screening solvation model) solvent model in the Gaussian 09 package program was used to explain the solvent effect of H<sub>2</sub>O on the AP + ·OH reaction energy [15].

## RESULTS AND DISCUSSION

For any molecule, the subsequent steps should be considered in order to determine the fragmentation path. Even though it is known that the longest bond and the widest bond angles of atoms will be fragmented first, monitoring the energy values and environments of the electronegative atoms is the determining factor for the fragmentation. It is essential that double-bonded or closed-ring structures are more stable than others, and if fragmentation occurs, breaking away of these stable structures will be at the last stage [16].

As given in Table 1, the energy values of all possible reaction pathways for each fragment were calculated in both the gaseous and aqueous phases. Every fragment that could be formed after the interaction of the main molecule AP with the OH radical was included in the study. Since the digits after the comma are close to each other when converting the results to SI units, which also leads to a difficulty in observing the energy difference between the fragments, the energy values are given in atomic mass units (AU).

When the Mulliken charges of the AP molecule (see Table 2) are examined, the electronegative atoms are O<sub>30</sub>, O<sub>17</sub>, O<sub>29</sub>, C<sub>24</sub>, C<sub>22</sub>, C<sub>18</sub>, respectively. In Fig. 1, O<sub>29</sub> is stable because it makes a double bond with C<sub>28</sub>, and although O<sub>29</sub> is the third electronegative atom according to Table 2, this bond is not expected to be broken.

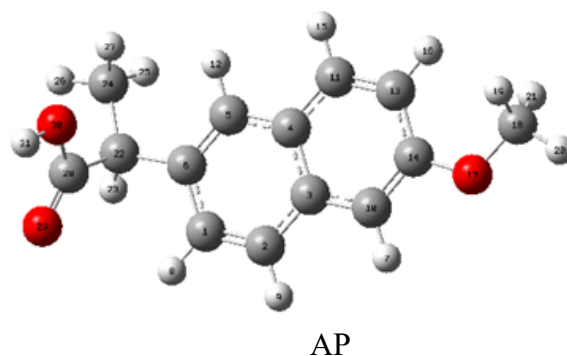


**Fig. 1.** In the geometric structure of the Apranax (AP) molecule optimized by the DFT method, the C atom is represented in grey, the O atom in red, and the H atom in white.

According to Table 1, the A<sub>1</sub> fragment of the molecule is the fragment with the lowest energy (in atomic mass units-Au) of -728.065048 Au, it is the most stable. This fragment is formed by breaking the O<sub>17</sub>-C<sub>18</sub> bond with a length of 1.41818 Å according to Fig. 2 (a) and removing the methyl group from the molecule. This bond length is not the longest bond length in the molecule, but the bond angle of C<sub>14</sub>-O<sub>17</sub>-C<sub>18</sub> is the widest bond angle at 118.76650° according to Fig. 2 (b).

The O<sub>17</sub> atom is the second electronegative atom with a value of -0.510088 (Table 2). The OH radical is a selective organic molecule scavenger. As a result of examining the molecule in terms of its reaction with OH radicals in air or water, this part of the molecule is the first to react.

**Table 1.**  $\Delta E$  (energy),  $\Delta H$  (enthalpy) and  $\Delta G$  (Gibbs free energy) values of the AP molecule and its fragments in gas and water phases.

(AU)	AP	A <sub>1</sub>	A <sub>2</sub>	A <sub>3</sub>
$\Delta E$	-767.340690	-728.065048	-728.058301	-692.097954
Gas phase $\Delta H$	-767.339746	-728.064104	-728.057357	-692.097009
$\Delta G$	-767.399548	-728.120317	-728.114497	-692.154919
Water phase	-767.351790	-728.078283	-728.069433	-692.107155
	-767.350846	-728.077339	-728.068489	-692.106210
	-767.410901	-728.133929	-728.125993	-692.164391
	A <sub>4</sub>	A <sub>5</sub>	A <sub>6</sub>	A <sub>7</sub>
	-652.854532	-688.782675	-652.814627	613.572178
Gas phase	-652.853588	-688.781731	-652.813683	-613.571234
	-652.907137	-688.835296	-652.868863	-613.622106
	-652.863690	-688.795917	-652.823952	-613.581316
Water phase	-652.862746	-688.794973	-652.823008	-613.580372
	-652.916915	-688.849045	-652.878269	-613.631589
	A <sub>8</sub>	A <sub>9</sub>	A <sub>10</sub>	A <sub>11</sub>
	-500.224176	-539.513017	-538.328373	-425.027148
Gas phase	-500.223232	-539.512073	-538.327429	-425.026204
	-500.268414	539.561234	-538.376379	-425.069205
	-500.229842	-539.518748	-538.335816	-425.030971
Water phase	-500.228898	-539.517804	-538.334872	-425.030027
	-500.274103	-539.566972	-538.384073	-425.073003
	A <sub>12</sub>	A <sub>13</sub>		
	-460.949586	-385.738101		
Gas phase	-460.948642	-385.737157		
	-460.990157	-385.776091		
	-460.957008	-385.741854		
Water phase	-460.956063	-385.740910		
	-460.997569	-385.779854		

**Table 2.** Mulliken atomic charges of the AP molecule

	AP	A <sub>1</sub>	A <sub>2</sub>	A <sub>3</sub>
Mulliken atomic charges	O <sub>17</sub> -0.510088	O <sub>17</sub> -0.644225	C <sub>18</sub> -0.214859	C <sub>18</sub> -0.215461
	C <sub>18</sub> -0.214741	C <sub>18</sub> -0.227769	C <sub>22</sub> -0.411621	C <sub>22</sub> -0.219371
	C <sub>22</sub> -0.227955	C <sub>20</sub> -0.464094	C <sub>24</sub> 0.575113	C <sub>24</sub> -0.473059
	C <sub>24</sub> -0.463800	C <sub>24</sub> 0.587793	O <sub>25</sub> -0.457604	C <sub>28</sub> 0.266246
	O <sub>29</sub> -0.468068	O <sub>25</sub> -0.467892	O <sub>26</sub> -0.560323	O <sub>29</sub> -0.388433
	O <sub>30</sub> -0.565811	O <sub>26</sub> -0.565833		
	A <sub>4</sub>	A <sub>5</sub>	A <sub>6</sub>	A <sub>7</sub>
	C <sub>17</sub> -0.228769	O <sub>17</sub> -0.643993	O <sub>17</sub> -0.509248	C <sub>17</sub> -0.412000
	C <sub>19</sub> -0.464121	C <sub>18</sub> -0.411896	C <sub>18</sub> -0.215717	C <sub>19</sub> 0.575202
	C <sub>23</sub> 0.587811	C <sub>20</sub> 0.575225	C <sub>22</sub> -0.416238	O <sub>20</sub> -0.456608
	O <sub>24</sub> -0.467005	O <sub>21</sub> -0.457244	C <sub>24</sub> 0.263829	O <sub>21</sub> -0.559514
	O <sub>25</sub> -0.565016	O <sub>22</sub> -0.560294	O <sub>25</sub> -0.382001	
	A <sub>8</sub>	A <sub>9</sub>	A <sub>10</sub>	A <sub>11</sub>
	O <sub>17</sub> -0.510468	O <sub>17</sub> -0.511301	C <sub>17</sub> -0.417131	C <sub>17</sub> -0.532257
	C <sub>18</sub> -0.214254	C <sub>18</sub> -0.213556	C <sub>19</sub> 0.263685	
		C <sub>22</sub> -0.531819	O <sub>20</sub> -0.380335	
	A <sub>12</sub>	A <sub>13</sub>		
	C <sub>13</sub> -0.156415	C <sub>1</sub> -0.134946		
	C <sub>14</sub> 0.354987	C <sub>2</sub> -0.190872		
	O <sub>17</sub> -0.644507	C <sub>5</sub> -0.190768		
		C <sub>6</sub> -0.135011		
		C <sub>10</sub> -0.190765		
		C <sub>11</sub> -0.190866		
		C <sub>13</sub> -0.134947		
		C <sub>14</sub> -0.135010		

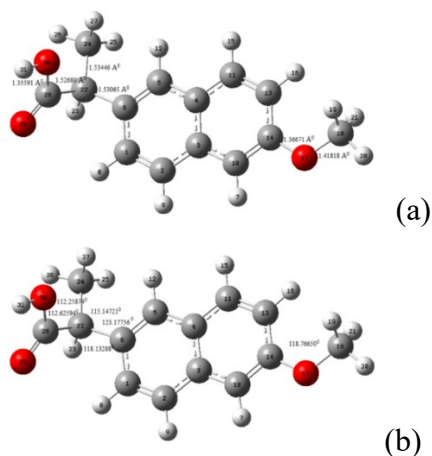


**Fig. 2.** Bond lengths (a) and bond angles (b) between the atoms connected to the closed ring in the AP molecule (C atom is represented in grey, O atom in red and H atom in white).

O<sub>30</sub> is the most electronegative atom according to Table 2. When the methyl groups of C<sub>18</sub> and C<sub>24</sub> at the ends of the AP molecule and the OH group of O<sub>30</sub>

are removed from the molecule, the A<sub>1</sub>, A<sub>2</sub> and A<sub>3</sub> fragments formed are low-energy fragments with values of -728.065048 A<sup>0</sup>, -728.058301 A<sup>0</sup>, and -692.097954 A<sup>0</sup>, respectively. By comparing with the energy values of all other fragments, three different separation methods were assumed from these three fragments.

After determining the three main fragmentation pathways of the AP molecule, all possible fragments of each pathway were created by removing atoms from the ends of the A<sub>1</sub>, A<sub>2</sub>, and A<sub>3</sub> fragments. We already know that the OH radical acts as an electrophile and the O radical acts as a nucleophile [8-14]. Thus, we identified all hydroxylation products of the AP molecule. In order to prevent any incompleteness, all fragments, which were fragmented from around different atoms of MA molecule, were investigated in terms of their optimized figure, electrochemical values, bond lengths and angles, and the most stable fragments were chosen accordingly.

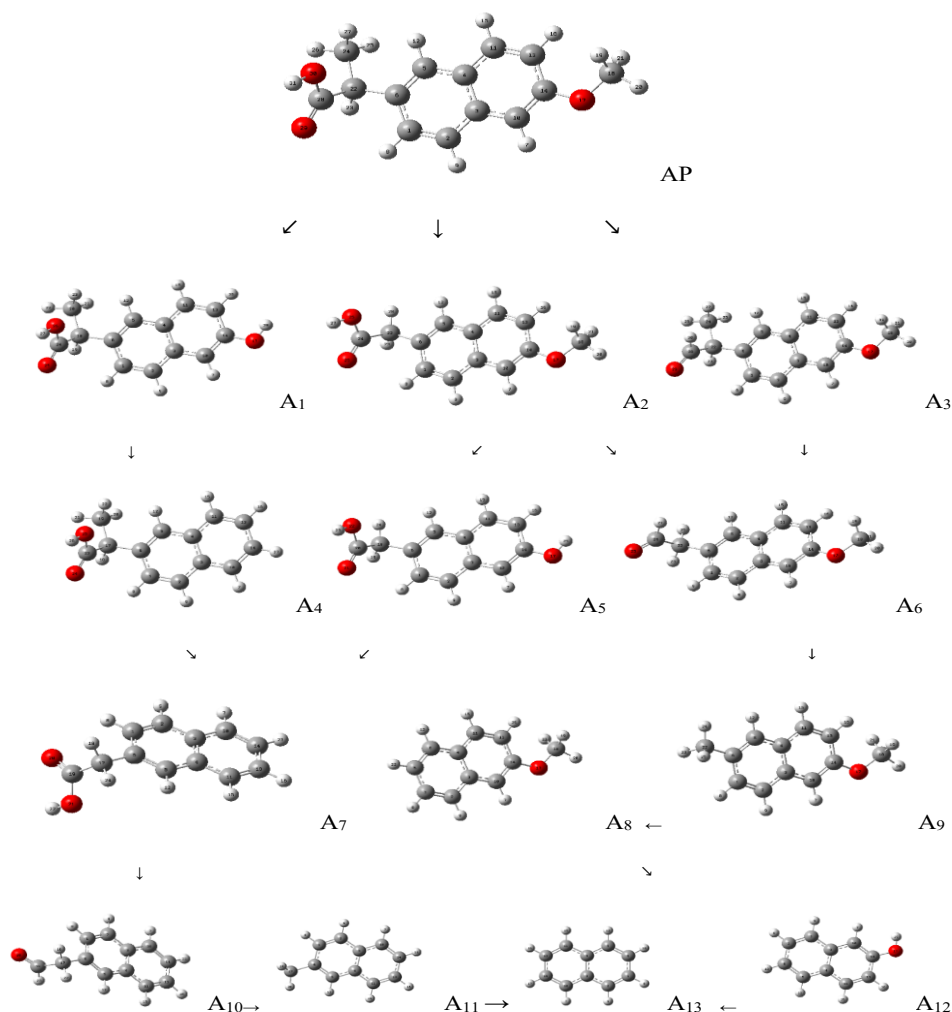


**Fig. 3.** Degradation pathway (degradation mechanism) of the Apranax (AP) molecule (the C atom in the geometric structures of the AP molecule and in all fragments optimized by the DFT method is represented in grey, the O atom in red and the H atom in white).

## CONCLUSION

The Mulliken charges of the atoms in the molecule were examined as described, and the electronegative atoms in the molecule and the arrangement of the atoms around them, stable double bonds, weak bonds at the end of the molecule, calculated energies, bond lengths and bond angles between the atoms helped us to select all the fragments that would determine the degradation mechanism. The degradation pathway of the AP molecule is shown on Fig. 3. The OH radical is a selective organic molecule scavenger. As a result of examining the molecule in terms of its reaction with OH radicals in air or water, the fragmentation reaction of each molecule was written, starting from the low-energy fragments, and its fate in nature could be determined in this way. In our study, the path that the active ingredient of the researched product follows in nature, in water or in the atmosphere, that is, the degradation reactions with OH radicals, was theoretically investigated without using any chemicals. The results obtained can be compared with the fragments we specified in our fragmentation reaction, if desired, when the necessary samples are taken from the wastewater and analyzed by HPLC.

**Acknowledgement:** The current study was supported by Tekirdag Namik Kemal University Scientific Research Project Coordination Centre, (Project No: NKUBAP.00.GA.23.506).

## REFERENCES

1. M. Polat, M. Korkmaz, *International Journal of Pharmaceutics*, **244**, 169 (2002).
2. S. Bozdag, S. Calis, H. S. Kas, M. T. Ercan, I. Peksoy, A. A. Hincal, *Journal of Microencapsulation*, **18**, 443 (2001).
3. S. Çaliş, S. Bozdağ, H.S. Kaş, M. Tunçay, *Il Farmaco*, **57**, 55 (2002).
4. R. Ommaty, *Vademecum: medical drug reference book*, Tribune publishing ltd company. Istanbul, 2008.
5. M. J. O'Neil, *The Merck Index- An Encyclopedia of Chemicals, Drugs, and Biologicals*. Cambridge, UK, 2013.
6. <https://www.drugbank.ca/drugs/DB00788>
7. B. Eren, Y. Yalcin Gurkan, *J. Serb. Chem. Soc.*, **82**, 277 (2017).
8. M. Anbar, P. Neta, *Int. J. Appl. Radiat. Isot.*, **18**, 493 (1967).
9. S. M. Aschmann, E. C. Tuazon, R. Atkinson, *J. Phys. Chem., A*, **109**, 11828 (2005).
10. S. M. Aschmann, R. Atkinson, *J. Phys. Chem., A*, **110**, 13029 (2006).
11. S. M. Aschmann, E. C. Tuazon, W. D. Long, R. Atkinson, *J. Phys. Chem., A*, **114**, 3523 (2010).
12. R. Atkinson, S. M. Aschmann, M. A. Goodman, A. M. Winer, *Int. J. Chem. Kinet.*, **20**, 273 (1998).
13. R. Atkinson, J. Arey, *Chem. Rev.*, **103**, 4605 (2003).
14. B. Halliwell, M. Grootveld, J. M. C. Gutteridge, *Methods Biochem. Anal.*, **33**, 59 (1998).
15. Gaussian 09, Revision B.04, Gaussian, Inc., Pittsburgh, PA, 2009.
16. B. Eren, Y. Yalcin Gurkan, *Innovative Research in Engineering*, Duvar Publishing, İzmir, Turkey, 2023, **4**, p. 49.

## Carvacrol and 4-IP-2-MeO-1-MB derivatives: DFT computations and drug-likeness studies

G. Serdaroğlu\*

Sivas Cumhuriyet University, Faculty of Education, Department of Mathematics and Science Education, 58140, Sivas, Turkey

Received May 26, 2024; Accepted: August 17, 2024

This work deals with the detailed computational investigation of carvacrol and 4-IP-2-MeO-1-MB (4-isopropyl-2-methoxy-1-methylbenzene) derivatives which include an -OCH<sub>3</sub> functionality instead of an -OH group. Molecular orbital studies were performed at B3LYP/6-311G\*\* level of the theory, in the gas phase. FMO analyses disclosed that CM compound would gain higher charge transfer capability in the presence of halogen. Also, the lipophilicity, water-solubility, drug-likeness, and ADMT properties were predicted to enlighten the possible bioavailability, physicochemical, and pharmacokinetic characteristics, as well as the adverse effects on both health and environment.

**Keywords:** Carvacrol, DFT, FMO & MEP, drug likeness

### INTRODUCTION

Carvacrol molecule, as a member of the monoterpene phenols, has a characteristic pungent odor and is a component of different volatile oils such as oregano, thyme, Lippia, Nigella Sativa, etc. [1-3]. It has been known in traditional medicine for a long time [4] because of its many bioactivity characteristics such as antimicrobial, antioxidant, anticancer, anti-HIV, etc. [5, 6]. Mouwakeh and co-workers have explored the microbial activity and capability of resistance modifiers of the compounds that are the main components of *Nigella sativa* volatile oil; carvacrol and p-cymene can be used as resistance modifiers in MRSA strains [3]. Recently, Anjos and co-workers [7] have prepared biodegradable films including carvacrol and thymol to evaluate their potency on tick control; the inclusion of thymol and carvacrol in the biofilm has increased the mortality rates of larvae and engorged females of the tick *R. microplus* [7]. Kazemi and colleagues have explored the potencies of carvacrol (CAR) and p-cymene in preventing synaptic plasticity impairment; the results imply that combined treatment with carvacrol and p-cymene to prohibit the destructive effects of A $\beta$  on hippocampal LTP couldn't be successful, in spite of their useful effects against Alzheimer's disease (AD) [8]. In previous works, monoterpenes such as carvone, terpineol, limonene [9], and structurally related pyrimidine and cumene [10] derivatives have been reported: the possible bioavailability, physicochemical, and chemical reactivity properties have been investigated by using computational tools.

The main motivation of this work is to enlighten the key electronic, physicochemical, and biomedical properties of carvacrol and structurally related compounds. First, all compounds were optimized at DFT/B3LYP/6-311G\*\* level and then confirmed by having no negative frequency. Then, physicochemical properties were elucidated in light of the computed lipophilicity and water-solubility scores, which are important in terms of designing/modifying future drug agents. Furthermore, the pharmacokinetic and possible toxicity tendencies of the data set were predicted and evaluated. The obtained results of these simple molecular systems are hoped to provide information on exploring the proper precursors which can be used in further drug-design works.

### COMPUTATIONAL DETAILS

All DFT/B3LYP/6-311G\*\* level [11, 12] computations were employed by G09W [13] in the gas phase, and the optimized geometries, FMO plots were visualized by GaussView 6.0.16 [14]. The statistical thermodynamic principles [15, 16] were used for elucidation of the thermochemical quantities of the data set.

The  $I$  “ionization energy” and  $A$  “electron affinity” were predicted by HOMO and LUMO energies according to Koopmans' theorem [17]. The  $I$  and  $A$  values were used to calculate the other reactivity parameters, which are  $\chi$  “electronic chemical potential”,  $\eta$  “global hardness”,  $\omega$  “electrophilicity”,  $\Delta N_{\max}$  “maximum charge transfer capability index” [18, 19],  $\omega^-$  “electrodonating power”,  $\omega^+$  “electroaccepting power” [20], and  $\Delta E_{\text{back-donat}}$  “back-donation energy” [21].

\* To whom all correspondence should be sent:  
E-mail: [goncagul.serdaroglu@gmail.com](mailto:goncagul.serdaroglu@gmail.com)

$$I = -E_{\text{HOMO}} \text{ and } A = -E_{\text{LUMO}}$$

$$\chi = -\left(\frac{I+A}{2}\right)$$

$$\eta = \frac{I-A}{2}$$

$$\omega = \frac{\mu^2}{2\eta}$$

$$\Delta N_{\text{max}} = (I + A)/2(I - A)$$

$$\omega^+ \approx (I + 3A)^2/(16(I - A))$$

$$\omega^- \approx (3I + A)^2/(16(I - A))$$

$$\Delta \varepsilon_{\text{back-donation}} = -(\eta/4)$$

The lipophilicity [22-26] and water-solubility [27, 28] features of the data set were determined by using SwissADME [29] tools. Also, drug-likeness [25, 30-33], bioavailability [34], and ADMET [35] parameters of the data set were determined.

## RESULTS AND DISCUSSION

### Physicochemistry

The optimized structures and the data set's thermodynamic quantities/physical values are given in Fig. 1 and Table 1, respectively. As expected, the  $\mu$  and  $\alpha$  values were calculated for the carvacrol molecule at 1.254 D and 115.190 au, respectively. The  $\Delta E$ ,  $\Delta H$ , and  $\Delta G$  (au) values of carvacrol were calculated at -464.639712, -464.627152, and -464.676987 au, respectively. Instead of the -OH group, the -OCH<sub>3</sub> substitution on the substituted methylbenzene (CM) made these quantities increase, that is, they were calculated for CM at -503.921202 ( $\Delta E$ ), -503.907295 ( $\Delta H$ ), and -503.960320 au ( $\Delta G$ ), respectively. Table 1 shows that the thermodynamic values slightly change according to the position of the halogen atom on the core CM structure. For

instance, the  $\Delta E$ ,  $\Delta H$ , and  $\Delta G$  (au) values of the CM1 were slightly greater predicted -603.194716, -603.179844, and -603.235346, au, respectively, than those of the CM2. Among the carvacrol derivatives, the highest  $\alpha$  values were determined for the bromine-substituted derivatives CM5 and CM6 at 146.746 and 146.254 au, respectively.

Furthermore, Table 2 shows the other two key physicochemical parameters lipophilicity and water-solubility in drug-design research. As is well known, these parameters have shown some different orders depending on the used approach, wherein 5 approaches have been used. Looking at the results of lipophilicity, CM4 (4.94) would show the most lipophilic features according to the XLOGP3, the other methods implied that the bromine-substituted derivatives CM5 and CM6 would be more lipophilic among the compounds. On the other hand, the Avg. LogPo/w order, which was CV (2.82) < CM (3.21) < CM1=CM2 (3.44) < CM3 (3.67) < CM4 (3.85) < CM6 (3.75) < CM5 (3.76) implied that carvacrol would be less lipophilic and CM5 could be more lipophilic than the other derivatives. As expected from the lipophilic features of the derivatives, the halogenated compounds would have lower water-solubility than the CV and CM compounds. According to the SILICOS-IT approach, the CV and CM molecules would be more water-soluble, while all halogenated derivatives would have moderate solubility in water. On the other hand, CM4-CM6 derivatives could exhibit a medium-level water-solubility, whereas the remaining compounds would be soluble in water. All methods implied that CM4 would present lower solubility than the others.

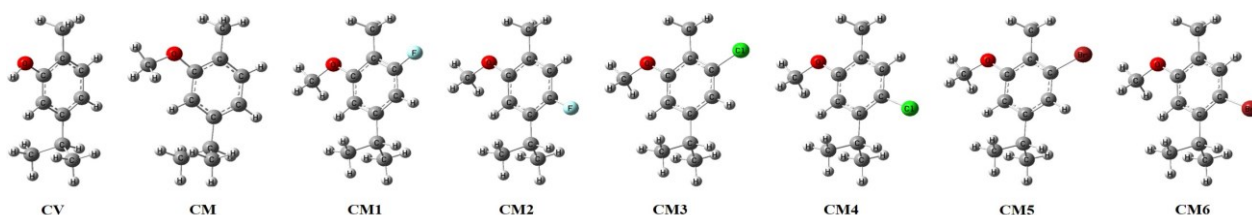


Fig. 1. Optimized chemical structures of the data set

Table 1. Thermochemical and physical values of the data set

Compound	$\Delta E$ (au)	$\Delta H$ (au)	$\Delta G$ (au)	$E_{\text{therm}}$	Cv	S	$\mu$	$\alpha$
CV	-464.639712	-464.627152	-464.676987	142.606	44.249	104.886	1.254	115.190
CM	-503.921202	-503.907295	-503.960320	161.181	48.726	111.600	1.319	128.045
CM1	-603.194716	-603.179844	-603.235346	156.700	51.744	116.814	2.864	127.588
CM2	-603.193057	-603.178217	-603.233994	156.693	51.715	117.393	2.370	127.536
CM3	-963.551686	-963.536369	-963.593622	156.026	52.660	120.499	3.423	140.193
CM4	-963.550795	-963.535546	-963.593304	156.079	52.633	121.562	3.008	139.798
CM5	-3077.472454	-3077.456881	-3077.515348	155.796	53.086	123.055	3.345	146.746
CM6	-3077.471787	-3077.456280	-3077.514697	155.841	53.077	122.950	2.937	146.254

**Table 2.** Lipophilicity and water-solubility

	CV	CM	CM1	CM2	CM3	CM4	CM5	CM6
<i>Lipophilicity</i>								
iLOGP	2.24	2.76	2.87	2.87	3.03	3.00	3.12	3.08
XLOGP3	3.49	3.82	3.48	3.48	4.01	4.94	4.08	4.08
WLOGP	2.82	3.13	3.69	3.69	3.78	3.78	3.89	3.89
MLOGP	2.76	3.05	3.46	3.46	3.60	3.60	3.74	3.74
SILICOS-IT	2.79	3.29	3.72	3.72	3.94	3.94	3.97	3.97
Avg. LogPo/w	2.82	3.21	3.44	3.44	3.67	3.85	3.76	3.75
<i>Water-solubility</i>								
Log S (ESOL)	-3.31	-3.50	-3.37	-3.37	-3.81	-4.39	-4.13	-4.13
Solubility (mg/mL)×10 <sup>-2</sup>	7.40	5.16	7.74	7.74	3.09	0.803	1.81	1.81
Class	S	S	S	S	S	MS	MS	MS
Log S (Ali)	-3.60	-3.71	-3.36	-3.36	-3.91	-4.87	-3.98	-3.98
Solubility (mg/mL)×10 <sup>-2</sup>	3.79	3.21	8.02	8.02	2.47	0.267	2.55	2.55
Class	S	S	S	S	S	MS	S	S
Log S (SILICOS-IT)	-3.01	-3.73	-4.01	-4.01	-4.36	-4.36	-4.59	-4.59
Solubility (mg/mL)×10 <sup>-2</sup>	14.6	3.09	1.76	1.76	0.875	0.875	0.619	0.619
Class	S	S	MS	MS	MS	MS	MS	MS

*Drug-likeness and ADMET study*

According to the Lipinski, Veber and Egan rules, all compounds could be prospective structures in terms of drug-likeness (see Table S1). On the other hand, the Muegge method implied that none of the compounds would have been a proper structure in view of the drug-likeness; heteroatom numbers for all compounds are smaller than 2. In addition to heteroatom numbers, except for CM5 and CM6 compounds, the other violation is the molecular weight < 200. Except for CV, all compounds seem to obey to Ghose rules (Table S1).

From Table S2 (suppl. data), Caco-2 permeability scores of all compounds were calculated in the range of -4.400 and -4.775, which were higher than that of the optimal value (-5.15 Log unit). All compounds could fail by looking at the MDCK permeability and Pgp-inhibitor. Fortunately, the PAMPA, Pgp-substrate, and HIA scores of the data set seem to satisfy expectations. Except for CM3, the VD (volume distribution) of all compounds was predicted in the optimal range of 0.04-20L/kg. CV, CM, CM2, and CM4 would have the capability of BBB (Blood-Brain Barrier) penetration, whereas the others would also be capable of BBB penetration, but not as much as these compounds. The CYP2C9 and CYP2D6 substrate potencies of all compounds would be satisfying. Furthermore, the hERG blockers, genotoxicity, RPMI-8226, A549, and Hek293 cytotoxicity scores implied that all compounds could be safe in terms of avoiding possible medicinal toxicity (Table S3). The calculated scores of the Tox21 pathway implied that none of the compounds could show any toxic effect, except for the CV compound. Namely, the calculated

SR-MMP score of CV implied that this compound could affect the mitochondrial membrane potential.

*FMO and MEP analyses*

The reactivity values obtained from FMOs' energies were used to predict the possible reactivity tendency and region of the molecular systems; wherein the determined reactivity values of the compounds change in the following orders:

$\Delta E$  (L-H): CM (5.821) < CM1 (5.965) < CM2 (5.542) < CM3 (5.826) < CM4 (5.587) < CM5 (5.799) < CM6 (5.565) < CV (5.852)

$\mu$ : CM (-2.966) > CM1 (-3.148) > CM2 (-3.118) > CM3 (-3.292) > CM4 (3.217) > CM5 (-3.298) > CM6 (-3.206) > CV (-3.051)

$\eta$ : CM2 (2.771) < CM6 (2.783) < CM4 (2.793) < CM5 (2.900) < CM (2.911) < CM3 (2.913) < CV (2.926) < CM1 (2.982)

$\omega$ : CM (0.056) < CV (0.058) < CM1 (0.061) < CM2 (0.064) < CM3 = CM4 = CM6 (0.068) < CM5 (0.069)

$\omega^+$ : CM (0.014) < CV (0.016) < CM1 (0.017) < CM2 (0.020) < CM3 (0.021) < CM4 = CM5 = CM6 (0.022)

$\omega^-$ : CM (0.123) < CV (0.128) < CM1 (0.133) < CM2 (0.135) < CM4 = CM6 (0.140) < CM3 (0.142) < CM5 (0.143)

$\Delta N_{\max}$ : CM (1.019) < CV (1.043) < CM1 (1.055) < CM2 (1.125) < CM3 (1.130) < CM5 (1.137) < CM4 = CM6 (1.152)

$\Delta E_{\text{back}}$ : CM1 (-0.746) < CV (-0.731) < CM = CM3 (-0.728) < CM5 (-0.725) < CM4 (-0.698) < CM6 (-0.696) < CM2 (-0.693)

Accordingly, the CM molecule would prefer the intra-molecular interactions than an action toward an external system, less stable electronically, and *vice*

versa for CV. Also, the CM molecule would be less electrophile and have less charge transfer capability. Furthermore, the halogen substitution would gain the main structure more charge transfer capability, especially the -Cl and -Br substitution. On the other hand, the CM1 could gain stability by back-donation more than the other molecules, whereas the CM2 would benefit from back-donation, but not as much as the other molecules.

Fig. 2 shows that the HOMO mostly extended on the aromatic rings, methyl, and methoxy groups, except for CM3, which HOMO did not seem on the methoxy group. The LUMO of CM1 and CM3 expanded on the oxygen of the methoxy group a little, whereas it did not seem on the halogen of CM2 (-F) and CM4 (-Cl). The HOMO and LUMO representations imply the nucleophilic and electrophilic attack sites, respectively. Herein, the -F and -Cl halogens and -OCH<sub>3</sub> substitutions for CM2 and CM4 molecules could not have any role in electrophilic attacks; the isopropyl unit for all compounds would not relate to the nucleophilic attacks. Furthermore, the MEP presentations provide information on the possible reactive regions of the systems by showing the electron-rich ( $V < 0$ , red) and electron-poor ( $V > 0$ , blue) sites as a function of the electrostatic potential on the surface. As expected, the -H atom of the -OH group of the CV molecule was seen as blue, and the aromatic ring was covered

by a yellow color. First, the halogen substitution would affect the electron density on the aromatic ring for all derivatives due to the resonance donation to the ring. Thus, the oxygen atoms and aromatic rings of all compounds seem red colored indicating the regions for the electrophiles, and -OCH<sub>3</sub> groups' H is seen with blue color indicating the electron-poor site for the nucleophiles.

## CONCLUSION

Herein, comprehensive computational works are presented to the evaluation of the reactivity, physicochemical, and bioavailability features of carvacrol and its derivatives. The lipophilicity scores indicated that the CM4 compound would be more lipophilic, and CV was less lipophilic. In contrast, the CV molecule would have the best water-soluble capability among the compounds, while the -Br substituted compounds CM5 and CM6 could be more soluble in water. FMO analyses implied that the halogen substitution on the CM molecule provides higher electron density on the aromatic ring *via* resonance. According to the Lipinski, Veber and Egan rules, all compounds could be promising agents, while none of them, depending on the Muegge method, would be a proper structure in terms of drug-likeness.

**Table 6.** Chemical reactivity parameters

	H (-I)/ eV	L (-A)/ eV	$\Delta E$ (L-H)/ eV	$\mu$ / eV	$\eta$ / eV	$\omega$ / au	$\omega^+$ / au	$\omega^-$ / au	$\Delta N_{\max}$ / eV	$\Delta E_{\text{back}}$ / eV
CV	-5.977	-0.125	5.852	-3.051	2.926	0.058	0.016	0.128	1.043	-0.731
CM	-5.877	-0.055	5.821	-2.966	2.911	0.056	0.014	0.123	1.019	-0.728
CM1	-6.13	-0.165	5.965	-3.148	2.982	0.061	0.017	0.133	1.055	-0.746
CM2	-5.889	-0.347	5.542	-3.118	2.771	0.064	0.020	0.135	1.125	-0.693
CM3	-6.205	-0.379	5.826	-3.292	2.913	0.068	0.021	0.142	1.130	-0.728
CM4	-6.011	-0.424	5.587	-3.217	2.793	0.068	0.022	0.140	1.152	-0.698
CM5	-6.197	-0.398	5.799	-3.298	2.900	0.069	0.022	0.143	1.137	-0.725
CM6	-5.988	-0.423	5.565	-3.206	2.783	0.068	0.022	0.140	1.152	-0.696

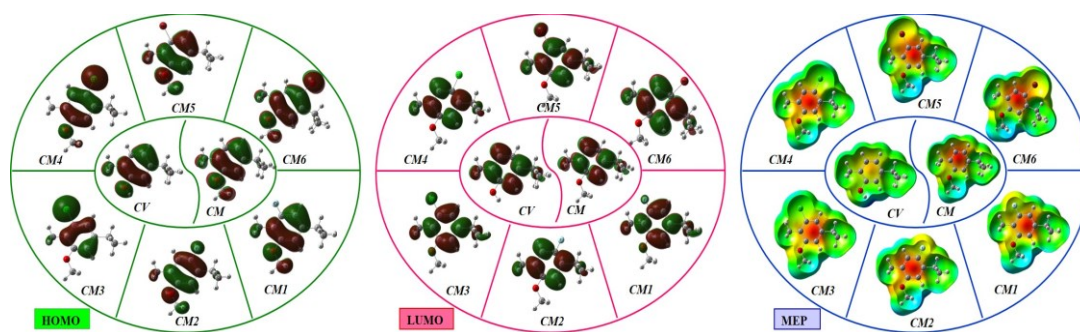


**Fig. 2.** HOMO and LUMO amplitudes of the data set

**Acknowledgement:** All calculations have been carried out at TUBITAK ULAKBIM, High Performance and Grid Computing Center (TR-Grid e-Infrastructure). The author thanks the Scientific Research Projects Department of Sivas Cumhuriyet University (Project No: EĞT-2023-098).

#### REFERENCES

1. M. Sharifi-Rad, E. M. Varoni, M. Iriti, M. Martorell, W. N. Setzer, M. Contreras, B. Saleh, A. Soltani-Nejad, S. Rajabi, M. Tajbakhsh, J. Sharifi-Rad, *Phytother. Res.*, **32**(9), 1675 (2018).
2. Ş. Yıldız, S. Turan, *Atatürk Üniversitesi Ziraat Fakültesi Dergisi*, **52** (1), 108 (2021).
3. A. Mouwakeh, A. Kincses, M. Nové, T. Mosolygó, C. Mohácsi-Farkas, G. Kiskó, G. Spengler. *Phytother. Res.*, **33** (4), 1010 (2019).
4. N. B. Rathod, P. Kulawik, F. Ozogul, J. M. Regenstein, Y. Ozogul. *Trends Food Sci. Tech.*, **116**, 733 (2021).
5. S. Peter, N. Sotondoshe, B. A. Aderibigbe, *Molecules*, **29** (10), 2277 (2023).
6. C. Zhang, Z. Li, D. Hu, *J. Drug. Deliv. Sci. and Tech.*, **97**, 105779 (2024).
7. O. O. Anjos, M. N. Gomes, C. P. Tavares, D. M. Sousa, C. J. Mendonça, J. Reck, A. P. Maciel, L. M. Costa-Junior, *Vet. Parasitol.*, **327**, 110149 (2024).
8. S. Kazemi, S. Safari, S. Komaki, S. A. Karimi, Z. Golipoor, A. Komaki, *CNS Neurosci. Ther.*, **30** (3), e14459 (2024).
9. G. Serdaroğlu, *JOTCSA.*;11(2), 869 (2024).
10. G. Serdaroğlu, E. Soyutek, Ş. Koçarslan, C. Uludağ, *Results Chem.*, **6**, 101106 (2023)
11. A. D. Becke, *J. Chem. Phys.*, **98**, 1372 (1993)
12. C. Lee, W. Yang, R.G. Parr, *Phys. Rev.*, **B37**, 785 (1988).
13. M. J. Frisch et al. Gaussian 09W, Revision D.01, Gaussian, Inc, Wallingford CT, 2013.
14. GaussView 6.0.16, Gaussian, Inc, Wallingford CT, (2016).
15. D. A. McQuarrie, Statistical Thermodynamics, Harper & Row Publishers, New York, 1973.
16. G. Serdaroğlu, S. Durmaz, *Indian J. Chem.*, **49**, 861 (2010).
17. T. Koopmans, *Physica*, **1** (1), 104 (1934).
18. R. G. Pearson, *Proc. Natl. Acad. Sci. USA*, **83**, 8440 (1986).
19. R. G. Parr, L.V. Szentpaly, S. Liu, *J. Am. Chem. Soc.*, **121**, 1922 (1999).
20. J. L. Gazquez, A. Cedillo, A. Vela, *J. Phys. Chem. A*, **111** (10), 1966 (2007).
21. B. Gomez, N. V. Likhanova, M. A. Domínguez-Aguilar, R. Martínez-Palou, A. Vela, J. L. Gazquez, *J. Phys. Chem., B* **110** (18), 8928 (2006).
22. A. Daina, O. Michielin, V. Zoete, *J. Chem. Inf. Model.*, **54**(12) 3284 (2014).
23. T. Cheng, Y. Zhao, X. Li, F. Lin, Y. Xu, X. Zhang, Y. Li, R. Wang, *J. Chem. Inf. Model.*, **47**(6), 2140 (2007).
24. S. A. Wildman, G. M. Crippen, *J. Chem. Inf. Comput. Sci.*, **39**, 868 (1999).
25. C. A. Lipinski, F. Lombardo, B. W. Dominy, P. J. Feeney, *Adv. Drug Deliver. Rev.*, **46**, 3 (2001).
26. Silicos-IT, [online], Available: <https://www.silicos-it.be>.
27. S. Delaney, *J. Chem. Inf. Comput. Sci.*, **44**, 1000 (2004).
28. J. Ali, P. Camilleri, M. B. Brown, A. J. Hutt, S. B. Kirton, *J. Chem. Inf. Model.*, **52**, 2950 (2012).
29. A. Daina, O. Michielin, V. Zoete, *Sci Rep.*, **7**, 42717 (2017).
30. A. K. Ghose, V. N. Viswanadhan, J. J. Wendoloski, *J. Comb. Chem.*, **1**, 55 (1999).
31. D. F. Veber, S. R. Johnson, H.-Y. Cheng, B. R. Smith, K. W. Ward, K. D. Kopple, *J. Med. Chem.*, **45**, 2615 (2002).
32. W. J. Egan, K. M. Merz, Jr., J. J. Baldwin, *J. Med. Chem.* **43**, 3867 (2000).
33. I. Muegge, S. L. Heald, D. Brittelli, *J. Med. Chem.*, **44**(12), 1841 (2001).
34. Y. C. Martin, *J. Med. Chem.*, **48** 3164 (2005).
35. ADMETlab 2.0

## SUPPLEMENTARY DATA

## Table of Contents

Fig. S1. The chemical structures of <i>the data set</i> .....	252
Table S1. Drug-likeness and bioavailability scores.....	252
Table S2. Absorption, Distribution, and Metabolism.....	253
Fig. S2. Boiled-Egg model and radar graphs.....	253
Table S4. Toxicity values of the data set.....	254

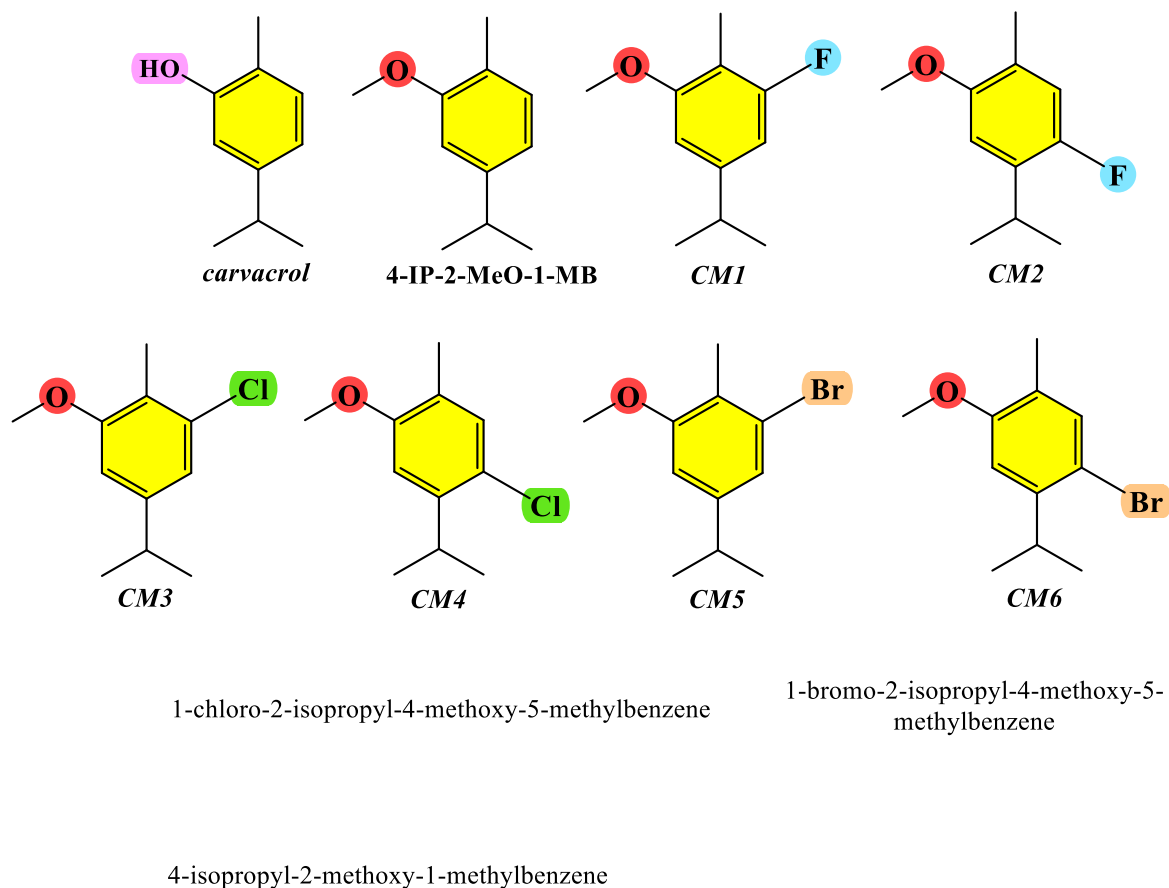
Fig. S1. The chemical structures of *the data set*

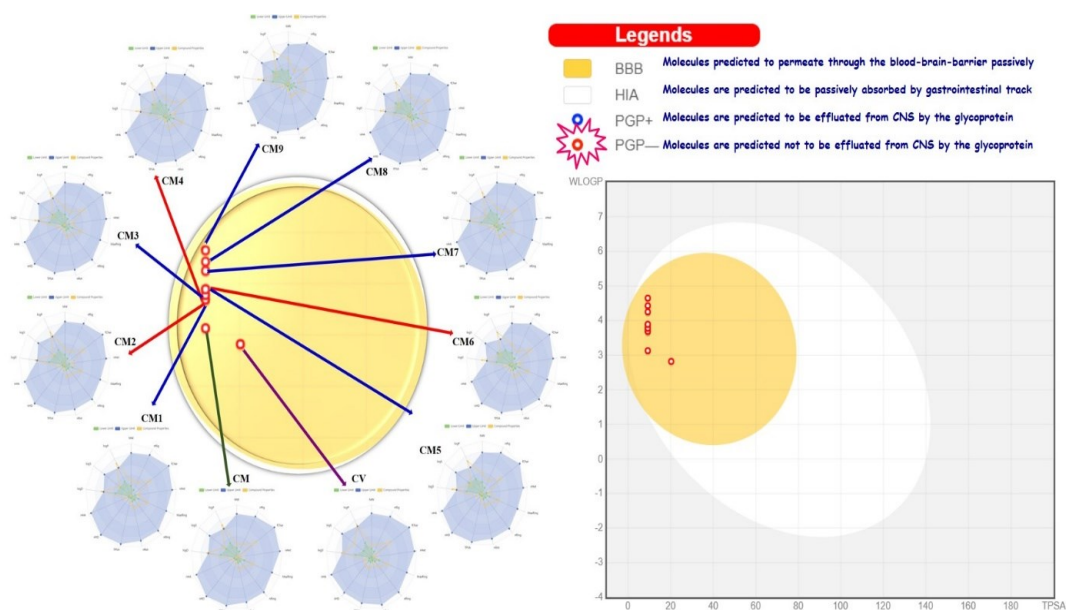
Table S1. Drug-likeness and bioavailability scores

	Lipinski	Ghose	Veber	Egan	Muegge	Bioavail. Score
<i>CV</i>	Yes	No; MW<160	Yes	Yes	No; MW<200, heteroatoms<2	0.55
<i>CM</i>	Yes	Yes	Yes	Yes	No; MW<200, Heteroatoms<2	0.55
<i>CM1</i>	Yes	Yes	Yes	Yes	No; MW<200, Heteroatoms<2	0.55
<i>CM2</i>	Yes	Yes	Yes	Yes	No; MW<200, Heteroatoms<2	0.55
<i>CM3</i>	Yes	Yes	Yes	Yes	No; MW<200, Heteroatoms<2	0.55
<i>CM4</i>	Yes	Yes	Yes	Yes	No; MW<200, Heteroatoms<2	0.55
<i>CM5</i>	Yes	Yes	Yes	Yes	No; Heteroatoms<2	0.55
<i>CM6</i>	Yes	Yes	Yes	Yes	No; Heteroatoms<2	0.55

**Table S2.** Absorption, Distribution, and Metabolism

	CV	CM	CM1	CM2	CM3	CM4	CM5
<b>Absorption</b>							
Caco-2 Pe.	-4.4	-4.576	-4.68	-4.652	-4.775	-4.737	-4.763
MDCK Pe. ( $\times 10^{-5}$ ) cm/s	-4.681	-4.627	-4.651	-4.665	-4.681	-4.687	-4.663
PAMPA	0.027	0.011	0.047	0.002	0.032	0.001	0.022
Pgp-inh.	0.931	0.987	0.898	0.993	0.909	0.987	0.982
Pgp-subs.	0.064	0.163	0.216	0.081	0.079	0.046	0.033
HIA	0.012	0.017	0.021	0.002	0.025	0.001	0.100
F <sub>20%</sub>	0.385	0.227	0.166	0.037	0.128	0.034	0.158
F <sub>30%</sub>	0.719	0.393	0.307	0.074	0.400	0.134	0.555
F <sub>50%</sub>	0.933	0.917	0.906	0.259	0.955	0.615	0.922
<b>Distribution</b>							
PPB %	91.894	97.603	97.716	98.178	98.91	98.928	98.139
VD (L/kg)	0.206	0.217	0.05	0.264	-0.077	0.234	0.187
BBB Pen.	0.179	0.135	0.331	0.142	0.338	0.296	0.401
Fu %	7.482	2.041	1.998	1.392	0.762	0.731	1.703
<b>Metabolism</b>							
CYP1A2 inh.	0.952	0.966	0.964	0.930	0.991	0.994	0.995
CYP1A2 subs.	0.948	0.981	0.991	0.922	0.997	0.938	0.792
CYP2C19 inh.	0.799	0.941	0.923	0.98	0.952	0.993	0.974
CYP2C19 subs.	0.889	0.994	0.971	0.985	0.985	0.996	0.185
CYP2C9 inh.	0.859	0.691	0.894	0.959	0.726	0.859	0.967
CYP2C9 subs.	0.004	0.004	0.043	0.004	0.272	0.228	0.003
CYP2D6 inh.	0.006	0.678	0.152	0.348	0.533	0.859	0.234
CYP2D6 subs.	0.001	0.041	0.003	0.067	0.007	0.154	0.001
CYP3A4 inh.	0.153	0.293	0.471	0.135	0.489	0.755	0.266
CYP3A4 subs.	0.969	0.865	0.266	0.703	0.825	0.969	0.168
CYP2B6 inh.	1.000	0.985	0.908	0.993	0.995	0.995	0.998
CYP2B6 subs.	0.534	0.967	0.241	0.842	0.936	0.992	0.007
CYP2C8 inh.	0.998	0.981	0.995	0.999	0.985	0.998	0.997
HLM Stability	0.868	0.967	0.886	0.959	0.958	0.960	0.882

\* Permeability, Pe; Penetration, Pen, Inhibitor, Inh; Substrate, subs

**Fig. S2.** Boiled-Egg model and radar graphs.

**Table S3.** Toxicity values of the data set

	<i>CV</i>	<i>CM</i>	<i>CM1</i>	<i>CM2</i>	<i>CM3</i>	<i>CM4</i>	<i>CM5</i>	<i>CM6</i>
<b>Medicinal</b>								
hERG Blockers	0.106	0.129	0.127	0.163	0.136	0.188	0.107	0.118
hERG Blockers (10um)	0.633	0.612	0.573	0.566	0.628	0.656	0.608	0.623
DILI	0.202	0.291	0.374	0.436	0.41	0.52	0.629	0.679
AMES Mutagenicity	0.398	0.405	0.396	0.534	0.317	0.356	0.316	0.361
Rat Oral Acute Toxicity	0.417	0.364	0.531	0.479	0.418	0.415	0.553	0.535
FDAMDD	0.359	0.3	0.385	0.405	0.365	0.336	0.674	0.568
Skin Sensitization	0.717	0.637	0.562	0.411	0.716	0.631	0.829	0.716
Carcinogenicity	0.606	0.628	0.552	0.704	0.628	0.678	0.664	0.709
Eye Corrosion	0.968	0.961	0.936	0.844	0.975	0.938	0.993	0.978
Eye Irritation	0.996	0.991	0.988	0.981	0.987	0.979	0.997	0.996
Respiratory	0.675	0.642	0.748	0.746	0.733	0.719	0.712	0.692
Human Hepa totoxicity	0.488	0.55	0.651	0.635	0.56	0.531	0.432	0.421
Drug-induced Nephrotoxicity	0.261	0.447	0.7	0.81	0.505	0.609	0.338	0.372
Ototoxicity	0.334	0.356	0.464	0.472	0.408	0.415	0.271	0.271
Hematotoxicity	0.335	0.475	0.487	0.55	0.499	0.524	0.213	0.244
Genotoxicity	0.119	0.046	0.166	0.254	0.048	0.09	0.194	0.225
RPMI-8226 Immunitoxicity	0.049	0.056	0.062	0.079	0.059	0.067	0.061	0.066
A549 Cytotoxicity	0.11	0.08	0.08	0.116	0.119	0.155	0.103	0.102
Hek293 Cytotoxicity	0.183	0.139	0.151	0.211	0.181	0.249	0.181	0.19
Drug-induced Neurotoxicity	0.487	0.545	0.675	0.72	0.558	0.648	0.598	0.645
<b>Environmental Toxicity</b>								
BCF	1.834	2.719	2.647	2.444	2.972	2.738	2.928	2.738
IGC <sub>50</sub>	3.75	3.992	3.903	3.716	4.164	4.021	4.188	4.088
LC <sub>50</sub> FM	4.418	4.427	4.399	4.213	4.695	4.535	4.862	4.694
LC <sub>50</sub> DM	4.578	4.282	4.503	4.346	4.761	4.73	4.972	4.977
<b>Tox21 Pathway</b>								
NR-AhR	0.005	0.001	0.001	0.003	0.002	0.002	0.002	0.001
NR-AR	0.0	0.0	0.0	0.001	0.001	0.0	0.001	0.0
NR-AR-LBD	0.0	0.0	0.0	0.0	0.0	0.0	0.0	0.0
NR-Aromatase	0.0	0.0	0.0	0.0	0.001	0.0	0.0	0.0
NR-ER	0.17	0.273	0.132	0.074	0.241	0.083	0.211	0.098
NR-ER-LBD	0.0	0.0	0.0	0.0	0.002	0.0	0.001	0.0
NR-PPAR-gamma	0.0	0.0	0.0	0.0	0.0	0.0	0.0	0.0
SR-ARE	0.01	0.001	0.004	0.001	0.01	0.001	0.007	0.001
SR-ATAD5	0.0	0.0	0.0	0.0	0.0	0.0	0.0	0.0
SR-HSE	0.006	0.001	0.004	0.0	0.021	0.0	0.007	0.0
SR-MMP	0.866	0.037	0.061	0.019	0.187	0.03	0.08	0.012
SR-p53	0.0	0.0	0.0	0.0	0.0	0.0	0.0	0.0

\* The abbreviations are defined as: Tox, Toxicity; sens, Sensitization; BCF, the unit of bioconcentration factors, IGC<sub>50</sub>, LC<sub>50</sub>FM, and LC<sub>50</sub>DM are given in  $-\text{Log}_{10}[(\text{mg/L})/(1000 \times \text{MW})]$ .

## Removal of penicillin group antibiotics azlocillin, cloxacillin, methicillin from wastewater by DFT method

N. Guven<sup>1</sup>, B. Gurkan<sup>2</sup>, Y. Yalcin Gurkan<sup>1\*</sup>

<sup>1</sup>Tekirdag Namik Kemal University, Department of Chemistry, Tekirdag, Turkey

<sup>2</sup>Gebze Technical University, Department of Physics, Kocaeli, Turkey

Received June 11, 2024; Accepted: August 17, 2024

Antibiotics administered to living things are excreted either unchanged or with little transformation in living metabolism. Discarded antibiotic residues should not be treated in conventional wastewater treatment plants and may enter the receiver directly. Low temperatures of antibiotic residues in the recipient environment may cause increased resistance of microorganisms, while high amounts may cause them to remain toxic. For this reason, wastewater containing antibiotic residues must be treated. Possible reactions of the penicillin group antibiotics were investigated using the DFT method, which is a molecular modeling method. The penicillin group antibiotic molecules examined are azlocillin, cloxacillin and methicillin. No previous studies have been conducted on the molecules examined. The optimized geometries were drawn with Gauss View 5.0 and then calculated with the Gaussian 09W program using functional density theory (DFT). The geometric structure (bond angles and bond lengths) and possible degradation products of all three molecules were calculated with the DFT method and the 6-31G(d) basis set. Thus, the possible degradation type of these three antibiotic molecules in water was determined. These results will guide experimental workers.

**Keywords:** Antibiotics, azlocillin, cloxacillin, methicillin, Gaussian 09, DFT

### INTRODUCTION

Antibiotics are an important group within the antibacterial group. Antibiotics are chemical substances synthesized from various microorganisms such as bacteria, fungi and actinomycetes and prevent the development of other microorganisms or kill them. Today, some of the antibiotics are fully synthesized or the desired derivatives are prepared by semi-synthesis. That's why they are included in the chemotherapeutic class.

An ideal antibiotic should have a broad spectrum of microorganisms. It should have a bactericidal effect and not a bacteriostatic effect. Resistance should not occur easily. The potency should not change in long- and short-term use. It should not cause serious side effects. It should not cause sensitization in the organism. All methods should be used with the same effectiveness. It should dissolve well in water and should not decompose for a long time at room temperature. Absorption, distribution, metabolism and excretion properties must provide a rapid and continuous bactericidal effect. It should be easily accessible and cheap [1]. All bacteria have three growth phases: slow growth, rapid growth and rest periods. Antibiotics are effective during the fast and slow growth periods of bacteria. This interaction either kills bacteria or stops their development and reproduction.

Penicillins, aminoglycosides, cephalosporins, vancomycin, fluoroquinolones and bacitracin have bactericidal effects, while tetracyclines, macrolides and sulfonamides have bacteriostatic effects [2]. The presence of antibiotics in the aquatic environment is the subject of many studies in some countries. More than 30 antibiotic substances have been detected in sewage inlet and outlet water samples, surface waters, and even groundwater and drinking water. Metabolites or degradation products of antibiotics reach the aquatic environment through the application of sludge or manure to agriculturally used areas, or directly through animal feces on the land, through superficial rains, or by percolation in the deep layers of the earth. In this way, soils can act as a source of antibiotic pollution of the aquatic environment.

Owing to non-compliance with the necessary sanitary rules in fish farms, diseases occur frequently and cause great economic losses. The most common method of treating bacterial diseases of fish is the use of antibiotics and some other chemicals. The unconsumed portion of the antibiotics given to the fish by mixing them with the feed dissolves in water or settles on the ground. Some of the drug, which enters the environment with waste feed, is taken up by fish and crustaceans in the natural environment and accumulates in the body, reaching high concentrations.

\* To whom all correspondence should be sent:

E-mail: [yyalcin@nku.edu.tr](mailto:yyalcin@nku.edu.tr)

Overuse of antibiotics also encourages the development of pathogens that are resistant to standard antimicrobial practices. The antibiotics used have negative effects on other living things through the food chain or the aquatic ecosystem [3-7].

In this study, firstly, the initial geometries of the molecules were determined and geometric blocks based on DFT/B3LYP/6-31G(d) (B3LYP) were created. The energy values calculated from the DFT method include possible fragmentation reactions for each molecule. All programming was done by modeling the solvent effect in both the gas phase and the water phase.

### METHODOLOGY

The reaction model used in this study is the reaction between azlocillin, cloxacillin, methicillin molecules and photo-generated  $\bullet\text{OH}$  radicals [8]. Molecular models consist of average bond distances, geometric allowances of benzene rings, tetrahedral angles for  $\text{sp}^3$  hybridized carbon and oxygen atoms, and  $120^\circ$  for  $\text{sp}^2$  hybridized carbon atoms. In the structure of hydroxylated radicals, the aromatic ring was produced planely outside the attack position. Due to the attack of the  $\bullet\text{OH}$  radical on the carbon atom, the hybridization block was formed from  $\text{sp}^2$  to  $\text{sp}^3$  and assuming a tetrahedral angle with the C-H bond. Hydroxyl radicals forming organic compounds through single electron exchange by detachment of oxygen from single bonds, incorporation into double bonds, and loss of water from multiple hydroxyl radical additives. may change with systems. It is well known that serious problems arise in quantum calculations of open-shell

molecules. Electronic developments, the absence of which is the main case of HF methods, are taken into account in DFT methods. The latter involve less spin contamination than HF methods, and these features include systems with effects suitable for programming. For this reason, the geometric structures of the reactants were made by the DFT method. The DFT method is a Gaussian 09 software program *via* B3LYP [9]. Frequencies were calculated to determine them as real minima on potential energy surfaces [10-12].

### RESULTS AND DISCUSSION

In search of a reasonable mechanism for the photocatalytic degradation of azlocillin, cloxacillin, methicillin molecules, calculations were made with the DFT method to gain information about the region most sensitive to hydroxyl radical attacks. Figure 1 shows the optimized structures of azlocillin, cloxacillin, methicillin molecules.

The reaction paths of the three molecules shown in Figures 2-4 reveal that the specific regions of azlocillin, cloxacillin, methicillin molecules are close to those of the  $\bullet\text{OH}$  radical. The predicted reaction pathways were validated by comparison with examples on simple structures from the literature, as described below. The lowest energy structure is a stable structure. The calculations in this disintegration were theoretically calculated and supported by looking at the Gibbs free energy values in Tables 1-3. Energy, enthalpy, Gibbs free energies of compounds are shown in Tables 1-3.

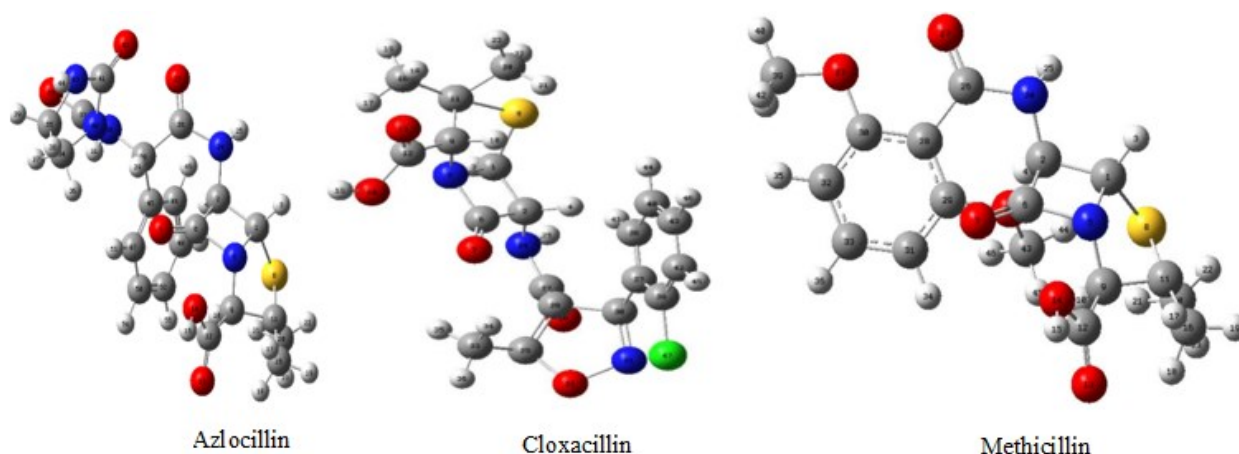


**Fig. 1.** Optimized geometric structure of azlocillin, cloxacillin, methicillin molecules by DFT method (grey, C; white, H; red, O; blue, N; green, Cl; yellow, S)

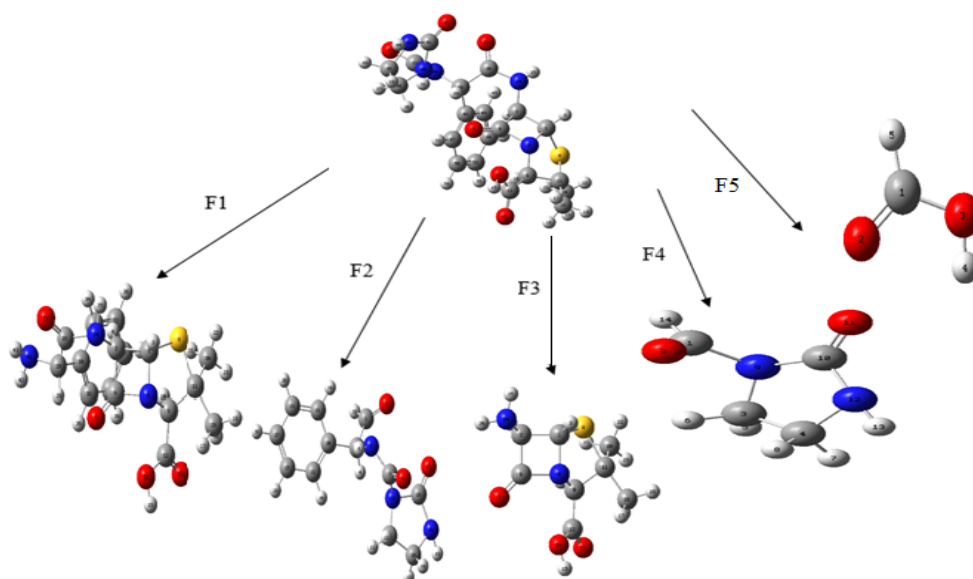


**Fig. 2.** Possible reaction pathways for the photocatalytic degradation of azlocillin (grey, C; white, H; red, O; blue, N; yellow, S)

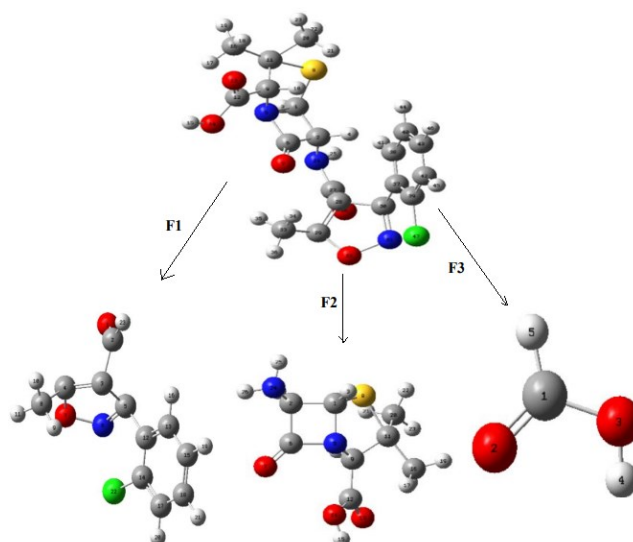


**Fig. 3.** Possible reaction pathways for the photocatalytic degradation of cloxacillin (grey, C; white, H; red, O; blue, N; green, Cl; yellow, S)

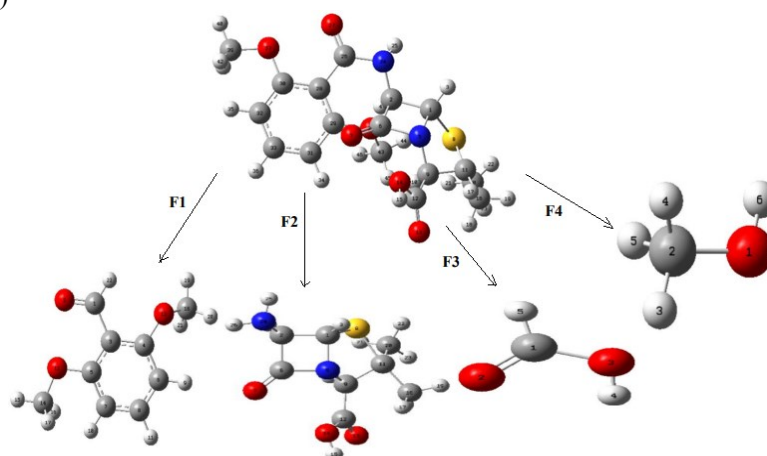


**Fig. 4.** Possible reaction pathways for the photocatalytic degradation of methicillin (grey, C; white, H; red, O; blue, N; yellow, S)

**Table 1.** Energy, enthalpy and Gibbs free energy values according to the DFT method.

Molecules	Phase	$\Delta E$ Energy (kcal mol <sup>-1</sup> )	$\Delta H$ Enthalpy (kcal mol <sup>-1</sup> )	$\Delta G$ Gibbs free energy (kcal mol <sup>-1</sup> )
Azlocillin	Gas	-1191540.257	-1191539.665	-1191599.153
	<i>COSMO</i>	-1191556.146	-1191555.554	-1191615.422
F1	Gas	-931289.848	-931289.256	-931339.481
	<i>COSMO</i>	-931304.967	-931304.374	-931353.967
F2	Gas	-536388.182	-536387.590	-536426.732
	<i>COSMO</i>	-536395.613	-536395.021	-536435.109
F3	Gas	-655872.8002	-655872.208	-655907.600
	<i>COSMO</i>	-655882.548	-655881.956	-655917.185
F4	Gas	-260979.003	-260978.410	-261003.316
	<i>COSMO</i>	-260987.491	-260986.899	-261011.936
F5	Gas	-119049.984	-119049.392	-119067.076
	<i>COSMO</i>	-119054.194	-119053.602	-119071.294

**Table 2.** Energy, enthalpy and Gibbs free energy values according to the DFT method.

Molecules	Phase	$\Delta E$ Energy (kcal mol <sup>-1</sup> )	$\Delta H$ Enthalpy (kcal mol <sup>-1</sup> )	$\Delta G$ Gibbs free energy (kcal mol <sup>-1</sup> )
Cloxacillin	Gas	-1338943.463	-1338942.871	-1338999.588
	<i>COSMO</i>	-1338958.286	-1338957.694	-1339014.568
F1	Gas	-683798.496	-683797.904	-683833.100
	<i>COSMO</i>	-683804.928	-683804.335	-683839.470
F2	Gas	-655872.800	-655872.208	-655907.600
	<i>COSMO</i>	-655882.548	-655881.956	-655917.185
F3	Gas	-119049.984	-119049.392	-119067.076
	<i>COSMO</i>	-119054.194	-119053.602	-119071.294

**Table 3.** Energy, enthalpy and Gibbs free energy values according to the DFT method.

Molecules	Phase	$\Delta E$ Energy (kcal mol <sup>-1</sup> )	$\Delta H$ Enthalpy (kcal mol <sup>-1</sup> )	$\Delta G$ Gibbs free energy (kcal mol <sup>-1</sup> )
Methicillin	Gas	-1291030.538	-1291029.945	-1291096.658
	<i>COSMO</i>	-1291051.841	-1291051.249	-1291118.715
F1	Gas	-360463.595	-360463.003	-360494.578
	<i>COSMO</i>	-360472.131	-360471.539	-360503.087
F2	Gas	-655872.800	-655872.208	-655907.600
	<i>COSMO</i>	-655882.548	-655881.956	-655917.185
F3	Gas	-119049.984	-119049.392	-119067.076
	<i>COSMO</i>	-119054.194	-119053.602	-119071.294
F4	Gas	-72577.466	-72576.873	-72593.789
	<i>COSMO</i>	-72580.673	-72580.081	-72597.018

### CONCLUSIONS

In this study, fragmentation mechanisms for three molecules were determined. The energy values, electronegative atoms in the molecule, bond lengths and the angles are examined and explained. In the study, antibiotic active ingredients and water molecules were examined. Possible reaction pathways were determined for the reaction between the fission reaction producing the energy it requires.

That's why these chemicals break down the OH in water. using radicals. The most stable structure of a molecule is its lowest energy state. When we rank the antibiotic active ingredients from the most stable to the most unstable, the order is: cloxacillin - 1338943.463 kcal/mol, methicillin -1291030.538 kcal/mol, azlocillin -1191540.257 kcal/mol. Our aim is to reduce the antibiotic active ingredients to the smallest harmless ones. It was to

break it down to substances. As a result, the first molecule, azlocillin, when we rank the 5 fragments, which are the breakdown products, from the most stable to the unstable, F1 is -931289.848 kcal/mol, F3 -655872.800 kcal/mol, F2 -5363881.828 kcal/mol, F4 -260979.003 kcal/mol, F5 is -119049.984 kcal/mol. Disintegration of the second molecule, cloxacillin when we rank the 3 fragments from the most stable to unstable, F1 is -683798.496 kcal/mol, F2 it is -655872.800 kcal/mol, F3 is -119049.984 kcal/mol. Methicillin, the 3rd molecule when we rank the 4 fragments, which are the breakdown products of the molecule, from the most stable to the unstable, F2 -655872.800 kcal/mol, F1 -360463.595 kcal/mol, F3 -119049.984 kcal/mol, F4 -72577.466. As can be seen from the results, this fragmentation was realised. These results determine the mechanism and will guide experimental workers. Prediction of the degradation of molecules occurred through cleavages of intramolecular fragments, followed by •OH radical reactions. With this reaction, the fragments turn into smaller species such as CO<sub>2</sub>, NO<sub>3</sub><sup>-</sup> and NH<sub>4</sub><sup>+</sup>.

**Acknowledgement:** The authors greatly appreciate Tekirdag Namik Kemal University Research Foundation for financial support. Project number: NKUBAP.01.GA.22.437.

#### REFERENCES

1. W. Xu, G. Zhang, S. Zou, X. Li, Y. Liu, *Environ. Pollut.*, **145**, 672 (2007).
2. M. Klavarioti, D. Mantzavinos, D. Kassinos, *Environ. Intern.*, **35**, 402 (2009).
3. I. Alemzadeh, G. Borghei, L. Vafi, R. Roostaazad, *Chem. Chem. Eng.*, **17** (1), 106 (2010).
4. L. Povyakel, O. Bobylioiva, S. Snoz, Y. Bardik, *Toxicology Letters*, **180**, 197 (2008).
5. V. G. Buxton, L. C. Greenstock, P. W. Helman, B. A. Ross, *Journal of Physical and Chemical Reference Data*, **17**, 513 (1988).
6. M. Anbar, P. Neta, *Int. J. Radiat. Isot.*, **18**, 495 (1965).
7. B. Halliwell, M. Grootveld, J. M. C. Gutteridge, *Methods of Biochemical Analysis*, **33**, 59 (1988).
8. N. San, M. Kilic, Z. Cinar, *J. Adv. Oxid. Technol.*, **10**(1), 51 (2007).
9. Gaussian 09, Revision B.04, in: Gaussian, Inc., 2009.
10. J. P. Stewart, *J. Comput. Chem.*, **10**, 221 (1989).
11. J. P. Lowe, *Quantum Chemistry*, 2nd edn., Academic Press, USA, 1993.
12. I. N. Lveine, *Quantum Chemistry*, Boston, Alloy and Bacon Inc., 1983.

## Determination of macro- and microelement contents in thyme oil and rosemary oil by ICP-OES

N. Tokatli Demirok<sup>1\*</sup>, A. Karasakal<sup>2</sup>

<sup>1</sup>Tekirdag Namik Kemal University, Department of Nutrition and Dietetics, Faculty of Health Sciences, Tekirdag, Turkey

<sup>2</sup>Tekirdag Namik Kemal University, Science and Letters Faculty, Department of Chemistry, Tekirdag, Turkey

Received May 7, 2024; Accepted: August 17, 2024

Essential oils are defined as complex mixtures of natural compounds that contain aldehydes, unsaturated and saturated phenols, hydrocarbons, alcohols, and terpenes. Thyme oil, obtained by steam distillation from the perennial plant and its flowers known as *Thymus vulgaris*, has antioxidant, antiseptic, antibacterial, antifungal and calming properties. It has been used as a medicinal plant since ancient times. It is also used as a preservative in foods and cosmetics. Rosemary (*Rosmarinus officinalis* L.) is one of the most preferred natural sources of active drug substances. Rosemary oil is a natural oil obtained from the leaves and flowers of the rosemary plant. Rosemary oil has antibacterial and antioxidant properties. In addition, it is stated that rosemary is among the plants that the body supports in protecting against cancerous cell formation. The content of elements (Cu, B, P, Fe, Na, Mg, K, Ca) in commercial thyme and rosemary oils was investigated by ICP-OES after wet digestion. 0.5 g sample was weighed and HNO<sub>3</sub>-H<sub>2</sub>O<sub>2</sub> (10 ml, 2:1, v/v) was added. The oil samples were heated at 80 °C until clear solutions were obtained. The method was validated through accuracy, precision, linearity, recovery, LOD (limit of detection) and LOQ (limit of quantification) parameters. The lowest metal content in thyme oil was found for Fe (0.68 µg/g) while the highest metal content - for P (100.73 µg/g). For rosemary oil, the lowest metal content was found for Mg (0.15 µg/g) while the highest metal content - for P (220.98 µg/g).

**Keywords:** Thyme oil; Rosemary oil; ICP-OES, Essential oil, Wet digestion

### INTRODUCTION

Salvia species are used in cosmetics, food and traditional medicine. Salvia species are rich in terms of essential oils. Salvia leaves have biological properties such as antioxidants, antibacterial, anti-inflammatory, anticancer, and antimutagenic. *Salvia* leaves and essential oils are used in heart disease treatments. [1]. The *Lamiaceae* family has the most aromatic and medicinal plants. More than 3000 aromatic plants are known to exist in Turkey's flora. Medicinally important species of the genera *Salvia*, *Origanum*, *Mentha* and *Thymus* have been the focus of recent studies in Turkey. There are many studies in the literature with respect to *Salvia* species. Maral *et al.* investigated the essential oil components and antioxidant activities of *Salvia karamanensis* [2]. Chang *et al.* analysed the selected compounds from *Salvia* herbs by HPLC method [3]. Raskovic *et al.* studied the chemical composition of *Rosmarinus officinalis* aerial essential oil by GC/MS [4].

The leaves of *Thymus* species are used in traditional medicine for the treatment of colds. In addition, thyme plant has an important biological activity in terms of antioxidant, antimicrobial, analgesic and anti-inflammatory properties [5]. Bazylko *et al.* determined the content of luteolin in

*T. vulgaris*, and its liquid and dry extracts [6]. Malankina *et al.* examined the composition of the essential oil of cultivars of *Thymus serpyllum* L. by GC-MS [7].

Essential oils are defined as complex mixtures of natural products that include phenols, aldehydes, unsaturated and saturated hydrocarbons, terpenes, and alcohols [8]. In this study, we aim to determine the element concentrations in commercial thyme and rosemary oils by ICP-OES after wet digestion.

### EXPERIMENTAL

#### Instrumentation

An inductively coupled plasma-optical emission spectrometry (ICP-OES) (Spectro/ Spectroblue) was used for the measurements. The nebulizer argon gas, plasma-Ar, and auxiliary gas flow rate were 1.0 L min<sup>-1</sup>, 12 L min<sup>-1</sup>, and 1.0 L min<sup>-1</sup>, respectively. Rf power was 1.4 kW.

#### Reagents and standards

Nitric acid (65%) (Sigma-Aldrich, Steinheim, Germany) and hydrogen peroxide (35%) were used for digestion procedure. Concentration ranges of standard solutions prepared by dilution from 1000 µg/mL stock solution: 1.25 - 25 µg/mL for Na, 5-100 µg/mL for Mg, 15-300 µg/mL for Ca and K, 5-100

\* To whom all correspondence should be sent:  
E-mail: [ntokatli@nku.edu.tr](mailto:ntokatli@nku.edu.tr)

µg/mL for P, 2.5-50 µg/mL for Fe, 0.5-10 µg/mL for Cu and B.

*Preparation of samples*

Commercial thyme and rosemary oil samples were purchased in Turkey. The oil samples were analyzed by ICP-OES to determine element concentrations.

*Wet digestion procedure*

0.5 g samples were weighed and HNO<sub>3</sub>-H<sub>2</sub>O<sub>2</sub> (10 ml, 2:1, v/v) was added. The oil samples were heated at 80 °C until clear solutions were obtained. The samples were dissolved in 5 ml of 0.2 M HNO<sub>3</sub>, filtered and made up to 10 ml with ultrapure water. ICP-OES was used for determination of metal contents. Analyses were repeated 3 times.

**RESULTS AND DISCUSSION**

Vegetable oils are the oldest known medicinal products. People frequently use plants in the treatment of various ailments and plants are also used today in oil and food production. Prevention

and detection of contamination is important for human health [9].

In this work, an ICP-OES method was developed for the determination of Na, Ca, K, B, P, Cu, Fe, Mg in commercial thyme and rosemary oils. For this purpose, the samples were digested using a mixture of nitric acid and hydrogen peroxide.

Limit of detection (LOD) and limit of quantitation (LOQ) were evaluated for method validation. LOD and LOQ values are given in Table 1. Calibration standards were used for the determination of LOD and LOQ values. LOD and LOQ were calculated as 3.3 and 10 σ/S, respectively. σ is the standard deviation of the intercept of the regression equation and S is the slope of the calibration curve. All experiments were performed in triplicate and the results expressed as mean. The concentrations (µg/g) of Na, Ca, Mg, K, B, Fe, Cu, and P in thyme and rosemary samples are presented in Figures 1-8. Relative standard deviations (RSD) were found below 2%.

**Table 1.** LOD and LOQ values

	P	Mg	Cu	Na	K	Fe	Ca	B
LOD, ng/mL	0.01	0.0004	1.7	0.0004	0.032	6.1	0.04	2.4
LOQ, ng/mL	0.04	0.0013	5.6	0.0014	0.107	20.4	0.14	7.9

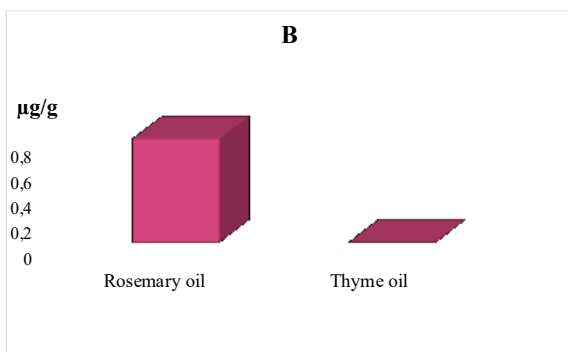


**Fig. 1.** B element concentrations of oil samples

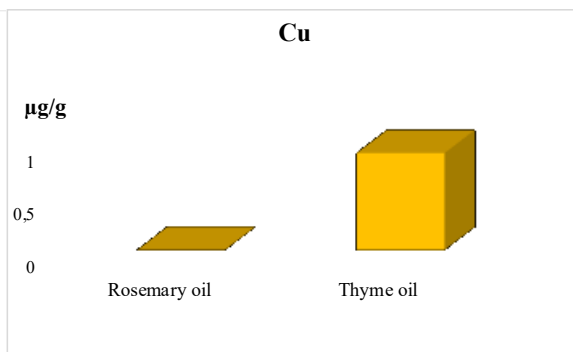


**Fig. 2.** Cu element concentrations of oil samples

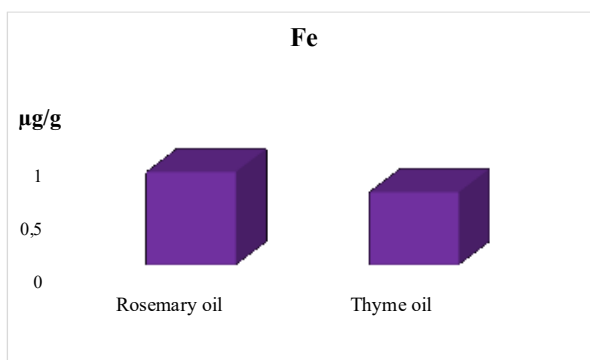


**Fig. 3.** Fe element concentrations of oil samples

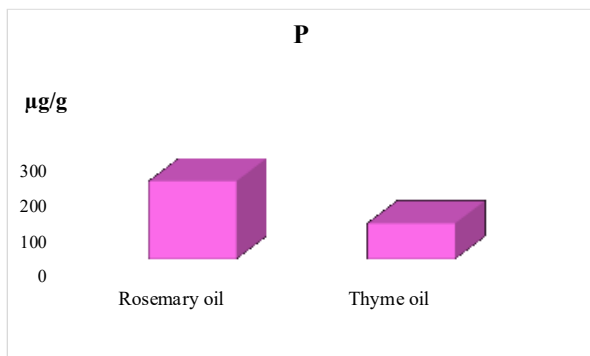


Fig. 4. P element concentrations of oil samples

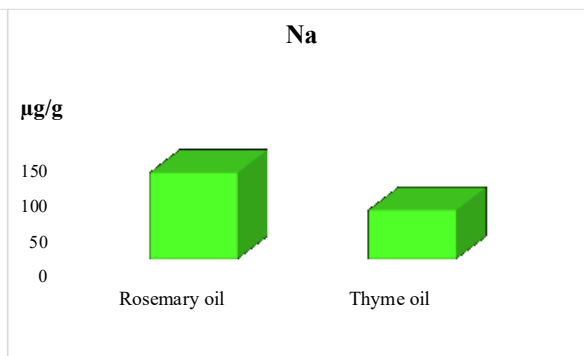


Fig. 5. Na element concentrations of oil samples

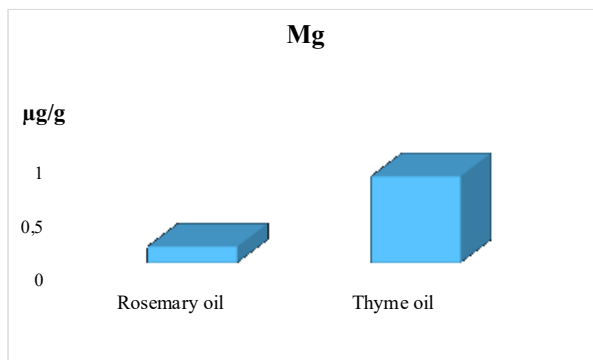


Fig. 6. Mg element concentrations of oil samples

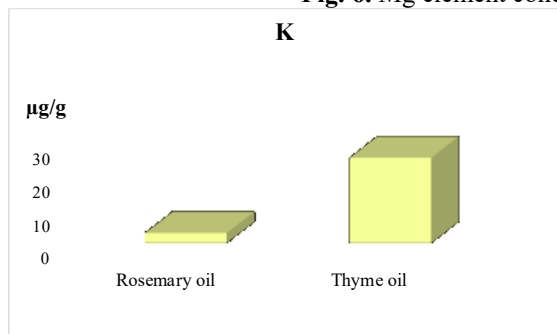


Fig. 7. K element concentrations of oil samples

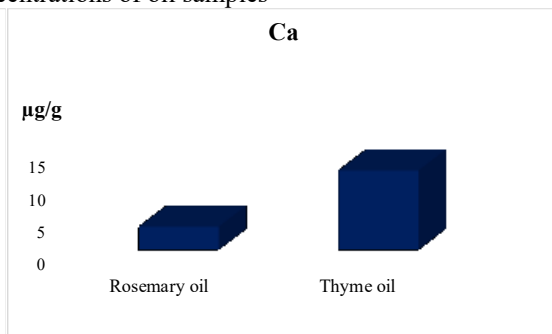


Fig. 8. Ca element concentrations of oil samples

The element concentrations after wet digestion were determined as 122.45 µg/g for Na, 3.44 µg/g for Ca, 0.15 µg/g for Mg, 3.04 µg/g for K, 0.8 µg/g for B, 0.87 µg/g for Fe and 220.98 µg/g for P in rosemary oil samples. The order of element concentrations in rosemary oil samples is P>Na>Ca>K>Fe>B>Mg>Cu. The lowest metal concentrations in rosemary oil samples were found for Mg and Cu. The highest metal concentrations were found for P.

Then the element composition, antioxidant property, and polyphenol content of *Salvia officinalis* leaves were analyzed. Ca, S, and K were determined in macerated and infused (20 % alcoholic water) extracts (3726-4600, 28071-19010 and 38500-47983 µg/100 mL, respectively). As the alcohol content of the tincture increased, the mineral content of the extract decreased. K and Ca were higher than our results [10]. Hebatallah *et al.* investigated the effects of foliar application of

riboflavin at different concentrations (0, 25, 50, and 100 mg/L) on rosemary plants during two cutting seasons. In addition, rosemary leaves's element concentrations were determined by FAAS and ICP-MS [11].

The element concentrations in thyme oil samples after wet digestion were found to be 69.36 µg/g for Na, 11.9 µg/g for Ca, 0.81 µg/g for Mg, 25.25 µg/g for K, 0.92 µg/g for Cu, 0.68 µg/g for Fe and 100.73 µg/g for P. The order of element concentrations in thyme oil samples is P>Na>K>Ca>Cu>Mg>Fe>B. The lowest metal concentrations in thyme oil samples were observed for B and Fe. The highest metal concentrations were found for P.

The antioxidant - antibacterial activity and chemical composition of *Thymus praecox* was investigated by Sener *et al.* [12]. Experimental results showed that thyme extracts have antibacterial activities against some bacteria. Cu, Fe, Na, Mg and Ca concentrations were 0.97 µg/g; 93 µg/g; 100.944

µg/g; 2300 µg/g; 40000 µg/g, respectively. Fe, Na, Mg, Ca concentrations determined in thyme oil in our study were lower than those of Sener *et al.* Cu concentrations were similar to our results [12]. Drioiche *et al.* investigated the chemical composition and antimicrobial activities of *Thymus vulgaris*, *Thymus satureioides* and *Thymus zygis* essential oils. Fe concentrations in our study were similar to their study [5].

Arsenijevic *et al.* analysed the volatile fraction of the leaves of *Thymus pannonicus* by headspace extraction. Cu, Ni, Cr, Na, Mn, Co, Zn, Fe, Ca, Mg, and K were determined using FAAS, GFAAS and ICP-OES. Their assay results were higher than our results [13]. Adequate dietary iron intake is crucial to reduce the incidence of anaemia. High doses of iron can lead, however, to tissue damage. Cu is an important element for human health, but high doses can cause damage to the liver and kidneys. Copper deficiency in children can lead to hypochromic anaemia, leukopenia and osteoporosis [14]. Fe and Cu have many positive effects on human health. Inadequate intake of these metals can lead to undesirable pathological problems. It has been observed that possible contamination with Cu and Fe may originate from oil processing equipment and Cu contamination in oils may be due to environmental pollution [9]. Potassium is an important electrolyte which ensures the conductivity of the nerves and the active transport of the mineral apatite in the bones. Excess sodium in the body can cause heart disease. Ca is important for patients with kidney failure. In a study, Ca levels in hardaliye were reported as 0.310-711.1 mg/kg [15]. Recommended dietary intakes (RDI) for Na and Ca have been established by the Food and Nutrition Board, Institute of Medicine, National Academies, Washington, DC, USA. Potassium is important with regard to human health. A diet with a low level of potassium can lead to heart problems [16]. Potassium is important in the regulation of intracellular osmolarity, cell membrane transport and activation of enzymes including glycolysis and respiration. The necessary potassium requirement is 782 mg per day [17]. Playing an important role in human metabolism, phosphorus is an essential nutrient. The required daily amount of phosphorus is approximately 800-1200 mg. Magnesium is an important element in the body as it is a component and activator of many enzymes and the daily requirement of magnesium is between 300 and 500 mg. Table 2 shows the recommended daily allowance (RDA) data [18].

**Table 2.** Reference values for recommended daily allowance [16]

Mineral nutrients and trace elements	Recommended daily allowance (RDA)
Calcium	1000 mg
Sodium	2400 mg
Magnesium	350 mg
Iron	15 mg
Boron	< 20 mg
Potassium	3500 mg
Manganese	5 mg
Phosphorus	1000 mg
Zinc	15 mg
Copper	2 mg

## CONCLUSION

The concentrations of Ca, K, P, B, Mg, Cu, Fe, and Na in commercial thyme and rosemary oil samples were determined. This study was the first to investigate the oils of thyme and rosemary by means of wet digestion-ICP-OES. The HNO<sub>3</sub>-H<sub>2</sub>O<sub>2</sub> digestion method was used for determination of the multi-element contents. The element concentrations were below the RDA levels, so the analysis results indicate that as a contribution to dietary intake, thyme and rosemary oils are not a good source of essential elements.

**Acknowledgement:** This work was supported by the Research Fund of the University of Tekirdag Namik Kemal University (Project Number NKUBAP. 01.YL.23.529).

## REFERENCES

1. R. Cozzolino, S. Ramezani, A. Martignetti, A. Mari, S. Piacente, B. D. Giulio, *Natural Product Research*, **30**(7), 841 (2016).
2. H. Maral, O. Çecen, A. Turk Baydir, M. Turkmen, *Biochemical Systematics and Eco.*, **113**, 104795 (2024).
3. H.T. Cheng, X.L. Li, X.R. Li, Y.H. Li, L.J. Wang, M..Xue, *Food Chem.*, **130**, 1031 (2012).
4. A. Rašković, I. Milanović, N. Pavlović, T. Čebović, S. Vukmirović, M. Mikov, *Comp. and Altern. Med.*, **14**, 225 (2014).
5. A. Drioiche, F.Z. Radi, A. Ailli, A. Bouzoubaa, A. Boutakiout, S. Mekdad, O.A. Kamaly, A. Saleh, M. Maouloua, D. Bousta, S. Sahpaz, F.E. Makhoukhi, T. Zair. *Saudi Pharm. J.*, **30**, 1200 (2022).
6. A. Bazylo, H. Strzelecka. *Fitoterapia*, **78**, 391 (2007).
7. E. L. Malankina, L. N. Kozlovskaya, A. N. Kuzmenko, A. A. Evgrafov, *Moscow Uni. Chem. B.*, **74**(6), 310 (2019).
8. F. Tokay, R. Günaydin, S. Bagdat, *Talanta*, **230**, 122312 (2021).
9. D. Bakircioglu, N. Topraksever, S. Yurtsever, Y. Bakircioglu Kurtulus, *Atom. Spec.*, **39**(1), 38 (2018).
10. M. Then, R. Szóllósy, K. Vásárhelyi-Perédi, K. Szentmihályi. *Acta Horti.*, **629**, 123 (2004).
11. H. Aly, F.A. Gharib, E.Z. Ahmed, *Egyptian Journal*

- N. Tokatli Demirok, A. Karasakal: Determination of macro- and microelement contents in thyme oil and rosemary oil... of Botany*, **64**(1), 125 (2024).
12. I. Sener, F. Tekelioglu, M. Zurnacı, P. Baloglu, M. Gur, K. Guney. *Kastamonu Univ., J. of Forestry Fac.*, **21**(1), 65 (2021).
  13. J. Arsenijevic, J. Markovic, I. Sostaric, S. Razic, *Plant Physiology and Biochem.*, **71**, 298 e306 (2013).
  14. D. Bakircioglu, Y. Bakircioglu Kurtulus, S. Yurtsever, *Food Chem.*, **138**, 770 (2013).
  15. D. Bakircioglu, N. Topraksever, Y. Bakircioglu Kurtulus, *Journal of AOAC Inter.*, **100**(5), 1531 (2017).
  16. A. Karasakal, *Food Analytical Methods*, **14**, 44 (2021).
  17. R. R. Gamela, V. C. Costa, E. R. Pereira-Filho. *Food Analytical Methods*, **13**, 69 (2020).
  18. <https://www.lennotech.com/recommended-daily-intake.htm> Accessed 03 May 2024.

## Photophysical study of benzanthrone 3-isothiocyanate as novel fluorescent label

E. Kirilova\*, R. Fridmans, A. Puckins, J. Oreha, S. Osipovs

*Institute of Life Sciences and Technology, Daugavpils University, Daugavpils, Latvia*

Received June 19, 2024; Accepted: August 17, 2024

In modern biochemical research, much attention is paid to the development and synthesis of new fluorescent markers used for protein labeling. Reaction with an isothiocyanate group is one of the most widely used methods for fluorescent labeling of amino acids and proteins. In the present work, an isothiocyanate derivative of benzanthrone was obtained and characterized as a possible fluorescent marker. The interaction of 3-isothiocyanatobenzanthrone with a number of natural amino acids was studied. The study also examined the processes of conjugation of the synthesized isothiocyanate with albumin, pepsin and gelatin. The photophysical parameters of the obtained conjugates were studied in detail. Considering the fluorescent properties of the obtained conjugates, the isothiocyanate under study appears promising for fluorescent labeling purposes.

**Keywords:** Luminescent label; Benzanthrone; Isothiocyanate; Amino acids; Proteins; Fluorescence

### INTRODUCTION

Among numerous imaging and detection methods, the fluorescence approach shows significant advantages in terms of ease of fabrication, low cost, and high sensitivity, which has been widely used to study various biomolecules. It is important to develop and synthesize fluorescent markers with good biological activity and optical properties. Therefore, new labels and new methods are constantly being developed [1, 2]. In modern research, much attention is paid to the development and synthesis of new fluorescent markers used for labeling amino acids, peptides and proteins [3, 4]. This includes molecular design considering the best choice of a reactive group in the fluorophore structure through which conjugation to the target biomolecule occurs. The procedure for introducing active groups into the fluorophore structure is used to obtain the necessary spectral properties of conjugates for their further detection and analysis [5, 6].

Typically, direct chemical labeling of proteins targets the amino and thiol groups. The most commonly used amine-reactive markers include succinimidyl ethers, imidoethers, sulfonyl chlorides, and isothiocyanates [6-8]. Fluorescein- and rhodamine-derived isothiocyanates are among the most popular conjugation reagents for amine modification during protein labeling [9-11].

In this research we designed a new potential fluorescent marker for proteins, isothiocyanate-functionalized benzanthrone derivative with a target NCS group at position 3 of the aromatic core. 3-Substituted benzanthrone derivatives are compounds

with excellent emissive properties, making these luminescent dyes find numerous applications in biomolecular research and bioimaging, mainly as non-covalent labels [12-15]. Further in the present work, the reactions of the newly obtained 3-isothiocyanatobenzanthrone with a number of amino acids were studied in order to find out the applicability of this isothiocyanate for the labeling of amino acids. The developed marker was also applied in bioconjugation reactions with proteins.

### EXPERIMENTAL

All reagents, solvents, amino acids and proteins were purchased from Sigma-Aldrich Co. (St. Louis, MO, USA).

The progress of the synthesis and the purity of substances were controlled by thin layer chromatography (TLC) using silica gel plates (Fluka F60254, 20×10, 0.2 mm) with toluene as eluent. Melting points were obtained on an MP70 Melting Point System apparatus.

Fourier-transform infrared (FT-IR) spectroscopy measurements were carried out by a Bruker Vertex 70v vacuum spectrometer equipped with an attenuated total reflection accessory. <sup>1</sup>H NMR spectra were registered by a Bruker equipment at a frequency of 500 MHz in CDCl<sub>3</sub> (with tetramethylsilane as internal standard) at ambient temperature.

Shimadzu GCMS-QP2010 system (Shimadzu Corporation, Kyoto, Japan) was used for the analysis. The gas chromatograph was equipped with an electronically controlled split/splitless injection port and a 5% diphenyl-/95% dimethylpolysiloxane

\* To whom all correspondence should be sent:

E-mail: [jelena.kirilova@du.lv](mailto:jelena.kirilova@du.lv)

fused-silica capillary column (Rtx-5SIL-MS, 30 m×0.32 mm, 0.25 μm film thickness). Mass spectra (MS) were registered by a mass spectrometer in electron ionization mode (ionization energy of 70 eV). Detection was realized in scanning mode within the range of  $m/z$  35–500.

Absorption spectra were recorded on a UV–visible spectrophotometer Specord UV/VIS. Fluorescence spectra were obtained using FLSP920 (Edinburgh Instruments Ltd.) spectrofluorometer in the spectral range of 430–800 nm. Emission measurements were performed in quartz cells with an absorbing layer thickness of 1 cm.

### Synthesis

3-Aminobenzanthrone (**1**) was synthesized by nitration of benzanthrone and subsequent reduction of the 3-nitroderivative according to the literature procedures [16, 17].

- *Synthesis of 3-isothiocyanatobenzanthrone (2).* In a 25 ml round-bottom flask, a mixture of 3-aminobenzanthrone (0.25 g, 1 mmol), carbon disulfide (0.50 g, 6.5 mmol), N,N'-dicyclohexylcarbodiimide (0.25 g, 1.2 mmol) and pyridine (7 ml) was stirred in an ice bath at 0°C for 4–5 h. Then, 0.10 g of DCCD was added and the resulting mixture was continuously stirred at ambient temperature during 12–14 h. The progress of ongoing reaction was monitored by TLC. The pyridine was then evaporated and the reaction mixture is dissolved in 20–30 ml of ethyl acetate. The product is purified by column chromatography on a 1.5 × 30 cm column packed with silica gel 40/100 (eluent: dichloromethane) to give a yellow solid in 60% yield, m. p. 200–201°C. FT-IR spectra,  $\lambda_{\max}$  (KBr),  $\text{cm}^{-1}$ : 2925, 2851, 2120, 1661, 1627, 1572, 1553, 1505, 1448, 1347, 1229, 1087, 1044, 892, 772, 641. NMR (500 MHz,  $\text{CDCl}_3$ )  $\delta$  8.83 (dd,  $J=7.3$ ; 1.3 Hz, 1H), 8.47–8.57 (m, 2H), 8.39 (d,  $J=7.2$  Hz, 1H), 8.29 (d,  $J=7.8$  Hz, 1H), 7.92 (dd,  $J=8.3$ ; 7.3 Hz, 1H), 7.79 (ddd,  $J=8.1$ ; 7.2; 1.6 Hz, 1H), 7.49–7.67 (m, 2H). MS ( $m/z$ ): 287 [ $M^+$ ] (100), 259 (15), 227 (14), 200 (17), 129 (11), 100 (11).

- *Conjugation with amino acids.* A freshly prepared solution of 3-isothiocyanatobenzanthrone in anhydrous DMSO (0.3 mL with concentration of 3 mg/mL) was poured dropwise with continuous stirring to an appropriate amino acid solution (4 mL, 1 mg/mL) in 0.1M bicarbonate buffer (pH 9.3). The prepared mixture was protected from light and stored at ambient temperature for 0.5 h with constant slow stirring. The solution should be left for 8 h at 4°C without light.

- *Conjugation with proteins.* A freshly prepared solution of 3-isothiocyanatobenzanthrone

in anhydrous DMSO (0.1, 0.2 or 0.3 mL with concentration of 1 mg/mL) was poured dropwise with continuous stirring to an appropriate protein solution (4 mL, 2 mg/mL) in 0.1M bicarbonate buffer (pH 9.3). The reaction mixture was protected from light and stored at ambient temperature for 0.5 h with constant slow stirring. Then the reaction mixture was incubated at 4°C for 12 h.

## RESULTS AND DISCUSSION

### Synthesis and characterization of the new label

Isothiocyanate group is a very useful building block in synthetic chemistry for the preparation of both sulfur- and nitrogen-containing organic compounds [18–20]. Owing to their synthetic and biological importance, numerous methods for the preparation of isothiocyanates from amines, dithiocarbamates, organic halides, nitriles, olefins, aldoximes, etc. have been developed [21].

In the present research we used 3-aminobenzanthrone for synthesis of the appropriate isothiocyanate (see Fig. 1). This method involves converting the amine into appropriate isothiocyanate in a solution of pyridine in the presence of an aqueous binder – N,N'-dicyclohexylcarbodiimide is a highly versatile dehydrating reagent. During the reaction, the color of the solution changed from red to orange.

Monitoring the progress of the isothiocyanate synthesis in the reaction mixture by TLC shows the formation of a new yellow product with a bright green luminescence, in contrast to the initial amine, which has a red color and emission. The structure of the obtained derivative **2** was confirmed by FT-IR, NMR and mass spectrometry data.

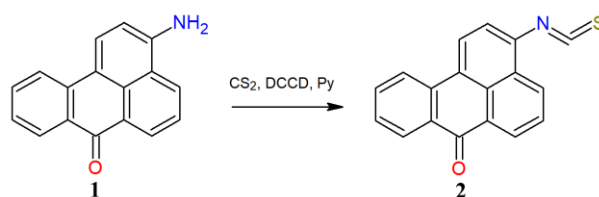


Fig. 1. Synthesis of 3-isothiocyanatobenzanthrone (**2**).

The  $^1\text{H}$  NMR spectrum contains only multiplet signals (from  $\delta$  7.50 to 8.85 ppm) of nine aromatic hydrogen atoms, which is typical for 3-substituted benzanthrone derivatives [22].

In the IR spectrum, characteristic vibrations of the isothiocyanate group are observed at  $2120\text{ cm}^{-1}$ , which also confirms the obtaining of the target substance.

The spectral absorption and emission data of the synthesized isothiocyanate solutions in various organic solvents are summarized in Table 1.

Positions of absorption maxima are situated between 425–435 nm. The obtained compound is fluorescent in solutions in the region of 500–560 nm, showing a hypsochromic shift of 100–130 nm compared to the parent amine **1** and many 3-substituted amino and amidino derivatives, which emit in the red region [23]. In addition, the Stokes shifts are smaller than those for amines and amidines.

#### Conjugation with amino acids and proteins

In the present research the conjugation with seven natural amino acids (glycine, L-alanine, L-oxypoline, L-aspartic acid, L-cysteine, L-methionine and L-arginine) and with three proteins (bovine serum albumin, porcine pepsin and gelatin) was studied. For conjugation with amino acids the literature procedure for known isothiocyanates was applied [5, 6].

It is well known that the isothiocyanate group can react with thiol and amino groups present in amino acids and proteins by forming appropriate C-S or C-N covalent bond [24, 25]. Two possible ways of interaction of the synthesized isothiocyanate **2** with the mentioned reactive groups are shown in Fig. 2.

The spectral properties of the obtained amino acids conjugates were investigated. As can be seen from the results obtained (Fig. 3), the reaction of all amino acids with the marker produces fluorescent products, the emission of which significantly exceeds the luminescence of the original compound. The largest increase in emission of 27 times was observed for the arginine conjugate. The conjugates of methionine, glycine and alanine showed a 20-23 times increased emission. The smallest increase in emission was observed for cysteine and aspartic acid conjugates. Differences were also observed in the location of the fluorescence maxima of the conjugates compared to the starting isothiocyanate. The fluorescence maxima of the conjugates of arginine, methionine, glycine and alanine are shifted hypsochromically by 15-20 nm, the fluorescence of the oxypoline conjugate is red-shifted by 20 nm compared to compound **2**, and for derivatives of cysteine and aspartic acid the positions of the maxima do not change.

**Table 1.** Absorption and emission properties of compound **2** in  $10^{-5}$  M solutions.

Solvent	Absorption $\lambda_{\text{abs}}$	$\lg \epsilon$	Fluorescence $\lambda_{\text{em}}$	Stokes shift, $\text{cm}^{-1}$
Hexane	425	4.23	498	3449
Benzene	431	4.21	520	3971
Chloroform	433	4.23	520	3864
Ethyl acetate	425	4.23	552	5413
Acetone	423	4.24	543	5224
Ethanol	424	4.19	538	4998
Dimethylformamide	426	4.20	556	5489
Dimethylsulfoxide	432	4.21	552	5032

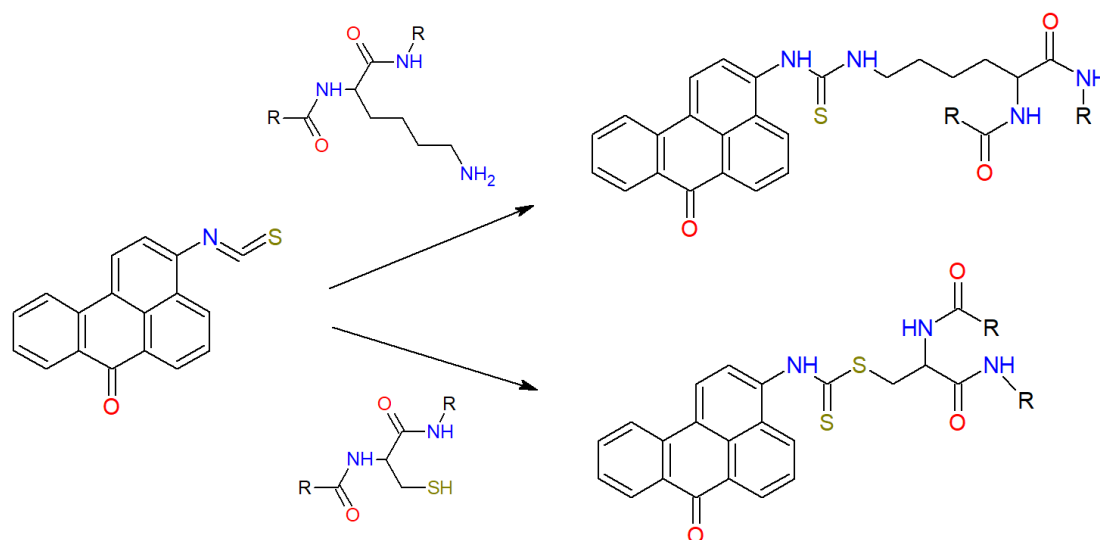


**Fig. 2.** Interaction of 3-isothiocyanatobenzanthrone with nucleophilic groups: with an amino group, forming thiourea (top); with a thiol group, giving dithiocarbamate (bottom).

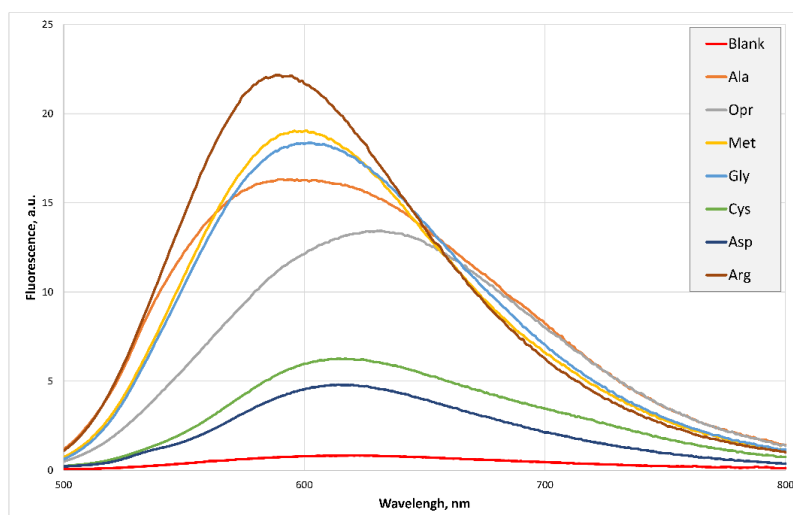


**Fig. 3.** Fluorescence spectra of compound **2** (blank) and its amino acid conjugates.

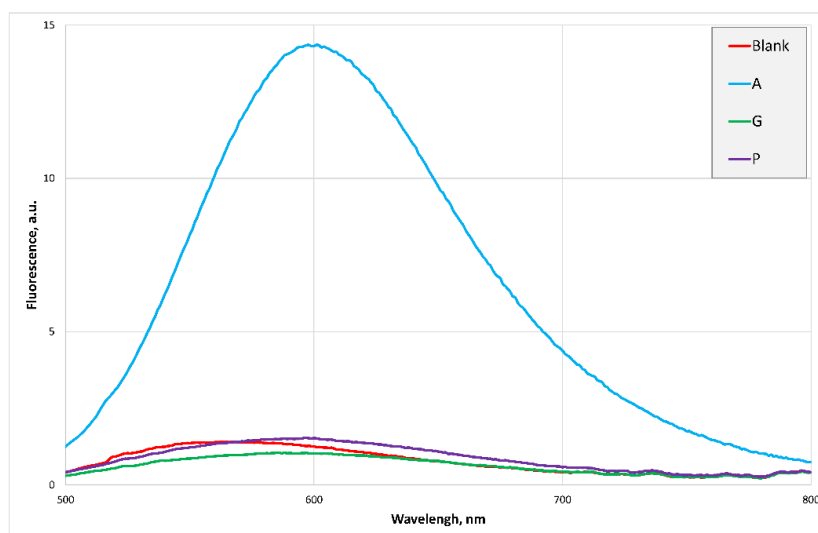


**Fig. 4.** Fluorescence spectra of compound **2** (blank) and its pepsin (P), gelatin (G) and albumin (A) conjugates.

Developed marker **2** was then used in bioconjugation reactions with three proteins at different isothiocyanate:protein ratios (0.1:8, 0.2:8 and 0.3:8 mg).

The most pronounced changes in the photophysical properties of the obtained protein conjugate compared to the initial isothiocyanate are observed for albumin (see Fig. 4). While the emission of gelatin and pepsin conjugates is almost the same as that of the starting compound **2**, the luminescence intensity of the albumin conjugate turned out to be 10 times higher than the isothiocyanate emission. A common feature of all conjugates is a bathochromic shift of the luminescence maximum by 20-30 nm compared to the initial marker.

Undoubtedly, the differences in the properties of the obtained conjugates are associated with their composition and structure. Bovine serum albumin is a globular protein which consists of 583 amino acid

residues (including 35 cysteine, 60 lysine, 26 arginine residues, etc.) in a single chain with a molecular weight of 66 kDa [26, 27]. Pepsin is a gastric aspartic proteinase with a molecular weight of 3.4 kDa containing 327 amino acid residues in a single polypeptide chain [28, 29]. Gelatin is a product of collagen destruction, its molecular weight is about 100 kDa, it contains practically no cysteine and contains a small amount of lysine compared to albumin [30]. Apparently, albumin not only contains quite a lot of amino acid residues that react with the isothiocyanate group, but these residues are also located on the outside of the albumin globule, which results in the formation of a highly emissive conjugate.

## CONCLUSION

3-Isothiocyanatobenzanthrone was designed as a fluorescent probe for amino acids and protein bioconjugation, and its application was tested using

bovine serum albumin, porcine pepsin and gelatin as model proteins. The highest emission response was observed for albumin, what can later be used for studying the biochemical processes in which this protein is involved. Thus, it can be summarized that the isothiocyanate developed and studied in this research appears promising for fluorescent labeling purposes.

**Acknowledgement:** This work is supported by fundamental and applied research projects of the Latvian Council of Science. Project No. lzp-2022/1-0436 "Novel fluorescent anthrone-derived functional materials for bioimaging applications."

#### REFERENCES

1. A. Zhang, J. Zheng, X. Qin, N. Yu, K.-N. Wang, *Adv. Sensor Energy Mater.*, **3**, 100092 (2024).
2. E. O'Connor, J. Micklefield, Y. Cai, *Curr. Opin. Biotechnol.*, **87**, 103125, (2024).
3. A. Boaro, L. Ageitos, M. Torres, F. H. Bartoloni, C. de la Fuente-Nunez, *Cell Rep. Phys. Sci.*, **1**, 100257 (2020).
4. J. Zhang, C. Yue, Y. Ke, H. Qu, L. Zeng, *Advanced Agrochem*, **2**, 127-141 (2023).
5. J. Spottel, J. Brockelt, S. Falke, S. Rohn, *Molecules*, **26**, 6247 (2021).
6. V. G. Amorim, S. M.G. Melo, R. F. Leite, P. A. Coutinho, S. M.P. da Silva, A. R. Silva, F. G. Amorim, R. G.W. Pires, J. B. Coitinho, F. S. Emery, L. C.D. Rezende, *Dyes Pigm.*, **182**, 108646 (2020).
7. J. Hong, G. Feng, *Sens. Actuators B Chem.*, **326**, 129016 (2021).
8. M. Zhang, S. Wang, Y. Fu, M. Meng, H. Jin, W. Zhao, *Sens. Actuators B Chem.*, **366**, 132013, (2022).
9. T. L. Kirley, A. B. Norman, *Biochem. Biophys. Rep.*, **35**, 101520 (2023).
10. X. Zhang, Y. Hemar, L. Lv, T. Zhao, Y. Yang, Z. Han, M. Li, J. He, *Int. J. Biol. Macromol.*, **140**, 377 (2019).
11. V. Nasufovic, P. Then, F. Droge, M. Duong, C. Kaether, B. Dietzek, R. Heintzmann, H. D. Arndt, *Org. Biomol. Chem.*, **19**, 574 (2021).
12. I. Kalnina, L. Klimkane, E. Kirilova, M. M. Toma, G. Kizane, I. Meirovics, *J. Fluoresc.*, **17**, 619 (2007).
13. Shivraj, B. Siddlingeshwar, A. Thomas, E. Kirilova, D. D. Divakar, A. Alkheraif, *Spectrochim. Acta A*, **218**, 221 (2019).
14. I. Gavarane, E. Kirilova, I. Rubenina, L. Mezaraupe, S. Osipovs, G. Deksnis, A. Puckins, I. Kokina, A. Bulanovs, M. Kirjusina, *Microsc. Microanal.*, **25**, 1491 (2019).
15. N. Orlova, I. Nikolajeva, A. Puckins, S. Belyakov, E. Kirilova, *Molecules*, **26**, 2570 (2021).
16. A. Luttringhaus, H. Neresheimer. *Ann.*, **273**, 259 (1929).
17. I. Grabchev, I. Moneva. *Dyes Pigm.*, **38**, 155 (1998).
18. M. M. Hemdan, A. F. M. Fahmy, N. F. Aly, I. A. Hegazi, A. A. El-Sayed, *Phosphorus Sulfur Silicon Relat. Elem.*, **187**, 181 (2012).
19. M. G. Assy, H. A. El-Sayed, N. H. Ouf, A. Hamza, H. A. Morsy, *J. Heterocyclic Chem.*, **56**, 2954 (2019).
20. A. A. El-Sayed, E. S. Nossier, A. A. Almehizia, A. E.-G. E. Amr, *J. Mol. Struct.*, **1247**, 131285 (2022).
21. B. Maeda, K. Murakami, *Chem. Comm.*, **60**, 2839 (2024).
22. E. M. Kirilova, I. A. Meirovics, S. V. Belyakov, *Chem. Heterocycl. Comp.*, **38**, 789 (2002).
23. M. Olipova, A. Maleckis, A. Puckins, A. Kirilova, E. Romanovska, E. Kirilova, *Bulg. Chem. Commun.*, **54**, 253 (2022).
24. E. Basle, N. Joubert, M. Pucheault, *Chem. Biol.*, **26**, 213 (2010).
25. H. Sahoo, *RSC Adv.*, **2**, 7017 (2012).
26. D.C. Carter, J. X. Ho, *Adv. Protein Chem.*, **45**, 153 (1994).
27. K. A. Majorek, P. J. Porebski, A. Dayal, M. D. Zimmerman, K. Jablonska, A. J. Stewart, M. Chruszcz, *Mol. Immunol.*, **52**, 174 (2012).
28. J. Tang, P. Sepulveda, J. Jr. Marciniszyn, K. C. Chen, W. Y. Huang, N. Tao, D. Liu, J. P. Lanier, *Proc. Natl. Acad. Sci. USA*, **70**, 3437 (1973).
29. K. Stanforth, M. Wilcox, P. Chater, I. Brownlee, M. Zakhour, K. Banecki, J. Pearson, *Ann. Esophagus*, **5**, 31 (2022).
30. S. R. Derkach, Y. A. Kuchina, A. V. Baryshnikov, D. S. Kolotova, N. G. Voron'ko, *Polymers*, **11**, 1724 (2019).

## Synthesis of substituted 4-methylphenyl-2-iminothiazolidinone compounds *via* one-pot method

F. T. Tuğcu\*

Faculty of Arts and Sciences, Department of Chemistry, Yildiz Technical University, Istanbul, Turkey

Received June 3, 2024; Accepted: August 17, 2024

Iminothiazolidinone derivatives, a class of nitrogen-containing heterocycles, have garnered significant attention in chemical research due to their remarkable biological and pharmacological activities such as antimicrobial, anti-inflammatory, anticonvulsant, antioxidant, antidiabetic, antitumor, and sedative characteristics [1-3]. This study aims to contribute to the field by synthesizing new iminothiazolidinone derivatives with potential biological activity. The synthesis is conducted using a one-pot multicomponent reaction technique, allowing for efficient and cost-effective production of these compounds. The chosen methodology involves a single-step approach, wherein thiourea derivatives, hetaryl aldehydes, and chloroacetic acid are subjected to a one-pot reaction, progressing in a domino-process fashion. This method offers advantages over traditional multi-step organic reactions, ensuring ease of execution within a shorter timeframe and at reduced costs.

**Keywords:** Iminothiazolidinone, thiourea, one-pot reaction, multicomponent reaction, solvent free

### INTRODUCTION

In the recent years, a significant portion of chemical research is dedicated to the synthesis of novel compounds with the potential for biological activity, and the subsequent measurement of their activities. Iminothiazolidinone derivatives, which are nitrogen-containing heterocycles, have recently gained substantial importance due to their elevated biological and pharmacological activities. Among heterocyclic compounds, iminothiazolidinones, particularly those exhibiting antimicrobial, anti-inflammatory, anticonvulsant, anti-hyper lipidemic, antihypertensive, neuroleptic, and sedative properties, play a crucial role, contributing to the production of macrocyclic complex drugs and holding significance in industrial applications [1-6].

Considering literature research, the primary objective of this study is to synthesize some new iminothiazolidinone derivatives with potential biological activity. The synthesis of these new iminothiazolidinone derivatives is undertaken to contribute not only to the class of heterocyclic compounds but also to benefit synthetic drug production. In this study, the new compounds are synthesized using a one-pot multicomponent reaction technique.

The reactions, conducted by a one-pot method, progress in a domino-process fashion, making them more straightforward to execute compared to

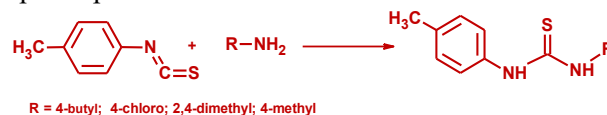
classical multi-step organic reactions. This method enables the synthesis of new organic molecules in a shorter time and at a lower cost.

Utilizing the one-pot multicomponent reaction technique, cyclization is achieved by exploiting thiourea derivatives, hetaryl aldehydes, and chloroacetic acid, resulting in new 2-imino-4-thiazolidinone derivatives [7].

### EXPERIMENTAL

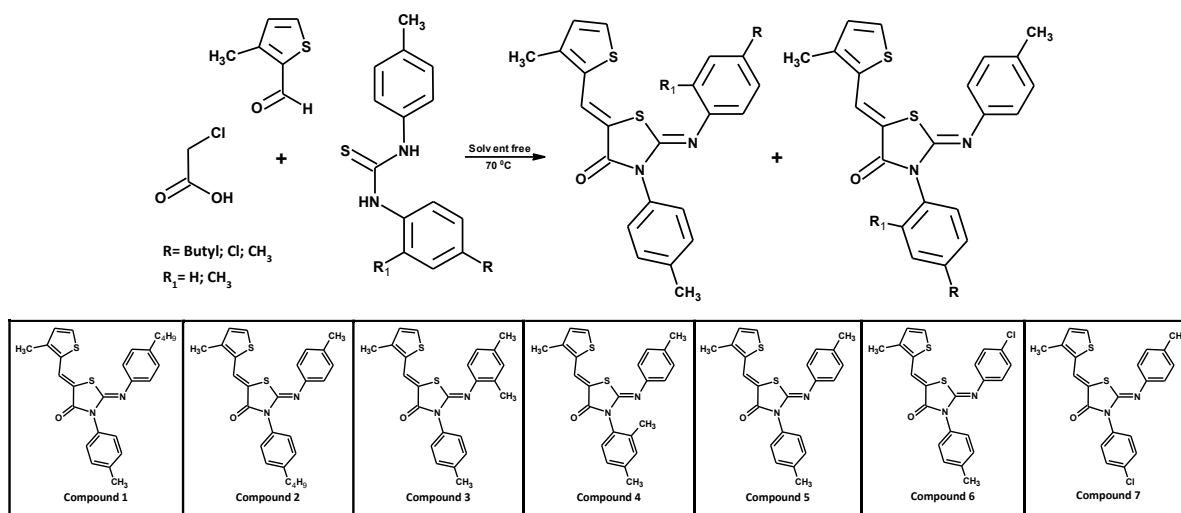
The study consists of two parts. In the first part, substituted thiourea compounds, which were planned to be used as substrates in the reactions, were obtained from substituted phenyl isothiocyanate and substituted amine compounds (Scheme 1).

In the second part, original imino-thiazolidinone compounds were synthesized by reacting the prepared substituted thiourea compounds with chloroacetic acid and thiophene aldehyde using the one-pot multicomponent method (Scheme 2). Measurements to elucidate the structures of the compounds obtained were performed using spectrophotometric methods.



**Scheme 1.** Synthesis of the thiourea compounds

\* To whom all correspondence should be sent:  
E-mail: [ftugcu@yildiz.edu.tr](mailto:ftugcu@yildiz.edu.tr)



**Scheme 2.** Synthesis of the iminothiazolidinones

**Compound 1:** 3-(4-butylphenyl)-5-[(3-methylthiophen-2-yl)methylene]-2-(p-tolylimino)thiazolidin-4-one: Mixture of 0.126 g (1.0 mmol) thiophene-3-aldehyde, 0.298 g (1.0 mmol) 1-(4-butylphenyl)-3-(4-methylphenyl) thiourea and 0.113 g (1.0 mmol) chloroacetic acid was placed in a round-bottomed balloon. TLC control was performed at regular intervals, and it was mixed first at room temperature for 24 hours and then at 40°C for 24 hours with the help of a magnetic stirrer. After the reaction was completed, the two isomer products were purified by applying column chromatography (dichloromethane/hexane: 4/1) to the dark solid mixture that was left to cool.  $\text{C}_{26}\text{H}_{26}\text{N}_2\text{OS}_2$  (446.63 g/mol). FT-IR (ATR): 3029, 2924, 2854, 1716, 1639, 1599, 1504, 1360, 1261, 1171, 1141, 879, 836  $\text{cm}^{-1}$ .  $^1\text{H}$  NMR ( $\text{CDCl}_3$ ):  $\delta$  0.95 (3H, t), 1.37 (2H, m), 1.60 (2H, m), 2.41 (3H, s), 2.42 (3H, s), 2.61 (2H, t), 6.88 (2H, d,  $J=8.2$  Hz), 6.98 (1H, d,  $J=5.0$  Hz), 7.16 (2H, d,  $J=8.2$  Hz), 7.34 (4H, s), 7.48 (1H, d,  $J=5.0$  Hz), 8.05 (1H, s) ppm.  $^{13}\text{C}$  NMR ( $\text{CDCl}_3$ ):  $\delta$  14.02, 14.52, 21.35, 22.40, 33.61, 35.18, 118.65, 120.95, 122.57, 127.77, 129.15, 129.46, 129.99, 131.06, 132.35, 132.54, 138.83, 139.41, 142.43, 145.81, 150.44, 166.63 ppm.

**Compound 2:** 2-(4-butylphenylimino)-5-[(3-methylthiophen-2-yl)methylene]-3-p-tolylthiazolidin-4-one:  $\text{C}_{26}\text{H}_{26}\text{N}_2\text{OS}_2$  (446.63 g/mol). FT-IR (ATR): 3069, 2954, 2856, 1712, 1638, 1595, 1506, 1366, 1269, 1167, 1147, 839, 796  $\text{cm}^{-1}$ .  $^1\text{H}$  NMR ( $\text{CDCl}_3$ ):  $\delta$  0.95 (3H, t), 1.40 (2H, m), 1.64 (2H, m), 2.35 (3H, s), 2.42 (3H, s), 2.66 (2H, t), 6.88 (2H, d,  $J=8.2$  Hz), 6.97 (1H, d,  $J=5.0$  Hz), 7.14 (2H, d,  $J=8.2$  Hz), 7.33 (2H, d,  $J=8.6$  Hz), 7.36 (2H, d,  $J=8.6$  Hz), 7.47 (1H, d,  $J=5.0$  Hz), 8.04 (1H, s) ppm.  $^{13}\text{C}$  NMR ( $\text{CDCl}_3$ ):  $\delta$  13.98, 14.52, 21.02, 22.50, 33.31, 35.47, 118.62, 120.99, 122.57, 127.69,

129.28, 129.44, 129.85, 131.05, 132.42, 132.53, 134.34, 142.42, 143.65, 145.80, 150.72, 166.65 ppm.

**Compound 3:** 2-(2,4-dimethylphenylimino)-5-[(3-methylthiophen-2-yl)methylene]-3-p-tolylthiazolidin-4-one:  $\text{C}_{24}\text{H}_{22}\text{N}_2\text{OS}_2$  (418.54 g/mol). FT-IR (ATR): 3099, 3066, 3011, 2918, 2853, 1708, 1634, 1589, 1510, 1355, 1261, 1169, 1113, 867, 809  $\text{cm}^{-1}$ .  $^1\text{H}$  NMR ( $\text{CDCl}_3$ ):  $\delta$  2.12 (3H, s), 2.31 (3H, s), 2.42 (6H, s), 6.78 (2H, d,  $J=7.9$  Hz), 6.97 (1H, d,  $J=5.0$  Hz), 7.16 (2H, d,  $J=8.2$  Hz), 7.34 (4H, s), 7.48 (1H, d,  $J=5.0$  Hz), 8.05 (1H, s) ppm.  $^{13}\text{C}$  NMR ( $\text{CDCl}_3$ ):  $\delta$  14.59, 17.95, 21.09, 21.47, 118.96, 119.83, 122.67, 127.24, 127.87, 129.54, 129.77, 130.04, 130.15, 131.15, 131.51, 132.54, 132.66, 134.42, 139.01, 142.49, 144.55, 150.29, 166.77 ppm.

**Compound 4:** 3-(2,4-dimethylphenyl)-5-[(3-methylthiophen-2-yl)methylene]-2-(p-tolylimino)thiazolidin-4-one:  $\text{C}_{24}\text{H}_{22}\text{N}_2\text{OS}_2$  (418.54 g/mol). FT-IR (ATR): 3077, 3062, 3007, 2920, 2851, 1703, 1633, 1591, 1503, 1364, 1273, 1157, 828, 724  $\text{cm}^{-1}$ .  $^1\text{H}$  NMR ( $\text{CDCl}_3$ ):  $\delta$  2.26 (3H, s), 2.34 (3H, s), 2.37 (3H, s), 2.42 (3H, s), 6.85 (2H, d,  $J=8.2$  Hz), 6.97 (1H, d,  $J=5.0$  Hz), 7.14 (2H, d,  $J=8.2$  Hz), 7.17 (1H, s), 7.18-7.20 (2H, m), 7.47 (1H, d,  $J=5.0$  Hz), 8.04 (1H, s).  $^{13}\text{C}$  NMR ( $\text{CDCl}_3$ ):  $\delta$  14.59, 17.74, 20.71, 21.16, 118.74, 120.88, 122.74, 128.08, 128.48, 129.56, 129.92, 130.02, 131.19, 131.67, 132.01, 132.55, 134.46, 135.84, 139.55, 142.53, 145.94, 150.21, 166.52 ppm.

**Compound 5:** 5-[(3-methylthiophen-2-yl)methylene]-3-p-tolyl-2-(p-tolylimino)thiazolidin-4-one:  $\text{C}_{23}\text{H}_{20}\text{N}_2\text{OS}_2$  (404.55 g/mol). FT-IR (ATR): 3029, 2924, 2854, 1716, 1639, 1599, 1504, 1360, 1261, 1171, 1141, 879, 836  $\text{cm}^{-1}$ .  $^1\text{H}$  NMR ( $\text{CDCl}_3$ ):  $\delta$  2.35 (3H, s), 2.41 (3H, s), 2.42 (3H, s), 6.88 (2H,

d, J=8,2 Hz), 6.97 (1H, d, J=5,0 Hz), 7.15 (2H, d, J=7.9 Hz), 7.34 (4H, s), 7.48 (1H, d, J=5,0 Hz), 8.04 (1H, s) ppm.  $^{13}\text{C}$  NMR ( $\text{CDCl}_3$ ):  $\delta$  14.52, 21.02, 21.35, 118.60, 120.99, 122.60, 127.77, 129.45, 129.83, 130.03, 131.05, 132.32, 132.52, 134.33, 138.88, 142.44, 145.78, 150.72, 166.64 ppm.

**Compound 6:** 2-[(4-chlorophenyl) imino]-3-(4-methylphenyl)-5-[(3-methylthiophen-2-yl) methylidene]-1,3-thiazolidin-4-one:  $\text{C}_{22}\text{H}_{17}\text{ClN}_2\text{OS}_2$  (424.97 g/mol). FT-IR (ATR): 3069, 1691, 1633, 1587, 1491, 1356, 890, 834  $\text{cm}^{-1}$ .  $^1\text{H}$  NMR ( $\text{CDCl}_3$ ):  $\delta$  2.41 (3H, s), 2.42 (3H, s), 6.99 (1H, d, J=5.0 Hz), 7.34 (4H, s), 7.41 (2H, brd, J=8.8 Hz), 7.50 (1H, d, J=5.0 Hz), 7.51 (2H, brd, J=8.8 Hz), 8.05 (1H, s) ppm.  $^{13}\text{C}$  NMR ( $\text{CDCl}_3$ ):  $\delta$  14.60, 21.30, 114.22, 118.65, 120.81, 122.34, 123.64, 129.35, 129.58, 131.62, 132.35, 133.50, 134.60, 138.74, 141.14, 143.01, 154.18, 166.38 ppm.

**Compound 7:** 3-(4-chlorophenyl)-2-[(4-methylphenyl) imino]-5-[(3-methylthiophen-2-yl) methylidene]-1,3-thiazolidin-4-one:  $\text{C}_{22}\text{H}_{17}\text{ClN}_2\text{OS}_2$  (424.97 g/mol). FT-IR (ATR): 3069, 1680, 1621, 1568, 1497, 1345, 882, 828  $\text{cm}^{-1}$ .  $^1\text{H}$  NMR ( $\text{CDCl}_3$ ):  $\delta$  2.35 (3H, s), 2.42 (3H, s), 6.87 (2H, d, J=8,2 Hz), 6.92 (2H, brd, J=8.6 Hz), 6.98 (1H, d, J=5.0 Hz), 7.14 (2H, d, J=8.2 Hz), 7.32 (2H, brd, J=8.6 Hz), 7.49 (1H, d, J=5.0 Hz), 8.04 (1H, s) ppm.  $^{13}\text{C}$  NMR ( $\text{CDCl}_3$ ):  $\delta$  14.60, 21.30, 114.62, 118.25, 120.41, 122.54, 123.69, 129.55, 129.88, 131.42, 132.45, 133.10, 134.34, 138.15, 141.01, 142.91, 153.88, 166.30.

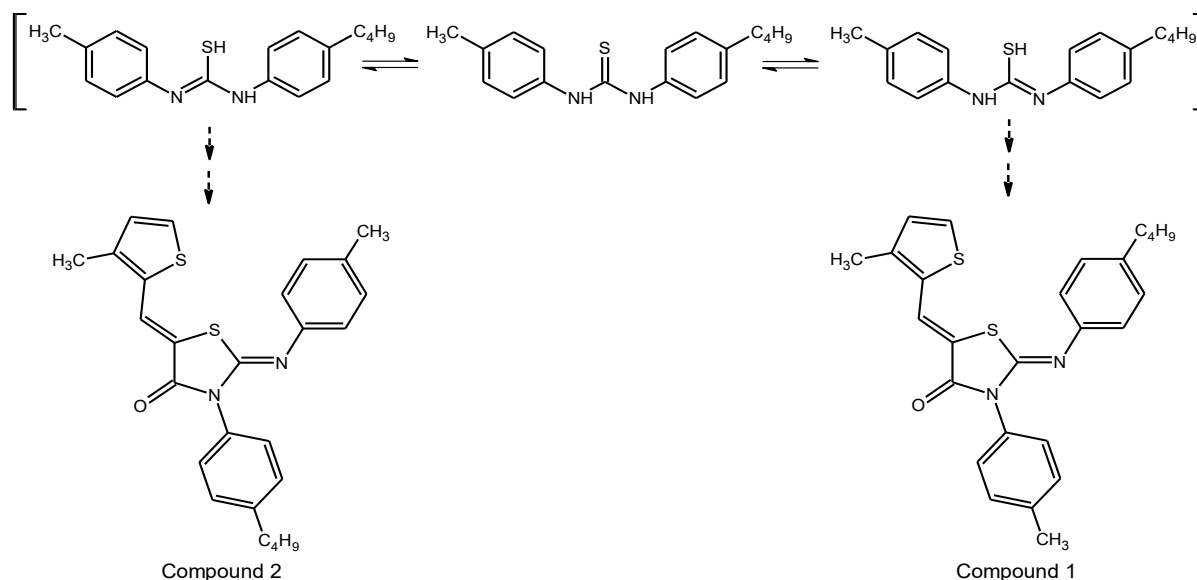
## RESULTS AND DISCUSSION

To synthesize the targeted iminothiazolidinone compounds with the highest yield, studies were carried out to determine the optimum ratios of the starting materials and the ratio of 1:1:1.2 (aldehyde, thiourea and chloroacetic acid, respectively) was determined as the optimum condition.

As is known from literature studies, heterocyclic compounds are generally formed by intramolecular or intermolecular cyclization reactions of substances in a straight chain structure. In arylthioureas, when the groups attached to both nitrogen atoms are different, the two structures obtained when the thionthiol tautomer is written can give a cyclocondensation reaction with chloroacetic acid, thus two isomer products are synthesized. The synthesis of compounds 1 and 2 is given below as an example [8].

The structures of the iminothiazolidinone compounds synthesized as a result of these one-pot three-component condensation reactions carried out in a solvent-free environment were elucidated by IR,  $^1\text{H}$  and  $^{13}\text{C}$  magnetic resonance spectroscopy methods. The results obtained are supported by the values stated in the sources [9-11].

As a result, in this study, 3 substituted thioureas and 7 original (new) 5-substituted-2-imino-4-thiazolidinone compounds were synthesized in very high yields and their structures were elucidated by FT-IR,  $^1\text{H}$  NMR and  $^{13}\text{C}$  NMR data.



REFERENCES

1. J. C. Campos, P. T. Campos, N. P. Bona, M. S. Soares, P. O. Souza, E. Braganhol, W. Cunico, G. M. Siqueira, *Med. Chem.*, **18**(4), 452 (2022).
2. M. A. S. El-Sharief, S. Y. Abbas, A. M. S. El-Sharief, N. M. Sabry, Z. Moussa, S. M. El-Messery, A. R. Elsheakh, G. S. Hassan, M. T. El Sayed, *Bioorganic Chem.*, **87**, 679 (2019).
3. A. Atteeque, A. Mubashir, A. E. Syeda, A. C. Pervaiz, S. Aamer, Z. Seema, A. W. Tanveer, H. Asad, A. Qamar, R. Hussain, K. Song Ja, *Biomolecules*, **12**(11), 1696 (2022).
4. P. Vicini, A. Geronikaki, K. Anastasia, M. Incerti, F. Zani, *Bioorg. Med. Chem.*, **14**, 3859 (2006)
5. G. Bansal, P. V. Thanikachalam, R. K. Maurya, P. Chawla, S. Ramamurthy, *J Adv. Res.*, **23**, 163 (2020).
6. K. Manpreet, K. Navjeet, M. Arunachalam, K. Sachin, *Res. J. Pharm. Tech.*, **15**(12), 5405 (2022).
7. S. Kasmi-Mir, A. Djafri, L. Paquin, J. Hamelin, M. Rahmouni, *Molecules*, **11**, 597 (2006).
8. L. V. Sudha, D. N. Sathyanarayana, S. Manogaran, *Spectrochimica Acta*, **42A** (12), 1373 (1986).
9. N. B. Colthup, L. H. Daly, S. E. Wiberley, Introduction to infrared and Raman spectroscopy, Academic Press, New York, 1975.
10. R. M. Silverstein, G. C. Bassler, T. C. Morrill, Spectrometric identification of organic compounds, 4<sup>th</sup> edn., John Wiley and Sons Inc., New York, 1981.
11. Q. N. Porter, Mass spectrometry of heterocyclic compounds, John Wiley and Sons, New York, 1985.

# Synthesis, characterization and effects to cholesteric lyotropic liquid crystal media of -ONNO- type Schiff bases and metal complexes

S. Meral<sup>1\*</sup>, A. Alaman Ađar<sup>2</sup>

<sup>1</sup> Boyabat Vocational School, Sinop University, Sinop, Turkey

<sup>2</sup> Faculty of Arts and Sciences, Department of Chemistry, Ondokuz Mayıs University, Samsun, Turkey

Received June 1, 2024; Accepted: August 17, 2024

Lyotropic liquid crystals (LLC) are remarkable candidates in biomimetic applications, and in this respect, their interaction mechanisms with the target molecule are controversial. The study aims to create an ordered host system for biosimilar guest molecules to determine interactions. -ONNO- type tetradentate julolidine derivative, symmetric Schiff bases were synthesized with 1,2-ethandiamine and 1,4-butanediamine, and then copper complexes were obtained from Schiff bases with a cage-like structure. To characterize the synthesized compounds FT-IR, <sup>13</sup>C and <sup>1</sup>H-NMR and UV-vis spectroscopies were employed. Decylammonium chloride (DACl), NH<sub>4</sub>Cl, H<sub>2</sub>O and the optically active amphiphilic molecule L-alanine decyl ester (L-ADE) as a chiral dopant were utilized in the host system. The properties of lyotropic cholesteric phases and the effects of the synthesized compounds were examined using a polarized optical microscope (POM) by measuring the helical pitch as a parameter. Synthesized Schiff bases and metal complexes (2.5-20 mM) were added to the cholesteric phase whose helical pitch was measured at 110 μm without destroying anisotropic properties. The synthesized compounds caused a lengthening in helical pitch due to settled micelles on the surface or within the micelle core, leading to a change in micelle-micelle interaction. Specifically, Cu(ac)<sub>2</sub>·H<sub>2</sub>O shortened the helical pitch.

**Keywords:** Cholesteric lyotropic liquid crystal, julolidene derivative Schiff base, Metal complex, Host-guest interaction

## INTRODUCTION

Liquid crystal is a smart material that has solid-like molecular order and anisotropic structure, as well as liquid-like mobility, which has been observed *in vivo* or *in vitro* biological environments. LLC, one of its notable types, is a solvent environment in which micelle formation and interaction of micelles are fundamental processes resulting from the interaction of hydrophobic and hydrophilic molecules [1, 2]. Long-range order in one, two, or three dimensions is effective in different LLC phases, thus demonstrating the ability to self-assemble into micelles. The mentioned ordered media are suitable for biological and industrial applications due to controllable ingredient quantities, making them applicable due to different polar domains and huge surface areas for molecule carrier systems. Nowadays, water-soluble peptides, insoluble drug molecules, and degradable enzymes can be delivered to desired areas. In addition, cream-like ingredients applied to the skin can be used more effectively in different polar regions [3-6]. Positional and orientational order, changing molecular mobility, symmetrical and optical properties are also driving factors that enable the formation of well-defined micellar domains through interaction, thus becoming applicable and adaptable in crystallization or polymerization reactions [7, 8].

As an important N-heterocyclic aromatic compound containing three six-membered-ring systems julolidene is a structural derivative of aniline [9, 10]. The electro-optical properties and fluorescence efficiency attract attention in sensor applications with high sensitivity to many desired biological compounds and in molecular rotors used as viscosity sensors [11-16]. Especially Schiff bases and metal complexes of julolidene derivatives are commonly researched because of diverse biological properties, and remarkable electro-optical properties with extensive conjugation [17-19]. Imine compounds have carbon-nitrogen double bonds that behave as Lewis acids and are preferred molecules for developing new drugs [20-22]. Imine compounds, especially 2-hydroxy derivatives, act as donor molecules. This behavior is frequently encountered in biological processes because they form highly coordinated compounds with metal ions, leading to increased biological and chemical effects [23, 24].

The LLC acts as a well-ordered supramolecular host, with all its controllable and adaptable properties, and is a remarkable field for determining the interactions of compounds and influencing factors. Especially for important issues of today, such as imaging and diagnostic applications, LLC offers a unique controllable, and biocompatible

\* To whom all correspondence should be sent:  
E-mail: [smeral@sinop.edu.tr](mailto:smeral@sinop.edu.tr)

encapsulation material. This ordered environment containing polar-nonpolar domains provides an evaluation environment for investigating the properties of screening compounds, such as optimal charge and activity [25-27]. In the study, the interactions between the prepared LLC systems and the synthesized compounds were evaluated by measuring the changes in the helical pitch depending on concentration and temperature.

## EXPERIMENTAL

### Synthesis of Schiff bases and copper complexes

To synthesize a symmetric Schiff base, 8-hydroxy-1,1,7,7-tetramethyl-2,3,6,7-tetrahydro-

1h,5h-pyrido[3,2,1-ij]quinoline-9-carbaldehyde (1) was refluxed with 1,2-ethandiamine and 1,4-butandiamine separately at a 2:1 stoichiometric ratio in ethanol for about 18 h. The yellow needle crystals that had collapsed in the reaction mixture were separated, washed three times with diethyl ether and ethanol, and recrystallized in a hot ethanol solution. To obtain copper complexes, the synthesized Schiff bases and  $\text{Cu}(\text{ac})_2 \cdot \text{H}_2\text{O}$  were reacted at a 1:1 stoichiometric ratio in ethanol for approximately 12 h. Excess  $\text{Cu}(\text{ac})_2 \cdot \text{H}_2\text{O}$  was washed with water and the complexes were recrystallized in ethanol. The synthesized compounds are given in Figure 1.

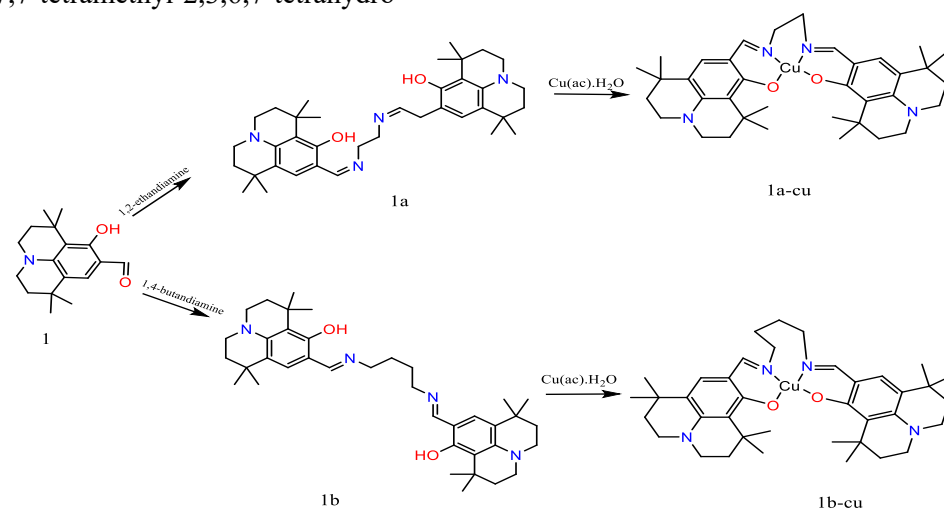


Fig. 1. The synthesized compounds

### Preparation of the LLC system

DACI were synthesized according to [28] and L-ADE [29]. To obtain the lyotropic phases, the required amounts of components were weighed for DACI/  $\text{NH}_4\text{Cl}$  / $\text{H}_2\text{O}$ ; DACI/ L-ADE/  $\text{NH}_4\text{Cl}$ /  $\text{H}_2\text{O}$  and DACI/ DEOH/ L-ADE/  $\text{NH}_4\text{Cl}$ /  $\text{H}_2\text{O}$  systems and heated in a water bath at 50°C. After the dissolution process was completed, the mixture was centrifuged and the obtained phase was examined with a polarized optical microscope. For investigation of the effect of the guest molecules on LLC, n-decanol solutions of the synthesized compounds were prepared in different concentrations and then added to the LLC media, heated in a water bath at 50°C to obtain a homogenous mixture, centrifuged, and examined with a polarized optical microscope.

## RESULTS AND DISCUSSION

Imine groups are easily functionalized substances that behave like Lewis acids and are inclined to electron transfer to metal ions. The synthesized symmetrical Schiff bases have a

hydroxyl group near the imine group and a -ONNO-type tetra-dentate structure. The alkyl chain can also provide flexibility, which facilitates the formation of chelates by surrounding the metal. The Schiff bases and copper complexes were obtained by condensation reaction and investigated using FT-IR,  $^1\text{H}$  NMR and  $^{13}\text{C}$  NMR, UV-vis spectroscopies.

In Figure 2, the FT-IR spectra of the compounds are given. Upon examining the FT-IR spectrum of the synthesized compound in 1a, one distinct hydroxyl peak was replaced by a broad peak in the 2400-2600  $\text{cm}^{-1}$  region due to the tautomeric structure and conjugation. Still, in 1b, a distinct hydroxyl peak was observed at 3396  $\text{cm}^{-1}$  due to the increased flexibility of the molecule with a butane chain [30, 31]. The C=O bond was transformed to a C=N bond, shifting the carbonyl peak to a lower wavelength at around 1615  $\text{cm}^{-1}$  and 1619  $\text{cm}^{-1}$  for 1a and 1b respectively, providing a crucial clue for the desired molecules [32, 33]. Amine groups are detected at 3300-3400  $\text{cm}^{-1}$  as a double peak [34] and for synthesized symmetrical Schiff bases the mentioned peaks testified that both amine groups are transformed into imine bonds.

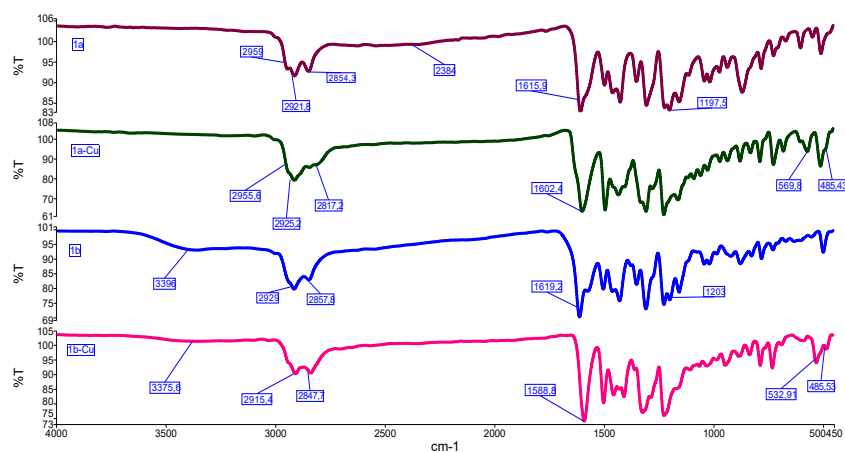


Fig. 2. FT-IR spectra of the synthesized compounds

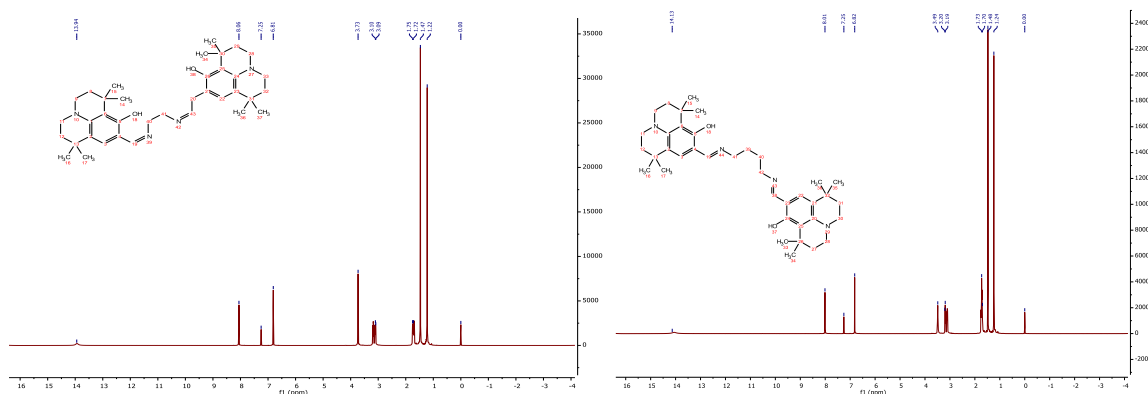


Fig. 3. <sup>1</sup>H NMR spectra of 1a and 1b

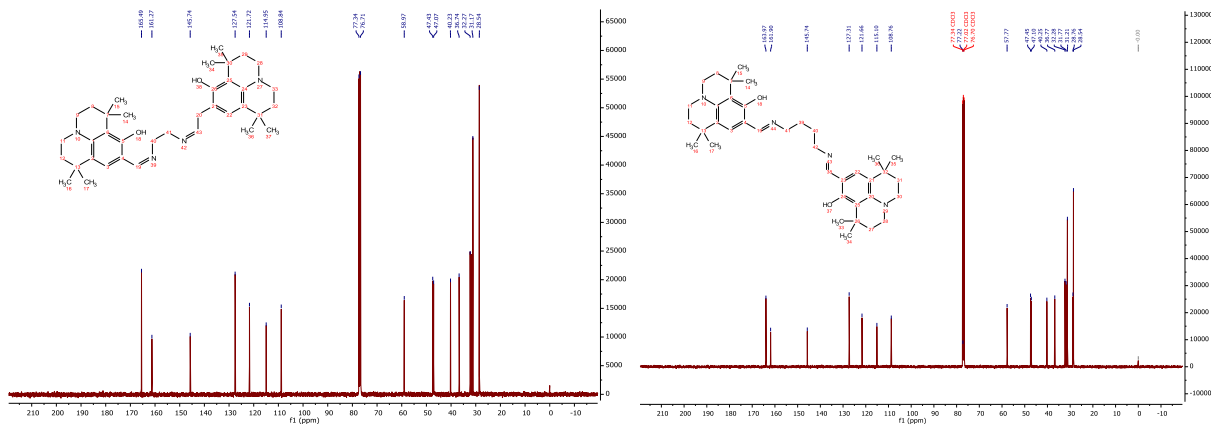


Fig. 4. <sup>13</sup>C NMR spectra of 1a and 1b

Copper ions participated in the formation of the complex through oxygen and nitrogen atoms, and in this case, the imine peaks shifted to lower regions at 1602 and 1588  $\text{cm}^{-1}$ , and at the same time, the hydroxyl peaks were not observed in 1a-Cu, whereas for 1b-Cu they were determined at a lower wavelength at 3375  $\text{cm}^{-1}$  [35, 36]. In copper complexes, new peaks were detected in the FT-IR spectra at 485 and 569-532  $\text{cm}^{-1}$ , indicating M-N and M-O bonds [37, 38]. Line with the literature aliphatic C-H, aromatic C-H and C=C vibrations were observed at 2955-2820 and 1420-1497  $\text{cm}^{-1}$  for

the synthesized compounds [39]. In Figure 3, <sup>1</sup>H NMR spectra of the synthesized compounds in chloroform are provided. In harmony with FT-IR spectra, the imine proton was observed in the <sup>1</sup>H NMR spectrum replacing the aldehyde proton at 8.06 and 8.01 ppm as a single peak for 1a and 1b, respectively. Looking at the chemical structure, the hydroxyl peak was seen at 13.94 and 14.13 ppm for 1a and 1b upfield with the tautomeric interaction hydroxyl proton [40]. Aromatic protons were detected at 6.82-7.25 ppm as multiplet peaks, CH<sub>2</sub> protons between two conjunctive julolidene moieties

at 3.73 and 3.49 ppm, -N attachment aromatic protons at 3.09-3.10 and 3.19-3.20 ppm and CH<sub>3</sub> protons at 1.75 ppm for 1a and 1b [41, 42].

In Figure 4, <sup>13</sup>C NMR spectra are given for 1a and 1b in chloroform. The most important peak in the <sup>13</sup>C NMR spectra of compounds 1a and 1b is the imine peak, which was replaced by the carbonyl peak downfield at 165 and 163 ppm, respectively [43]. The <sup>13</sup>C NMR spectra of both compounds showed a peak at 161 ppm due to their phenolic carbons [40]. At 145 ppm, the aromatic carbon atoms attached to nitrogen were determined and at the same time, aromatic carbons were in the 127-108 ppm range. At 77 ppm, the ethylene carbons attached to the julolidene moiety were observed in 1a, while in 1b, butyl carbons were observed at 77-76 ppm. The compounds have cycloalkane carbons attached to nitrogen atoms and are observed in the 58-31 ppm range for 1a and 1b. The peaks observed around 28 ppm are attributed to aliphatic carbons [44, 45].

In electronic spectra, n-π\* and π-π\* transitions were detected in a range of 200-400 nm concerning chromophore groups. In Figure 5, UV-vis spectra of synthesized compounds in different polar protic and aprotic solvents such as methanol, ethanol, acetonitrile and chloroform are seen. Observation of a blue shift at 263 nm with increasing polarity corresponds to n-π\* transition for 1a, while detected at 279 nm for 1a-Cu indicated electron transfer to the copper ion. The π-π\* transition of 1a was recorded at 346 nm with a red shift resulting from the increased polarity. For the copper complex of 1a, π-π\* transition was observed at 353 nm. Similarly, it was determined that the n-π\* transition at 266 nm showed a red shift with increasing polarity in compound 1b, and this transition was observed at higher wavelengths in the copper complex of 1b [46, 47]. The π-π\* transition for 1b was seen at 346 nm in ethanol and higher wavelength due to complex

formation. The coordinated metal ion is also seen in complexes' spectra in the range 640-680 nm. d-d transitions are observed with a weak intensity for 1a-Cu and 1b-Cu [48].

To design and control interactions for biosimilar molecules, the lyotropic liquid crystal was preferred in the study because it can provide an environment similar to biological systems, where compounds with different polarities are stable and can be dissolved within applicable limits. It is crucial to investigate the formation and properties of a superstructure from micelles and synthesized compounds with flexible and similar structural regions, particularly how the type or concentration of components can control it. The host system contains two surfactants and a co-surfactant and therefore the micelles have a significant non-polar character and also the optically active LADE ensures that the micelles are arranged in a helical structure and the system has chirality. The guest molecules have a large structure that can easily be accommodated in micelles with apolar aromatic bodies and the polar imine moiety in the polar heads. As a result, this association can be determined by the observed changes in phase type or helical pitch length, leading to growth, division, gap formation and disorientation in micelles. Many host-guest interactions have been interpreted in the literature, especially in the liquid crystal environment, and it has been reported that the system properties are very sensitive to additives, but there is not enough information about Schiff bases and metal complexes as a guest molecule, which contain molecular groups with remarkable interaction types [49]. Firstly, the nematic phase was determined with threaded texture and after adding chiral LADE, the fingerprint texture was formed. The amounts of the components are given in Table 1 and phase textures obtained from POM are given in Figure 6.

**Table 1.** Amounts of compounds in prepared systems and helical pitch

System	1	2	3	4	5	6	7	8	9
DACl (% <sub>oxi</sub> )	5.45	5.44	5.43	5.42	5.42	5.35	4.045	4.026	4.184
NH <sub>4</sub> Cl	1.97	1.97	1.97	1.96	1.96	1.94	1.467	1.460	1.517
H <sub>2</sub> O	92.58	92.43	92.27	91.97	92.17	91.08	93.872	93.434	97.117
LADE	-	0.16	0.33	0.65	1.43	1.62	0.235	0.701	0.972
DEOH	-	-	-	-	-	-	0.006	0.006	0.006
P(μm)	N	100	60	40	30	L	150	110	L

D: Droplet phase

I: Isotrope phase

N: Nematic phase

L: Lamellar phase

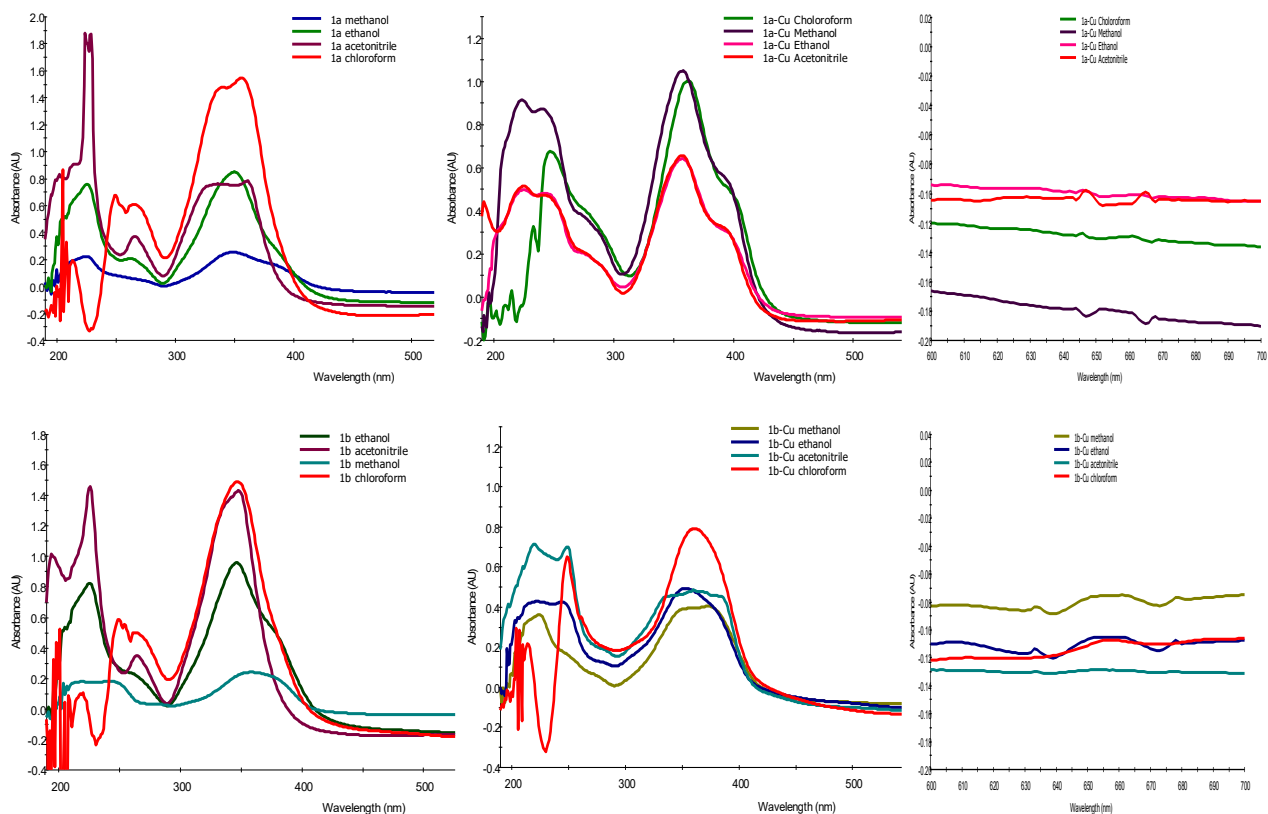


Fig. 5. UV-vis spectra of compounds in different solvents



Fig. 6. Nematic and cholesteric phase textures

Table 2. Helical pitch of DACI/ NH<sub>4</sub>Cl/ H<sub>2</sub>O/ L-ADE/Aldehyde(1) and DACI/NH<sub>4</sub>Cl/H<sub>2</sub>O/ L-ADE/ Cu(ac)<sub>2</sub>.H<sub>2</sub>O systems

DACI/ NH <sub>4</sub> Cl/ H <sub>2</sub> O/ L-ADE/ 1					DACI/ NH <sub>4</sub> Cl/ H <sub>2</sub> O/ L-ADE/ Cu(ac) <sub>2</sub> .H <sub>2</sub> O				
System	10	11	12	13	System	14	15	16	17
Con/ Tem. (mM/ °C)	2.5	5	10	20	Con/Tem. (mM/ °C)	2.5	5	10	20
25	130	140	200	200	25	110	100	90	90
27	120	130	200	200	27	110	100	90	90
30	120	130	190	190	30	110	100	90	90
35	120	130	190	190	35	110	100	90	90
40	120	130	190	190	40	110	100	90	90
45	I	I	190	190	45	110	I	D	D
50	I	I	I	I	50	I	I	I	I

For the DACI/ NH<sub>4</sub>Cl/ H<sub>2</sub>O/ L-ADE systems, the helical pitch was shortened as the amount of optically active L-ADE increased. It is mentioned in the literature that the micelle size in the cholesteric

phase may be smaller or larger than that in the nematic phase depending on adding chiral dopant [50]. The observed shortening in the helical pitch can be explained by the fact that chiral micelle-micelle

interactions at appropriate distances become more effective with increasing chirality. For system 6, an arrangement in which the hydrophilic tail is aligned along the water surface and the hydrophobic tail parts are surrounded by water layers, in other words, the lamellar phase, was detected. The mentioned system is an important arrangement seen in biological membrane bilayers [51]. The fact that LADE is an amphiphilic molecule like DACI and its non-polar parts are compatible and increasing specific packing of the head groups can be seen as the reason for the increase in density [29]. Decanol was added to the prepared system as a co-surfactant to easily incorporate the synthesized compounds and increase the interaction, and it was determined that the helical pitch shortened with the increase in the amount of LADE, similar to the system without decanol. In systems with and without decanol, with the increase in amphiphilic molecules, a lamellar phase was observed. To determine each structural effect, the aldehyde used,  $\text{Cu}(\text{ac})_2 \cdot \text{H}_2\text{O}$ , 1a, 1b, 1a-Cu and 1b-Cu, were added to the system with a helical pitch of 110  $\mu\text{m}$ . The added amounts of aldehyde,  $\text{Cu}(\text{ac})_2 \cdot \text{H}_2\text{O}$  and helical pitch are given in Table 2 and some selected system phase textures are given in Figure 7.



Fig. 7. Some obtained cholesteric phase textures

The aldehyde used (1) contains various functional groups, including an aromatic ring, a non-bonding electron pair connected to the  $\pi$  system, alkyl and hydroxyl groups. Owing to these different chemical groups, it could be incorporated into the liquid crystal system within a range of 2.5-20 mM without disrupting the anisotropy feature. With the increasing amount of aldehyde added at 25  $^{\circ}\text{C}$ , the helical pitch lengthened. At 20 mM, the helical pitch lengthened by 81 %. With the increase in temperature, the helical pitch was shortened by 5-7 %. After 45  $^{\circ}\text{C}$ , the liquid crystal phase feature began to disappear and an isotrope phase was observed. On the other hand, when  $\text{Cu}(\text{ac})_2 \cdot \text{H}_2\text{O}$  was added to the system, it was observed that, unlike the aldehyde, the

helical pitch was shortened and it was not affected by temperature. These differences imply that micelles may exhibit different types of interactions depending on the nature of the added components.  $\text{Cu}^{2+}$  ions can be expected to settle around the head group, thus preventing the interaction between the micelles by surrounding the ions with an electrical double layer of ions [26]. Therefore, while the helical pitch was the same at low concentrations, a change was observed with increasing concentrations. The shortening observed in the helical pitch at high concentrations caused an increase in the chirality interaction and an increase in the helical order. The added amounts of 1a, 1b and helical pitch are given in Table 3.

The synthesized Schiff bases have two imine units attached to an alkyl chain, which provides a flexible structure, while the benzene and hydroxyl groups have a rigid structure. This flexible and symmetric structure is expected to be significantly compatible with polar and non-polar groups in lyotropic environments. The results showed that in the added concentration range, both Schiff bases settled into the lyotropic medium without disturbing the anisotropic property. For 1a, at 25  $^{\circ}\text{C}$  a phase transition to nematic phase was determined but at higher temperatures cholesteric phase was obtained with a long helical pitch. The situation demonstrated that 1a compound changed micelle interaction and a less ordered structure occurred. The same situation was detected for compound 1b, but unlike 1a, the increasing alkyl chain caused transformation to the cholesteric phase over a higher temperature range. 1b has a more flexible alkyl chain and can cause situations that can affect the molecular order, such as the disintegration of micelles or aggregation so that the helical order can only be reestablished at higher temperatures [52]. The added amounts of 1a-Cu, 1b-Cu and helical pitch are given in Table 4. Copper complexes, like the other components examined, were found to be suitable for lyotropic media and similarly caused a lengthening of the helical pitch with changing concentration. Compared to copper complexes and Schiff bases, alkyl chains appear to have a significant effect. It can be stated that with complexation, the flexibility of the molecule settled around the metal decreases and it exhibits a harder structure. The molecule with increased rigidity can take part in the existing order by settling into the micelle or on its surface.

**Table 3.** Helical pitch of DACI/ NH<sub>4</sub>Cl/ H<sub>2</sub>O/ L-ADE/ 1a and DACI/ NH<sub>4</sub>Cl/ H<sub>2</sub>O/ L-ADE/1b systems

DACI/ NH <sub>4</sub> Cl/ H <sub>2</sub> O/ L-ADE/ 1a					DACI/ NH <sub>4</sub> Cl/ H <sub>2</sub> O/ L-ADE/ 1b				
System	18	19	20	21	System	22	23	24	25
Con/Tem. (Mm)/(°C)	0.625	1.25	2.5	5.0	Con/Tem. (Mm)/(°C)	1.25	2.5	5.0	10.0
25	N	N	N	N	25	N	N	N	N
27	120	150	150	150	27	N	N	N	N
30	120	150	150	150	30	200	200	210	210
35	120	120	150	150	35	200	200	210	210
40	120	120	120	120	40	200	200	210	210
45	120	120	120	120	45	200	200	210	210
50	I	I	I	I	50	I	I	I	I

**Table 4.** Helical pitch of DACI/ NH<sub>4</sub>Cl/ H<sub>2</sub>O/ L-ADE/ 1a-Cu and DACI/ NH<sub>4</sub>Cl/ H<sub>2</sub>O/L-ADE/1b- Cu systems

DACI/ NH <sub>4</sub> Cl/ H <sub>2</sub> O/ L-ADE/ 1a-Cu					DACI/ NH <sub>4</sub> Cl/ H <sub>2</sub> O/ L-ADE/ 1b-Cu				
System	26	27	28	29	System	30	31	32	33
Con/Tem. (Mm)/(°C)	0.625	1.25	2.5	5.0	Con/Tem. (Mm)/(°C)	0.156	0.312	0.526	1.25
25	130	130	N	N	25	150	160	180	200
27	130	130	200	N	27	140	160	180	200
30	120	130	200	N	30	140	160	180	200
35	120	120	150	N	35	140	160	180	200
40	120	120	150	D	40	140	160	180	200
45	I	D	D	D	45	D	D	D	D
50	I	I	I	D	50	I	I	I	I

## CONCLUSION

The synthesized molecules were added as guest molecules in the cholesteric phase as a component in a co-surfactant. Interactions were examined on an optically active, an optically inactive amphiphilic molecule and imine compounds. The addition of any substance can greatly affect the size and shape of the micelle, which in turn changes the properties of the host phase. This effect depends on the substance's ability to interact with the hydrophilic surface and the hydrophobic core of the micelle. The helical pitch was used as a parameter of molecular interactions of the host-guest system. Cu(ac)<sub>2</sub>.H<sub>2</sub>O shortened the helical pitch due to increasing helical order, other compounds extended it. It is possible to establish the necessary distance for chirality transfer due to electrostatic interaction in this case. It seems that the transfer of chirality in Schiff bases does not continue, particularly at low temperatures. This may be due to increased aggregation in micelles with the alkyl chain of Schiff bases or irregular movements caused by increased flexibility. Compared to the synthesized molecules used, copper complexes are more suitable for maintaining cholesteric order with their rigid structures. It is observed that this rigid structure settles within the inner part of the micelles, maintaining their existing order. The molecules or parts of the molecules that are close to the surface have a major effect on the interaction between

micelles. Temperature was adjusted to accommodate guest molecules without destroying their anisotropic character. Researched host-guest systems are suitable for controlling interactions, especially within the biological temperature range, to utilize different phenomena in lyotropic systems. It has been determined that the investigated host-guest system, phase type, that is, packing ratio and interfacial mean curvature, can be controlled by the chemical structure and concentration of the synthesized compound. The host-guest system allows the placement of julolidene-containing compounds, which are not water-soluble and can exhibit fluorescence properties, in a biocompatible and water-containing environment.

**Acknowledgement:** This work was supported by Sinop University Scientific Research Coordination Unit. (Project Number BMYO-1901-21-001).

## REFERENCES

1. X. Mulet, B. J. Boyd, C. J. Drummond, *J. Colloid Interface Sci.*, **393**, 1 (2013).
2. C. V. Kulkarni, O. Glatter, in: *Self-Assembled Supramolecular Architectures*, John Wiley & Sons, Inc. New York, 2012, p. 157.
3. K. Garbovskiy, J. Larsson, *Phys. Chem.*, **93**, 7304 (1989).
4. W. Q. Ding, H. Liu, S. Y. Qin, Y. Jiang, X. Lei, A. Q. Zhang, *ACS Appl. Bio. Mat.*, **12**, 8989 (2020).

5. E. Kemiklioglu, B. Gurboga, E. B. Tuncgovde, *Optik*, **248**, 168110 (2021)
6. H. Suhaimi, L. C. Rose, *Orient. J. Chem.*, **32**, 2073 (2016).
7. R. C. Pasquali, C. Bregni, R. Serrao, *Acta Farm Bonaer.*, **453** (2005).
8. M. A. DePierro, C. A. Guymon, *Macromolecules*, **47**, 5728 (2014).
9. P. A. S. Smith, T. Yu, *J. Org. Chem.*, **17**, 1281 (1952).
10. J. J. Holt, B. D. Calitree, J. Vincek, M. K. Gannon, M. R. Detty, *J. Org. Chem.*, **72**, 2690 (2007).
11. F. Jbilou, I.N. Georgousopoulou, S. Marinkovic, S. Vouyiouka, C. D. Papaspyrides, B. Estrine, P. Dole, A. Cottaz, C. Joly, *Eur. Polym. J.*, **78**, 61 (2016).
12. E. Ablinger, S. Leitgeb, A. Zimmer, *Int. J. Pharm.*, **441**, 255 (2013).
13. D. J. Lichlyter, M. A. Haidekker, *Sens. and Actuators B: Chem.*, **139**, 648 (2009).
14. Y. Yang, F. Liu, H. Wang, M. Zhang, H. Xu, S. Bo, J. Liu, L. Qiu, Z. Zhen, X. Liu, *Phys. Chem. Chem. Phys.*, **16**, 1 (2014).
15. P. Li, R. Li, K. Wang, Q. Liu, B. Ren, Y. Ding, R. Guan, D. Cao, *Spectrochim. Acta A Mol. Biomol. Spectrosc.*, **276**, 121213 (2022).
16. V. R. Holland, B. C. Saunders, *Tetrahedron*, **27**, 2851 (1971).
17. O. Halter, H. Pleni, *Eur. J. Inorg. Chem.*, **25**, 2935 (2018)
18. D. Maity, A. K. Manna, D. Karthigeyan, T. K. Kundu, S. K. Pati, T. Govindaraju, *Chem. - Eur. J.*, **17**, 11152 (2011).
19. W. Akarasarenon, S. Chanmungkalakul, L. Xiaogang, P. Rashatasakhon, *J. Photochem. Photobiol. A: Chem.*, **437**, 114422 (2023).
20. R. S. Joseyphus, C. Shiju, J. Joseph, C. J. Dhanaraj, D. Arish, *Spectrochim. Acta A Mol Biomol. Spectrosc.*, **133**, 149 (2014).
21. A. Datta, N. K. Karan, S. Mitra, G. Rosair, *Naturforsch.*, **57**, 999 (2002).
22. S. Kothavale, A. G. Jadhav, N. Sekar, *Dyes and Pigm.*, **137**, 329 (2017).
23. R. I. Kureshy, N. H. Khan, S. H. R. Abdi, S. T. Patel, P. Iyer, *J. Mol. Catal. A Chem.* **150**, 175 (1999).
24. P. Mayurachayakul, O. Chantarasriwong, N. Yotapan, A. Kamkaew, W. Mingvanish, C. Srisuwannaket, M. Sukwattanasinitt, N. Niammont, *Spectrochim. Acta A Mol Biomol. Spectrosc.*, **279**, 121382 (2022).
25. N. Alcaraz, B. J. Boyd, *Curr. Med. Chem.*, **24**, 470 (2017).
26. B. W. Muir, D. P. Acharya, D.F. Kennedy, X. Mulet, R. A. Evans, S. M. Pereira, *Biomaterials*, **33**, 2723 (2012).
27. S. Sivakumar, K. L. Wark, J. K. Gupta, N. L. Abbott, F. Caruso, *Adv. Funct. Mater.*, **19**, 2260 (2009)
28. M. Acımiş, L. W. Reeves, *Can. J. Chem.*, **58**, 1542 (1980).
29. M. Acımiş, E. Akpınar, *Phys. Chem. Chem. Phys.*, **5**, 4197 (2003).
30. V. T. Kasumov, A. A. Medjidov, N. Yaylı, Y. Zeren, *Spectrochim. Acta A*, **60**, 3037 (2004).
31. Z. Popovic, G. Pavlovic, D. M. Calogovis, V. Roje, I. J. Leban, *Mol. Struct.*, **615**, 23 (2002).
32. K. Z. Ismail, *Transit. Met. Chem.*, **25**, 522 (2000).
33. B. Dutta, P. Bag, B. Adhikary, U. Florke, K. J. *Org. Chem.*, **69**, 5419 (2004).
34. B. S. Garg, P. K. Singh, J. L. Sharma, *Synth. React. Inorg. Met.-Org. Chem.*, **30**, 80 (2000).
35. J. M. Sece, M. Quiros, M. J. G. Garmendia, *Polyhedron*, **19**, 1005 (2000).
36. M. Thomas, M. K. M. Nair, P. K. Radhakrishnan, *Synth. React. Inorg. Met Org. Chem.*, **25**, 471 (1995).
37. A. Jain, R. Goyal, D. D. Agarwal, *J. Inorganic Nuclear Chem.*, **43**, 2005 (1981).
38. M. I. Khan, A. Khan, I. Hussain, M. A. Khan, S. Gul, M. Iqbal, F. Khuda, *Inorg. Chem. Commun.*, **35**, 104 (2013).
39. A. Cınarlı, D. Gürbüz, A. Tavman, A. S. Birteksöz, *Bull. Chem. Soc. Ethiop.*, **25**, 407 (2011).
40. E. Tas, M. Aslanoglu, M. Ulusoy, H. Temel, *J. Coord. Chem.*, **57**, 677 (2004).
41. H. L. Siddiqui, A. Iqbal, S., Ahmad, G. W. Weaver, *Molecules*, **11**, 206 (2006).
42. T. F. Anjong, Y. M. Park, H. Y. Jang, J. Kim, *Bull. Korean Chem. Soc.*, **37**, 905 (2016).
43. J. Y. Noh, S. Kim, I. H. Hwang, G. Y. Lee, J. Kang, S. Kim, J. Min, S. Park, C. Kim, J. Kim, *Dyes and Pigments*, **99**, 1016 (2013).
44. S. Y. Lee, S. Y. Kim, J. A. Kim, C. Kim, *J. Lumin.*, **179**, 602 (2016).
45. Y. Kaya, H. Mutlu, G. Irez, *G. U. J. Sci.*, **23**, 1318 (2010).
46. A. Gonciarz, M. Zuber, J. Zwoździak, *Chemistry Open*, **30**, 677 (2018).
47. P. R. Reddy, S. Rajeshwar, B. Satyanarayana, *J. Photochem. Photobiol. B*, **160**, 217 (2016).
48. E. Akpınar, G. Frank, M. Acımiş, *Liquid Crystals*, **40**, 1183 (2013).
49. H. D. Dörfler, *Adv. Colloid. Interface Sci.*, **98**, 285 (2002).
50. L. L. M. Van Deenen, The molecular basis of membrane function, Prentice-Hall, New Jersey. 1969, p. 47.
51. V. Luzzati, F. Husson, *Med. J. Cell Biol.*, **12**, 207 (1962).
52. Y. Zhao, X. Yue, X. Wang, X. Chen, *J. Colloid Interface Sci.*, **389**, 199 (2013).

## Evaluating the efficacy of cherry stem extracts against calcium oxalate monohydrate crystallization in kidney stone treatment

E. Akyol<sup>1\*</sup>, M. Danisman<sup>2</sup>

<sup>1</sup>Department of Chemical Engineering, Yildiz Technical University, Davutpasa Campus Esenler, Istanbul 34210, Turkey

<sup>2</sup>Department of Chemistry and Chemical Processing Technologies, Bayramic Vocational School, Çanakkale 18 Mart University, Çanakkale 17700, Turkey

Accepted: June 16, 2024

Urethritis is one of the oldest known diseases of urinary stone formation. Urinary system stone disease ranks third among urinary diseases after urinary infection and prostate diseases. Calcium oxalate monohydrate (COM) crystals are known to be the main cause of urinary tract and kidney stones. In addition to the fact that surgical methods and drug treatments used in the treatment of kidney stones are painful and costly, the fact that traditionally used herbs are thought to be natural and harmless, has led to an increased interest in herbal medicines in recent years. Dried cherry stems have diuretic properties and can be used in the treatment of kidney stones reported in Iranian Traditional Medicine documents. When infused in hot water, they can be used as an herbal remedy in the treatment of high blood pressure and kidney stone disease. In the light of this information, in this study, the effects of cherry stem extracts as a natural additive on the growth of calcium oxalate monohydrate (COM) crystals, which is of great importance in investigating the crystallization mechanism in terms of biomineralization, was investigated *in vitro*. Structural characterizations of CaOx crystals were performed by FT-IR analyses, and morphological characterization and morphological changes were investigated by SEM images. The *in vitro* inhibitory effect of extracts of natural additives on calcium oxalate crystallization was determined by the time course of concentration measured in solution at extract concentrations of 0.5, 1, 5, 10 and 50 mL. Our findings demonstrate that cherry stem extracts significantly inhibit COM crystal growth and promote the formation of calcium oxalate dihydrate (COD) crystals, which are more easily excreted from the body.

**Keywords:** kidney stone; calcium oxalate; crystallization; inhibition; cherry stem

### INTRODUCTION

Urinary tract and kidney stone formation is one of the most common and important clinical problems known since ancient times [1]. Records of bladder and kidney stones were found in Egyptian mummies dating back to 4800 BC [2]. Kidney stones are a major health issue [3]. Urinary stone development is a prevalent worldwide health issue that can impact individuals of all ages [4]. Urinary system stone disease is the third most common urinary disease, following urinary infection and prostate diseases [5]. In mature men, the likelihood of developing stones is 20%, whereas in women it ranges from 5% to 10%. The incidence of nephrolithiasis recurrence is predicted to range from 50% to 80% within 5 years after the first formation of the stone [6]. The global incidence of this condition appears to be rising in both males and females mostly as a result of a sedentary lifestyle, eating patterns, and issues related to global warming [7, 8]. The United States incur an estimated annual economic impact of over \$5 billion due to kidney stones [9].

Calcium oxalate monohydrate (COM) crystals are known as the main cause of urinary tract and kidney stones [10]. Calcium oxalate accounts for approximately 70-80% of urinary stones [10, 11]. Calcium oxalate stones are usually small, rough, hard, yellow-brown-gray colored stones with spiny protrusions and are the most abundant, most difficult to treat and most difficult to understand among calcium oxalate crystals [10-12]. Two main steps in stone formation are clearly distinguished. The first is the formation of a nucleus by a number of particles in the solid phase retained in the kidney, and the second is the development of a kidney stone as a result of the continuous deposition of CaOx on the nucleus. Under these conditions, molecules that prevent crystal growth (inhibitors) significantly reduce the formation of nuclei [13, 14]. Preventing the formation and enlargement of calcium oxalate monohydrate (COM) crystals, or the transformation of COM nuclei into calcium oxalate dihydrate (COD) crystals which are less stable, is effective in stopping the formation of kidney stones [15]. In many previous studies it has been determined that

\* To whom all correspondence should be sent:  
E-mail: [ekyol@yildiz.edu.tr](mailto:ekyol@yildiz.edu.tr)

the crystals in the COD structures can be readily eliminated from the body by urine [16]. Although there are now effective treatments that can eliminate the vast majority of kidney stones, this issue persists and impacts on a significant number of individuals. For this reason, many studies have been conducted to prevent the formation of calcium oxalate stones and to elucidate the impact of various additives on calcium oxalate crystallization. In this context, plants attract attention as natural additives [17, 18].

Plants, algae and fungi have been used as medicines for the treatment of various diseases throughout human history [19]. The use of plants for relief and treatment of various diseases dates back to ancient times [20]. Especially in recent years, the clinically proven immunomodulatory, adaptogenic and antimutagenic properties of plants and herbal medicines have led to an increased interest in herbal medicines among people [21]. Plants, on the other hand, are considered to be very safe with little or no toxic properties. Their costs are low and they are readily available [6]. All these reasons have increased the popularity of herbal medicines in recent years [21].

In the preparation of herbal medicines, various parts of plants, even whole plant, root, leaf, stem are used, while tablets, powders, boiling of fresh or dry parts and extracts are the most common methods [20]. Cherry is a plant belonging to the genus *Prunus* of the *Rosaceae* family whose Latin name is *Prunus Avium*. In addition to its rich mineral content, it contains high amounts of vitamins A, B group, C and anthocyanin, which show antioxidant properties [22]. The skin and stem of cherries are a natural source of biogenic substances and antioxidants [23]. Dried cherry stem has a unique simple chemical structure and excellent biochemistry. It has an uncomplicated, regular and distinct cellulosic structure. The low and independent content of active substances makes cherry stem a powerful therapeutic herb. Dried cherry stem facilitates both circulation and removal of toxins from the body. Apart from these, it is effective against prostate hyperthyroidism causing residual urine and difficulty in urination caused by bladder neck obstruction [24]. The stems of the cherry fruit are sold as herbal medicine in Iran and are used against kidney stones, edema and hypertension. Due to the high flavonoid and potassium content of cherry stems, they have a mild diuretic effect and can be used in the treatment of kidney stones, reported in Iranian Traditional Medicine documents [24-26].

For all these reasons, calcium oxalate crystallization has been an important topic of interest to researchers in biomineralization. In this study, the

effects of cherry stem as a natural additive to calcium oxalate crystallization, which is very important in terms of biomineralization, were investigated.

## MATERIALS AND METHODS

### Materials

Calcium chloride ( $\text{CaCl}_2 \cdot 2\text{H}_2\text{O}$ ) and sodium oxalate ( $\text{Na}_2\text{C}_2\text{O}_4$ ) obtained from J. T. Baker were used in the experiments. Dried cherry stalks were used as natural additives. 0.2  $\mu\text{m}$  polyamide filter paper was used for filtration. Plant extracts were frozen and stored. They were thawed and used immediately before the experiments.

### Methods

Spontaneous crystallization method was used in this study to evaluate the effect of cherry stem extract on calcium oxalate monohydrate crystallization process. First of all, 10 g of cherry stem used as a natural additive was heated at 100 °C for 15 min. Then, the solution obtained was filtered through 0.2  $\mu\text{m}$  polyamide filter paper and extracted to obtain cherry stem extract. The plant extracts obtained were frozen and stored. They were thawed immediately before the experiments.

Crystallization experiments were initiated by mixing equal molarities of  $\text{CaCl}_2$  and  $\text{Na}_2\text{C}_2\text{O}_4$  solutions. An automatic temperature-controlled water bath was used to keep constant temperature of the 1 L double walled glass reactor used in the experiments. During the reaction, the temperature was kept constant at  $37 \pm 0.1^\circ\text{C}$  based on human body temperature. Stirring throughout the reaction was achieved with a magnetic stirrer.

During the experiments, conductivity, temperature and pH values were recorded using a computer with the "Multi-Lab pilot" program. Using the data obtained, conductivity vs. time graphs were plotted without and with additives. The experiments were repeated three times for consistency of the results.

The crystallization rate obtained without additives was defined as ( $R_0$ ) and the crystallization rate obtained with additives was defined as ( $R$ ) and the  $R_0/R$  ratios were calculated by finding the slope values from the graphs drawn.

Each of the experiments was carried out for 6 h. At the end of the 6<sup>th</sup> h, the crystals formed in the solution were filtered through a 0.2  $\mu\text{m}$  polyamide membrane filter. The crystals were washed with distilled water to remove the saturated solution. The obtained samples were dried in a 60°C vacuum oven for 24 h and stored in a desiccator.

The morphology and size of the crystals obtained were examined by scanning electron microscopy (SEM) images.

## RESULTS AND DISCUSSION

### *Effect of the amount of cherry stem extract on the crystallization rate at constant initial supersaturation*

In order to investigate the effect of cherry stem extract on calcium oxalate crystallization, 2 series of experiments were performed for constant initial supersaturation experiments. The first series of experiments were carried out at concentrations of  $\text{CaCl}_2 \cdot 2\text{H}_2\text{O}$  and  $\text{Na}_2\text{C}_2\text{O}_4$  at  $3.25 \cdot 10^{-4}$  M and the second series of experiments at  $6.5 \cdot 10^{-4}$  M. 0.1 ml, 0.5 ml, 1 ml, 5 ml, 10 ml and 50 ml of cherry stem extract, respectively.

Conductivity vs. time graphs and the effect of cherry stem extract on the crystallization rate at  $3.25 \cdot 10^{-4}$  and  $6.5 \cdot 10^{-4}$  initial supersaturation are given in Figures 1 and 2, respectively. In the experiment with 0.1 ml of cherry stem extract, the delay time was 1 min, in the experiment with 0.5 ml of cherry stem extract the delay time was 1.5 min, in the experiment with 1 ml and 5 ml of cherry stem

extract the delay time was 2 min. In the experiment with 10 ml of cherry stem extract, it was observed that the delay time was spread over almost the entire 6 h, and in the experiment with 50 ml of cherry stem extract, crystallization was completely stopped.

### *Effect of initial supersaturation on the crystallization rate*

In the experiments carried out to investigate the effect of initial supersaturation on the crystallization rate, the temperature and stirring conditions were not changed. In the experiments, 10 ml of cherry stem extract was used for easy observation of the results.  $\text{CaCl}_2 \cdot 2\text{H}_2\text{O}$  and  $\text{Na}_2\text{C}_2\text{O}_4$  starting solutions of  $3.5 \cdot 10^{-4}$  M,  $4.5 \cdot 10^{-4}$  M,  $5.5 \cdot 10^{-4}$  M and  $6.5 \cdot 10^{-4}$  M, respectively, were used. Conductivity vs. time graphs obtained as a result of the experiments are given in Figure 3.

When the initial supersaturation was increased in the experiments without additive, an increase was observed in the rate of crystallization. However, in the experiments with a constant cherry stem extract additive, it was observed that increasing the initial supersaturation reduced the inhibitory effect of the cherry stem extract on the crystallization rate.

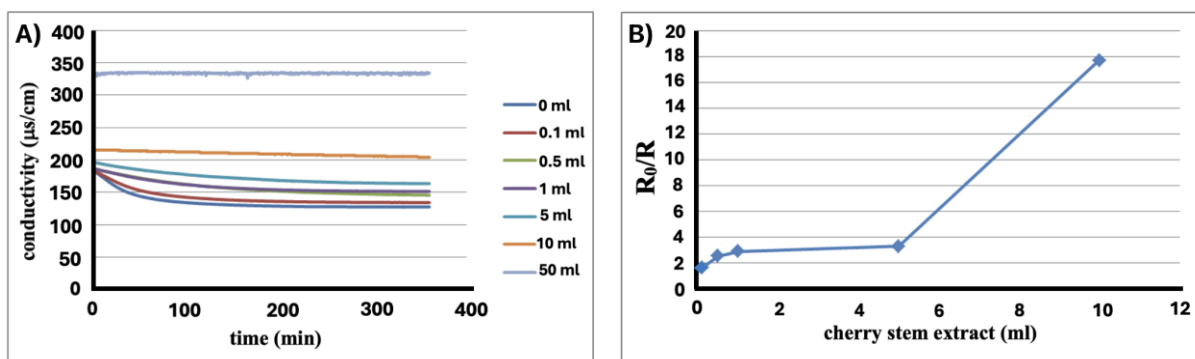


Figure 1. Graphs of conductivity vs. time (A) and  $R_0/R$ -cherry stem extract (B) at experiments at  $3.25 \cdot 10^{-4}$  M initial supersaturation

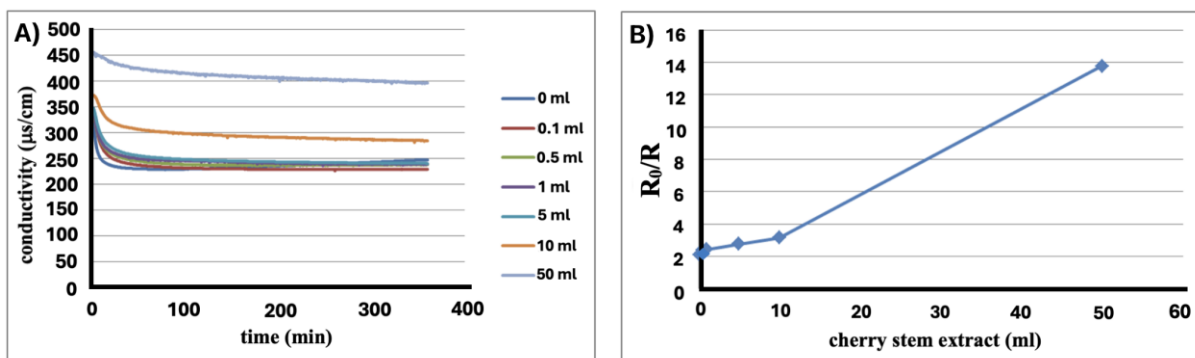
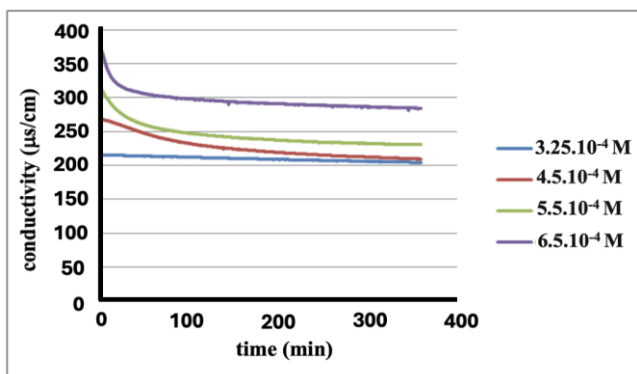


Figure 2. Graphs of conductivity vs. time (A) and  $R_0/R$ -cherry stem extract (B) at experiments at  $6.5 \cdot 10^{-4}$  M initial supersaturation



**Figure 3.** Conductivity vs. time graphs of experiments with 10 ml of cherry stem extract added to calcium oxalate solution at different initial supersaturations

*SEM analysis*

The crystals obtained as a result of the experiments with natural additives were photographed using scanning electron microscopy (SEM) to examine their morphology and size. Measurements were made by averaging between 50 and 150 crystal samples taken from different parts of the SEM photographs.

SEM images of the crystals obtained as a result of the experiments performed with 1 ml, 5 ml, 10 ml

and 50 ml cherry stem extract additives in order to observe the effect of cherry stem extract additive on crystal morphologies and sizes during the formation of calcium oxalate crystals at  $3.25 \cdot 10^{-4}$  M initial supersaturation, are given in Figure 4. The size and deviation of the crystals were calculated from these images and the calculated values are given in Table 1.

In the SEM images it is seen that the crystals obtained as a result of the experiments performed with 1 ml and 5 ml cherry stem extract additives are in COM structure. It is seen that some of the crystals obtained by increasing the additive amount to 10 ml started to form in COD structure and all of the crystals obtained after 50 ml additive amount were in COD structure. It is also seen in Table 1 that the crystal sizes decreased with the increase in cherry stem extract additive.

SEM images of the crystals obtained from the experiments performed with 1 ml, 5 ml and 50 ml cherry stem extract at  $6.5 \cdot 10^{-4}$  M initial supersaturation are given in Figure 5. The size and deviation of the crystals were calculated from these images and the calculated values are given in Table 2.

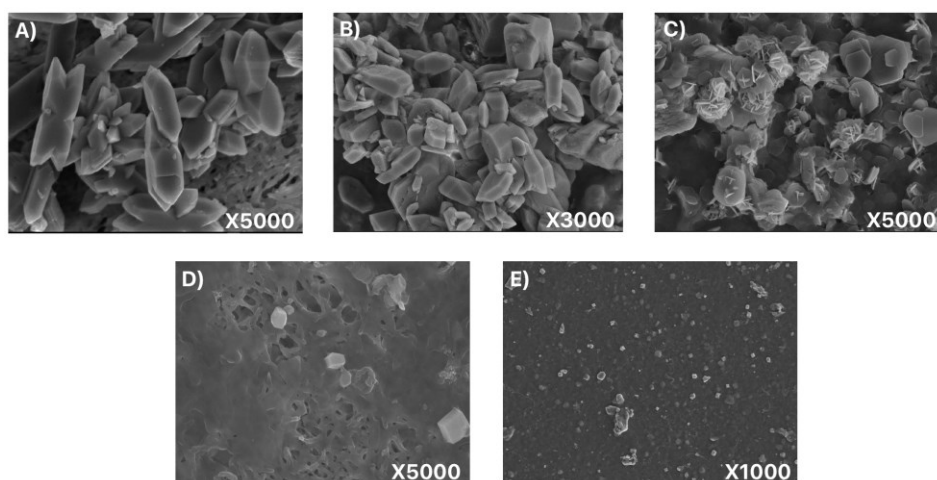


**Figure 4.** SEM images of the crystals obtained with 0 ml (A), 1 ml (B), 5 ml (C), 10 ml (D) and 50 ml (E) cherry stem extract additives at  $3.25 \cdot 10^{-4}$  M initial supersaturation

**Table 1.** Size values of calcium oxalate crystals obtained from crystallization experiments with different amounts of cherry stem extract at  $3.25 \cdot 10^{-4}$  M initial supersaturation

Cherry stem extract amount	COM		COD		
	Width( $\mu$ m)	Length( $\mu$ m)	Width( $\mu$ m)	Length( $\mu$ m)	Diagonal( $\mu$ m)
	$W_{av}$	$L_{av}$	$W_{av}$	$L_{av}$	$D_{av}$
1 ml	4.05( $\pm$ 1.1)	7.70( $\pm$ 2.04)	-	-	-
5 ml	2.50( $\pm$ 0.60)	3.15( $\pm$ 0.75)	-	-	-
10 ml	2.20( $\pm$ 0.29)	2.74( $\pm$ 0.56)	2.71( $\pm$ 0.82)	3.07( $\pm$ 0.70)	3.98( $\pm$ 1.16)
50 ml	-	-	2.63( $\pm$ 0.8)	2.75( $\pm$ 0.66)	3.42( $\pm$ 1.02)

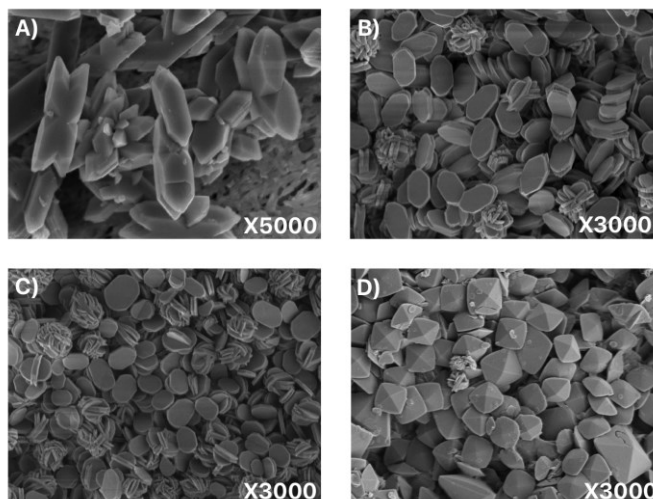


**Figure 5.** SEM images of the crystals obtained with 0 ml (A), 1 ml (B), 5 ml (C) and 50 ml (D) cherry stem extract additives at  $6.5 \cdot 10^{-4}$  M initial supersaturation

**Table 2.** Size values of calcium oxalate crystals obtained from crystallization experiments with different amounts of cherry stem extract at  $6.5 \cdot 10^{-4}$  M initial supersaturation

Cherry stem extract amount	COM		COD		
	Width( $\mu$ m)	Length( $\mu$ m)	Width( $\mu$ m)	Length( $\mu$ m)	Diagonal( $\mu$ m)
	$W_{av}$	$L_{av}$	$W_{av}$	$L_{av}$	$D_{av}$
1ml	5.00( $\pm$ 0.73)	9.43( $\pm$ 1.32)	-	-	-
5 ml	4.22( $\pm$ 0.89)	6.21( $\pm$ 1.07)	-	-	-
50ml	-	-	5.87( $\pm$ 1.95)	7.88( $\pm$ 2.85)	9.60( $\pm$ 2.53)

In the SEM images obtained it is observed that the structure of the crystals obtained from the experiments using 1 ml and 5 ml of additive is COM, while the structure of the crystals obtained in the experiment with 50 ml of additive is COD. In addition, as seen in Table 2, as the amount of additive increases, the size of the crystals decreases.

#### FT-IR analysis

FT-IR spectra of the crystals obtained by adding 0 ml and 50 ml of cherry stem extract at an initial supersaturation of  $6.5 \cdot 10^{-4}$  M are given in Figure 6.

In the first spectrum, peaks belonging to the O-H band are seen around  $3480 \text{ cm}^{-1} - 3000 \text{ cm}^{-1}$ . The peaks seen at  $1623 \text{ cm}^{-1}$ ,  $662 \text{ cm}^{-1}$  and  $599 \text{ cm}^{-1}$  belong to the H-O-H vibration. The peaks seen around  $1366 \text{ cm}^{-1}$  and  $1317 \text{ cm}^{-1}$  belong to the C-O bonds in the COM structure. In the second spectrum, the peaks belonging to the O-H band became widespread around  $3472 \text{ cm}^{-1} - 3250 \text{ cm}^{-1}$ . Peaks belonging to H-O-H are seen around  $1619 \text{ cm}^{-1}$  and  $614 \text{ cm}^{-1}$ . The peaks belonging to the C-O bond are seen at  $1325 \text{ cm}^{-1}$ . These characteristic changes between the spectra support that the first spectrum corresponds to the COM structure and the crystals turn into the COD structure in the second spectrum [27].

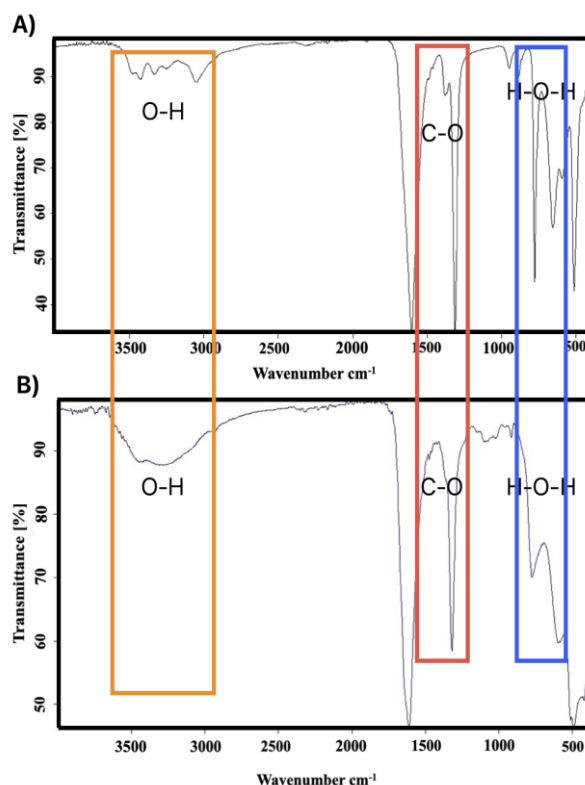


**Figure 6.** FT-IR spectra of crystals obtained by adding 0 ml (A) and 50 ml (B) of cherry stem extract at  $6.5 \cdot 10^{-4}$  M initial supersaturation

## CONCLUSION

In order to inhibit the crystal growth of calcium oxalate monohydrate, studies were carried out with cherry stalks in a laboratory environment under conditions similar to the human body and positive results were obtained from these studies. As a result of the experiments carried out using different ratios of natural additives at constant initial supersaturation, a decrease in crystal size was observed with increasing additive concentration. It was observed that the formation of COM crystals gradually decreased and COD crystals were formed as the additive concentration increased and the formation of COM crystals was completely prevented at high concentrations.

In the experiments performed with and without cherry stem extracts at different initial supersaturations, an increase in crystallization rate and size was observed with increasing initial supersaturation. It was observed that crystallization rates and crystal sizes were lower in the experiments with natural additives compared to the experiments without additives.

As a result of the studies, it was observed that cherry stem extract used in sufficient concentrations was successful in preventing calcium oxalate crystallization. The fact that the additives used are natural, is very important for biomineralization studies. The shrinking effect of the additives on CaOx crystals and the conversion to COD structure support the view that these natural additives may be useful in the treatment of kidney stone disease.

**Acknowledgement:** The current study was supported by Yildiz Technical University (Project No: 2012-07-01-YL05).

## REFERENCES

1. S. Atanassova, *J. Cryst. Growth*, **312**, 1940 (2010).
2. M.E: Salem, G. Eknayan, *Am. J. Nephrol.*, **19(2)**, 140 (1999).
3. J. Medetognon-Bemissan, S. Tardivel, C. Hennequin, M. Daudon, T. Drücke, B. Lacour, *Urol. Res.*, **27**, 69 (1999).
4. A. Nimavat, A. Trivedi, A. Yadav, P. Patel, *J. Pharm. Pharmacol.*, **10**, 195 (2022).
5. H. E. Garcia-Perdomo, P. B. Solarte, P. P. Espana, *Urol. Colomb.*, **25**, 118 (2016).
6. N. Sharma, B. S. Tanwer, R. Vijayvergia, *Int. J. Pharmtech. Res.*, **3(1)**, 110 (2011).
7. M. Akram, M. Idrees, *Int. J. Immunopathol. Pharmacol.*, **33**, (2019).
8. A. Y. Muslumanoglu, M. Binbay, E. Yuruk, T. Akman, A. Tepeler, T. Esen, A. H. Tefekli, *Urol. Res.*, **39**, 309 (2011).
9. E. S. Hyams, B. R. Matlaga, *Transl. Androl. Urol.*, **3(3)**, 278 (2014).
10. X. Y. Sun, M. Xu, J. M. O. *ACS Omega*, **2(9)**, 6039 (2017).
11. Y. Shen, W. Yue, A. Xie, Z. Lin, F. Huang, *Colloids and Surfaces A: Physicochem. Eng. Aspects*, **234**, 35 (2004).
12. J. Cloutier, L. Villa, O. Traxer, M. Daudon, *World J. Urol.*, **33(2)**, 157 (2015).
13. F. Tamborino, R. Cicchetti, M. Mascitti, G. Litterio, A. Orsini, S. Ferritti et al., *Int. J. Mol. Sci.*, **25(5)**, 3075 (2024).
14. A. Al-Dubai, E. Akyol, *Bulg. Chem. Commun.*, **55(3)**, 278 (2023).
15. T. Jung, W. Kim, C. K. Choi, C.K., *J. Cryst. Growth*, **279**, 154 (2005).
16. J. Yu, H. Tang, B. Cheng, *J. Colloid Interface Sci.*, **288**, 407 (2005).
17. I. Das, S. K. Gupta, S. A. Ansari, V. N. Pandey, R. P. Rastogi, *J. Cryst. Growth.*, **273**, 546 (2004).
18. E. Akyol, K. Ongun, S. Kirboga, M. Öner. *Biointerface Res Appl Chem*, **6**, 1064 (2016).
19. E. Yarnar. *World J. Urol.*, **20**, 285 (2002).
20. B. Ballabh, O. P. Chaurasia, Z. Ahmed, S. B. Singh, *J. Ethnopharmacol.*, **118(2)**, 331 (2008).
21. H. R. Chitme, S. Alok, S. K. Jain, M. Sabharwal, (2010). *Int. J. Pharm. Sci.*, **1(2)**, 24 (2010).
22. M. Petruzzello, *Encyclopedia Britannica*, 2024.
23. R. D. Cagno, R. F. Surico, G. Minervini, C. G. Rizzello, R. Lovino, M. Servili, A. Taticchi, S. Urbani, M. Gobbetti, *Food Microbiol.*, **28**, 900 (2011).
24. İ. A. Saracuglo, *Medicinal Plants and Herbal Health Guide*, Gun Ofset, Istanbul, 2009.
25. N. Hooman, F. Mojab, B. Nickavar, P. Pouryousefi-Kermani, *Pak. J. Pharm. Sci.*, **22(4)**, 381 (2009).
26. M. Rameshk, *Trad. Integr. Med.*, **9(1)**, 74 (2024).
27. M. Maruyama, K. P. Sawada, Y. Tanaka, A. Okada, K. Momma, M. Nakamura, R. Mori et al., *PLoS One*, **18(3)**, 1 (2023)

## Investigation of *in vitro* digestive process in optimization of ultrasound-assisted extraction with citric acid anhydride for antioxidant production from red beet, Swiss chard, and dragon fruit

E. G. Reis<sup>1\*</sup>, G. S. Pozan Soylu<sup>2</sup>

<sup>1</sup>Istanbul Arel University, Incubation and Entrepreneurship Application And Research Center, Istanbul Arel University, Buyukcekmece, 34537, Istanbul, Turkey

<sup>2</sup>Department of Chemical Engineering Faculty of Engineering, Istanbul University-Cerrahpasa, Avclar, 34320 Istanbul, Turkey

Received Mqy 19, 2024; Accepted: August 17, 2024

This study aims to investigate the *in vitro* digestive process for optimizing ultrasound-assisted extraction with citric acid anhydride. Extracts were obtained from red beet, dragon fruit and Swiss chard plants by using different parameters using citric acid anhydride with the Box-Behnken experimental design method. Optimum extraction conditions were determined by analyzing total antioxidant capacity, and total phenolic substance amount during the digestion stages. In the studies conducted with red beet, dragon fruit and Swiss chard, as a result of the optimization made with the Box Behnken method using ultrasound extraction, 52.59 °C, 48.66 min, 1:5 substance-solvent ratio, 2.11% citric acid anhydride ratio were determined as the most optimum conditions. The best results were obtained for red beet as the undigested stage showed values of 865.03±6.18 mg TE/100 g dw for DPPH, 421.28±3.45 mg TE/100 g dw for ABTS, and 170.03±6.18 mg GAE/100 g for total phenolic content. During the stomach digestion stage, the values were 770.61±0.64 mg TE/100 g dw for DPPH, 215.58±0.87 mg TE/100 g dw for ABTS, and 121.61±0.64 mg GAE/100 g for total phenolic content. In the intestine digestion stage, the values were 732.51±3.40 mg TE/100 g dw for DPPH, 153.09±5.33 mg TE/100 g dw for ABTS, and 96.51±3.65 mg GAE/100 g for total phenolic content.

**Keywords:** Phenolic content, digestion, bioavailability, antioxidant, extraction

### INTRODUCTION

The incorporation of antioxidant-rich foods into one's diet can effectively support overall health and well-being. *In vitro* studies examining the digestive process and extraction techniques have further illuminated the potential of betalains, specifically in red beet, Swiss chard, and dragon fruit, for antioxidant production [1]. Optimization techniques, such as the Box-Behnken experimental design method, have been shown to enhance the antioxidant properties of betalain-rich plant extracts, further underlining the significance of these compounds [2]. By incorporating a variety of antioxidant-rich foods into their diet, individuals can ensure obtaining a wide range of antioxidants and reap associated health benefits. Betalains, with their antioxidant properties, have been of particular interest due to their potential health benefits and significant role in combating oxidative stress [3].

Studies on the extraction, processing, and stability of betalains are crucial for preserving and enhancing their antioxidant properties. as discussed the perspectives on the extraction, processing, and potential health benefits of red beet root betalains,

emphasizing the importance of these natural pigments in plant roots [4] demonstrated that ultrasonic-assisted extraction of betalains from red beet yielded extracts with higher betalain and total phenolic contents, enhancing their antioxidant activity [5]. Understanding the behavior of antioxidants during digestion is crucial for optimizing their bioavailability and health benefits, studying the effects of *in vitro* gastrointestinal digestion on the antioxidant capacity and anthocyanin content of cornelian cherry fruit extract, highlighting the importance of digestion in preserving antioxidant properties [6]. Research on the effects of different encapsulation agents and drying processes on the stability of betalains extract emphasized the potential use of betalains from red beet plants as natural colorants [7]. Furthermore, the study of prickly pear peel flour as a bioactive and functional ingredient rich in polyphenols and betalain compounds, showcasing the diverse sources of antioxidants in plant-based foods [8].

The use of ultrasound-assisted extraction has been shown to be effective in extracting bioactive

\* To whom all correspondence should be sent:

E-mail: elifgungorreis@arel.edu.tr

compounds from various plant sources, as demonstrated in studies such as the extraction of quinoa protein [9]. The antioxidant potential of the extracted compounds is crucial, as antioxidants play a vital role in health and nutrition. Studies on the high dopamine content in Cavendish bananas and the evaluation of antioxidative potency highlight the importance of assessing the antioxidant capacity of the extracted compounds [10]. Furthermore, the identification of betalains in Swiss chard and other sources provides insights into the potential sources of antioxidants beyond traditional sources like red beets [11].

Studies have shown that betalains are crucial compounds responsible for the antioxidant properties of red beet and dragon fruit [12]. The utilization of the Box-Behnken experimental design method for optimizing ultrasound-assisted extraction with citric acid anhydride can play a pivotal role in maintaining the integrity of betalains and improving the antioxidant potential of the extracts [13]. By exploring the impact of extraction parameters such as temperature, extraction time, substance-solvent ratio, and citric acid anhydride ratio, researchers can gain valuable insights into maximizing the benefits of betalain-rich sources like red beet and dragon fruit [14]. Studies on the impact of *in vitro* digestion on the antioxidant capacity of various plant extracts emphasize the need to investigate how extraction parameters influence the preservation of bioactive compounds [15]. Studies have shown that betalains, present in red beet and dragon fruit, significantly contribute to the antioxidant capacity of these fruits [16]. The high antioxidant capacity of beet root juice, attributed to its betalains and other nutritional components, underscores the potential benefits of optimizing extraction methods for antioxidant-rich sources [17]. By utilizing the Box-Behnken experimental design method to optimize ultrasound-assisted extraction, researchers can determine the most suitable conditions for extraction, which can impact the preservation of betalains and other antioxidant compounds [18]. This optimization process can lead to enhanced antioxidant properties in the extracts, aligning with the findings that betalains are valuable dietary antioxidants [19]. Exploring the impact of extraction parameters such as temperature, extraction time, and citric acid anhydride ratio on betalain content and antioxidant capacity can provide crucial insights into maximizing the benefits of red beet, Swiss chard, and dragon fruit [20]. Researches have shown that betalains can be extracted using different methods such as ultrasound-assisted extraction, high-pressure carbon

dioxide extraction, and supercritical fluid extraction [4, 21]. These techniques have been effective in isolating betalains from plant sources like beets and cactus pears [22, 23]. Additionally, the choice of solvents for extraction, such as water, methanol, ethanol-water mixtures, and ethyl acetate, can impact the extraction efficiency of betalains [24]. Aqueous methanol (50-80%) has been highlighted as a suitable solvent for betalain extraction [25], and a range of 20%-50% v/v methanol or ethanol has been recommended for complete extraction of betalains [26]. Additionally, the study done by Zin and co-workers found that acidifying the extraction medium can help handle the biosynthesis reaction of compounds present in the matrix, thereby aiding in the extraction of betalains without the use of alcohol [26]. Acidified extraction media adjusted to pH 3.5 using ascorbic acid have been shown to enhance the yield of betanin, a type of betalain, to the highest levels [27]. Studies have demonstrated that betalains exhibit strong antioxidant activity, and the addition of ascorbic acid can further enhance this property which the combination of citric acid and ascorbic acid in the extraction process may help preserve the bioactive properties of betalains, making them suitable for various applications in food and medicine [28]. Furthermore, the use of innovative extraction techniques, such as ultrasound-assisted extraction, in combination with citric acid and ascorbic acid, can improve the efficiency of betalain extraction. Ultrasound-assisted extraction has been shown to be more efficient than conventional methods, and the addition of citric acid and ascorbic acid can potentially enhance the extraction process [23]. Additionally, understanding the mechanisms underlying the breakdown of betalains during digestion stages is essential for developing strategies to improve their stability and bioavailability [29]. For the red beet, ABTS values ranged from 20.5 to 45.7 mmol Trolox equivalents per 100 g fresh weight, as reported by Dudonné and co-workers in their study conducted in 2009 [30]. In the same study for Swiss chard extract, ABTS values ranged from 12.3 to 28.6 mmol Trolox equivalents per 100 g fresh weight [30]. ABTS results for dragon fruit indicated antioxidant activity levels between 15.8 and 32.4 mmol Trolox equivalents per 100 g fresh weight [30]. For the extraction of red beet, DPPH assay results indicated IC<sub>50</sub> values ranging from 12.4 to 28.9 µg/mL [31]. In a study by Arsul and co-workers, it was found that the DPPH IC<sub>50</sub> values of the Swiss chard extracts ranged between 8.7 and 21.5 µg/mL, indicating their antioxidant potential [31]. A study by Kim and co-workers, demonstrated DPPH IC<sub>50</sub> values of dragon fruit extracts ranging

from 10.2 to 25.6 µg/mL, indicating strong antioxidant activity [32]. CUPRAC values of the red beet extracts ranged from 18.6 to 36.4 mmol Trolox equivalents per 100 g fresh weight, as reported by Arsul and co-workers [31]. Recent studies have demonstrated CUPRAC values ranging from 10.7 to 25.9 mmol Trolox equivalents per 100 g fresh weight of Swiss chard extracts [31]. According to a study by Korstjens & Moser, *in vitro* digestion of red beet extracts resulted in a 30% increase in the release of phenolic compounds and a corresponding 25% increase in antioxidant activity post-digestion [33]. During the *in vitro* digestion process, researchers observed a 20% decrease in antioxidant activity in Swiss chard extracts [34]. Results from studies on betalains and antioxidant properties can provide valuable insights into the potential benefits of red beet, Swiss chard, and dragon fruit extracts. Additionally, red beet extracts were found to have three to eight times higher total betalain content compared to golden beet extracts [35]. Furthermore, the absorption maxima of betalains from red dragon fruit peel and flesh were reported around 537 and 537.5 nm, respectively [36]. In terms of betalain content, *Opuntia stricta* was found to have approximately five times higher betalain content compared to *Opuntia ficus-indica* and even higher content than red beet [37]. Moreover, the betalain/tyrosine molar ratios in red beet genotypes were reported to range between 43 and 104, while in yellow beet genotypes, the ratios were between 0.1 and 8.2 [38]. This indicates significant variations in betalain content between different genotypes of beets.

Distinguished from previous studies, this research uniquely explores the bioavailability of phenolic compounds through both stomach and intestinal digestion phases with a refined focus on the impact of extraction methods. The innovative use of ultrasound-assisted extraction with citric acid anhydride, tailored for each specific fruit type, represents a significant departure from typical extraction methodologies. The primary aim of this research is to optimize the extraction process of antioxidants from fruits, enhancing bioavailability across different stages of digestion. These endeavors not only underscore the study's novelty but also its potential practical applications, proposing a pathway for advancing efficiency in natural antioxidant extraction and sustainable utilization of food waste. Therefore, the pursuits of this research offer a valuable enhancement to the existing compendium of knowledge within the field of food science and technology.

## MATERIALS AND METHODS

### *Plant material*

Fresh red beets, dragon fruit, and Swiss chard were obtained from a local market (MIGROS). The samples were washed, the red beets were peeled, and all the ingredients were cut into small pieces before being stored at -20°C for further analysis. Citric acid anhydride was obtained from Cagdas Chemical Company.

### *Ultrasound-assisted extraction*

The ultrasound-assisted extraction involved mixing 5 g of plant material with a citric acid anhydride solution at a predetermined ratio. The mixture was then subjected to ultrasonic treatment at a specific temperature for a designated period of time. After extraction, the solution was centrifuged and the supernatant collected for further analysis. In this study, variable parameters included temperatures ranging from 35°C to 70°C, times ranging from 15 min to 45 min, raw material-solvent ratios of 1:5 and 1:30, as well as citric acid anhydride solution concentrations of 0.5% to 1%. The samples used were prepared in the form of cubes measuring 10mm × 10mm × 5mm.

### *Box-Behnken experimental design*

The Box-Behnken experimental design method was used to find the best conditions for ultrasound-assisted extraction. Factors including temperature, extraction time, substance-solvent ratio, and citric acid anhydride ratio were changed at three levels, and a total of 27 experiments were conducted according to the design.

Box-Behnken design is a surface response methodology used as an experimental design model. In the Box-Behnken model, the following formula is used depending on the variables [39]:

$$N = 2k(k-1) + C_0 \quad (1)$$

where N is number of experiments; k is number of variables; C<sub>0</sub> is number of central points.

### *In vitro digestion*

The *in vitro* digestion of extracted samples involves simulating the human gastrointestinal tract, including stages for undigested, stomach digestion, and small intestine digestion phases. This allows studying the impact of digestion on antioxidant capacity and total phenolic substance amount of the extracts [40]. Evaluating how the process affects stability, bioavailability, and potential health benefits of bioactive compounds is possible through this method. Alterations in the polyphenolic profile have been observed during the digestion process.

The study followed the protocol developed by Minekus *et al.* [41] for *in vitro* gastrointestinal simulation.

The protocol outlined specific steps for each phase of digestion. For the oral digestion simulation, an emulsion (5 mL) was combined with saliva water (4 mL), 0.3 mol/L CaCl<sub>2</sub> (25 µL), and distilled water (975 µL). The mixture was then incubated at 37 °C for two h in a shaking water bath. Moving on to the gastric digestion simulation, gastric juice (7.5 mL), pepsin (1.6 mL), and CaCl<sub>2</sub> (5 µL) were added to the solution, followed by adjusting the pH to 3.0 using 1 mol/L HCl, and making volume adjustments with pure water before incubating at 37 °C for additional two h. The stomach mixture was then combined with 8.25 mL of intestinal juice, 3.75 mL of pancreatin, 1.875 mL of bile, and 30 µL of CaCl<sub>2</sub>. Subsequently, the pH was adjusted to 7.0 using NaOH, and the total volume was made up to 30 mL with distilled water before incubating the mixture at 37 °C for two h in a shaking water bath.

#### *Analysis of antioxidant capacity and phenolic substance amount*

The antioxidant capacity of the extracts was determined using DPPH and ABTS assays. The total phenolic substance amount was quantified using the Folin-Ciocalteu method. Both analyses were performed at each digestion stage to assess the variations in antioxidant properties and phenolic substance content.

The amount of phenolic substances was determined by applying the method developed by Vitali [42]. In the method, a Folin-Ciocalteu solution was used and spectrophotometric measurement at 750 nm wavelength was made. In the analysis, a Lowry A solution and a Lowry B solution were prepared. Lowry A solution: 2% Na<sub>2</sub>CO<sub>3</sub> in 0.1 mol/L NaOH. Lowry B solution; 0.5% CuSO<sub>4</sub> in 1% NaKC<sub>4</sub>H<sub>4</sub>O<sub>6</sub>. Lowry A and Lowry B solutions were mixed in a ratio of 50:1 (v/v) and Lowry C solution was created. The DPPH free radical analysis is based on the reduction principle, where antioxidants interact with the stable DPPH radical, leading to its conversion into 1,1-diphenyl-2-picryl hydrazine, a non-radical form. This reaction allows for the assessment of the antioxidant capacity of compounds by measuring the decrease in absorbance at 517 nm after a specified incubation period, typically 30 min [43].

## RESULTS AND DISCUSSION

The study yielded significant results in understanding the impact of digestion on the

extraction process and the subsequent effects on antioxidant production from natural sources. The *in vitro* digestion stages, including stomach digestion and small intestine digestion, were found to have a substantial influence on the antioxidant capacity and total phenolic substance amount of the extracts.

#### *Antioxidant capacity and phenolic substance amount*

The analysis of the extracts at each digestion stage revealed variations in the antioxidant properties and phenolic substance content. The use of DPPH and ABTS assays provided insights into the differences in the antioxidant capacity of the enzymatic hydrolysates or crude solvent extracts. Additionally, the quantification of total phenolic substance amount using the Folin-Ciocalteu method allowed for a comprehensive understanding of the phenolic content throughout the digestion process. Table 1 shows the total phenolic compounds and total antioxidant values in ultrasound-assisted extraction of red beet sample.

#### *Optimization of ultrasound-assisted extraction*

The results supported the hypothesis that optimizing ultrasound-assisted extraction with citric acid anhydride for antioxidant production requires specific considerations for each digestion stage. As shown in Table 2, ultrasonic extraction experiment model is designed with Box-Behnken result optimization, experiment 13 which is thought to have the most suitable conditions: 52.59°C, 48.66 min, 1:5.02 solids/solvent, 2.11% concentration - 178.64 mg/L gallic acid, ABTS: 623.33 mg TE/100 g dw. DPPH: 914.02 mg TE/100 g dw. Within these conditions dragon fruit and Swiss chard were also extracted. Samples were stored in 1.5 mL Eppendorf tubes and frozen at -18 °C.

Table 3 shows the antioxidant activity (DPPH and ABTS) of the extracts in the stomach and intestinal phases of the *in vitro* gastrointestinal simulation under the optimized conditions. The antioxidant potency of extracts derived from dragon fruit and Swiss chard was rigorously evaluated. As delineated in Table 3, the antioxidant activities measured *via* DPPH and ABTS assays of these extracts were assessed at both stomach and intestinal stages of the simulated gastrointestinal digestion.

Complementary research by Donlao [44] corroborates the results establishing that *in vitro* digestion radically diminishes antioxidant activity in complete tea infusions. Table 1 shows the total phenolic compound results in the digestive stages of red beet, dragon fruit, swiss chard and their extracts.

**Table 2.** Total phenolic compounds and total antioxidant values in ultrasound-assisted extraction of red beet samples

Sample	Temperature (°C)	Time (min)	Citric acid amount (g)	Citric acid concentration (%)	Gallic acid (mg/L)	ABTS (mg TE/ 100 g dw)	DPPH (mg TE/ 100 g dw)
x-17	50	10	75	2.5	22.9	73.87	612.54
x-21	50	50	25	1.5	153.9	581.26	865.09
x-22	70	50	75	1.5	98.9	344.11	771.13
x-18	50	10	125	1.5	2.9	42.83	568.15
x-13	50	30	75	1.5	38.9	135.65	696.58
x-1	30	50	75	1.5	92.9	259.49	806.9
x-7	50	50	75	2.5	107.9	276.47	785.36
x-2	30	30	125	1.5	10.9	48.4	650.89
x-15	50	30	75	1.5	15.9	72.99	612.11
x-11	50	30	25	0.5	87.9	254.52	802.59
x-3	30	30	25	1.5	117.9	411.45	862.5
x-8	50	50	125	1.5	24.9	91.73	662.53
x-12	50	30	25	2.5	106.9	345.28	822.42
x-23	70	30	25	1.5	169.9	582.43	860.78
x-24	70	30	125	1.5	37.9	94.36	609.52
x-19	50	10	25	1.5	51.9	190.1	698.3
x-14	50	30	125	0.5	25.9	101.1	653.05
x-10	50	30	75	1.5	59.9	215.58	730.19
x-25	70	30	75	0.5	32.9	83.53	606.93
x-4	30	30	75	2.5	36.9	119.54	697.87
x-5	30	10	75	1.5	18.9	66.55	647.01
x-16	50	30	125	2.5	24.9	75.33	620.73
x-26	70	10	75	1.5	46.9	173.42	668.13
x-6	30	30	75	0.5	23.9	65.09	638.83
x-20	50	10	75	0.5	51.9	132.43	652.62
x-9	50	50	75	0.5	60.9	139.75	710.37
x-27	70	30	75	2.5	42.9	135.65	647.88

**Table 3.** Ultrasound-assisted extraction experiment model design with Box-Behnken result optimization

Sample	Temperature (°C)	Time (min)	Citric acid amount (g)	Citric acid concentration (%)	Gallic acid (mg/L)	ABTS (mg TE/ 100 g dw)	DPPH (mg TE/ 100 g dw)	Desired value
1	63.04	49	5.25	2.47	199.41	677.39	907.88	1
2	37.2	49.84	5.04	2.18	176.89	601.26	929.43	1
3	69.33	42.92	5.23	1.91	175.20	621.98	870.76	1
4	45.75	49.81	5.62	2.33	176.93	599.15	915.35	1
5	68.29	49.31	5.25	1.08	177.91	609.63	868.73	1
6	30.81	49.84	5.52	2.35	176.74	582.64	926.13	1
7	65.73	49.64	7.79	2.49	179.44	589.36	866.63	1
8	30.26	49.94	5.29	2.17	175.57	586.75	929.44	1
9	69.34	48.47	5.34	1.48	185.43	649.54	882.16	1
10	51.39	48.82	5.98	2.45	175.58	590.49	900.86	1
11	42.91	49.86	5.12	1.92	171.42	594.90	920.40	1
12	58.2	48.64	5.12	1.53	171.05	603.22	894.94	1
13	52.59	48.66	5.02	2.11	178.64	623.33	914.02	1
14	58.09	45.09	5.07	2.36	174.82	606.63	893.16	1
15	68.61	48.58	5.88	1.88	187.21	653.89	885.39	1
16	54.32	49.52	6.57	2.43	174.64	585.22	892.82	1
17	36.99	49.31	5.44	2.32	173.79	582.79	921.01	1
18	32.92	49.8	5.09	1.97	171.55	583.72	927.47	1
19	69.77	49.97	7.82	2.46	187.46	615.60	865.53	1
20	60.07	49.78	5.11	2.06	190.39	664.59	912.90	1
21	61.48	49.03	5.28	1.36	171.37	599.80	884.93	1

**Table 4.** Continued

22	69.99	40.61	5	2.5	179.69	620.89	862.31	0.996
23	67.71	50	5	0.84	176.35	590.46	861.81	0.996
24	30	50	5.83	1.89	163.62	551.21	915.28	0.967
25	70	37.12	5	2.22	162.69	578.78	846.91	0.962
26	30	50	5	1.13	153.95	508.51	900.45	0.920
27	70	35.43	5	0.66	141.05	453.29	806.37	0.796
28	30	32.8	5	1.44	108.39	371.89	847.32	0.712
29	30	20.31	5	0.86	83.89	241.98	791.89	0.512
30	30	12.33	5	0.77	77.26	197.74	765.90	0.439

**Table 5.** Total antioxidant compound results in the digestive stages of red beet, dragon fruit, swiss chard and their extracts obtained by ultrasonic assisted extraction

Sample name	Without digestion mg TE/100 g dw		Gastric phase mgTE/100 g dw		Intestine phase mg TE/100 g dw	
	DPPH		DPPH		DPPH	
Dragon fruit	DPPH	690.38±5.98	DPPH	626.23±6.16	DPPH	582.23±1.25
	ABTS	120.65±1.70	ABTS	116.28±2.98	ABTS	81.56±2.28
Dragon fruit extract	DPPH	590.22±5.44	DPPH	546.21±3.61	DPPH	472.67±1.21
	ABTS	100.87±3.00	ABTS	92.85±2.22	ABTS	80.54±2.42
Swiss chard	DPPH	682.97±3.20	DPPH	652.45±4.26	DPPH	572.13±3.25
	ABTS	162.11±5.33	ABTS	156.62±5.67	ABTS	121.56±8.29
Swiss chard extract	DPPH	524.62±1.11	DPPH	454.85±2.69	DPPH	372.85±3.32
	ABTS	114.16±4.20	ABTS	106.39±3.63	ABTS	91.21±4.21
Red beet	DPPH	963.01±17.31	DPPH	738.18±6.48	DPPH	706.66±19.33
	ABTS	616.90±11.22	ABTS	319.25±6.55	ABTS	276.69±2.09
Red beet extract	DPPH	865.03±6.18	DPPH	770.61±0.64	DPPH	732.51±3.40
	ABTS	421.28±3.45	ABTS	215.58±0.87	ABTS	153.09±5.33

**Table 6.** Total phenolic compound results in the digestive stages of red beet, dragon fruit, swiss chard and their extracts obtained by ultrasound-assisted extraction

Sample	Without digestion (mg GAE/100 g)	Gastric phase TFB (mg GAE/100 g)	Intestine phase TFB (mg GAE/100 g)
Dragon fruit	231.67±2.82	105.15±5.73	97.88±2.11
Dragon fruit extract	191.13±2.99	112.44±3.23	92.29±4.82
Swiss chard	243.21±2.86	102.12±5.53	96.11±1.26
Swiss chard extract	122.23±3.42	98.18±1.87	68.61±2.71
Red beet	250.01±17.31	127.18±6.48	94.66±6.33
Red beet extract	170.03±6.18	121.61±0.64	96.51±3.65

Our investigation into the phenolic content of various fruit samples, both raw and extracted, revealed significant retention of these compounds throughout digestive processes. Specifically, phenolic retention in the stomach and intestine was as follows: dragon fruit at 45.39% and 42.25%; dragon fruit extract at 58.83% and 48.29%; Swiss chard at 41.99% and 39.52%; Swiss chard extract at 63.96% and 56.13%. Strikingly, the red beet extract sample exhibited an impressive 72% and 57% phenolic content retention in the stomach and intestine, respectively.

Raw dragon fruit maintains a consistent phenolic content of 45.39% through digestive stages,

suggesting its potential bioavailability. In comparison, the dragon fruit extract content decreases from 58.83% in the stomach to 48.29% in the intestine, indicating good bioavailability in the stomach with some reduction during the intestinal phase.

Red beets show a decrease in phenolic substances from 50% in the stomach to 38% in the intestine, indicating some loss and potentially reduced bioavailability, especially during the intestinal phase.

Swiss chard shows a consistently high phenolic content of 57.89% through the stomach and intestine, implying favorable stability and high

bioavailability potential. The Swiss chard extract has a slight reduction in phenolic substances from 62.5% in the stomach to 57.02% in the intestine, indicating moderate stability and bioavailability.

The Swiss chard extract maintains its phenolic content at 57.59% through both stomach and intestine stages, suggesting good stability and potential for high bioavailability. The raw Swiss chard's phenolic content remains stable at 41.99% in both digestive stages, suggesting consistent bioavailability throughout digestion. The Swiss chard extract, however, presented high stability and possible bioavailability considering its increased phenolic retention of 63.96% in the stomach and 56.13% in the intestine.

This study highlights the potential of utilizing fruit residues as a source of natural antioxidants [45] It also emphasizes the importance of optimizing extraction conditions and considering the effects of digestion in order to maximize antioxidant production. The practical implications of this study are significant, highlighting the value of fruit residues as reservoirs of natural antioxidants and stressing the importance of fine-tuning extraction conditions *in tandem* with the digestive impact to magnify antioxidant yield.

The results of the *in vitro* digestion stages, particularly the stomach digestion and small intestine digestion, shed light on the influence of digestive processes on the antioxidant capacity and total phenolic substance amount of the extracts. This understanding is significant in assessing the stability of bioactive compounds during digestion, highlighting the need for tailored extraction approaches to maximize antioxidant production in different fruits.

Furthermore, the analysis of antioxidant capacity using DPPH and ABTS assays, along with the quantification of total phenolic substance amount utilizing the Folin-Ciocalteu method at each digestion stage, revealed notable variations in the antioxidant properties and phenolic substance content. These findings emphasize the dynamic nature of antioxidant production throughout the digestion process and stress the importance of considering the effects of digestion in extraction optimization.

The statistical analysis provided crucial insights into the effects of extraction parameters and digestion stages on the antioxidant capacity and phenolic substance amount of the extracts. These analyses underscore the significance of the factors and their interactions in influencing the production of antioxidants from natural sources, adding depth to the understanding of the complex relationship

between extraction processes, digestion stages, and antioxidant production.

The findings of this study align with previous research that highlights the potential of fruit residues as a rich source of natural antioxidants.

## CONCLUSION

In conclusion, this study has provided essential insights into the optimization of ultrasound-assisted extraction with citric acid anhydride for antioxidant production from fruit extracts. The findings underscore the dynamic nature of antioxidant production and emphasize the necessity of considering the effects of digestion on extraction processes. Additionally, the importance of tailored approaches for each digestion stage has been highlighted to maximize the antioxidant yield from natural sources.

The future directions of this research involve exploring the mechanism of reaction between phytochemicals and different radicals, as well as determining the optimal conditions for ultrasound-assisted extraction with citric acid anhydride for different fruits. It is imperative to conduct further studies to evaluate the antioxidant capacities and phenolic content of various fruit extracts to identify potent sources of natural antioxidants for different industries.

In summary, the results obtained from this study provide a solid foundation for the development of more efficient methods for extracting antioxidants from fruit residues, thereby contributing to the sustainable utilization of food waste and the advancement of natural sources of antioxidants. Furthermore, the integration of natural antioxidants into various food products and packaging materials can provide consumers with healthier alternatives while maintaining oxidative stability and sensory acceptance.

**Acknowledgement:** The authors would like to sincerely express their thanks to the Scientific Research Projects (BAP) Coordination Unit of Istanbul University-Cerrahpaşa for supporting the project under project no/ID: 37224.

## REFERENCES

1. M. I. Khan, *Compr. Rev. Food Sci. Food Saf.*, **15**, 316 (2016).
2. M. Herrero, L. Jaime, P. J. Martín-Álvarez, A. Cifuentes, E. Ibáñez, *J. Agric. Food Chem.*, **54**, 5597 (2006).
3. Q. Hua, Q. Zhou, S. Gan, J. Wu, C. Chen, J. Li, Y. Ye, J. Zhao, G. Hu, Y. Qin, *Int. J. Mol. Sci.*, **17**, 1606 (2016).
4. Y. Fu, J. Shi, S. Y. Xie, T. Y. Zhang, O. P. Soladoye, R. E. Aluko, *J. Agric. Food Chem.*, **68**, 11595 (2020).

5. H. Righi Pessoa da Silva, C. da Silva, B.C. Bolanho, *J. Food Process Eng.*, **41**, e12833 (2018).
6. L. David, V. Danciu, B. Moldovan, A. Filip, *Antioxidants*, **8**, 114 (2019).
7. K. Ravichandran, R. Palaniraj, N.M.M.T. Saw, A.M.M. Gabr, A. R. Ahmed, D. Knorr, I. Smetanska, *J. Food Sci. Technol.*, **51**, 2216 (2014).
8. L. Parafati, C. Restuccia, R. Palmeri, B. Fallico, E. Arena, *Foods*, **9**, 1189 (2020).
9. X. He, B. Wang, B. Zhao, F. Yang, *Foods*, **11**, 771, (2022).
10. K. Kanazawa, H. Sakakibara, *J. Agric. Food Chem.*, **48**, 844 (2000).
11. F. Kugler, F. C. Stintzing, R. Carle, *J. Agric. Food Chem.*, **52**, 2975 (2004).
12. O. Rojo-Poveda, L. Barbosa-Pereira, G. Zeppa, C. Stévigny, *Nutrients*, **12**(4), 1123 (2020).
13. M. R. González-Centeno, K. Knoerzer, H. Sabarez, S. Simal, C. Rosselló, A. Femenia, *Ultrason. Sonochem.*, **21**, 2176 (2014).
14. J.P. Balentic, Đ. Ačkar, S. Jokic, A. Jozinovic, J. Babic, B. Miličević, D. Ubaric, N. Pavlovic, (2018)
15. J. Pérez-Jiménez, F. Saura-Calixto, *J. Agric. Food Chem.*, **53**, 5036 (2005).
16. H. M. C. Azeredo, *Int. J. Food Sci. Technol.*, **44**, 2365 (2009).
17. P. C. Wootton-Beard, A. Moran, L. Ryan, *Food Res. Int.*, **44**, 217 (2011).
18. H. Z. Li, Z. J. Zhang, J. Xue, L. X. Cui, T. Y. Hou, X. J. Li, T. Chen, *Food Sci. Technol. (Brazil)*, **36**, 686 (2016).
19. A. Peláez-Acero, D. B. Garrido-Islas, R. G. Campos-Montiel, L. González-Montiel, G. Medina-Pérez, L. Luna-Rodríguez, U. González-Lemus, A. de J. Cenobio-Galindo, *Molecules*, **27**, 5825 (2022).
20. Y.-H. Wong, C.-P. Tan, K. Long, K.-L. Nyam, *Czech Journal of Food Sciences*, **32**, 177 (2014).
21. T.T.M. Thu, T.T. Tuan, Nguyen Thi Nhu, Y. Tran Nguyen, P.L. Jerz, *J. Chem. Technol. Biotechnol.*, **99**, 820 (2024).
22. A. Smeriglio, S. Bonasera, M.P. Germanò, V. D'Angelo, D. Barreca, M. Denaro, M. T. Monforte, E. M. Galati, D. Trombetta, *Phytother. Res.*, **33**, 1526 (2019).
23. I. Gómez-López, G. Lobo-Rodrigo, M.P. Portillo, M.P. Cano, *Antioxidants(Basel/Switzerland)*, **10**, 1786 (2021).
24. S.J. Calva-Estrada, M. Jiménez-Fernández, E. Lugo-Cervantes, *Food Chem. Mol. Sci.*, **4**, 100089 (2022).
25. T. Kujala, J. Lojonen, K. Pihlaja, *Z. Naturforsch. C J. Biosci.*, **56** (5-6), 343 (2001).
26. M.M. Zin, C.B. Anucha, S. Bánvölgyi, *Foods*, **9**, 918 (2020).
27. M.M. Zin, S. Bánvölgyi, *Biomass Convers. Biorefin.*, **13**, 10759 (2023).
28. Y. Cai, M. Sun, H. Corke, *J. Agric. Food Chem.*, **51**, 2288 (2003).
29. S. O. Salawu, O. F. Alao, O. F. Faloye, A. A. Akindahunsi, A. A. Boligon, M. L. Athayde, *Nutr. Food Sci.*, **46**, 171 (2016).
30. S. Dudonné, X. Vitrac, P. Coutière, M. Woillez, J. M. Mérillon, *J. Agric. Food Chem.*, **57**, 1768 (2009).
31. M. I. Arsul, N. Syamsi, N. Putri, N. A. A. Nur, M. Mukhriani, N. Hamzah, *Curr. Res. Biosci. Biotechnol.*, **4**, 242 (2022).
32. D. O. Kim, K. W. Lee, H. J. Lee, C. Y. Lee, *J. Agric. Food Chem.*, **50**, 3713 (2002).
33. N. Li, G. Zhang, D. Zhang, *J. Chem.*, **2022**, 2472513 (2022).
34. P. Subramanian, P.S.R. N.J., B.G.M., *Food Funct.*, **14**, 8229 (2023),
35. J. Wang, G. K. Jayaprakasha, B.S. Patil, *J. Food Drug Anal.*, **28**, 217 (2020).
36. E. B. Rodriguez, M. L. P. Vidallon, D. J. R. Mendoza, C. T. Reyes, *J. Sci. Food Agric.*, **96**, 4679 (2016). <https://doi.org/10.1002/jsfa.7680>
37. Esatbeyoglu, A. E. Wagner, V. B. Schini-Kerth, G. Rimbach, *Mol. Nutr. Food Res.*, **59**, 36 (2015).M. Wang, S. Lopez-Nieves, I.L. Goldman, H.A. Maeda, *J. Agric. Food Chem.*, **65**, 4305 (2017).
38. A. Ahmad, K.M. Alkharfy, T.A. Wani, M. Raish, *Int. J. Biol. Macromol.*, **72**, 990 (2015).
39. X. Jiao, B. Li, Q. Zhang, N. Gao, X. Zhang, X. Meng, *Int. J. Food Sci. Technol.*, **53**, 61 (2018).
40. M. Minekus, M. Alminger, E. Alvito, S. Ballance, T. Bohn, C. Dupont D. Egger, A. Janssen, A. C. Karakaya, M. Koziol, C. Lemmens, *Int. J. Food Sci. Technol.*, **5**, 1113 (2014).
41. D. Vitali, I.V.D.B.Š., *Food Chem.*, **114**, 1462 (2009).
42. S. Baliyan, R. Mukherjee, A. Priyadarshini, A. Vibhuti, A. Gupta, R. P. Pandey, C. M. Chang, *Molecules*, **27**, (2022).
43. N. Donlao, Y. Ogawa, *LWT*, **89**, 648 (2018).
44. C. Dimou, K.H.C., S.D., K.A.E., *Current Pharmaceutical Biotechnology*, **20**, 776 (2019).

# Dehydration of industrial isopropanol wastewater by pervaporation using carboxy methyl cellulose and graphene oxide hybrid membranes

D. Unlu

Bursa Technical University, Faculty of Engineering and Natural Sciences, Chemical Engineering Department, 16310, Bursa, Turkey

Received May 4, 2024; Accepted: August 17, 2024

Isopropanol (IPA) is widely used as an industrial solvent, cleaning agent, and in producing chemicals, fuels and medical products. Many applications require anhydrous IPA without water. IPA-containing wastewaters are generated from its production and uses. Dewatering and recycling IPA from these waste streams is important for both economic and environmental reasons. IPA and water form an azeotropic mixture, making conventional dehydration methods like distillation and extraction challenging. Membrane-based processes such as pervaporation offer advantages over these processes, as it can break azeotropes while requiring lower energy and having a smaller footprint. In this study, hybrid membrane was used to dehydration of industrial isopropanol wastewater by pervaporation. The study focused on preparing hybrid membranes for pervaporation dehydration by incorporating graphene oxide into a carboxy methyl cellulose matrix. This integration of graphene oxide led to an enhancement in the dehydration separation performance of the hybrid membranes. Additionally, the research systematically characterized and evaluated the impact of graphene oxide concentration, operation temperature, and feed IPA concentration on various properties such as hydrophilicity, swelling, and dehydration. These analyses aimed to understand the influence of these factors on the overall performance and properties of the hybrid membranes. Optimum process conditions have been determined and under these conditions, water flux 4.7 kg/m<sup>2</sup>h and separation factor value of 128 were obtained. The study's findings pave the way for the future development of carboxy methyl cellulose (CMC) based hybrid membranes for implementation in pervaporative dehydration processes.

**Keywords:** Dehydration; Isopropanol; Membrane; Pervaporation; Wastewater

## INTRODUCTION

Understanding the challenges in recovering isopropyl alcohol (IPA) from pharmaceutical industry wastewater is crucial due to the complexity of the components involved. The presence of solvents, inorganic salts, and organic compounds makes the separation process intricate. IPA, being a common solvent in drug synthesis, forms azeotropic mixtures with water, especially at around 13 wt% water under ambient pressure, leading to challenges in separation. Additionally, mixtures with close boiling points further complicate the recovery process. Dehydration is a critical step in the recovery of IPA from such wastewater streams as it helps in separating IPA from water and other components effectively. By leveraging dehydration techniques, such as distillation or molecular sieves, it is possible to overcome the challenges posed by the presence of water and the formation of azeotropic mixtures during the recovery process. Implementing a well-designed separation strategy that includes dehydration steps can facilitate the efficient recovery of IPA from pharmaceutical industry wastewater [1-3].

Traditional separation methods for IPA/water mixtures, such as azeotropic distillation and extraction distillation, are known for their high energy consumption and waste generation. Azeotropic distillation typically requires the addition of di-isopropyl-ether or cyclohexane, and extractive distillation uses ethylene glycol as a separating agent. However, these methods are costly due to the high energy consumption and the use of additional chemicals [1-3]. Pervaporation (PV) stands out as an alternative separation process to these traditional methods, known for its energy efficiency, environmental friendliness, and ease of operation. PV is a membrane-assisted separation process that is considered advantageous due to its lower energy requirements and minimal environmental impact [4-8]. It is commonly employed for the dehydration of alcohols and offers a promising solution for the separation of IPA/water mixtures [9].

Pervaporation is a membrane-based separation process that finds significant utility in effectively separating liquid azeotropes.

\* To whom all correspondence should be sent:  
E-mail: [derya.unlu@btu.edu.tr](mailto:derya.unlu@btu.edu.tr)

Unlike traditional separation methods reliant on the vapor-liquid equilibrium, pervaporation separation is unique in that the transport resistance is determined by the mobility of the components across the membrane and the sorption equilibrium. The application of pervaporation in separating IPA/water mixtures is particularly intriguing due to the challenges posed by the formation of azeotropic mixtures during conventional distillation processes. Notably, there have been reports indicating the installation of 16 industrial pervaporation units specifically dedicated to the dehydration of IPA, highlighting the practical importance and successful implementation of this technology in the pharmaceutical industry. By leveraging the advantages offered by pervaporation, such as its independence from vapour-liquid equilibrium and its efficient separation capabilities, industries can achieve enhanced separation efficiency and cost-effective recovery of valuable solvents like IPA from complex mixtures in processes like drug synthesis and pharmaceutical wastewater treatment.

Pervaporation is a separation process where a component in a liquid mixture selectively permeates through a dense membrane, facilitated by a chemical potential gradient. It offers economic and environmental advantages, being energy-efficient and eco-friendly [10-12]. In pervaporation, the liquid mixture encounters a dense, homogeneous membrane that separates the feed and the permeating stream. The components dissolve in the membrane, diffusing through it at varying speeds before evaporating downstream. The resulting vapor is condensed back into a liquid form. The efficiency of pervaporation hinges on the interaction between the components and the membrane material, with the membrane's chemical nature and structure playing a pivotal role in determining performance [13]. The mass transfer mechanism in pervaporation currently relies on the solution diffusion model. This model posits that species dissolve at the surface of the membrane with higher chemical potential, diffuse through the polymer's free volume in a sorbed state, and transition to the fluid phase downstream where the chemical potential is lower. The dense polymeric membrane actively participates in both the dissolution and diffusion processes, making it a crucial element in the efficiency and effectiveness of pervaporation for separating components in liquid mixtures [14-18].

The membrane is critical in pervaporation applications. Polymeric, inorganic and hybrid membranes have been widely used for pervaporative separation. However, polymer applications were limited by several issues, including low mechanical

and biostability and low reject rates. Inorganic membranes have been limited by the high cost of manufacturing. The inclusion of inorganic components into polymeric membranes is expected to enhance the membranes' separation properties. The synergistic effects of combining polymers with inorganic fillers/particles is hypothesized to result in higher performing membranes for the separation. The key requirements of these hybrid membranes are that the polymer component confers chemical/thermal stability, ease of processing and high hydrophilicity [4].

In this study, pervaporative recovery of isopropanol from pharmaceutical industry wastewater was investigated with GO/CMC hybrid membrane. The compatibility of the polymers used in the prepared hybrid membrane was visualized by SEM analysis. The chemical bond structure of the GO/CMC blend membrane was determined by FTIR. The effect of GO concentration, feed water concentration and temperature on the separation performance was investigated.

## EXPERIMENTAL

### *Materials*

In this study, the materials used for the membrane synthesis and experimental procedures were purchased from specific suppliers. Carboxymethyl cellulose (CMC) was supplied from Denkim Denizli Kimya Inc. Graphene oxide were acquired from Hazerfen Kimya A.Ş. Glutaraldehyde, acetone and hydrochloric acid were obtained from Sigma Aldrich.

- *Membrane preparation.* 5 wt.% of CMC is dissolved in deionized water to obtain a homogeneous polymeric membrane solution. A certain amount of GO particles (ranging from 0.5 wt.% to 4 wt.%) based on the mass of the polymer were added to the CMC solution. Solution casting method was used for the casting and drying of membrane. After drying, the membrane was crosslinked to improve its stability and mechanical properties. The dry membrane underwent a cross-linking process using a combination of glutaraldehyde (1% by weight), HCl (1% by weight), acetone (85% by weight), and water (15% by weight) [18]. Following the cross-linking procedure, the hybrid membrane was washed with distilled water and subsequently allowed to dry. This cross-linking treatment is essential to enhance the stability and performance of the membrane for its intended applications.

- *Membrane characterization.* In the study, the synthesized membranes underwent characterization using Fourier-transform infrared

spectroscopy (FTIR) and scanning electron microscopy (SEM). These characterization techniques are crucial for analyzing the chemical structure and structural morphology of the membranes.

FTIR analysis was conducted to assess alterations in the chemical structure of the carboxy methyl cellulose (CMC) membrane due to the incorporation of graphene oxide (GO). The FTIR analysis involved conducting 4 scans within the spectral range of 400-4000  $\text{cm}^{-1}$ . This analysis helps in understanding the chemical interactions and structural changes resulting from the addition of graphene oxide in the membrane matrix.

The compatibility and miscibility between GO and CMC were evaluated through SEM analysis by capturing cross-sectional images of the membrane. This method allows for a visual examination of the interface between GO and cellulose acetate within the membrane, providing insights into their interaction, distribution, and compatibility at a microscale level.

#### Pervaporative recovery of isopropanol

Pervaporative recovery of isopropanol was carried out in a laboratory-scale pervaporation system.

The system consists of a membrane cell containing the membrane and feed mixture, a mechanical mixer for homogenization of the mixture, a vacuum pump to ensure low pressure in the underflow and cooling traps where the flow through the membrane is collected. The membrane is placed in the membrane cell. The feed mixture was fed into the membrane cell through a feed pump and the mixture was mixed with the help of a mechanical mixer. Due to the use of hydrophilic membranes, the water in the mixture passed through the membrane and the purification process was carried out. IPA could not pass through the membrane and remained in the feed mixture. In the pervaporation process, one side of the membrane is in contact with the liquid while the other side is vacuum. Water passed through the membrane perfectly and evaporated at low pressure on the passing stream side. Then the water obtained as vapor in cooling traps was condensed with liquid nitrogen and obtained in liquid phase. The separation performance of the membrane was determined by flux and selectivity. Flux and separation were calculated using Equations 1 and 2, respectively.

$$J = \frac{m}{A \cdot t} \quad (1)$$

m is the amount of sample collected in the

passing stream, A is the membrane area and t is the time.

$$\alpha = \frac{y_{su} / y_{IPA}}{X_{su} / X_{IPA}} \quad (2)$$

y is the percentage by weight in the passing stream and x is the percentage by weight in the feed. Isopropanol concentration was determined by refractometer.

## RESULTS AND DISCUSSION

### Characterization results

- **FTIR analysis.** The FTIR spectra of GO/CMC hybrid membranes are given in Fig. 1.

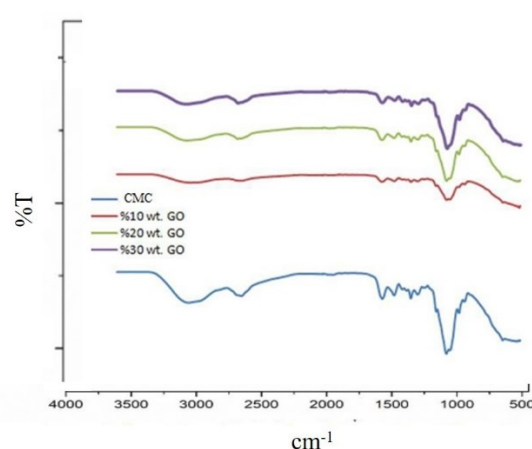


Fig. 1. FTIR spectra of the membranes

The strong absorption band at 3450  $\text{cm}^{-1}$  is due to O-H stretching vibrations of surface hydroxyl groups and adsorbed water. The peak at 2926  $\text{cm}^{-1}$  is the C-H vibration peak of the CMC polymer. The peaks at 1720  $\text{cm}^{-1}$  and 1651  $\text{cm}^{-1}$  belong to the COO- group of CMC. The multiple peaks of GO in the range 1000-1700  $\text{cm}^{-1}$  correspond to oxygen-containing functional groups [19, 20].

- **SEM analysis.** SEM analysis was performed with samples taken from GO/CMC hybrid membrane. Fig.c2 shows the cross-sectional image of GO/CMC hybrid membrane.

SEM images showed that the polymer and additive were well mixed, no phase separation was observed and exhibited coherent polymeric behavior. All these are the result of molecular interaction between the polymers. A certain number of hydroxyl groups are required for CMC to be miscible with GO. Therefore, there is an intermolecular interaction involving hydroxyl groups. Strong interpolymer interaction occurred between CMC and GO and thus no phase separation occurred. As a result, homogeneous hybrid films were obtained [25].

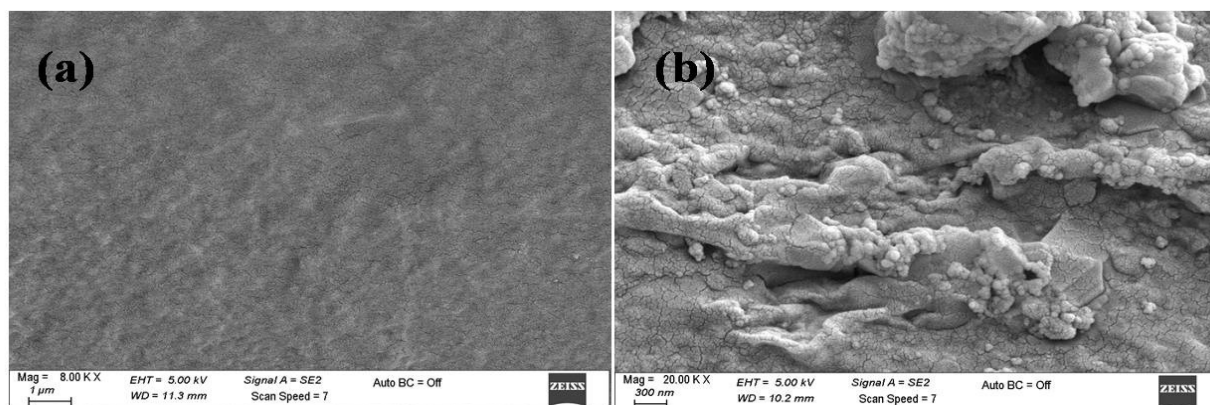


Fig. 2. Sectional image of GO/CMC hybrid membrane

### Pervaporation results

- *Effect of GO concentration.* Membranes with four different GO loading rates (0.5%, 1%, 2% and 4%) were used in the experimental study for pervaporative recovery of isopropanol. The experiments were carried out using isopropanol-water mixture containing 13% water at room temperature. The effect of the amount of GO on the separation performance of the membrane is given in Fig. 3.

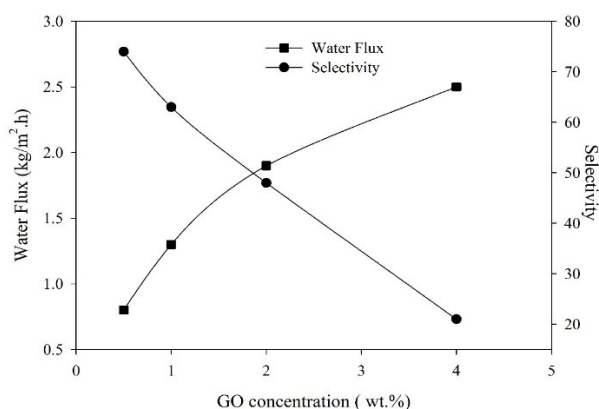


Fig. 3. Effect of GO concentration on flux and selectivity

The hydrophilic nature of CMC causes high water permeation. GO also increases water passage due to its hydrophilic nature. As the amount of GO increases, flux increases and selectivity decreases. As the amount of GO increases, the hydrophilicity of the membrane increases and the selectivity value decreases [26-28].

- *Effect of feed concentration.* The results of pervaporative recovery of isopropanol tested at room temperature using a GO/CMC hybrid membrane containing 0.5 wt.% GO are shown in Fig. 4. Isopropanol-water mixture is known to exhibit azeotropic mixing at 13 wt% water content. The effect of feed water concentration was investigated for isopropanol-water blends containing 6, 13, 20

and 27 wt% water. As expected, with increasing water concentration, the total flux increases due to the so-called ‘plasticizing effect’ of water, which leads to an increase in the free volume of the membrane allowing molecules to more easily pass through the membrane. Furthermore, more hydrogen bonds can be formed between the hydrophilic polar groups of the membrane and the water in the feed mixture at higher water concentrations, resulting in higher flux and correspondingly lower separation factor.

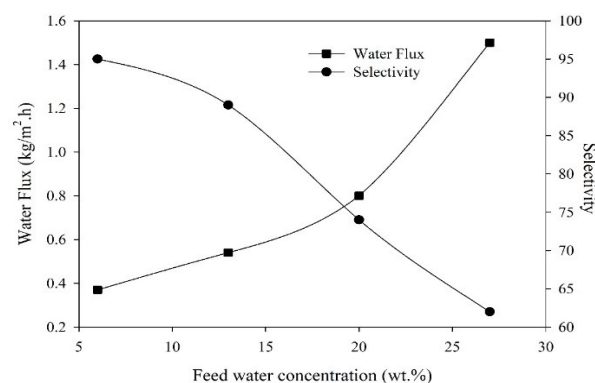
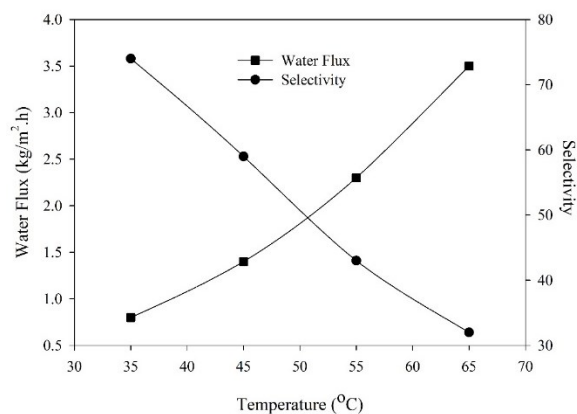


Fig. 4. Effect of feed water concentration on flux and selectivity

The plasticizing and swelling effects of water had a negative effect on the separation factor of the membrane; since the polymer chains can move quickly and easily, the resulting free volume results in a lower separation factor in low concentration IPA mixtures. As the water concentration in the feed mixture increased from 6% to 27%, the total flux increased from 0.37 kg/m<sup>2</sup>.h to 1.5 kg/m<sup>2</sup>.h, while the selectivity decreased from 95 to 62 [24, 20-32].

- *Effect of temperature.* The effect of temperature on the separation performance of GO/CMC hybrid membrane is shown in Fig. 5. As the operating temperature increases, the thermal mobility of the chains of the GO/CMC polymer intensifies, the free volume increases.



**Fig. 5.** Effect of temperature on flux and selectivity

The transfer of water is facilitated and an increase in water flux is observed as the temperature increases. Also, the vapor pressure of the feed increases as the temperature increases. This increase is to increase the driving force for mass transport through the membrane [33, 34]. This results in an increase in the flux value for both membranes. While 0.8 kg/m<sup>2</sup>h flux was obtained at 35°C, the flux value increased to 3.5 kg/m<sup>2</sup>h when the temperature increased to 65°C. The selectivity was 74 and 32 at 35°C and 65°C in the GO/CMC hybrid membrane.

#### CONCLUSION

The study introduces an innovative approach, the pervaporation process, for dehydrating isopropanol using a GO/CMC hybrid membrane. The research focused on understanding the impact of variables such as the concentration of graphene oxide (GO), feed water concentration, and temperature on the separation performance. It was observed that increasing the GO concentration led to enhanced membrane hydrophilicity and swelling, facilitating easier water passage through widened diffusion channels, thereby increasing flux. However, this also resulted in reduced diffusion selectivity, causing isopropanol to be carried along with water through the membrane, lowering the separation factor. Furthermore, elevating the water concentration in the feed solution increased the membrane's free volume by promoting greater contact between the membrane and water. This, in turn, increased flux but, as with the effect of GO concentration, decreased the separation factor. The experimental findings identified the optimal conditions for the process, which involved using a 0.5 wt.% GO loaded membrane at a feed water concentration of 13 wt% (azeotrope point) at 35°C. This configuration yielded the best separation performance, showcasing the efficiency of the pervaporation process for azeotropic mixtures of water and isopropanol at a 13% water concentration. Under these conditions,

the obtained flux and selectivity values were recorded at 0.82 kg/m<sup>2</sup>·h and 74, respectively. The study's results underscore the importance of fine-tuning key parameters such as membrane composition, feed water concentration, and temperature to optimize the pervaporation process for efficient dehydration of isopropanol, demonstrating the potential of this method in addressing challenges related to azeotropic mixtures in the pharmaceutical industry.

#### REFERENCES

1. A. Urriaga, E. Gorri and I. Ortiz, *Sep. Purif. Technol.*, **49**, 245 (2006).
2. J. Zuo, D. Hua, V. Maricar, Y. K. Ong, T.S. J. Chung, *Appl. Polym. Sci.*, **135**, 45086 (2017).
3. C. Y. Lai, Y. M. Sun, Y. L. Liu, *Journal of Membrane Science*, **685**, 121959 (2023).
4. X. W. Liu, Y. Cao, Y. X. Li, Z. L. Xu, Z. Li, M. Wang, X. H. Ma, *J. Membr. Sci.*, **576**, 26 (2019).
5. Q. Wang, N. Li, B. Bolto, M. Hoang, Z. Xie, *Desalination*, **387**, 46 (2016).
6. S. Assabumrungrat, J. Phongpatthanapanich, P. Praserthdam, T. Tagawa, S. Goto, *Chem. Eng. J.*, **95**, 57 (2003).
7. B. G. Park, T. T. Tsotsis, *Chem. Eng. Process.*, **43**, 1171 (2004).
8. D. Unlu, N. D. Hilmioglu, *J. Chem. Technol. Biotechnol.*, **91**, 122 (2016).
9. A. I. Kuzminova, M. E. Dmitrenko, D. Y. Poloneeva, A. A. Selyutin, A. S. Mazur, A. V. Emeline, V. Y. Mikhailovskii, N. D. Solovyev, S. S. Ermakov, A. A. Penkova, *J. Membr. Sci.*, **626**, 119194 (2021).
10. R. W. Baker, Membrane separation, in *Encyclopedia of Separation Science*, Academic Press, 2000, p. 205.
11. A. Basile, M. D. Marcello De Falco, G. Centi. G. Iaquaniello, *Membrane Reactor Engineering: Applications for a Greener Process Industry*. United Kingdom, Wiley, 2016.
12. P. Salehian, T. S. Chung, *J. Membr. Sci.*, **544**, 378 (2017).
13. A. Basile, A. Figoli, M. Khayet, *Pervaporation, Vapour Permeation and Membrane Distillation: Principles and Applications*. United Kingdom, Woodhead Publishing, 2015.
14. S. P. Dharupaneedi, R. V. Anjanapura, J. Han, T. M. Aminabhavi, *Ind. Eng. Chem. Res.* **53**, 14474 (2014).
15. J. K. Wu, M. J. Yin, W. Han, N. Wang, Q. F. An, *J. Mater. Sci.*, **55**, 2607 (2020).
16. D. P. Suhas, A. V. Raghu, H. M. Jeong, T. M. Aminabhavi, *RSC Adv.*, **3**, 17120 (2013).
17. R. Y. M. Huang, *Pervaporation Membrane Separation Processes*, Amsterdam, Elsevier Science Publishers BV, 1991.
18. H. E. A. Bruschke, N. P. Wynn, Membrane separations/pervaporation, in: I. D. Wilson, E. D. Adlard, M. Cooke, C. F. Poole (eds.), *Encyclopedia of Separation Science*, Academic Press, Germany, 2000, p. 1776.

*D. Unlu: Dehydration of industrial isopropanol wastewater by pervaporation using carboxy methyl cellulose and ,,*

19. Q. Zhao, J. Qian, Q. An, C. Gao, Z. Gui, H. Jin, *J. Membr. Sci.*, **333**, 68 (2009).
20. M. Ozekmekci, D. Unlu, M. Copur, *Korean J. Chem. Eng.*, **38**, 1859 (2021).
21. Y. M. Xu, N. L. Le, J. Zuo, T.S. Chung, *J. Membr. Sci.*, **499**, 317 (2016).
22. D. Ünlü, *Gümüşhane Üniversitesi Fen Bilimleri Enstitüsü Dergisi*, **10**, 275 (2020).
23. H. Wu, X. Fang, X. Zhang, Z. Jiang, B. Li, X. Ma, *Sep. Purif. Technol.*, **64**, 183 (2008).
24. X. H. Zhang, Q. L. Liu, Y. Xiong, A. M. Zhu, Y. Chen, Q. G. Zhang, *J. Membr. Sci.*, **327**, 274 (2009).
25. Y. Miyashita, T. Suzuki, Y. Nishio, *Cellulose*, **9**, 215 (2002).
26. Z. Wang, H. Yu, J. Xia, F. Zhang, F. Li, Y. Xia, Y. Li, *Desalination*, **299**, 50 (2012).
27. W. Jang, J. Yun, K. Jeon, H. Byun, *RSC Adv.*, **5**, 46711 (2015).
28. J. Zhang, Z. Xu, W. Mai, C. Min, B. Zhou, M. Shan, X. Qian, *J. Mater. Chem. A.*, **1**, 3101 (2013).
29. J. Lu, Q. Nguyen, J. Zhou, Z.H. Ping, *J. Appl. Polym. Sci.*, **89**, 2808 (2003).
30. K. Sunitha, Y. V. L. R. Kumar, S. Sridhar, *J. Mater. Sci.*, **44**, 6280 (2009).
31. Z. Raecisi, A. Moheb, M. Sadeghi, A. Abdolmaleki, M. Alibouri, *Chem Eng Res Des.*, **145**, 99 (2019).
32. T. Zhu, Y. Luo, Y. Lin, Q. Li, P. Yu, M. Zeng, *Sep. Purif. Technol.*, **74**, 242 (2010).
33. R. Castro-Muñoz, J. Buera-González, Ó. D. L. Iglesia, F. Galiano, V. Fíla, M. Malankowska, C. Rubio, A. Figoli, C. Téllez, J. Coronas, *J. Membr. Sci.*, **582**, 423 (2019).
34. V. T. Magalad, G. S. Gokavi, K. V. S. N., Raju, T. M. Aminabhavi, *J. Membr. Sci.*, **354**, 150, (2010).

## Optimization of ozonation in the removal of Basic Blue 41 in aqueous solution

K. Turhan\*

*Yıldız Technical University, Science and Art Faculty, Chemistry Department, Esenler-İstanbul, Turkey*

Received May 31, 2024; Accepted: August 17, 2024

This study involved the use of ozonation to decrease the content of a commercial basic dye, Basic Blue 41 (BB41), in synthetically produced wastewater. The optimization of this process was examined by assessing the chemical oxygen demand (COD) outcomes. Experiments were conducted in a 7-L reactor utilizing a batch bubble column of laboratory size. This study focused on investigating the optimal operating conditions by examining experimental factors such as pH, ozone dose, and reaction time. At pH 10, the COD of the basic dye wastewater decreased by 79.82%. Additionally, a significant reduction in color took place within a period of 9 min. The process of ozone depletion in the reaction medium continued for 16 min, and most of the degradation processes (94.56%) were successfully completed during this time. The ozonation kinetics were investigated and found to fit pseudo-first-order. The research showed that the rate constant exhibited a positive correlation with the applied ozone dosage and basic pH conditions and showed a logarithmic decrease with the initial dye concentration. These findings indicate that ozonation is more efficient for basic dyes when conducted under alkaline pH conditions than under acidic or neutral pH conditions.

**Keywords:** Basic blue 41; Ozonation; Decolorization; Optimization; Wastewater; Basic dyes

### INTRODUCTION

The textile sector significantly contributes to global economic growth and provides job opportunities for a large workforce. While the textile sector may meet environmental rules in many nations, it is now facing stricter constitutional pollution laws that demand higher-quality wastewater treatment. Physical, biological, and chemical techniques can partially eliminate wastewater pollutants. However, dyes present a challenge since they cannot be adequately broken down and are not easily eliminated from wastewater using traditional treatment systems.

The advanced oxidation process is a promising alternative for removing color and reducing the high wastewater levels generated by textile dyeing and finishing wastes. The decolorizing impact of ozone on dyes in water is due to its ability to react with unsaturated dyes to form ozonides. These ozonides then undergo rapid hydrolysis, causing the molecules to break down. Decolorization of wastewater using O<sub>3</sub> depends on ozone dosage, solution temperature, reaction time, and solution pH. Ozonation is an ideal method for removing dyes from aqueous solutions because of its quick reaction time, cost-effectiveness (excluding installation expenses), and high efficiency. Nevertheless, it is important to note that ozone typically generates harmless substances that transform into carbon dioxide (CO<sub>2</sub>) and water (H<sub>2</sub>O), depending on the prevailing circumstances.

Azo dyes are the predominant category of artificial colorants, accounting for approximately 60-70% of all such dyes. The azo group (-N=N-) is a defining characteristic of these dye groups, along with aromatic systems and auxochromes (OH, SO<sub>3</sub>, etc.). The combination of these chemical groups in the dye molecules presents a complicated challenge for their removal from wastewater. Several techniques employed to remove color from dyes rely on physical or chemical procedures. These methods [1] encompass membrane filtering [2-4], electrochemical technology [5, 6], and advanced oxidation processes (AOP), such as photochemical oxidation [7], photocatalysis [8, 9], and ultrasonic waves [10].

Dyes with cationic properties of their molecules are referred to as cationic or basic dyes. Basic Blue 41 (BB41) is a cationic azo dye widely used in dyeing nylon, acrylic, and woollen textiles. BB41 is highly resistant to degradation *via* chemical oxidation, photocatalysis, and biodegradation [11]. Compared to anionic dyes, cationic dyes exhibit higher toxicity and can easily penetrate cells by accumulating in the cytoplasm because of interaction with the negatively charged surfaces of cell membranes. Hence, the removal of these dyes before they are emitted into wastewater has emerged as a significant concern.

Several studies have been published on the removal of color from Basic Blue 41 waste. Abbasi and Asl [10] on the sonochemical degradation of

\* To whom all correspondence should be sent:  
E-mail: [kturhan@yildiz.edu.tr](mailto:kturhan@yildiz.edu.tr)

nano TiO<sub>2</sub> and H<sub>2</sub>O<sub>2</sub>; Bouhelassa *et al.* [12] on the process of optimizing the photocatalytic decolorization of BB41 in a solar photoreactor prototype; and Humelnicu *et al.* [13] have studied the removal of BB4 from a water-based solution by an adsorption process using natural zeolite tuff in a batch method. Saravanan *et al.* [14] conducted research on the biological decolorization process of BB41 using composts enriched with beneficial microorganisms.

When ozone gas encounters organic substances, it enters into molecular or radical reactions. The degradation rate of ozone depends on pH and initial dye concentration. Under alkaline conditions, ozone rapidly decomposes, producing hydroxyl radicals and some other types of radicals in solution. Under acidic conditions, it can enter direct electrophilic reactions with organic substrates. Ozone is frequently used to decolorize dye wastes due to its capacity to react selectively with conjugated double bonds normally responsible for color. Molecular reactions of ozone can show selectivity and occur mostly through electrophilic attack; however, they can also proceed *via* nucleophilic or oxygen transfer pathways. Electrophilic attacks occur at sites with a significant concentration of negative charges, including atoms such as N, P, O, and S, as well as molecules with many bonds such as -C=C- or -N=N-. It can directly react with molecules containing functional groups such as -OH, -CH<sub>3</sub>, -OCH<sub>3</sub> and -NH<sub>2</sub> at the ortho- and para- substitution positions. Research has shown that the molecular ozone reaction mechanism is responsible for partial oxidation [15, 16]. The electron-rich chromophoric azo linkage is susceptible to direct attack and degradation by ozone, leading to immediate reduction of color. This process does not require the breakdown of bonds into hydroxyl radicals as a secondary oxidant [17-19]. Various variables, such as pH, contact time, ozone amount, and dye properties, affect the effectiveness of ozone in decolorizing wastewater dyes.

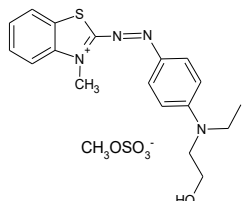
This study includes the relationship between varying ozonation time (ranging from 0 to 120 min), initial dye concentration (ranging from 150 to 600 mg/L), and ozone concentration (ranging from 4.21 to 24.03 g/m<sup>3</sup>). The effects of various factors, including initial pH (ranging from 2 to 12) depending on the concentration and removal of the dye, were evaluated. Efficient degradation of BB41 was achieved by maximizing both COD and color

removal. The pH of the dye solutions was observed to change over time as the initial dye concentrations changed.

## EXPERIMENTAL

The azo dye Basic Blue 41 (Table 1), along with all other chemicals, was acquired from Sigma-Aldrich.

**Table 1.** Characteristics of the azo dye studied in this work.

Disperse Dye	Formula	CAS No
C.I. Basic Blue 41 	C <sub>20</sub> H <sub>26</sub> N <sub>4</sub> O <sub>6</sub> S <sub>2</sub>	12270-13-2

The dye solution's color was quantified using a previously established integration approach [19]. This technique entailed measuring the absorbance of a sample across a range of wavelengths from 200 to 800 nm and calculating the total area under the absorbance curve. The integrated area is measured in integrated absorbance units (IAU), which are directly correlated to the color of the sample. The integration approach is less complex compared to the tristimulus filter method used by the American Dye Manufacturers Institute (ADMI), however, studies have demonstrated that both methods yield comparable outcomes [20, 21]. The indigo technique was used to assess the quantity of dissolved ozone in the research.

Figure 1 depicts the Fischer 502 model ozone generator, which is a laboratory-scale device. It consists of a cylindrical column reactor with a volume of 2 L, measuring 5 cm in diameter and 110 cm in height. Additionally, the setup includes a dye solution reactor with a capacity of 5 L, a dosimeter, washing bottles, oxygen gas, a gas cylinder, peristaltic pumps, and a temperature control unit. The temperature was maintained at a constant level of 20±1°C for all trials. Various pH values were utilized to conduct ozonation reactions to examine their impacts. The pH was regulated by adding 1 M H<sub>2</sub>SO<sub>4</sub> and 1 M NaOH. At 15-min intervals, samples were extracted from the reactor and the concentrations of the dyes in the solutions were measured using the Agilent 8453 spectrophotometer.

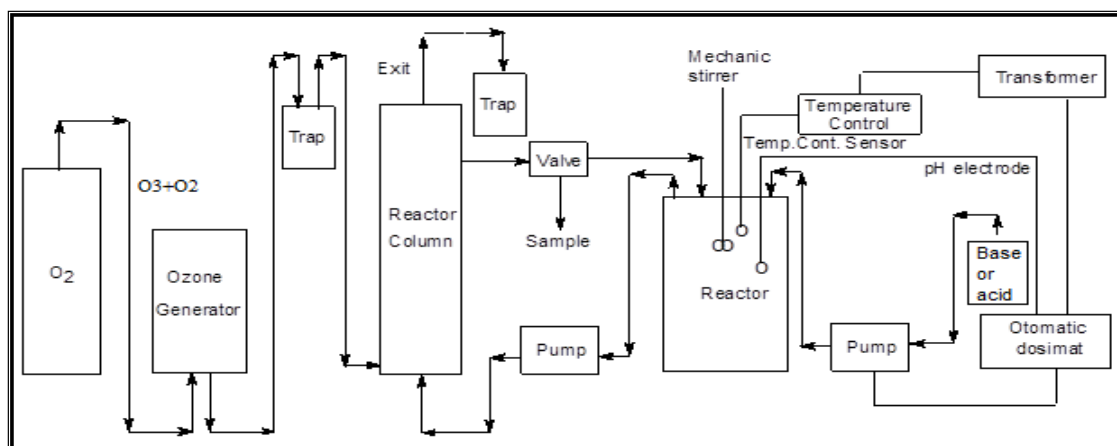


Figure 1. Schematic diagram of the bench-scale reactor system.

### Decolorization

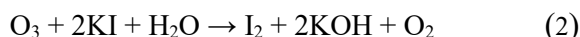
The assessment of dye removal was conducted by analysing the reduction in the maximum wavelength using a UV-Vis spectrophotometer. The percent removal values of dyestuffs were computed using Equation 1.

$$\text{Dye removal}(\%) = \frac{Abs(i) - Abs(f)}{Abs(i)} \times 100 \quad (1)$$

*Abs (i)*: Absorbance value of the dyestuff at its maximum wavelength.

*Abs (f)*: Absorbance value at the maximum wavelength at the end of the time after the adsorbent is added to the dyestuff.

A rubber tube was used to send ozone that hadn't been broken down from the top of the column reactor to the washing bottles that held 2% KI solution.



As we did in earlier studies, we found out how much unused ozone there was by titrating iodide with  $Na_2S_2O_3$  while a starch indicator was present. [16, 19, 22-26] The tests were done with an ozone air flow rate of 120 L/s because a high ozone flow rate and concentration are needed to treat wastewater effectively with ozone.

- *Decolorization kinetics of BB41.* Kinetic study is an important part of the ozone method to determine how well contaminated wastewater is treated. When hydroxyl radicals form, they consume the starting molecule and existing intermediates. If the ozone source is strong or the ozone concentration at the contact point remains the same, the oxidation rate follows the first-order dynamics of the decomposed organic matter concentration. This ratio is given in equation [3]:

$$-d[C_{dye}] / dt = k[C_{dye}] \quad (3)$$

To study the ozonation of dye solutions, the dye content ( $C_{dye}$ ) and the observed rate constant ( $k$ ) were used [22-26]. Multiplying the intrinsic rate

constant by the dissolved ozone concentration ( $C_{ozone}$ ) gives the apparent rate constant ( $k$ ):

$$k = -0.2461 \times C_{BB41}^{-0.5459} \quad (4)$$

Figure 2 shows that as the applied ozone dose ( $D_{ozone}$ ), temperature, and  $k$  increased, the initial dye concentration logarithmically decreased.

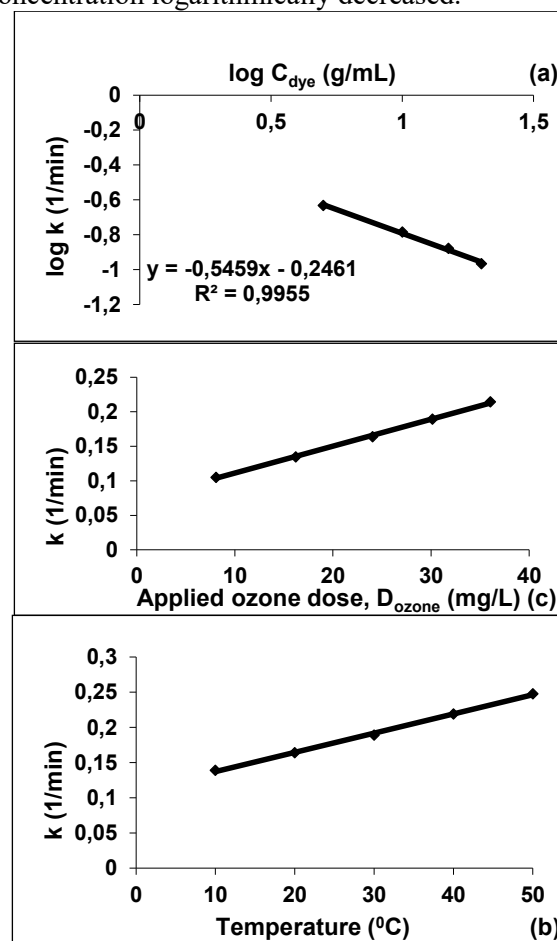


Figure 2. Dependence of the apparent rate constant of decolorization  $k$  on initial dye concentration, applied ozone dose and temperature for BB41. (a)  $D_{ozone} = 24,03$  mg/L.min,  $T = 20$  °C (b)  $C_{dye} = 300$  mg/L,  $T = 20$  °C (c)  $C_{dye} = 300$  mg/L,  $D_{ozone} = 24,03$  mg/L.min

The units for  $k$  and  $C_{dye}$  are given as L per min and g per L, respectively. It is important to observe that the rate constant that is observed, rather than the actual rate constant, varies with the initial concentration while keeping the temperature constant. This is because the actual rate is determined solely by the temperature. It is believed that the decrease in  $k$  is a result of the increased formation of intermediate compounds caused by the higher  $C_{dye}$  concentration. As the initial dye concentration increased, the consumption of ozone by these intermediates resulted in a decrease in  $C_{ozone}$ . Due to this, the rate constant appears to decrease as the dye concentration increases. The apparent rate constant and initial dye concentration in this study show a logarithmic relationship, which aligns with the findings of our previous studies [22-26].

Observing Figure 2, one can see that  $k$  rises as  $D_{ozone}$  and temperature increase. This can be attributed to the higher concentration of dissolved ozone. Decolorization happens more quickly with a higher amount of ozone applied, and the rate constant increases at higher temperatures. Table 2 presents the pH and corresponding  $k$  value for the dye under investigation. For further experiments, it was found that a basic pH environment yielded higher rate constant values, as indicated in Table 2.

*Impact of initial solution pH on COD*

At the start of the ozonation process, a volume of 7000 mL of BB41 solution with a concentration of 300 mg/L was introduced into the column. The experiment began with the introduction of ozone gas into the column. Regular time intervals were used to collect samples and measure the concentration of BB41 and COD at the sample port.

**Table 2.** Line-fitted values of rate constant  $k$ , (L/min).

Disperse dye	pH	k (L/min)			
		$C_0 = 5$ mg/L	$C_0 = 10$ mg/L	$C_0 = 15$ mg/L	$C_0 = 20$ mg/L
C.I. Basic Blue 41	6.0	0.159	0.140	0.122	0.099
	8.0	0.184	0.156	0.127	0.102
	10.0	0.233	0.174	0.132	0.108
	12.0	0.378	0.205	0.159	0.115

The pH of the raw basic dye wastewater was measured as 7.1. After 90 min of ozone bubbling treatment, the COD of the basic dyestuff wastewater decreased from 1358 mg/L to 546 mg/L. Considering the potential impact of pH on the results, a series of ozone treatment experiments were conducted using samples at different pH levels. The COD measurement after ozone treatment was conducted at different pH values ranging from 2 to 12. The corresponding results can be found in Figure 3. Under a basic condition of pH 10, the COD reduction observed in the direct dye wastewater was quite remarkable. At a pH of 10.0, the wastewater's COD with basic dyestuffs decreased to 274 mg/L, as observed. It has been noted that a significant number of bubbles are produced when the gas flow rate at the inlet is high, and a higher concentration of ozone has proven to be effective in reducing COD. A pH of 10 was chosen for the following experiments.

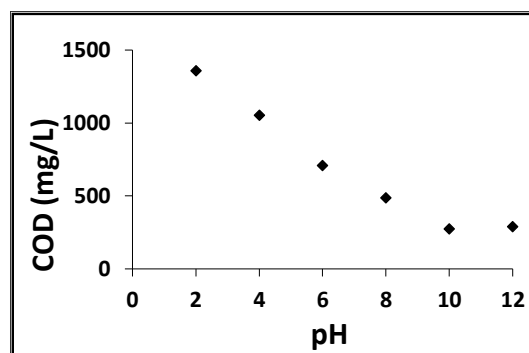


**Figure 3.** Effect of pH of the initial solution on COD (COD raw disperse dyestuff: 1358 mg/L for BB41); ozone concentration: 24 g/m<sup>3</sup>; dye concentration: 300 mg/L; dye solution: 7000 mL; ozone-air flow rate: 120 L/h; ozonation time: 90 min.).

*Spectrophotometric analysis of the process*

As the reaction time advanced, the absorption intensity of BB41 in solution gradually diminished. It was observed that BB41 molecules underwent degradation in the presence of ozone.

The absorption maximum of the BB41 solution at  $\lambda_{max}=609$  nm indicated a rapid degradation of the solution.

*Impact of reaction time*

Measurement of COD was also conducted during the reaction. According to Figure 4, the COD removal efficiencies of dye wastewater reached 79.82% after a 90-min reaction using ozonation at pH 10.0.

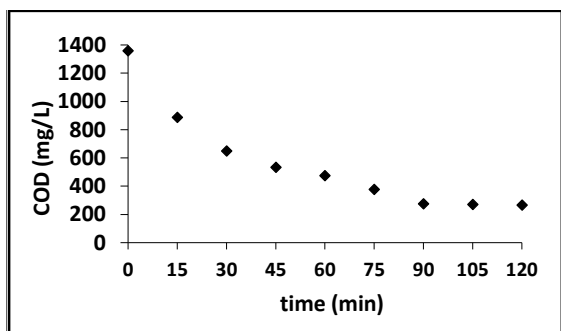


**Figure 4.** CODs of BB41 with ozone after different reaction time at pH 10 (ozone conc.: 24 g/m<sup>3</sup>; dye concentration: 300 mg/L; dye solution: 7000 mL; ozone-air flow rate: 120 L/h).

*Impact of initial dye concentration on the rate of dye decolorization*

Figure 5 illustrates the variation in dye concentration over time during ozonation at various initial dye concentrations. The rate of dye removal starts off strong and gradually decreases as time goes on.

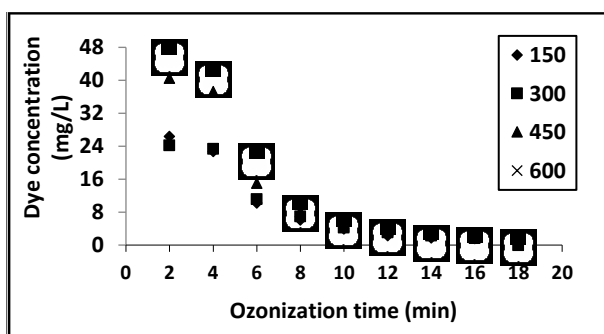


**Figure 5.** Ozonation time data for different dye concentrations treated with ozone (ozone conc.: 24 g/m<sup>3</sup>; dye solution: 7000 mL; ozone-air flow rate: 120 L/h; pH: 10).

*Effect of initial dye concentration on decolorization time*

Figure 6 shows the effect of initial basic dye concentrations on the time required for the decolorization process. The decolorization time increases with increasing the initial dye concentration in the waste. The data fit equation [5]:

$$t_D = m.c \tag{5}$$

where  $t_D$  is the dye decolorization time (min),  $m$  - a constant, and  $c$  - the initial dye concentration (mg/L).

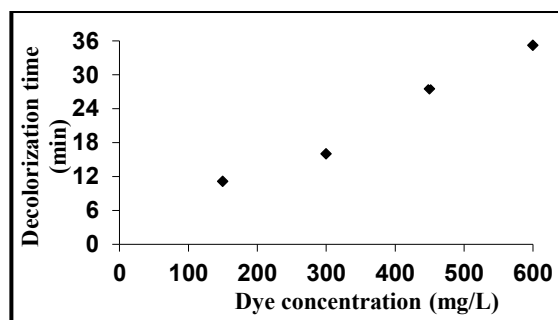


**Figure 6.** Effect of initial dye concentration on the decolorization time of BB41 (ozone conc.: 24 g/m<sup>3</sup>; dye solution: 7000 mL; ozone-air flow rate: 120 L/h; pH: 10).

*Impact of ozone concentration on decolorization time*

Figure 7 illustrates the relationship between ozone concentration and decolorization time. It is evident that as the ozone concentration increases, the decolorization time linearly decreases. Increasing ozone concentration in the gas phase from 4.21 to 24.03 g/m<sup>3</sup> lowers the time it takes to decolorize a 300 mg/L dye solution by about 91.23%. This outcome aligns with the mass transfer theory, which posits that as the ozone concentration in the air bubbles (which carry ozone) rises, the force that facilitates ozone transfer to the dye solution increases. Hence, both the ozone concentration in the solution and the rate of dye oxidation increase.

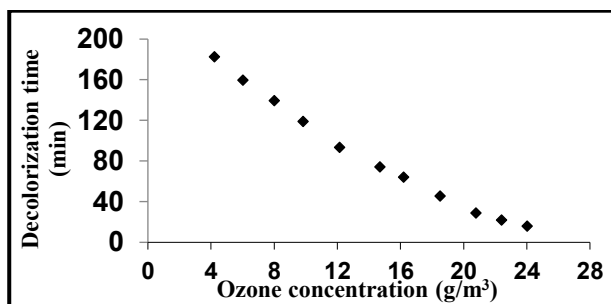


**Figure 7.** Effect of ozone concentration on dye decolorization time (dye conc.: 300 mg/L; dye solution: 7000 mL; ozone-air flow rate: 120 L/h; pH: 10).

#### Impact of initial dye solution pH on decolorization time

Figure 8 illustrates the impact of varying starting dye solution pH on the duration required for dye decolorization. Observations indicate that the duration of decolorization diminishes as the starting solution pH increases. The rate of ozone breakdown is enhanced by the generation of hydroxyl radicals at elevated pH levels. The dye decolorization time was reduced by 56.42% when the pH value was increased from 2 to 12.

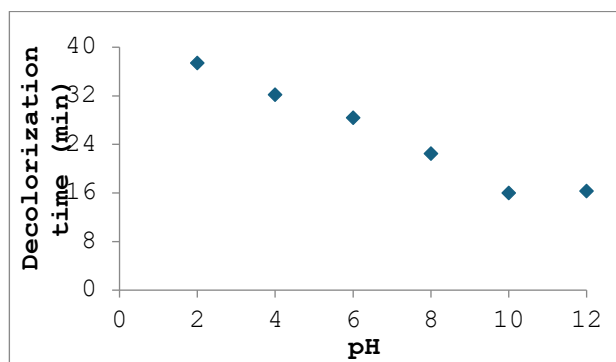


**Figure 8.** Effect of initial solution pH on decolorization time (dye concentration: 300 mg/L; dye solution: 7000 mL; ozone-air flow rate: 120 L/h; ozone concentration: 24 g/m<sup>3</sup>).

The untreated dyestuff wastewater samples exhibited a blue hue. The ozone treatment effectively decolorized the wastewater containing basic dyestuffs. After around 9 min of the reaction, an observable color change occurred, resulting in a translucent yellow hue. The process of decolorization was accomplished within a time frame of around 16 min. After a reaction time of 16 min, the absorbance of the basic dyestuff wastewater decreased by 94.56%.

#### RESULTS

The textile-finishing business generates wastewater with intense pigmentation, necessitating specialized treatment and assessment of the ecotoxicological impacts resulting from the discharge of process wastes into the surrounding environment. Scientific evidence has demonstrated that ozone treatment is highly successful in eliminating color; however, it only slightly reduces COD. Ozonation is a promising method for removing color and reducing the COD in wastewater that contains basic dyes. When dealing with ozone procedures, it is crucial to consider both the color and toxicity of the treated wastewater products. Hence, it is imperative to attain a suitable duration for ozonation.

For this experiment, we treated water-based solutions of a representative basic dye used in the

textile industry with ozone in a reactor that operates in a semi-batch mode. The purpose of our experiment was to see how well indirect ozonation with radical reactions could help the breakdown of model BB41 persistent pollutants in water solutions.

An in-depth analysis of the findings yields the following conclusions: The study found that wastewater containing primary dyestuffs underwent a reduction of 79.82% in COD. Additionally, a substantial decrease in color was detected at a pH level of 10.

The decolorization and degradation of the dye were fully accomplished during a duration of 16 min. A multitude of bubbles were generated when the gas flow rates at the entrance were high. The relationship between high ozone concentration and COD decrease was evident and substantial.

The study investigated the rate of ozonation and determined that it adheres to pseudo-first-order kinetics. The findings of this study suggest that the process of ozonation is more efficient in degrading basic dyes when conducted at alkaline pH, as opposed to acidic or neutral pH. The study found that color and COD were removed to a significant degree when the starting dye concentration was 300 mg/L, the pH was either acidic or neutral, and the ozonation time was short.

The results demonstrate that the ozonation procedure is an effective technique for treating azo dyes present in textile effluents.

#### REFERENCES

1. M. Abbasi, N. R. Asl, *J. Hazard. Mater.*, **153**(3), 942 (2008).
2. J. Cevallos-Mendoza, C. G. Amorim, J. M. Rodríguez-Díaz, M. Conceição, B. S. M. Montenegro, *Membranes*, **12**, 570 (2022).
3. L. Qalyoubi, A. Al-Othman, S. Al-Asheh, *Case Studies in Chemical and Environmental Engineering*, **3**, 100102 (2021).
4. A. Giwa, A. Yusuf, H. A. Balogun, N. S. Sambudi, M. B. I. Adeyemi, S. Chakraborty, S. Curcio, *Process Safety and Environmental Protection*, **146**, 220 (2021).
5. Ö. Gerçel, *Separation Sci. and Tech.* **51**(4), 711 (2015).
6. P. V. Nidheesh, M. Zhou, M. A. Oturan, *Chemosphere*, **197**, 210 (2018).
7. N. Bhargava, N. Bahadur, A. Kansal, *J. Water Process Eng.*, **56**, 104302 (2023).
8. H.-M. Su, D. Vasu, S.-Y. Chan, Y.-C. Liu, J. Jiang, Y.-F. You, T.-W. Chiu, S.-C. Chen, *Environ. Pollut.*, **345**, 123556 (2024).
9. M. F. Lanjwani, M. Tuzen, M. Y. Khuhawar, T. A. Saleh, *Inorganic Chem. Commun.*, **159**, 111613 (2024).

10. S. Y. Kim, I. Y. Kim, S.-H. Park, M. Hwangbo, S. Hwangbo, *Royal Society of Chemistry*, **14**, 11939 (2024).
11. Y. Liu, A. Yan, L. Ding, J. Wei, Y. Liu, Y. Niu, R. Qu, *Colloids and Surfaces A, Physicochemical and Engineering Aspects*, **680**, 132643 (2024).
12. M. K. Bouchareb, M. Bouhelassa, M. Berkani, *J. Chem. Tech. & Biotech.*, **89**(8), 1211 (2014).
13. I. Humelnicu, A. Băiceanu, M.-E. Ignat, V. Dulman, *Process Safety and Environmental Protection*, **105**, 274 (2017).
14. B. T. Pushpa, J. Josephraj, P. Saravanan, G. Ravindran, *Chemistry Select*, **4**, 10006 (2019).
15. A. López-López, A., J. S. Pic, H. Debbellefontaine, *Chemosphere*, **66**, 2120 (2007).
16. K. Turhan, S. Uzman, *Desalination*, **229**(1–3), 257 (2008).
17. A. Pandey, P. Singh, L. Iyengar, *Int. Biodeterioration & Biodegradation*, **59**(2), 73 (2007).
18. T.Y. Chen, C.M. Kao, A. Hong, C.E. Lin, S.H. Liang, *Desalination*, **249**(3), 1238 (2009).
19. K. Turhan, I. Durukan, S. A. Ozturkcan, Z. Turgut, *Dyes and Pigments*, **92**(3), 897 (2012).
20. W. J. Eiteman, M. A. Law, *J. Environ. Eng.*, **124**(3), 272 (1998).
21. American Public Health Association (APHA), American Water Works Association (AWWA), and Water Environment Federation (WEF), Standard methods for the examination of water and wastewater, American Public Health Association Publ., 21st edn., Washington, DC, 2005.
22. K. Turhan, Z. Turgut, *Fresen. Environ. Bull.*, **16**(7), 821 (2007).
23. K. Turhan, Z. Turgut, *Desalination*, **242**(1–3), 256 (2009).
24. K. Turhan, Z. Turgut, *Desalination and Water Treatment*, **11**(1-3), 184 (2009).
25. K. Turhan, *Global NEST Journal*, **23**(1), 143 (2021).
26. K. Turhan, *JOTCSA*, **5**(2): 835 (2018).

# Methyl violet dye removal investigation on submicron particle size rubber powder obtained from scrap tyre functionalized with agar-agar

Z. Kadioğlu, D. Şakar\*

*Yildiz Technical University, Chemistry Department, 34220, Esenler, Istanbul, Turkey*

Accepted: September 15, 2024

In this study, submicron particle size rubber powder adsorbent obtained from scrap tyre functionalized with agar-agar (RP-AA) was used to remove methyl violet (MV) dye from synthetic wastewater. The effects of different reaction parameters such as initial MV concentration, contact time and solution temperature on the adsorption of MV onto RP-AA at constant adsorbent dose and pH were investigated. To explain the adsorption character of MV adsorption on RP-AA some kinetic models and adsorption isotherms were applied.

**Keywords:** Scrap tyre; Methyl violet dye; Agar-agar; Kinetic studies; Adsorption isotherms

## INTRODUCTION

Methyl violet dye is mostly used in textile and paint industries. It is toxic and mutagenic, and because of this, it is harmful for the aquatic environment [1]. In industry, adsorption process is mostly used to treat the wastewater. Adsorption process is the process of separating chemical substances that cause pollution such as toxicity, color and odor, which are difficult to purify using classical purification, by adhering to the surface of a solid material (adsorbent) with chemical and physical bonds. The adsorption process is affected by pH, temperature and surface area of the adsorbent used [2]. Lots of adsorbents such as activated carbon, date seed, wood, zeolite, some waste sources, such as scrap tyre, have been used to remove dye from wastewater [3]. Agar-agar-functionalized activated carbon was used successfully to remove  $Pb^{2+}$  ion from wastewater [4]. This paper results demonstrated that agar-agar functionalization of adsorbent was useful to remove dye from wastewater.

In the present work, dye removal from a synthetic methyl violet solution with rubber powder obtained from scrap tyre functionalized with agar-agar adsorbent (RP-AA) was investigated. The adsorbent was characterized *via* FTIR-ATR spectral analysis to confirm the presence of agar-agar on rubber powder. RP-AA adsorbent was used to remove MV from synthetic wastewater solution and three kinetic isotherm models were applied.

## EXPERIMENTAL

Methyl violet dye ( $C_{24}H_{27}N_3ClH$ ) and agar-agar were purchased from Merck and Sigma-Aldrich, respectively (Fig. 1). Submicron particle size rubber powder ( $<300 \mu$ ) was obtained from scrap tyre waste. 5 g of rubber powder surface was functionalized with 3.75 g of agar-agar in 50 ml of hot water by mixing at 85 °C for 24 h. After functionalization, RP-AA was washed three times with cold water to remove non-adsorbed agar-agar from the medium and dried in vacuum oven at 100 °C. Thermo Fischer Scientific Nicolet 10 model FTIR-ATR spectrophotometer, Sigma 3-18K model ultracentrifuge device, Shimadzu Uvmini-1240 UV Visible spectrophotometer and Daihan Scientific Multi-Heat Mixer were used.

A calibration curve was obtained as  $A=0,1215C+0,0379$ ,  $R^2=0.993$  from the absorbance values at wavelength 578 nm of 2-4-6-8-10 mg/L dye solutions prepared by diluting MV from 1000 mg/L stock solution in pure water.

Methyl violet was removed from synthetic waste water by adsorption on RP-AA. In all measurements, the amount of adsorbent was kept constant as 80 mg at pH 7 and the mixing speed was kept constant as 300 rpm. In adsorption experiments, the effects of time (30-60-90-120-150-180-210-240 min at room temperature in 50 mg/L MV solution), temperature (20-25-30-35-40-45-50 °C in 50 mg/L MV solution for 150 min) and initial concentration (50-100-150-200-250-300-350-400-450-500 mg/L for 150 min at room temperature) of MV dye adsorbed on RP and RP-AA from synthetic waste aqueous media were examined (Fig. 1).

\* To whom all correspondence should be sent:  
E-mail: dsakar@yildiz.edu.tr

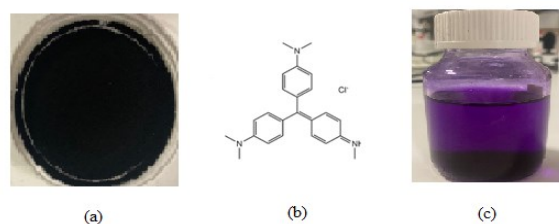


**Figure 1.** Picture of rubber powder (a), methyl violet dye (b), wastewater including methyl violet solution and adsorbent (c)

The adsorption capacity of RP-AA adsorbent, the amount of MV adsorbed at equilibrium, was calculated using Eq. 1:

$$q_e = \frac{(C_o - C_e).V}{w} \quad (1)$$

where  $q_e$  (mg/g) is the adsorbed amount of MV per gram adsorbent,  $C_o$  (mg/L) and  $C_e$  (mg/L) are MV dye solution concentration at the initial and equilibrium stages, respectively.  $V$  (L) is the volume of the MV solution, and  $w$  (g) is the amount of the RP-AA adsorbent.

The dye removal percent yield (RY, %) of the adsorbent was calculated using Eq. 2 [1]:

$$\%RY = \frac{(C_o - C_e)}{C_o} . 100 \quad (2)$$

## RESULTS AND DISCUSSION

FTIR-ATR analysis was carried out to determine the structure and functional group of agar-agar-modified scrap tyre rubber powder adsorbent and the FTIR-ATR spectra of RP and RP-AA are given in Figure 2.

Comparing the FTIR spectra of RP and RP-AA, the intensity of some peaks decreased, some new peaks were formed and some peaks were shifted.

Agar-agar-modified rubber powder showed characteristic bands at  $3310 \text{ cm}^{-1}$  (O–H stretching vibration of hydroxyl group of agar-agar) and  $1147$  (new sharp peak),  $1075$ ,  $994$ ,  $930 \text{ cm}^{-1}$  (C–O and C–C stretching vibrations of pyranose ring common to all polysaccharides)[5]. In order to investigate the contact time of the dye adsorption on adsorbents and to determine the optimum retention time of adsorption capacity, the adsorption removal efficiencies of RP-AA were examined for 30-60-90-120-150-180-210-240 min from the solution containing 50 mg/L dye. After the determined time passed, the batches were centrifuged for 10 min, the adsorption values of the solutions were taken with a UV-VIS spectrophotometer,  $C_e$  values were found from the calibration curve according to their absorbance at 578 nm, and adsorption capacity of adsorbent,  $q_e$  and dye removal yield percent (RY, %)

of RP-AA adsorbent were calculated according to Eqs.1 and 2, respectively, and results are given in Table 1. Time effect on  $ce$ ,  $q_e$ , RY parameters of MV dye removal with RP-AA is shown in Fig. 3.

The average dye removal efficiency was determined as  $37.5 \pm 0.20$  % for dye removal with RP-AA. It is seen that time did not affect the dye removal with RP-AA adsorbent.

The temperature effect on percent dye removal of RP and RP-AA adsorbents was studied within the temperature range of 20-25-30-35-40-45-50 °C in a 50 mg/L MV solution for 150 min.

Dye removal percent yield and adsorption capacity of adsorbents at equilibrium did not change significantly with increased temperature and it was obtained as average  $37.2\% \pm 0.23$ .

### Adsorption isotherms and kinetics

The adsorption isotherm shows the correlation between the adsorption capacity at equilibrium,  $q_e$  and the equilibrium concentration of adsorbate,  $C_e$ . Langmuir [6], Freundlich [7] and Temkin [8] adsorption isotherms were applied to MV adsorption on RP-AA. To plot adsorption isotherms, initial MV concentrations were used as 50-100-150-200-250-300-350-400-450-500 mg/L for 150 min at room temperature on the RP-AA adsorbent. The results are given in Table 3.

The Temkin isotherm adsorption model equation is expressed as follows [8]:

$$q_e = B \ln A + B \ln C_e \quad (3)$$

where  $R$  is universal gas constant ( $\text{J mol}^{-1}\text{K}^{-1}$ ),  $T$  is temperature (K),  $B$  represents  $\frac{RT}{b}$ ,  $A$  is Temkin isotherm equilibrium binding constant ( $\text{L.g}^{-1}$ ),  $b$  is Temkin isotherm constant.

For Temkin adsorption isotherm, the linear  $q_e$  versus  $\ln C_e$  plot was drawn and the Temkin adsorption isotherm parameters,  $A$  and  $b$  were obtained from the slope and the intersection point of this linear plot, respectively. The results are given in Table 4.

The Temkin isotherm corresponding to MV adsorption on RP-AA is plotted in Fig 4.

The regression coefficients of Langmuir, Freundlich and Temkin adsorption isotherms for RP-AA were determined as 0.44, 0.78 and 0.96, respectively. The experimental adsorption data fit well with the Temkin isotherm model for RP-AA since it had a higher correlation value than Freundlich and Langmuir isotherms.

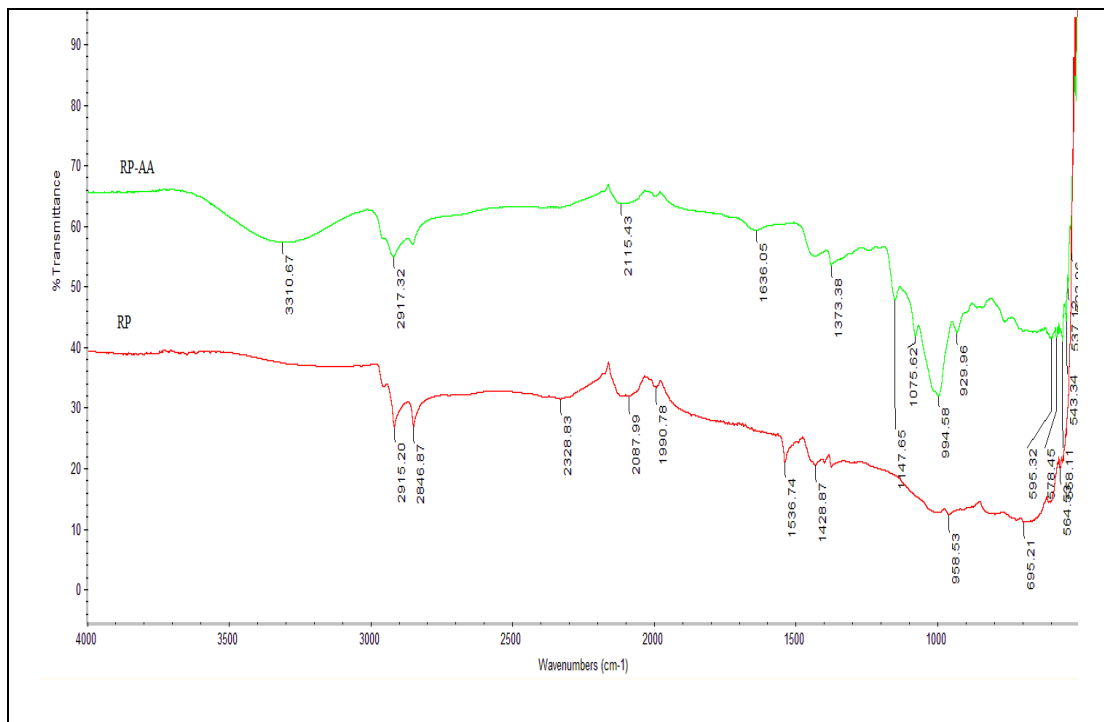


Figure 2. FTIR-ATR spectra of RP and RP-AA adsorbents

Table 1. MV dye solution concentration at the equilibrium stage, dye removal yield percent and adsorption capacity values of RP-AA adsorbents: effect of contact time.

t (min)	A	C <sub>e</sub> (mg/L)	RY (%)	q <sub>e</sub> (mg/g)
30	3.83	31.19	37.61	29.38
60	3.81	31.07	37.85	29.57
0	3.82	31.15	37.69	29.44
120	3.84	31.32	37.35	29.18
150	3.84	31.30	37.39	29.21
180	3.83	31.19	37.63	29.39
210	3.84	31.32	37.36	29.19
240	3.85	31.36	37.29	29.13

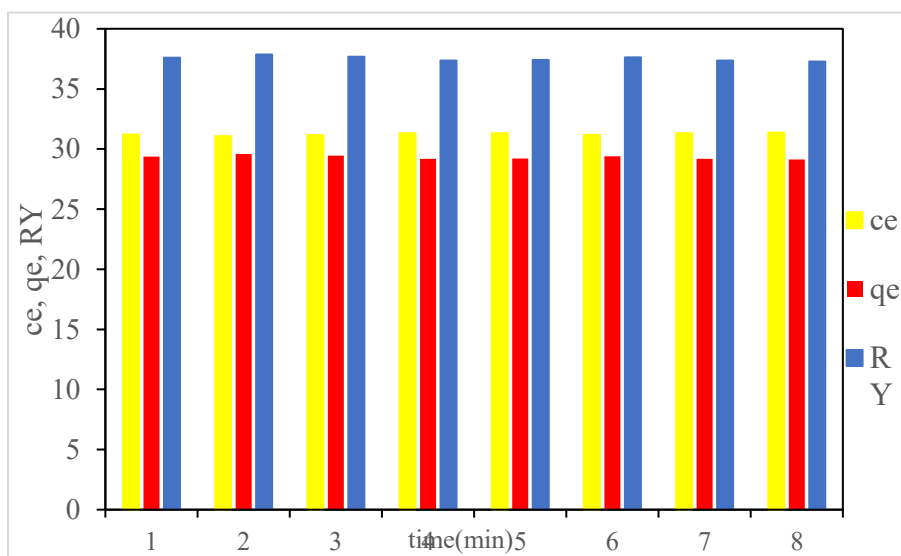


Figure 3. Changes of  $ce$ ,  $qe$  and  $RY$  parameters of MV dye adsorption on RP-AA vs. time (1.30-2.60-3.90-4.120-5.150-6.180-7.210-8.240 min)

**Table 2.** Adsorption of MV on RP-AA adsorbent: temperature effect

T (°C)	A	C <sub>e</sub> (mg/L)	RY (%)	q <sub>e</sub> (mg/g)
20	3.87	31.52	36.97	28.88
25	3.85	31.39	37.22	29.08
30	3.84	31.28	37.44	29.25
35	3.86	31.46	37.06	28.96
40	3.87	31.53	36.94	28.86
45	3.85	31.41	37.18	29.05
50	3.83	31.22	37.56	29.35

**Table 3.** Adsorption of MV on RP-AA adsorbent: concentration effect

C <sub>MV</sub> (mg/L)	A	C <sub>e</sub> (mg/L)	RY (%)	q <sub>e</sub> (mg/g)	lnC <sub>e</sub>
50	3.87	31.57	36.85	28.79	3.45
100	3.91	31.90	68.09	106.39	3.46
150	3.96	32.16	78.56	184.12	3.47
200	3.91	31.88	84.06	262.68	3.46
250	3.98	32.46	87.01	339.90	3.48
300	4.00	32.65	89.12	417.74	3.49
350	4.04	32.91	90.59	495.46	3.49
400	4.05	33.03	91.74	573.39	3.50
450	4.09	33.32	92.59	651.06	3.51
500	4.10	33.49	93.30	728.93	3.51

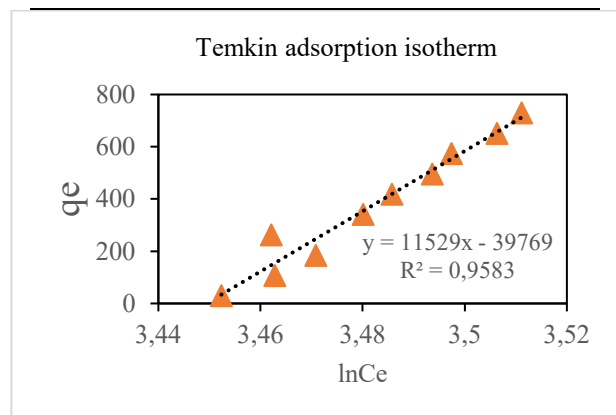


**Figure 4.** Temkin isotherm corresponding to MV dye adsorption on RP-AA

Adsorption kinetics reveals the adsorbed amount as a function of time and gives information about the adsorption speed, mechanism and adsorbent quality. The pseudo-first [9], pseudo-second order [10] and Webber-Morris intraparticle diffusion models (W-M

ID) [11] were applied for MV dye adsorption on RP-AA and kinetic parameters for the adsorption of MV on RP-AA adsorbent are given in Table 5. The kinetic model plots are given in Fig. 5.

**Table 4.** Parameters obtained from Freundlich and Temkin isotherms of MV adsorption on RP-AA adsorbent

Isotherm	RP-AA adsorbent	
Freundlich	K <sub>F</sub>	3.4.10 <sup>-65</sup>
	n	0.023
	R <sup>2</sup>	0.79
Temkin	B	11529
	lnA	-3.45
	b	0.21
	R <sup>2</sup>	0.96

**Table 5.** Adsorption kinetic parameters corresponding to MV adsorption on RP-AA

Kinetic Model	Parameters	RP-AA
Pseudo 1 <sup>st</sup>	k <sub>1</sub>	-7.10 <sup>-5</sup>
	R <sup>2</sup>	0.49
Pseudo 2 <sup>nd</sup>	k <sub>2</sub>	1.2.10 <sup>-3</sup>
	R <sup>2</sup>	0.99
W-M ID	k <sub>3</sub>	-0.03
	C	29.66
	R <sup>2</sup>	0.47

Comparing the correlation coefficients of the three kinetic models, it is seen that the kinetics of MV adsorption onto the RP-AA followed the pseudo-second-order model.

### CONCLUSION

In this manuscript, the effects of time, temperature and concentration on the methyl violet removal from synthetic wastewater with agar-agar functionalized rubber powder obtained from scrap tyres were investigated. It was concluded that time and temperature did not affect the dye removal efficiency of the RP-AA adsorbent. The adsorption data and kinetic models were fitted into Langmuir, Freundlich and Temkin isotherms. The Temkin adsorption isotherm and pseudo-second-order kinetic model were found to have the highest regression value and, hence, the best fit. It could be concluded that submicron particle size rubber powder adsorbent obtained from scrap tyre modified with agar-agar is a potential and active biosorbent for removal of methyl violet dye from its aqueous solution and industrial wastewater treatment.

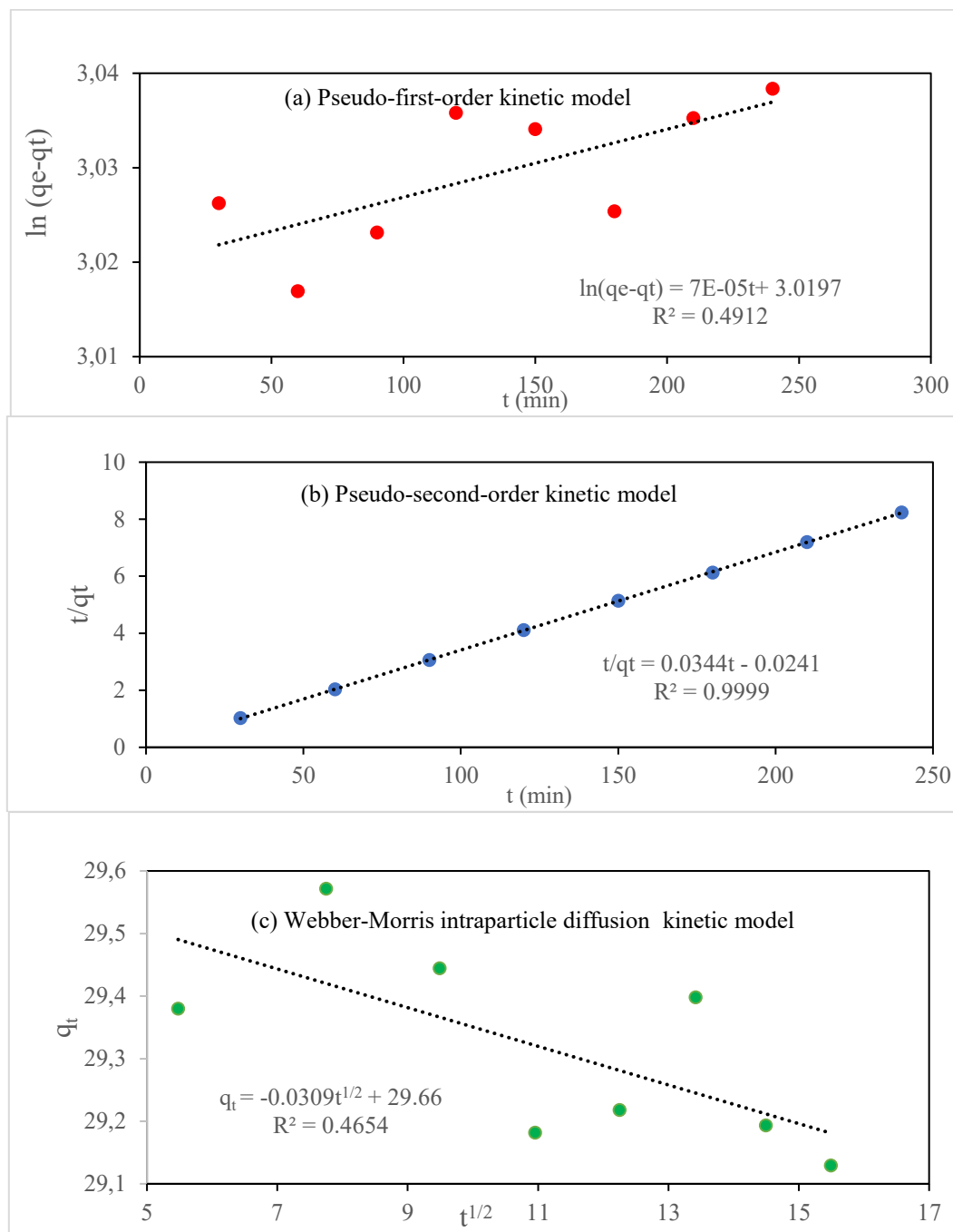


**Figure 5.** Kinetic studies: (a) pseudo-first-order, (b) pseudo-second-order, and (c) Weber-Morris intraparticle diffusion kinetic plots for the adsorption of MV onto RP-AA

#### REFERENCES

1. Y. Kerzabi, A. Benomara, S. Merghache, *Global NEST Journal*, **24**(4), 706 (2022).
2. S. Sharma, A. Bhattacharya, *Appl. Water Sci.*, **7**, 1043 (2017).
3. G. Crini, E. Lichtfouse, L. Wilson, N. Morin-Crini, *Green Adsorbents for Pollutant Removal*, Springer Nature, 2018, vol. 18, p.23.
4. S. Saidi, F. Boudrahem, I. Yahiaoui, F. Aissani-Benissad, *Water Science and Technology*, 1316 (2019).
5. E. Gómez-Ordóñez, P. Rupérez, *Food Hydrocolloids*, **25**(6), 1514 (2011).
6. I. Langmuir, *J. Am. Chem. Soc.* **40**, 1362 (1918).
7. N. D. Hutson, R. T. Yang, *J. Colloid Interf. Sci.*, 189 (2000).
8. M. Temkin V., Pyzhev, *Acta Physicochimica U.S.S.R.*, **12**, 327 (1940).
9. S. Lagergren, *Kungliga Svenska Vetenskapsakademiens Handlingar*, **24** (4), 1 (1898).
10. Y. S. Ho, G. McKay, *Process Safety and Environmental Protection*, **76** (2), 183 (1998).
11. W. J. Weber, J. C. Morris, *Journal of the Sanitary Engineering Division*, **89** (2), 31 (1963).

## Effects of additives on mechanical and barrier properties of polyhydroxyalkanoate-derived bionanocomposite films by solution casting

Ö. Yolaçan<sup>1,2</sup>, S. Deniz<sup>1\*</sup>

<sup>1</sup>*Yıldız Technical University, Department of Chemical Engineering, İstanbul, Turkey*

<sup>2</sup>*Huhtamaki Flexibles, İstanbul, Turkey*

Received June 4, 2024; Accepted: August 17, 2024

Polyhydroxyalkanoates are naturally occurring, non-toxic aliphatic polyesters. Nanocomposite fabrication is an effective and cost-efficient approach to modulate polymer properties. Within the scope of this study, poly(3-hydroxybutyrate-co-4-hydroxybutyrate) (P3HB4HB)/poly(3-hydroxybutyrate) (P3HB) (PHAs) bioblends were developed by using solution casting and extrusion methods. The optimum compositions of PHAs bioblends were determined as 80% P3HB4HB for solution casting method and 60% P3HB4HB for extrusion method. To obtain PHAs-based bionanocomposites, two types of copper-based metal organic frameworks (CuMOF and GO@CuMOF) nanocrystals (0.5; 1.0 wt% and 0.1; 0.5 wt%), and bentonite, sepiolite, high-purity sepiolite (1; 2; 3 wt%) nanoclays were added to the PHAs bioblend matrix. The effects of nanofillers on mechanical and optical properties, barrier performance and thermal behavior of bionanocomposites were investigated. When the mechanical properties of bionanocomposites obtained by the solution casting method were examined according to the polyethylene reference, the optimum ratio of all nanoclays was 3% while the optimum ratios of CuMOF nanocrystals were 1 and 0.1, respectively. PHAs/HPS-3 bionanocomposite films showed a 62.5% improvement in oxygen transmittance rate (OTR) compared to the flexible polyethylene reference. Material properties were recognized through solution casting studies, and it was determined that bionanocomposites have gained good qualities for flexible packaging with the use of CuMOF and high-purity sepiolite (HPS) nanofillers.

**Keywords:** Polyhydroxyalkanoate, solution casting, extrusion, bioblend, high-purity sepiolite

### INTRODUCTION

Traditional plastics ensure perfect functionality for use as flexible packaging materials, possessing mechanical and barrier properties in concur with low production costs [1]. Use of biopolymers in the sustainable packaging industry has shown intense progress because of recent trends in the market moving toward green packaging, recyclability and waste reduction [2]. Sustainability is vital as it encourages politics, industry and academia to develop sustainable and circular alternatives to preserve resources by focusing on biopolymers [3]. Biopolymers are polymers which include covalently bonded monomeric units, to compose chain-like molecules. Biopolymers are renewable and have, therefore, the capability to be degraded through the action of naturally occurring organisms leaving behind environmentally harmless organic by-products such as CO<sub>2</sub> and H<sub>2</sub>O [4]. Polyhydroxyalkanoates (PHAs) are produced in nature by bacterial fermentation. Depending on the carbon atoms, PHAs are classified in three groups: short-chain length PHAs (sCLPHAs) (4 to 6 carbon atoms), medium-chain length PHAs (mCL-PHAs) (more than six carbons), and long-chain length (ICL-

PHAs) (more than 14 carbons) [5]. Poly(3-hydroxybutyrate-co-4-hydroxybutyrate) (P3HB4HB), poly(3-hydroxybutyrate-co-3-hydroxyvalerate) (P3HB3HV), poly(3-hydroxybutyrate) (P3HB), polyhydroxyhexanoate (PHH) and polyhydroxyoctanoate (PHO) are widely used copolymers of PHAs. P3HB, P3HB4HB and P3HB3HV are the most popular among them [5]. In the study conducted by Vostrejs and his team in 2020, they intended to research the thermal, mechanical and gas permeability properties of crystalline PHB blended with amorphous PHA, to determine the effect of grape seed lignin association on thermal and mechanical properties of PHB/PHA blends and to assess the antibacterial effect of grape seed lignin associated in PHB/PHA films [6]. Within the scope of this study, a solution casting method and extrusion methods were employed to prepare P3HB4HB/PHB bioblends using a plasticizer (Joncryl® ADR4468). After the determination of optimum bioblend composition, P3HB4HB/PHB bionanocomposites were prepared with copper-based metal organic framework (CuMOF) and GO@CuMOF hybrid nanocrystals and different nanoclay types (bentonite, sepiolite, high-purity

\* To whom all correspondence should be sent:  
E-mail: deniz@yildiz.edu.tr

sepiolite). CuMOF nanocrystals were synthesized by the solvothermal synthesis method known as MOF199 or HKUST-1 [7]. While bentonite and sepiolite have a layered structure, high-purity sepiolite has a needle-point structure. The effects of nanofillers on mechanical and optical properties, barrier performance and thermal behavior of biocomposites were investigated.

### EXPERIMENTAL

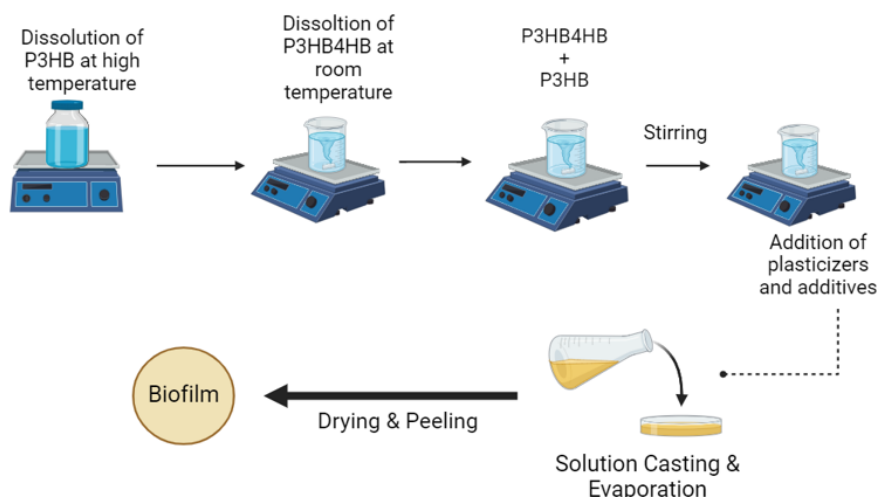
In the preparation of bionanocomposite films by solution casting method, firstly various ratio studies of P3HB4HB/P3HB (PHAs) in different composition (50:50; 60:40; 70:30; 80:20 wt%) were carried out with plasticizer (J; Joncryl® ADR 4468), and the optimum ratio of PHAs bioblends was determined. By adding metal organic frameworks based nanofillers (0.1; 0.5; 1%) and different nanoclay types (1; 2; 3%) into PHAs bioblend, bionanocomposites were prepared and subjected to characterization tests. The solution casting method is shown in Scheme 1.

In extrusion studies, after obtaining PHAs granules with different ratios in a twin-screw extruder then bioblends were produced by blown film extrusion. The optimum bioblend composition and operating parameters have been determined. Extrusion studies continued by adding 3% high purity sepiolite to the PHAs bioblend structure. The mechanical, optical, barrier and thermal properties of the PHAs/HPS-3 bionanocomposite were examined.

### MATERIALS

#### Preparation of bioblend films

Poly(3-hydroxybutyrate-co-4-hydroxybutyrate) (P3HB4HB) was supplied from CJ Biomaterials Co., Ltd. Poly(3-hydroxybutyrate) (P3HB) was purchased from Helian Polymers Co., Ltd. Joncryl® ADR 4468 (J) was accommodated from “BASF” company and used as plasticizer. Chloroform was provided from Interlab Co., Ltd. Bentonite (B), sepiolite (S) and high purity sepiolite (HPS) were supplied from Tolsa.



**Scheme 1.** Schematic representation of the solution casting method

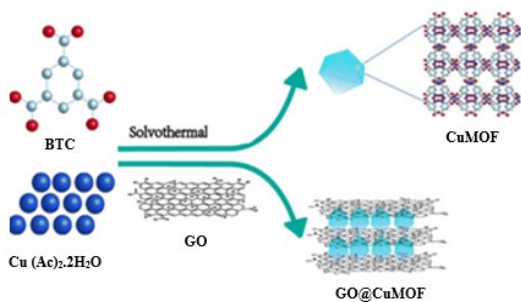


**Fig. 1.** Images of PHAs bioblend granules and blown film production

*Synthesis of CuMOF and GO@CuMOF nanocrystals*

1,3,5-Benzenetricarboxylic acid (BTC) was obtained from “Analitik Kimya” company. Copper acetate (Cu(Ac)<sub>2</sub>·2H<sub>2</sub>O) and triethylamine (TEA) were supplied from “Acros Organics” company. N,N-Dimethylformamide was obtained from “Tekkim” company. Ethanol was provided by “Sigma Aldrich” company. Graphene oxide (GO) was purchased from “Aerofen” company.

CuMOF nanocrystals were synthesized in the laboratory under room conditions by the solvothermal synthesis method, known as MOF199 or HKUST-1 [7].



**Scheme 2.** Schematic representation of the synthesis of CuMOF and GO@CuMOF hybrid nanocrystals [8]

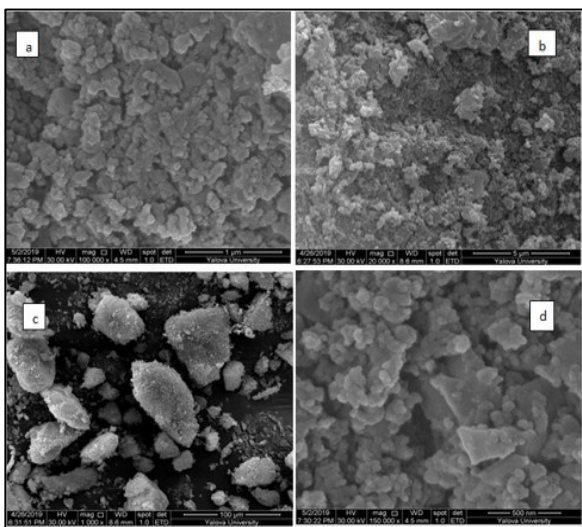


**Fig. 2.** SEM images of CuMOF nanocrystals (a:100000×; b:20000×; c:1000×; d:150000×)

It is seen from the SEM images the sizes of CuMOF nanocrystals were distributed in the range of 40-60 nm and there was aggregation in the synthesized CuMOF nanocrystals.

BET analysis results of CuMOF and GO@CuMOF nanocrystals - surface area, average pore volume and pore diameter values are shown in Table 1. The results show compatibility with the literature [9].

**Table 1.** BET analysis results of CuMOF and GO@CuMOF nanocrystals

Nanoparticles	BET surface area (m <sup>2</sup> .g <sup>-1</sup> )	Average pore volume (cm <sup>3</sup> .g <sup>-1</sup> )	Average pore diameter (nm)
CuMOF	1322.96	0.42	3.17
GO@CuMOF	227.21	0.12	0.32

Chemical composition and notation of P3HB4HB/P3HB (PHAs) bioblends by solution casting method are given in Table 2.

**RESULTS AND DISCUSSION:**

*Preparation of PHAs bionanocomposite films with solution casting method*

Mechanical, optical, barrier and thermal characteristics of PHAs bionanocomposites were examined. Mechanical properties of PHAs bioblends prepared with different ratios by solution casting method are shown in Table 3. When various pure and plasticizer containing bioblends were examined, it was determined that the optimum blend ratio was PHAs (80/20) compared to the reference polyethylene. Table 4 shows that the optimum usage rates of CuMOF and GO@CuMOF nanocrystals are 1% and 0.1%, respectively. In Table 5, the optimum nanoclay rates for bentonite, sepiolite and high purity sepiolite were determined as 3% compared to reference polyethylene.

Optical and barrier properties of PHAs bionanocomposites prepared by solution casting method are given in Table 6. The gloss value increased with the compatibility between the two biopolymers and the increase in the ratio of high purity sepiolite contribution. When the barrier results were evaluated, the inherently good OTR characteristics of PHA and PHB showed an improvement with the addition of CuMOF and high-purity sepiolite nanofillers compared to the reference polyethylene [10].

DSC curves of PHAs bionanocomposites are examined in Figure 3. It is seen that only CuMOF and HPS additives increased the bioblend crystallinity. Since polyethylene is a semi-crystalline raw material, the increase in crystallinity is a sign of the transition to flexible packaging.

*Preparation of PHAs bionanocomposite films with extrusion*

Mechanical, optical, barrier and thermal characterizations of the prepared biofilms were carried out. 100 μ polyethylene film was chosen as reference polyethylene.

**Table 2.** Chemical composition and notation of P3HB4HB/P3HB (PHAs) bioblends by solution casting method

Code	P3HB4HB (wt.%)	P3HB (wt.%)	Plasticizer (J, wt.%)	Nanofiller (wt.%)
P3HB4HB/P3HB	80	20	0	0
P3HB4HB/P3HB/J (PHAs)	80	20	1	0
PHAs/CuMOF-0.5	80	20	1	0.5
PHAs/CuMOF-1	80	20	1	1
PHAs/GO@CuMOF-0.1	80	20	1	0.1
PHAs/GO@CuMOF-0.5	80	20	1	0.5
PHAs/B-1	80	20	1	1
PHAs/B-2	80	20	1	2
PHAs/B-3	80	20	1	3
PHAs/S-1	80	20	1	1
PHAs/S-2	80	20	1	2
PHAs/S-3	80	20	1	3
PHAs/HPS-1	80	20	1	1
PHAs/HPS-2	80	20	1	2
PHAs/HPS-3	80	20	1	3

**Table 3.** Mechanical properties of PHAs bioblends prepared with different ratios by solution casting method

Bioblend Films (Thickness: 100±5 µ)	Tensile Strength (Mpa)	Elongation at Break (%)	E-Modulus (N/mm <sup>2</sup> )
Polyethylene (Reference film)	24±2	322±2	283±3
P3HB4HB80P3HB20	8±2	468±2	193±3
P3HB4HB70P3HB30	9±2	120±3	346±2
P3HB4HB60P3HB40	12±1	204±1	494±4
P3HB4HB50P3HB50	15±2	119±1	740±2
P3HB4HB80P3HB20/J	6±1	352±2	204±2
P3HB4HB70P3HB30/J	9±1	179±1	369±1
P3HB4HB60P3HB40/J	12±2	57±3	586±2
P3HB4HB50P3HB50/J	13±1	68±2	588±2

**Table 4.** Mechanical properties of PHAs/CuMOFs bionanocomposites by solution casting method

Bionanocomposite (Thickness: 100±5 µ)	Tensile Strength (Mpa)	Elongation at Break (%)	E-Modulus (N/mm <sup>2</sup> )
Polyethylene (Reference film)	24±2	322±2	283±3
P3HB4HB/P3HB	8±1	468±2	193±3
PHAs	6±1	352±2	204±2
PHAs/CuMOF-0.5	7±1	319±1	230±1
PHAs/CuMOF-1	10±2	423±3	256±1
PHAs/GO@CuMOF-0.1	8±1	416±2	233±2
PHAs/GO@CuMOF-0.5	7±1	446±2	174±1

**Table 5.** Mechanical properties of PHAs/nanoclay bionanocomposites by solution casting method

Bionanocomposite Films (Thickness: 100±5 µ)	Tensile Strength (Mpa)	Elongation at Break (%)	E-Modulus (N/mm <sup>2</sup> )
Polyethylene (Reference film)	24±2	322±2	283±3
P3HB4HB/P3HB	8±2	468±2	193±3
PHAs	6±1	352±2	204±2
PHAs/B-1	9±1	279±1	365±1
PHAs/B-2	8±2	270±3	304±1
PHAs/B-3	8±1	323±3	293±3
PHAs/S-1	7±1	274±2	287±2
PHAs/S-2	9±2	301±1	374±1
PHAs/S-3	8±1	224±1	341±1
PHAs/HPS-1	9±3	287±3	214±2
PHAs/HPS-2	9±1	299±1	238±3
PHAs/HPS-3	10±2	318±2	276±1

**Table 6.** Optical and barrier properties of PHAs bionanocomposites by solution casting method

Bionanocomposite Films (Thickness: 100±5 μ)	Gloss (60°) (%)	OTR (cc/m <sup>2</sup> )
<i>Polyethylene (Reference film)</i>	77±3	408±3
<i>P3HB4HB/P3HB</i>	22±2	344±1
<i>PHAs</i>	28±3	325±2
<i>PHAs/CuMOF-0.5</i>	31±1	297±3
<i>PHAs/GO@CuMOF-0.1</i>	29±1	318±2
<i>PHAs/B-3</i>	33±3	338±2
<i>PHAs/S-3</i>	34±2	301±1
<i>PHAs/HPS-3</i>	37±3	286±1

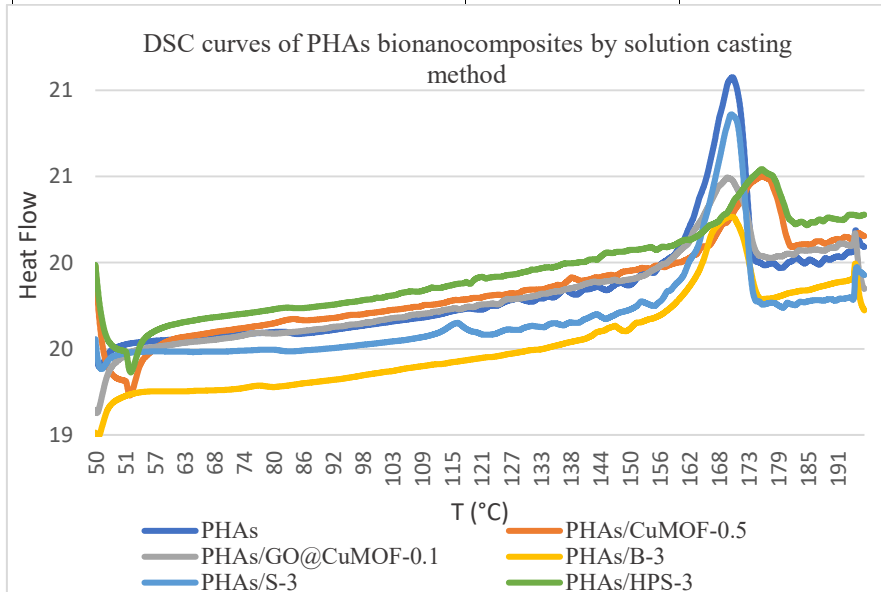


**Fig. 3.** DSC curves of PHAs bionanocomposites by solution casting method

**Table 7.** Mechanical properties of PHAs bioblends prepared with different ratios by extrusion method

Bioblend Films (Thickness: 100±5 μ)	Tensile Strength (Mpa)	Elongation at Break (%)	E-Modulus (N/mm <sup>2</sup> )
<i>Polyethylene (Reference film)</i>	24±2	322±2	283±3
<i>P3HB4HB50/P3HB50</i>	9±1	804±1	377±2
<i>P3HB4HB55/P3HB45</i>	10±2	797±3	354±4
<i>P3HB4HB60/P3HB40</i>	11±1	789±1	346±2
<i>P3HB4HB50P/P3HB50/J</i>	12±2	802±2	339±1
<i>P3HB4HB55/P3HB45/J</i>	12±2	813±3	326±3
<i>P3HB4HB60/P3HB40/J</i>	14±1	822±2	313±2

Mechanical properties of PHAs bioblends prepared with different ratios by extrusion method were given in Table 7. When various pure and plasticizer bioblend studies were examined compared to reference polyethylene, it was determined that the optimum composition of PHAs bioblend by extrusion method was as 60% of P3HB4HB and 40% of P3HB in presence of plasticizer.

Mechanical properties of PHAs/nanoclay bionanocomposites by extrusion method are shown in Table 8.

When the mechanical properties were evaluated according to bionanocomposites containing high purity sepiolite, it was determined that the optimum nanoclay usage rate was 3%.

Optical and barrier properties of PHAs bionanocomposites by extrusion method were given in Table 9. The gloss value increased with the compatibility between the two biopolymers and the increase in the ratio of high purity sepiolite contribution. Adding 3% HPS to PHAs bioblend, whose components have good OTR values on their own, improved the OTR value [10].

**Table 8.** Mechanical properties of PHAs/nanoclay bionanocomposites by extrusion method

Bionanocomposite Films (Thickness: 100±5 µ)	Tensile Strength (Mpa)	Elongation at Break (%)	E-Modulus (N/mm <sup>2</sup> )
<i>Polyethylene (Reference film)</i>	24±2	322±2	283±3
<i>P3HB4HB60/P3HB40</i>	11±1	789±1	346±1
<i>P3HB4HB60/P3HB40/J (PHAs)</i>	14±2	822±2	313±3
<i>PHAs/HPS-1</i>	9±1	566±3	322±2
<i>PHAs/HPS-2</i>	10±1	403±3	318±3
<i>PHAs/HPS-3</i>	12±2	387±2	306±1

**Table 9.** Optical and barrier properties of PHAs bionanocomposites by extrusion method

Bionanocomposite Films (Thickness: 100±5 µ)	Gloss (60°) (%)	OTR (cc/m <sup>2</sup> )
<i>Polyethylene (Reference film)</i>	77±3	408±3
<i>P3HB4HB60/P3HB40</i>	24±2	302±2
<i>PHAs</i>	28±3	287±3
<i>PHAs/HPS-1</i>	34±2	258±2
<i>PHAs/HPS-2</i>	39±1	245±1
<i>PHAs/HPS-3</i>	48±3	225±1

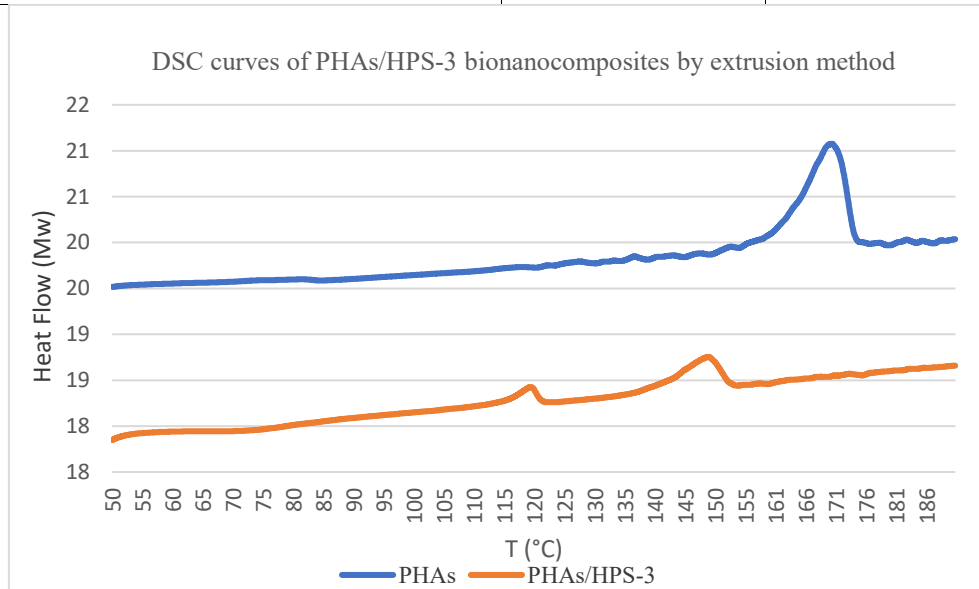


**Fig. 4.** DSC curves of PHAs/HPS-3 bionanocomposite by extrusion method

As seen in Figure 4 the addition of 3% HPS nanoclay to the PHAs bioblend enabled the structure to transition to a flexible form.

### CONCLUSION

In this study, where sustainability and newly developing polyhydroxyalkanoate technology were discussed, PHAs bionanocomposite films were examined by solution casting and extrusion methods. Joncryl ADR 4468 was used as plasticizer, nanoclay types and metal organic frameworks containing nanofillers were used. From the mechanical and optical results, it has been determined that metal organic frameworks containing nanofillers should be used up to a maximum of 1%, while optimum results are achieved with 3% additives in nanoclay types. When the barrier results were evaluated, the

inherently good OTR characteristics of P3HB4HB and P3HB showed improvement with the use of CuMOF and high purity sepiolite nanofillers compared to the reference polyethylene. The results of the study are promising in terms of recognizing material properties with the solution casting method and obtaining recipes for transition to large production with twin screw and blown film extrusion.

**Acknowledgement:** This study was conducted by utilizing Tübitak-2244 Industry Doctorate Program (Project No: 118C076) under the cooperation of Yıldız Technical University and R&D Center of Elif Plastik Ambalaj San. ve Tic. A.Ş.-Huhtamaki Flexibles-Istanbul.

REFERENCES

1. C. R. Álvarez-Chávez, S. Edwards, R. Moure-Eraso, K. Geiser, *J. Clean. Prod.*, **23**, 47 (2012).
2. K. H. Prashanth, R. Tharanathan, *Trends Food Sci. Technol.* **18**, 117 (2007).
3. C. L. Reichert, E. Bugnicourt, M. B. Coltelli, P. Cinelli, A. Lazzeri, I. Canesi M. Schmid, *Polymers*, **12** (7), 1558 (2020).
4. X. Z. Tang, P. Kumar, S. Alavi, K. P. Sandeep, *Crit. Rev. Food Sci. Nutr.*, **52** (5), 426 (2012).
5. A.B. Sathya, V. Sivasubramanian, A. Santhiagu, C. Sebastian, R. J. Sivashankar, *Polym. Environ.*, **26** (9), 3995 (2018).
6. P. Vostrejs, D. Adamcová, M. D. Vaverková, V. Enev, M. Kalina, M. Machovsky, A. Kovalcik, *RSC Advances*, **10** (49), 29202 (2020).
7. F. Z. N. Azizi, R. Homayoon, *Petrol. Sci. Technol.*, **37** (24), 2412 (2019).
8. S. Wang, B. Ye, C. An, J. Wang, Q. Li, *J. Materials Sci.*, **54** (6), 4928 (2019).
9. H. Sanaeepur, R. Ahmadi, A. E. Amooghin, D. Ghanbari, *J. Membr. Sci.*, **573**, 234 (2019.)
10. X. Wang, Z. Chen, X. Chen, J. Pan, K. Xu, *J. Appl. Polym. Sci.*, **117** (2), 838 (2010).

## Optimization and determination of the factors influencing the delamination in graphene/MoS<sub>2</sub>/PET nanocomposite under mechanical loading

B. Boyadjiev<sup>1\*</sup>, T. Petrova<sup>1</sup>, R. Vladova<sup>1</sup>, E. Kirilova<sup>1</sup>, A. Apostolov<sup>1</sup>, A. Moravski<sup>2</sup>

<sup>1</sup> Institute of Chemical Engineering, Bulgarian Academy of Sciences, Acad. G. Bonchev Str., Bl.103, 1113 Sofia, Bulgaria

<sup>2</sup> Faculty of Mathematics and Informatics, Sofia University "St. Kliment Ohridski", 5 James Bourchier Blvd., 1164 Sofia, Bulgaria

Received June 3, 2024; Accepted: August 17, 2024

The current theoretical study is devoted to the identification of the factors influencing the interface shear stress and respectively, the possibility of delamination appearing in three-layer nanocomposite structure graphene/MoS<sub>2</sub>/PET under mechanical loading. A model criterion for delamination in the structure is proposed and the model interface shear stress is calculated at different geometry and external loads [1]. Then, a multi-parametric optimization procedure is performed which shows the exact geometrical and external factors influencing the interface shear stress value – layer's thickness, load and length of the considered nanocomposite structure. The obtained results could be used to predict the safe design and working conditions in similar nanocomposite devices or parts of them, as sensors, nano- and optical electronic devices, energy devices, etc.

**Keywords:** Multi-parameter optimization; graphene/MoS<sub>2</sub>/PET nanocomposite; interface shear stress; delamination.

### INTRODUCTION

In the last ten years, the combinations of two and more 2D nanomaterials with different substrates, and respectively, the investigation of their properties, are in the focus of scientists in the world [3, 4, 6-10]. In [3, 4] and [7, 10] graphene/MoS<sub>2</sub> or WS<sub>2</sub>/MoS<sub>2</sub> were combined with polymers or Si/SiO<sub>2</sub> as parts of different electronic and sensor devices, etc. The obtained heterostructures and their properties, were studied mostly experimentally. The performance gain-oriented nano-structurization has opened a new pathway for tuning mechanical features of solid matter vital for application and maintained performance [8].

The 2D materials and their heterostructures offer excellent mechanical flexibility, optical transparency, and favorable transport properties for realizing electronic, sensing, and optical systems on arbitrary surfaces [4, 9]. The mechanical and physical properties of those heterostructures formed by stacking different two-dimensional materials show great potential for the next generation of electronic and optoelectronic materials. But, the interfacial mechanical behavior of those heterostructures with different substrates is still a critical problem in various fields [3, 10]. Understanding the mechanical properties and critical limits for safety work (without failure) in the

structure is extremely significant in the engineering [3].

The aim of this work is to find the optimal values of geometry (length and thicknesses of all three layers), as well as the maximal value of external load in graphene/MoS<sub>2</sub>/PET nanocomposite under mechanical loading, without delamination in it. The analytical solutions for ISS and model criteria guaranteeing no delamination in the nanocomposite [1] are implemented in the multi-parameter optimization problem. Two optimization procedures (with genetic algorithms [2] and Mathematica) were defined and solved with objective function – the model criteria for ISS limit. As a result, different sets of optimal geometry configurations of the layers (length and thicknesses of all three layers) and optimal load in the considered nanocomposite structure, have been obtained.

### Mathematical model

The mathematical model of the representative volume element (Fig. 1) of the three-layer statically loaded nanocomposite structure graphene/MoS<sub>2</sub>/PET describing the axial shear stress  $\sigma_1(x)$  is created using a two-dimensional stress-function method [1]. The model is described with the fourth-order ordinary differential equation (ODE) (1) with constant coefficients  $D_i$ :

$$2D_2\sigma_1'''' + (2 - 2D_4)\sigma_1'' + 2D_1\sigma_1 + D_5 = 0 \quad (1)$$

\* To whom all correspondence should be sent:  
E-mail: [boyan.boyadjiev@iche.bas.bg](mailto:boyan.boyadjiev@iche.bas.bg)

This mathematical model is created by making the following model assumptions:

1. The axial stresses in the layers are assumed to be functions of axial coordinate  $x$  only.

2. In the MoS<sub>2</sub> interface layer the axial stress is negligible in respect to the same ones in the other two layers.

3. All stresses in the layers (axial, normal (peel) and shear stresses) are determined under the assumption of the plane-stress formulation.

The interface layer is simulated by the approach in [5].

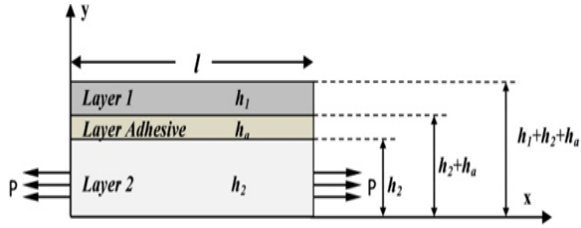


**Fig. 1.** Representative volume element of the three-layer nanocomposite structure. Layer 1 – graphene, Layer interface – MoS<sub>2</sub>, Layer 2 - PET

Boundary and contact conditions for stresses  $\sigma_{xx}^{(i)}$ ,  $\sigma_{xy}^{(i)}$ ,  $\sigma_{yy}^{(i)}$  of the layers  $i = 1, a, 2$  are:

For layer (1):

$$\begin{aligned} \sigma_{xx}^{(1)} &= \begin{cases} 0 & \text{if } x = 0; \\ 0 & \text{if } x = l; \end{cases} \\ \sigma_{xy}^{(1)} &= \begin{cases} 0 & \text{if } x = 0; \\ 0 & \text{if } x = l; \end{cases} \end{aligned} \quad (2)$$

$$y \in [h_2 + h_a, h_1 + h_2 + h_a].$$

$$\begin{aligned} \sigma_{yy}^{(1)} &= \begin{cases} 0 & \text{if } y = h_1 + h_2 + h_a; \\ \sigma_{yy}^{(a)} & \text{if } y = h_2 + h_a; \end{cases} \\ \sigma_{xy}^{(1)} &= \begin{cases} 0 & \text{if } x = h_1 + h_2 + h_a; \\ \sigma_{xy}^{(a)} & \text{if } x = h_2 + h_a; \end{cases} \quad x \in [0, l]. \end{aligned} \quad (3)$$

For layer (a):

$$\begin{aligned} \sigma_{xx}^{(a)} &= \begin{cases} 0 & \text{if } x = 0; \\ 0 & \text{if } x = l; \end{cases} \\ \sigma_{xy}^{(a)} &= \begin{cases} 0 & \text{if } x = 0; \\ 0 & \text{if } x = l; \end{cases} \end{aligned} \quad (4)$$

$$y \in [h_2, h_2 + h_a].$$

$$\begin{aligned} \sigma_{yy}^{(a)} &= \begin{cases} \sigma_{yy}^{(1)}(x, h_2 + h_a) & \text{if } y = h_2 + h_a; \\ \sigma_{yy}^{(2)}(x, h_2) & \text{if } y = h_2; \end{cases} \\ \sigma_{xy}^{(a)} &= \begin{cases} \sigma_{xy}^{(1)}(x, h_2 + h_a) & \text{if } y = h_2 + h_a; \\ \sigma_{xy}^{(2)}(x, h_2) & \text{if } y = h_2; \end{cases} \end{aligned} \quad (5)$$

$$x \in [0, l].$$

For layer (2):

$$\begin{aligned} \sigma_{xx}^{(2)} &= \begin{cases} \sigma_0 & \text{if } x = 0; \\ \sigma_0 & \text{if } x = l; \end{cases} \\ \sigma_{xy}^{(2)} &= \begin{cases} 0 & \text{if } x = 0; \\ 0 & \text{if } x = l; \end{cases} \end{aligned} \quad (6)$$

$$y \in [0, h_2].$$

$$\begin{aligned} \sigma_{yy}^{(2)} &= \begin{cases} \sigma_{yy}^{(a)}(x, h_2) & \text{if } y = h_2; \\ 0 & \text{if } y = 0; \end{cases} \\ \sigma_{xy}^{(2)} &= \begin{cases} \sigma_{xy}^{(a)}(x, h_2) & \text{if } y = h_2; \\ 0 & \text{if } y = 0; \end{cases} \end{aligned} \quad (7)$$

$$x \in [0, l].$$

The analytical solution of the ODE equation (1) for the axial stress  $\sigma_1(x)$  involves the discriminant of the respective characteristic equation. That discriminant can be either positive or negative, so the roots can be real or complex numbers, respectively. The sign of the discriminant depends on the thicknesses and material properties of the structure layers described by the coefficients  $D_i$ .

The possible general solutions of (1) for the axial stress  $\sigma_1(x)$  are:

$$\sigma_1 = C_1 e^{\lambda_1 x} + C_2 e^{\lambda_2 x} + C_3 e^{\lambda_3 x} + C_4 e^{\lambda_4 x} - A. \quad (8)$$

$$\begin{aligned} \sigma_1 &= e^{-\alpha x} [M_1 \cos(\beta x) + M_2 \sin(\beta x)] + \\ &+ e^{\alpha x} [M_3 \cos(\beta x) + M_4 \sin(\beta x)] - A. \end{aligned} \quad (9)$$

where (8) is the solution for the case with 4 real roots  $\lambda_i$  and (9) is the solution for the case with 4 complex roots  $\pm(\alpha \pm i\beta)$ .

In (8) and (9)  $C_i$  and  $M_i$  are the integration constants in the model solution, determined from the boundary conditions (2)–(7). The constant  $A$  is the solution for non-homogeneous ODE and depends on the external static load  $\sigma_0 = P/h_2$  and Young's modulus and thicknesses of the first and third layer in the structure as  $A = D_5/2D_1$  or:

$$A = \frac{\sigma_0 E^{(1)}}{\rho E^{(1)} + E^{(2)}}. \quad (10)$$

After finding solution for axial stress  $\sigma_1$ , all other stresses in the layers of the considered graphene/MoS<sub>2</sub>/PET structure can be obtained using this two-dimensional model relations:

$$\begin{aligned} \sigma_{xx}^{(1)} &= \sigma_1(x) = \sigma_1, & \sigma_{yy}^{(1)} &= \frac{1}{2}(y - y_t)^2 \sigma_1'', \\ \sigma_{xy}^{(1)} &= (y_t - y) \sigma_1', & \sigma_{xx}^{(a)} &\equiv 0, & \sigma_{xy}^{(a)} &= h_1 \sigma_1', \\ \sigma_{yy}^{(a)} &= \left[ \frac{h_1^2}{2} + h_1(c - y) \right] \sigma_1', & \sigma_{xx}^{(2)} &= \sigma_0 - \rho \sigma_1, \\ \sigma_{yy}^{(2)} &= \frac{-\rho}{2} [y^2 - y(y_t + h_a)] \sigma_1'', & \sigma_{xy}^{(2)} &= \rho y \sigma_1', \end{aligned}$$

where  $\rho = h_1/h_2$ .

(11)

The model criterion without delamination in the considered interface layer of the nanostructure is:

$$ISS = \sigma_{xy}^{(a)}(x) = h_1 \sigma_1' \leq \sigma_{USS}^{(a)}. \quad (12)$$

where USS is the ultimate shear stress of the interface layer and ISS is the interface shear stress.

This criterion will be used for multi-parameter optimization to determine the model parameters.

#### Multi-parameter optimization problem

The parameters in the model criterion without delamination in graphene/MoS<sub>2</sub>/PET are: length  $l$ , layers' thicknesses  $h_1$ ,  $h_a$ ,  $h_2$  and external load  $\sigma_0$ . They are included in the coefficients  $D_i$  in equation (1) and in the integration constants  $C_i$  or  $M_i$ , depending of the type of model solution obtained from equation (8) or (9).

We use genetic algorithms [2] to find all 5 parameters  $l$ ,  $h_1$ ,  $h_a$ ,  $h_2$ , and  $\sigma_0$  which fulfill the criterion (12) and assure that there is no delamination in the graphene/MoS<sub>2</sub>/PET nanocomposite.

The possible optimal solutions from the genetic algorithms represent a set of different combinations of all parameters, which vary within predefined boundaries, according to physical and technical prescriptions. The equation (12) is the objective function of the multi-parameter optimization and the abovementioned 5 parameters are the decision variables in the genetic algorithms. Those parameters are set to vary within predefined technological boundaries.

The block-scheme of genetic algorithms is presented on Fig. 2. In general, genetic algorithms are metaheuristics inspired by the process of natural

selection in which population of individuals (candidate solutions) evolves toward better solution.

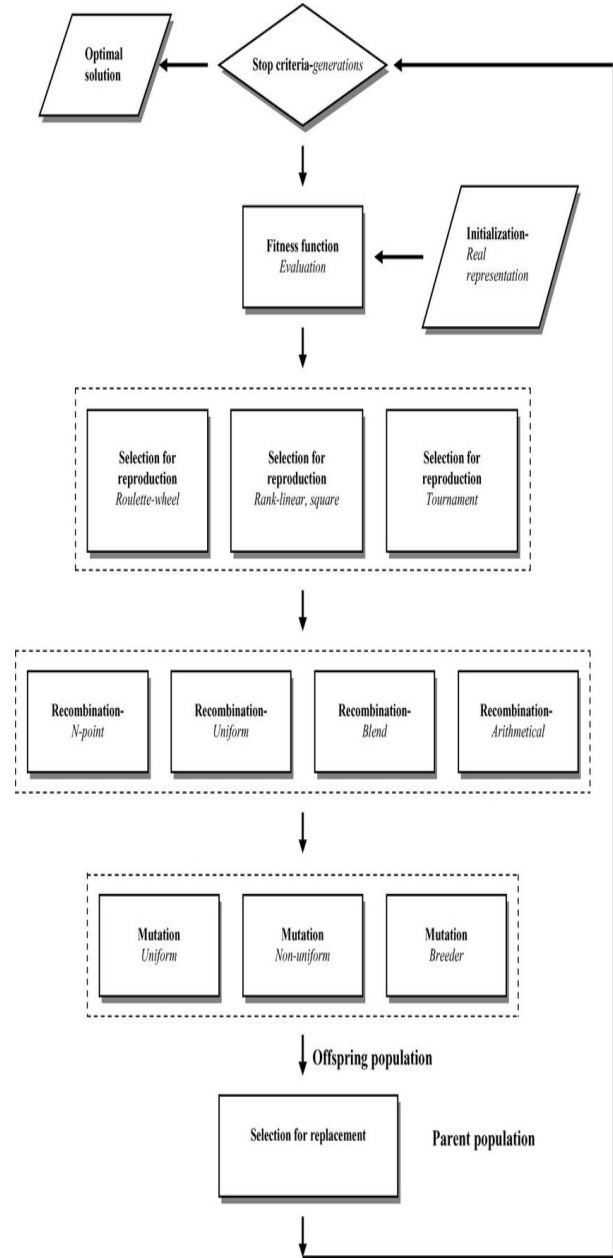


Fig. 2 Block-scheme of genetic algorithms [2]

Selection is the first stage of genetic algorithms, in which individuals are chosen from a population for later breeding. Selection mechanisms are also used to choose individuals for the next generation. There are several different methods of selection:

*a. Roulette wheel selection.* In the roulette wheel selection, the probability of choosing an individual for breeding of the next generation is proportional to its fitness, the better the fitness, the higher is the chance for that individual to be chosen. Choosing individuals can be depicted as spinning a roulette that has as many pockets as there are individuals in the current generation, with sizes depending on their

probability. Probability  $p_i$  of choosing individual  $i$  is:

$$p_i = f_i / \sum_{j=1}^n f_j \tag{13}$$

where  $f_i$  is the fitness of and is the size of current generation. In this method one individual can be drawn several times. The principle of roulette wheel selection is shown on Fig. 3.

*b. Tournament selection.* Tournament selection is another genetic algorithms method of selecting a solution from a population of individuals. Tournament selection involves running several "tournaments" among a few individuals randomly chosen from the population. The winner of each tournament is the one with the best fitness, which is then selected for crossover. The probability of an individual to participate in the tournament depends on tournament size. If the tournament size is larger, weak individuals have a smaller chance to be selected, because, if a weak individual is selected to be in a tournament, there is a higher probability that a stronger individual is also in that tournament. The principle of tournament selection is shown on Fig. 4.

*c. Selection for replacement.* Often, to get better results, selection of replacement strategies with partial reproduction is used. One of them is elitism, in which a small portion of the best individuals from the last generation is carried over (without any changes) to the next one. Then the generation is complemented with new individuals and the whole process is repeated again. The principle of the selection for replacement is shown on Fig. 5.

### RESULTS AND DISCUSSION

The mechanical properties of the heterostructure investigated in this work are presented in Table 1 and are given in [3].

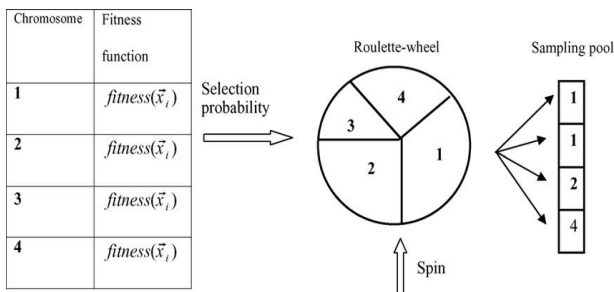


Fig. 3. Principle of roulette-wheel selection [2]

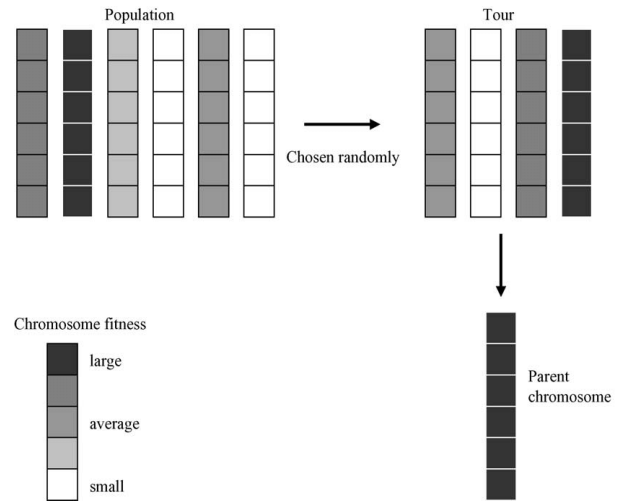


Fig. 4. Principle of tournament selection [2]

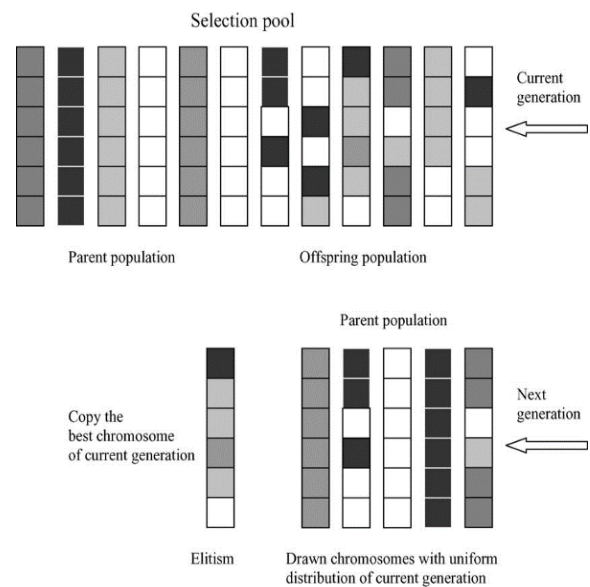


Fig. 5. Principle of the selection for replacement [2]

In Table 2 the obtained results from the performed GA multi-parameter optimization can be seen, for the case of complex roots solution for derivative of  $\sigma_l$  in the objective function in eq. (12). For the case of real roots for ISS the alternative Mathematica optimization procedure was developed and solved with the same optimization criterion eq. (12). The results from Mathematica are presented in Table 3.

Table 1. Input data

Material	Young modulus, GPa	Poisson ratio
Graphene	1000	0.13
MoS <sub>2</sub>	270	0.25
PET	2.3	0.43

**Table 2.** Obtained results from GA (complex roots).

Solution No.	1	2	3	4	5	6	8	9	10
Optimal load $\sigma_0$	2.84E+09	3.60E+09	3.74E+09	5.61E+09	1.53E+09	5.78E+09	2.77e+08	5.86e+09	4.70e+08
Optimal length $l$	1.76E-05	1.75E-05	1.73E-05	3.17E-05	1.87E-05	3.18E-05	7.49e-05	1.46e-05	4.48e-05
Optimal $h_1$	2.14E-09	3.05E-09	5.00E-09	3.82E-09	1.06E-09	4.49E-09	5.00E-09	4.81E-09	5.00E-09
Optimal $h_a$	1.00E-09	2.48E-09	1.00E-09	3.09E-09	3.61E-09	1.42E-09	6.83e-10	6.51e-10	6.65e-10
Optimal $h_2$	3.85E-04	4.15E-04	4.15E-04	8.70E-04	3.32E-04	8.81E-04	9.45e-04	4.64e-04	5.89e-04
GA population samples, generation, numbers	500	500	500	500	500	500	500	500	500
	200	200	200	200	200	200	200	200	200
	500	500	500	500	500	700	700	700	700
Methods used in GA*	TS, AC, NM	RWS, AC, NM	RWS, TPC, NM	TS, BC, NM	RS, BC, NM	TS, OPC, NM	TS, AC, NM	TS, AC, NM	TS, AC, NM

\* Tournament selection, Arithmetical crossover, Non-uniform mutation (TS, AC, NM);  
 Roulette wheel selection, Arithmetical crossover, Non-uniform mutation (RWS, AC, NM);  
 Roulette wheel selection, Two-points crossover, Non-uniform mutation (RWS, TPC, NM);  
 Tournament selection, Blend crossover, Non-uniform mutation (TS, BC, NM);  
 Rank selection, Blend crossover, Non-uniform mutation (RS, BC, NM);  
 Tournament selection, One-point crossover, Non-uniform mutation (TS, AC, NM).

**Table 3.** Optimal values of parameters from Mathematica optimization procedure for graphene/MoS<sub>2</sub>/PET (real roots)

Solution* No.	M2	M11	M12	M29	MLimit
Optimal load $\sigma_0$ , MPa	1	1	0.182	1	0.95
Optimal $l$ , m	1e-05	1e-05	1e-05	1.5e-05	1e-05
Optimal $h_1$ , m	0.35e-09	0.675e-09	0.675e-09	0.35e-09	1e-09
Optimal $h_a$ , m	1e-10	1e-10	1e-10	1e-10	1e-10
Optimal $h_2$ , m	1e-06	1e-06	5.5e-06	1e-06	1e-06

\* to differentiate the solutions in graphic results, these from Mathematica are noted with M

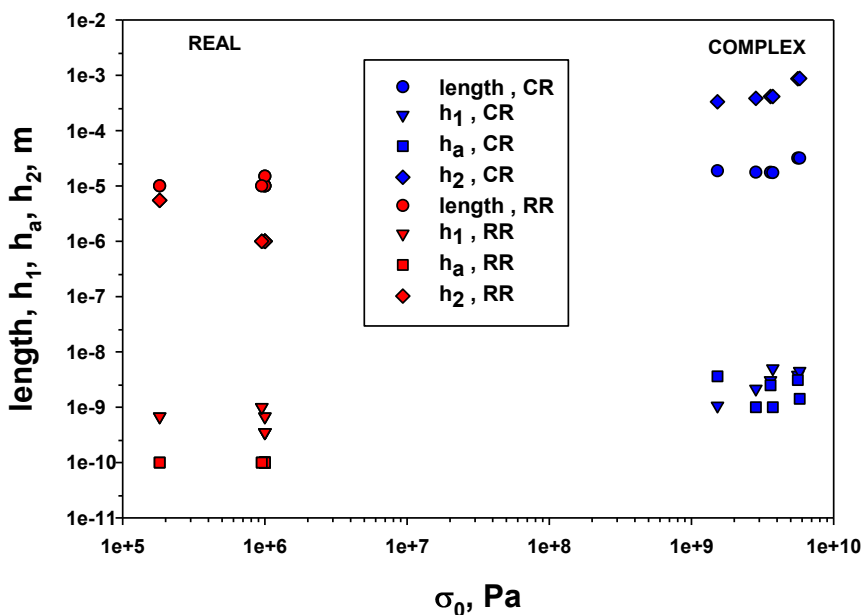


**Fig. 6.** Optimal solutions for 5 parameters from GA and Mathematica: complex roots CR (blue) and real roots RR (red)

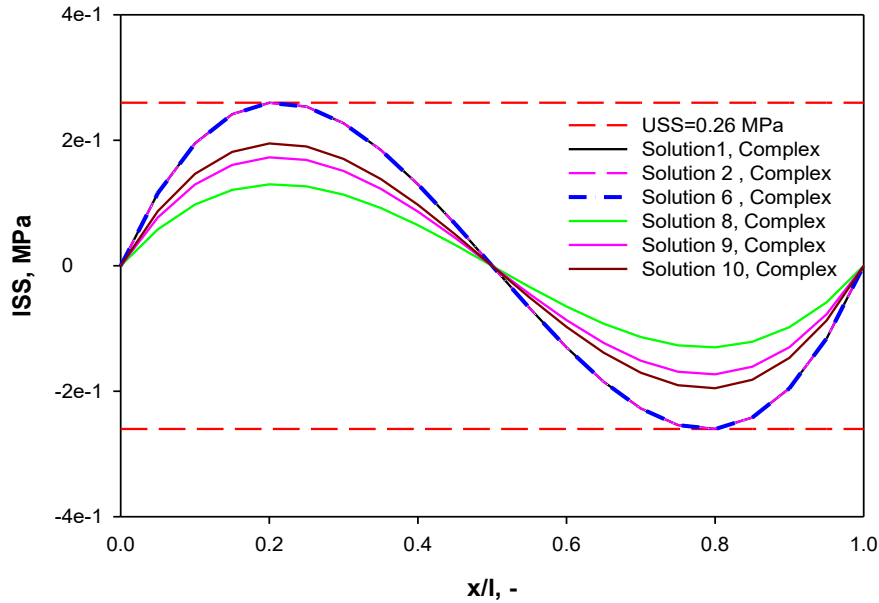


Fig. 7. Model Interface shear stress distribution calculated by the optimal values of parameters (complex roots)

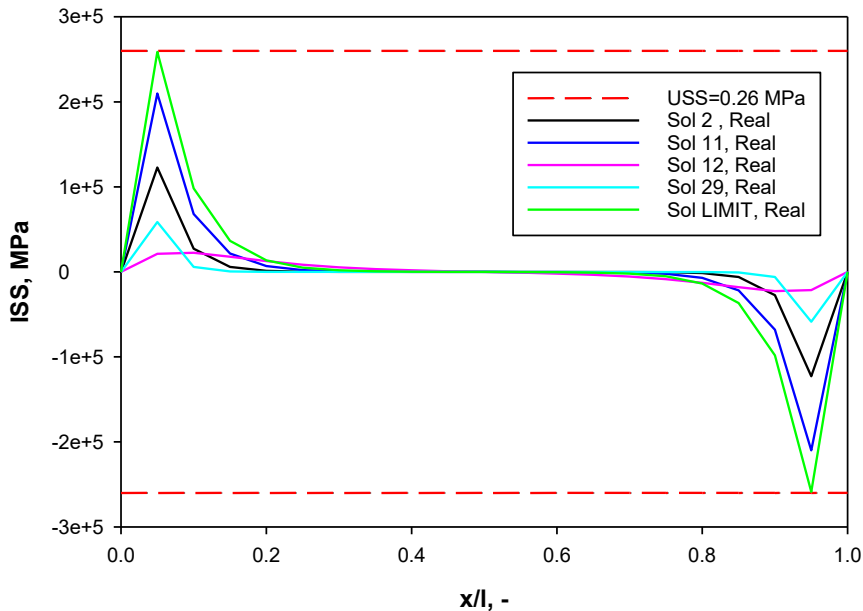


Fig. 8. Model interface shear stress distribution calculated at the optimal values of parameters (real roots)

In Figure 6, the sets of optimal values of the parameters (load, length, thicknesses of the three layers) are presented along with criterion equation (12) from both optimizations. It can be seen that along the ordinate each geometrical parameter changes within certain limits (intervals) for each of the two types of solutions (8) and (9) for ISS included in the objective function. The limits of the changes of the optimal thicknesses of PET  $h_2$  and of the interface layer  $h_a$ , for the cases of real and complex roots, are particularly well differentiated. The intervals of variation of  $l$  are almost similar for both possible solutions (8) and (9). On the abscissa, each different set of geometry data corresponds to a particular mechanical load such that for each group

of five parameters criterion (12) is met or the model-predicted ISS at these load and geometry values is equal to or below the critical USS value.

In order to verify the obtained results, the following Figures 7 and 8 present a part of the distributions of the ISS along the length of the nanocomposite obtained at the optimal values of the parameters. As can be seen, for each type of solution, the optimal values of the studied parameters actually meet the criterion of not having delamination in the nanocomposite structure. Graphically, on Figures 7 and 8, the ISS distribution for both cases does not exceed the straight horizontal line corresponding to the USS.

It turned out that the only data which can be compared with ours in the available literature, is the thickness of the interface layer – our common interval of obtained optimal values for  $h_a$  is (1e-10 ÷ 3.6e-09) for the investigated nanostructure. It is worth noting that the value obtained by Yu *et al.*, 2014 [4] (0.8 nm) for graphene/MoS<sub>2</sub>/Si is in the interval of the results obtained here, despite the different substrate used.

### CONCLUSIONS

The multi-parameter optimization problem for three-layer nanostructure safety work (without delamination) is formulated and solved with genetic algorithms and Mathematica approach for axially loaded graphene/MoS<sub>2</sub>/PET nanocomposite. The analytical model criterion based on the model ISS limit (no delamination), is included in the optimization procedures. The minimization of the later criteria as an objective function allows determining of the optimal values for 5 parameters: layers' thicknesses, length and mechanical loading for the considered nanocomposite.

The obtained optimal solutions represent a set of different combinations of all 5 parameters, which vary within predefined boundaries, according to physical and technical prescriptions.

The results show that at obtained optimal values of 5 parameters, the model ISSs confirmed and fulfilled the model criterion in graphene/MoS<sub>2</sub>/PET. The obtained optimal interval of values for  $h_a$  coincides well with available literature data [4]. They could be used for predicting the optimal geometry design and load for any material combinations for three-layer nanocomposite structure, which satisfied the model assumptions [1].

**Acknowledgement:** *This study is performed by the financial support under the contract No. KII-06-H57/3/15.11.2021 with Bulgarian National Science Fund for the project "Optimal safe loads and geometry for layered nanocomposites under thermo-mechanical loading".*

### Nomenclature

$A$  - constant, solution of non-homogeneous ODE (1) of 4<sup>th</sup> order;

$C_i, M_i$  - integration constants in the model solutions, determined from the respective boundary conditions;

$E$  - Young modulus of layer material, Pa;  
 $h_1, h_a, h_2$  - thickness of the 1<sup>st</sup>, middle and 2<sup>nd</sup> layer in the nanocomposite,  $m$  ;  
 ISS - model interface shear stress, Pa;  
 $l$  - length of the nanocomposite,  $m$ ;  
 $x, y P$  - applied tension force to the substrate, N.m;  
 - coordinate system,  $m$ ;  
 USS - ultimate shear stress of middle layer in nanocomposite, Pa;

### Greek symbols

$\lambda_i$  - real roots of the characteristic equation corresponding to 4<sup>th</sup> order ODE;  
 $\pm(\alpha \pm i\beta)$  - complex roots of the characteristic equation corresponding to ODE of 4<sup>th</sup> order;  
 $\nu$  - Poisson number (ratio), - ;  
 $\sigma_0$  - external loading stress, applied to substrate, Pa;  
 $\sigma_1, \sigma_{x,y}^a$  - model axial and shear stress, Pa;

### REFERENCES

1. T. S. Petrova, *Bulgarian Chemical Communications*, **55** (3), 349, (2023).
2. E. Shopova, N. Vaklieva-Bancheva, *Computers and Chemical Engineering*, **30**, 1293 (2006).
3. H. Du, Y., Kang, C., Xu, T., Xue, W., Qiu, H., Xie, *Optics and Lasers in Engineering*, **149**, 106825 (2022).
4. L. Yu, Yi-H. Lee, X. Ling, E. J. G. Santos, Y. C. Shin, Y. Lin, M. Dubey, E. Kaxiras, J. Kong, H. Wang, T. Palacios, *Nano Lett.*, **14** (6), 3055 (2014).
5. L. Zhu, K. A. Narh, Composites, *Journal of Polymer Science Part B: Polymer Physics*, **42** (12), 2391 (2004).
6. A. Castellanos-Gomez, M. Poot, G.A. Steele, H.S.J. van der Zant, N. Agrait, G. Rubio-Bollinger, *Adv. Mater.*, **24**, 772 (2012).
7. B. Cho, J. Yoon, S. K. Lim, A. R. Kim, D.-H. Kim, S.-G. Park, J.-D. Kwon, Y.-J. Lee, K.-H. Lee, B. H. Lee, H. C. Ko, M. G. Hahm, *ACS Applied Materials and Interfaces*, **7** (30), 16775 (2015).
8. B. Graczykowski, M. Sledzinska, M. Placidi, D. S. Reig, M. Kasprzak, F. Alzina, C. M. S. Torres, *Nano Letters*, **17** (12), 7647 (2017).
9. S. Susarla, P. Manimunda, Y. M. Jaques, J. A. Hachtel, J. C. Idrobo, S. A. S. Amnulla, D. S. Galvão, C. S. Tiwary, P. M. Ajayan, *ACS Nano*, **12** (4), 4036 (2018).
10. H. Xing, X. Wang, C. Xu, H. Du, R. Li, Z. Zhao, W. Qiu, *Carbon*, **204**, 566 (2023).

## The influence of gold nanorods' aspect ratio on the structure and spectroscopic properties of TiO<sub>2</sub> nanoparticles for solar cell utilization

Z. B. Al-Ruqeishi, O. K. Abou-Zied\*

Department of Chemistry, College of Science, Sultan Qaboos University, Box 36, Al-Khod 123, Sultanate of Oman

Received May 3, 2024; Accepted: August 15, 2024

In this study, gold nanorods (Au NRs) were employed to modify a TiO<sub>2</sub> semiconductor nanolayer for potential integration into dye-sensitized solar cells (DSSCs)' photoanode, aiming to enhance absorption in the visible to near-infrared (NIR) spectral region and mitigate electron-hole recombination. Two aspect ratios of Au NRs were synthesized and their interaction with TiO<sub>2</sub> was investigated. Both Au NR types show two distinct absorption peaks in the visible to NIR spectral region due to the surface plasmon resonance effect. The aspect ratios of the prepared Au NRs were determined using transmission electron microscopy. X-ray photoelectron spectroscopy measurements indicated electronic charge transfer from TiO<sub>2</sub> nanoparticles (NPs) to Au NRs, evidenced by blue shifts in the Ti 2p and O 1s peaks. Photoluminescence (PL) analysis revealed decreased emission intensity in TiO<sub>2</sub> NPs decorated with Au NRs, which is attributed to a formed Schottky barrier that reduces the electron-hole recombination process by acting as an electron sink. Notably, the PL intensity of TiO<sub>2</sub> NPs decorated with the larger aspect ratio of Au NRs (4.93) is lower, compared to that decorated with the smaller aspect ratio (2.41). This result suggests superior electron trapping and charge carrier separation, leading to reduced electron-hole recombination rates.

**Keywords:** Au nanorods; TiO<sub>2</sub> nanoparticles; dye-sensitized solar cells.

### INTRODUCTION

Titanium dioxide (TiO<sub>2</sub>) nanomaterial is considered a highly promising semiconductor in various scientific fields such as photocatalysis, lithium-ion batteries, water splitting, and solar cells due to its unique characteristics [1-4]. Particularly, TiO<sub>2</sub> has attracted the greatest attention as a potential photoanode for dye-sensitized solar cells (DSSCs) because of its large band gap, high surface area for dye adsorption, high chemical stability, lack of toxicity, and fast electron transfer rate [5, 6]. Despite the advantages of TiO<sub>2</sub>, it has low electron diffusion coefficients because of defects, surface states, grain boundaries, and other structures that act as electron trapping sites. This results in a decrease in charge-carrier mobility, a decrease in charge-carrier separation lifetime, and an increase in the rate of electron-hole recombination, which subsequently limits the efficiency of DSSCs [7, 8]. The most common approach for suppressing the charge recombination process in TiO<sub>2</sub>, is structural modification with metal nanoparticles, non-metals, semiconductor coupling, and hybridization with carbon materials [9-13]. Moreover, the surface plasmon resonance effect (SPR) of plasmonic metal nanostructures provides an enhancement of visible light absorption. The shape of a metal nanostructure

has an impact on the performance of DSSCs. In particular, rod-shaped Au nanostructures have a greater photovoltaic efficiency than Au nanoparticles (Au NPs) because they further boost light harvesting in the near-infrared (NIR) spectral region. Furthermore, the Au nanorods (Au NRs) provide higher carrier recombination resistance and faster charge carrier transportation compared to Au NPs [14].

In this study, we modified TiO<sub>2</sub> nanolayers by preparing nanocomposites with Au NRs of varying aspect ratios, aiming at potential application as photoanodes in DSSCs. The morphology and size of the Au NRs were determined through transmission electron microscopy while X-ray photoelectron spectroscopy was utilized to analyze the deposition of Au NRs onto TiO<sub>2</sub> nanomaterial. We observed a substantial enhancement in optical absorption within the visible (Vis) and NIR spectral regions for the new materials. The photoluminescence spectra indicate a large reduction in the electron-hole recombination process as a result of efficient electron trapping. These TiO<sub>2</sub>/Au NRs nanocomposites hold promise in enhancing light harvesting from the solar radiation, while facilitating interfacial charge transfer when employed as photoanodes in DSSCs.

\* To whom all correspondence should be sent:  
E-mail: [abouzied@squ.edu.om](mailto:abouzied@squ.edu.om)

## MATERIALS AND METHODS

### Synthesis of Au NRs@TiO<sub>2</sub> nanocomposites

The two aspect ratios of Au NRs were synthesized using a seed-mediated method following the procedure outlined by Feng *et al.* [15]. The aspect ratio was controlled by using different volumes of AgNO<sub>3</sub> (50 and 105 μL) in the growth solution. The nanocomposite was prepared by mixing 0.2 g of TiO<sub>2</sub> (P25), 0.4 ml of 24% NH<sub>3</sub>, 0.8 ml of mercaptoacetic acid, and 6.8 ml of H<sub>2</sub>O. The solution mixture was vigorously stirred for a duration of 24 h. Subsequently, 8 ml of the previously prepared Au NRs was added to the solution and maintained at the same stirring speed for additional 24 h. Purification of the nanocomposite involved removing the mercaptoacetic acid and repeated washing of the precipitate with water. The nanocomposite was then centrifuged for 10 min at a speed of 7,000 rpm, and the resulting precipitate was redispersed in deionized water before being allowed to completely dry at room temperature.

### Characterization techniques

The morphology of the prepared samples was examined using field emission transmission electron microscopy (FE-TEM, JEOL JEM-2100F). The optical absorption and photoluminescence properties were determined at room temperature using Agilent 8453 spectrophotometer and Perkin Elmer LS55 fluorescence spectrophotometer, respectively. X-ray photoelectron spectroscopy (XPS) (Scienta Omicron, Germany) utilizing Al-k ( $h\nu = 1486.6$  eV) at a working voltage of 15 kV under 10<sup>-8</sup> Pa was employed to investigate the elemental composition.

## RESULTS AND DISCUSSION

### Absorption spectra of Au NRs

The Vis–NIR absorption spectra of Au NRs were recorded to investigate their optical characteristics. Electronic excitation causes the Au NRs to have two SPR modes [16], transverse SPR (TSPR) due to electron oscillations in the Au NRs' transverse direction, and longitudinal SPR (LSPR) associated with electron oscillations in the Au NRs' longitudinal direction. The former appears as an

absorption band in the 510–530 nm region, while the latter absorption peak is modulated from Vis to NIR by changing the aspect ratio [15, 17].

The Vis–NIR absorption spectra of the two different aspect ratios of Au NRs prepared here are displayed in Fig. 1. The terminology in the figure (Au NR (n)) is based on the amount of AgNO<sub>3</sub> in the growing solution, where n is the concentration of AgNO<sub>3</sub> in micromoles (μM). The Au NRs show significant LSPR bands at 634 nm and 819 nm as the AgNO<sub>3</sub> concentration increases, and weak TSPR bands around 509–513 nm. As shown in the figure, the absorption wavelength of the LSPR band changes with the AgNO<sub>3</sub> concentration while that of the TSPR band is fixed. For the remainder of the paper, we will designate the two different NRs as Au NRs 634 and Au NRs 819.

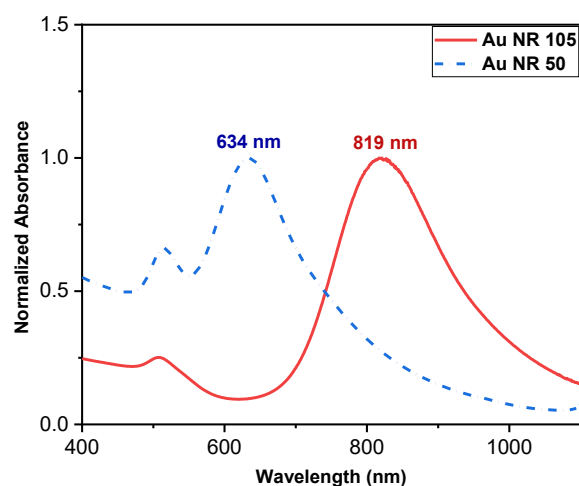


**Fig. 1.** Normalized absorption spectra of Au NRs prepared with different concentrations of AgNO<sub>3</sub> as follows: (a) 50 μM (Au NRs 634), (b) 105 μM (Au NRs 819).

### Morphology and dimensions of Au NRs

Fig. 2 displays the TEM images of the prepared Au NRs. Both samples have a nanorod-shaped morphology with few nanosphere particles formed. The high yield of Au NRs is due to the presence of the Ag<sup>+</sup> ions, whose concentration is proportional to the aspect ratio of the Au NRs (Table 1). It is clear from the table that the higher the concentration of Ag<sup>+</sup> the larger is the aspect ratio of the nanorods. From the TEM images, the two aspect ratios of the Au NRs were estimated to be 2.41 and 4.93.

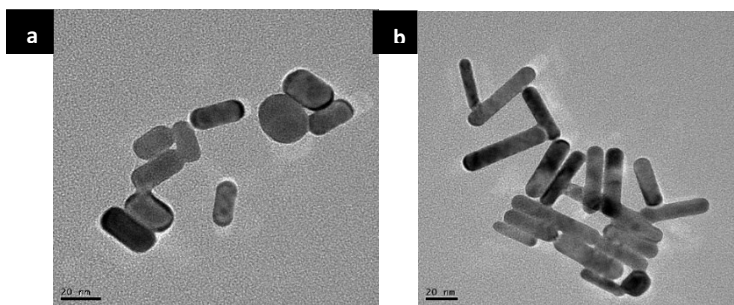


**Fig. 2.** TEM images of Au NRs with two aspect ratios: (a) Au NRs 634, (b) Au NRs 819.

**Table 1.** Average aspect ratios, lengths, and widths of the Au NRs.

	Au NRs 634	Au NRs 819
Average width	14.07	10.64
Average length	33.72	51.60
Aspect ratio	2.41	4.93

### Elemental composition of Au NRs@TiO<sub>2</sub>

The elemental composition of the nanocomposites was confirmed using XPS analysis, which was also used to examine the chemical shifts and the nature of the chemical bonds in the surface region. Fig. 3(a) shows the high-resolution XPS spectra of Ti 2p peaks for TiO<sub>2</sub> and Au NRs@TiO<sub>2</sub>. The Ti 2p spectrum for TiO<sub>2</sub> NPs exhibited two peaks at 457.8 eV and 463.6 eV which corresponds to the binding energies of the Ti 2p<sub>3/2</sub> and Ti 2p<sub>1/2</sub> core levels, respectively, due to the presence of the Ti(IV) state [4, 9]. Moreover, the high-resolution spectra of the O 1s energy state for both TiO<sub>2</sub> and the nanocomposite are depicted in Fig. 3(b). The binding

energy of the O 1s state for the samples was identified at 529.5 eV, corresponding to the bulk oxides (O<sup>2-</sup>) within the P25 lattice of TiO<sub>2</sub> [4]. Decorating Au NRs on TiO<sub>2</sub> NPs leads to a blue shift of the Ti 2p and O 1s peaks. This shift is attributed to the interaction between TiO<sub>2</sub> NPs and Au NRs, which suggests that the increased binding energies of Ti 2p and O 1s are due to an electronic charge transfer from TiO<sub>2</sub> NPs to Au NRs. Furthermore, the Au 4f spectrum of the nanocomposite contains two peaks at 82.9 eV and 86.5 eV, representing binding energies of the Au 4f<sub>7/2</sub> and Au 4f<sub>5/2</sub> core levels, respectively. This result indicates the presence of Au in its metallic state [4].

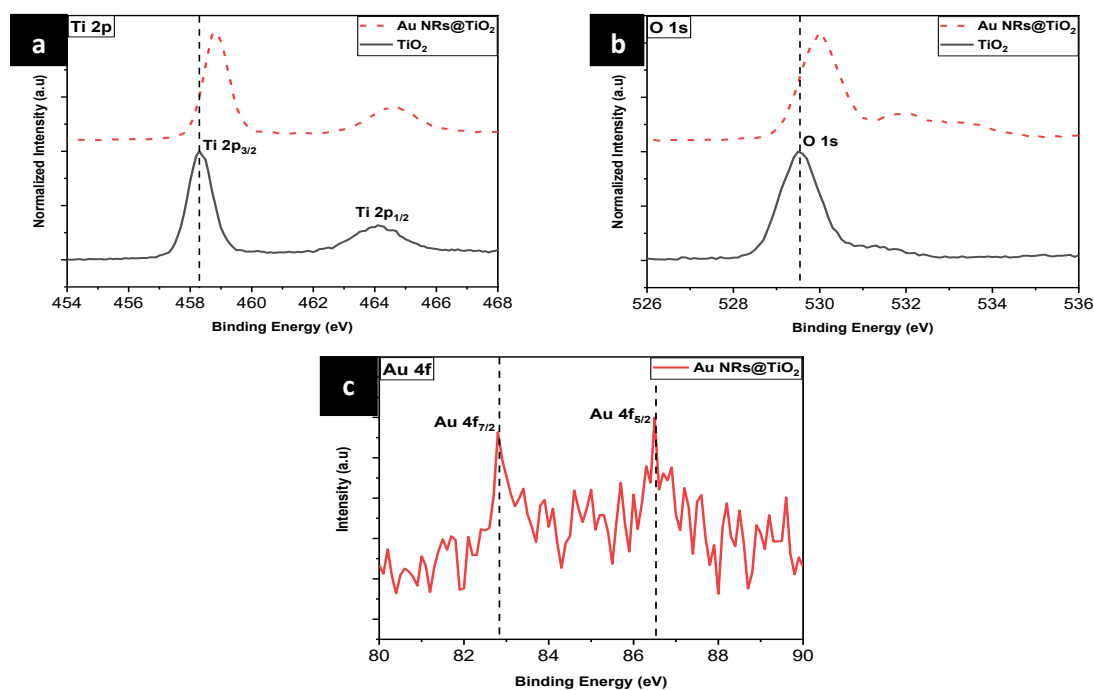


**Fig. 3.** High resolution XPS spectra: (a) Ti 2p, (b) O 1s, and (c) Au 4f for TiO<sub>2</sub> and Au NRs@TiO<sub>2</sub>

Photoluminescence of TiO<sub>2</sub> nanoparticles

The PL spectra of TiO<sub>2</sub> NPs decorated with the two different aspect ratios of Au NRs are presented in Fig. 4. The PL spectrum of pristine TiO<sub>2</sub> is included for comparison. Within the 385-530 nm range for Au NR 634@TiO<sub>2</sub> and Au NR 819@TiO<sub>2</sub>, five peaks are detected. Among these, a single peak appears in the ultraviolet region at 386 nm (3.21 eV), which is approximately equal to the bandgap energy of TiO<sub>2</sub>. In the visible range, the spectrum includes four peaks at 420 nm (2.95 eV), 444 nm (2.79 eV), 483 nm (2.57 eV), and 530 nm (2.34 eV). These visible peaks are caused by defect states in the TiO<sub>2</sub> NPs, which introduce new electron trap energy levels.

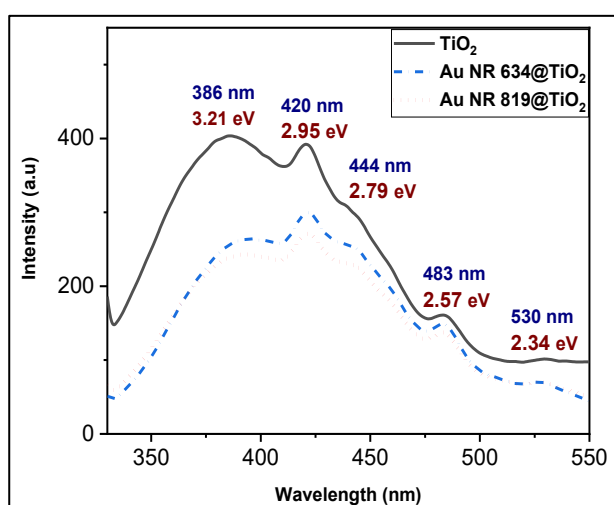


**Fig. 4.** Photoluminescence spectra of TiO<sub>2</sub> nanoparticles coated with two different aspect ratios of Au NRs.  $\lambda_{\text{ex}} = 310$  nm.

Deposition of Au NRs onto TiO<sub>2</sub> NPs causes significant decrease in the emission intensity. This demonstrates that the efficiency of electron-hole recombination was decreased in TiO<sub>2</sub> NPs coated with Au NRs, which can be attributed to relocation of the excited electrons in the conduction band to the surface of Au NRs, thus reducing electron-hole recombination. This is primarily related to the formation of a Schottky barrier at the contact between Au NRs and TiO<sub>2</sub> that effectively traps the electrons by acting as an electron sink [4, 18-20]. Furthermore, the intensity of the PL peaks of Au NR 819@TiO<sub>2</sub> is lower, compared to that of Au NR 634@TiO<sub>2</sub>. This suggests that the larger aspect ratio of Au NRs achieves the highest electron trapping and charge carrier separation along with the lowest rate of electron-hole recombination.

## CONCLUSION

This study investigates the utilization of Au NRs to modify the TiO<sub>2</sub> semiconductor nanolayer for potential integration into DSSCs as photoanodes. The objective is to improve absorption in the visible to NIR spectral region and alleviate electron-hole recombination. Two different aspect ratios of Au NRs were synthesized, and their interaction with TiO<sub>2</sub> was examined. Both types of Au NRs exhibit distinct absorption peaks in the visible to NIR spectral range owing to the surface plasmon resonance effect. The aspect ratios of the synthesized Au NRs were determined by transmission electron microscopy. X-ray photoelectron spectroscopy measurements indicated electronic charge transfer from TiO<sub>2</sub> NPs to Au NRs, as evidenced by blue shifts of the Ti 2p and O 1s peaks. PL analysis revealed a decrease in the emission intensity of TiO<sub>2</sub> NPs decorated with Au NRs, as a result of the formation of a Schottky barrier that reduces electron-hole recombination by serving as an electron sink. Remarkably, the PL intensity of TiO<sub>2</sub> NPs decorated with Au NRs of larger aspect ratio (4.93) is lower compared to those decorated with Au NRs of smaller aspect ratio (2.41), suggesting superior electron trapping and charge carrier separation, resulting in reduced electron-hole recombination rates.

**Acknowledgement:** The authors would like to acknowledge the financial support provided through the International Research Collaboration Co-Funding Program (IRCC) from Sultan Qaboos University and Qatar University, with Grant reference number CL/SQU-QU/SCI/24/01.

## REFERENCES

1. M. Farzadkia, E. Bazrafshan, A. Esrafil, J. K. Yang, M. Shirzad-Siboni, *J. Env. Health Sci. Eng.*, **13**, 35 (2015).
2. A. A. Kashale, K. P. Gattu, K. Ghule, V. H. Ingole, S. Dhanayat, R. Sharma, J.-Y. Chang, A. V. Ghule, *Compos. B*, **99**, 297 (2016).
3. N. Kunthakudee, T. Puangpetch, P. Ramakul, K. Serivalsatit, M. Hunsom, *Int. J. Hydrogen Energy*, **47**, 23570 (2022).
4. S. P. Lim, Y. S. Lim, A. Pandikumar, H. N. Lim, Y. H. Ng, R. Ramaraj, D. C. S. Bien, O. K. Abou-Zied, N. M. Huang, *Phys. Chem. Chem. Phys.*, **19**, 1395 (2017).
5. L. G. Devi, K. M. Reddy, *Appl. Surf. Sci.*, **257**, 6821 (2011).
6. H. Wei, J.-W. Luo, S.-S. Li, L.-W. Wang, *J. Am. Chem. Soc.*, **138**, 8165 (2016).
7. S. Nakade, Y. Saito, W. Kubo, T. Kitamura, Y. Wada, S. Yanagida, *J. Phys. Chem. B*, **107**, 8607 (2003).

8. P. Roy, D. Kim, K. Lee, E. Spiecker, P. Schmuki, *Nanoscale*, **2**, 45 (2010).
9. S. P. Lim, A. Pandikumar, N. M. Huang, H. N. Lim, *RSC Adv.*, **4**, 38111 (2014).
10. J. M. Macak, F. Schmidt-Stein, P. Schmuki, *Electrochem. Commun.*, **9**, 1783 (2007).
11. T. Ohno, M. Akiyoshi, T. Umabayashi, K. Asai, T. Mitsui, M. Matsumura, *Appl. Catal. A*, **265**, 115 (2004).
12. H. L. Meng, C. Cui, H. L. Shen, D. Y. Liang, Y. Z. Xue, P. G. Li, W. H. Tang, *J. Alloys Comp.*, **527**, 30 (2012).
13. L. Zhang, H. Fu, Y.-F. Zhu, *Adv. Funct. Mater.*, **18**, 2180 (2008).
14. P. S. Chandrasekhar, P. K. Parashar, S. K. Swami, V. Dutta, V. K. Komarala, *Phys. Chem. Chem. Phys.*, **20**, 9651 (2018).
15. L. Feng, Z. Xuan, J. Ma, J. Chen, D. Cui, C. Su, J. Guo, Y. Zhang, *J. Exp. Nanosci.*, **10**, 258 (2015).
16. R. Takahata, S. Yamazoe, K. Koyasu, T. Tsukuda, *J. Am. Chem. Soc.*, **136**, 8489 (2014).
17. Y. Okuno, K. Nishioka, A. Kiya, N. Nakashima, A. Ishibashi, Y. Niidome, *Nanoscale*, **2**, 1489 (2010).
18. J. Yu, L. Yue, S. Liu, B. Huang, X. Zhang, *J. Colloid Interface Sci.*, **334**, 58 (2009).
19. G. Žerjav, M. Roškarič, J. Zavašnik, J. Kovač, A. Pintar, *Appl. Surf. Sci.*, **579**, 152196 (2022).
20. N. Bagheri, J. Hassanzadeh, Z. B. Al-Ruqeishi, N. S. Abdul Manan, H. A. J. Al Lawati, O. K. Abou-Zied, *Phys. Chem. Chem. Phys.*, **25**, 19230 (2023).

## Multi-parameter optimization of layered hBN/PMMA nanocomposite under mechanical loading

T. Petrova<sup>1\*</sup>, E. Kirilova<sup>1</sup>, R. Vladova<sup>1</sup>, A. Apostolov<sup>1</sup>, B. Boyadjiev<sup>1</sup>, A. Moravski<sup>2</sup>

<sup>1</sup>

*Institute of Chemical Engineering, Bulgarian Academy of Sciences, Acad. G. Bonchev Str., Bl. 103, 1113 Sofia, Bulgaria*

<sup>2</sup>*Faculty of Mathematics and Informatics, Sofia University "St. Kliment Ohridski", 5 James Bourchier Blvd., 1164 Sofia, Bulgaria*

Received June 3, 2024; Accepted: August 17, 2024

In the present study, a methodology is proposed to find the optimal safe values for the geometry and the magnitude of the axially applied mechanical load for hBN/PMMA nanocomposite, so as to avoid the possibility of its delamination/fracture, by using Genetic Algorithms. First, the analytical solutions for the interface shear stress in the middle layer of the considered nanostructure are obtained, based on the application of the 2D method of the stress function and the minimization of the strain energy. Second, the theoretical criterion for no delamination in the interface layer, based on the model ISS is formulated, including the structure geometry and loading as parameters. The multi-parameter optimization problem involving this criterion is then defined and solved by the GA. By varying all parameters simultaneously, their safety intervals (without delamination) in the considered nanocomposite structure are obtained. The magnitude of the applied load was found to mainly affect the magnitude of the ISS. Layer thicknesses mostly affect the type of ISS solution, especially the substrate thickness. The effect of layer length on ISS is weaker than that of layer thickness at fixed load. The obtained results can be used for fast delamination prediction and appropriate design in such nanostructured devices to ensure their safe operation.

**Keywords:** Multi-parameter optimization, hBN/Interface/PMMA nanocomposite, interface shear stress, delamination

### INTRODUCTION

Boron nitride nanosheet (BNNS)-polymer composites are one of the important classes of materials with a wide range of applications: automotive, aerospace, energy storage [1], medicine, electronic engineering, etc. Properties of the hBN/polymer nanocomposites mainly depend up on filler size and dispersion, mixing conditions and type of interaction between polymer matrix and the nano filler [2]. Boron nitride (BN) nanomaterials have superior fracture strength (165 GPa), high Young's modulus (0.8 TPa), high thermal stability (up to 800 °C in the air), excellent thermal expansion coefficient ( $-2.72 \times 10^{-6} \text{ K}^{-1}$ ), and outstanding thermal conductivity (300–2000  $\text{W m}^{-1} \text{ K}^{-1}$ ) [3]. Among the abovementioned BNNS properties, in this review work [3], the fundamental parameters that control the molecular interactions of BNNSs with polymer matrices have been considered in detail. The authors take into account two groups of factors influencing the hBN/polymer nanocomposites properties – non-interfacial and interfacial factors. The latter ones show a strong effect on the stress-transfer efficiency of this kind of

nanocomposites and include: covalent and non-covalent interactions at the interfacial surface area, and at the BNNS-polymer interface. A transitional zone is created, termed as „interphase“, which is the origin of property changes in polymer nanocomposites. Interphases have a vital role in transferring mechanical stress, thermal heat, and electrical load from one phase into another.

At the moment, scientists still do not have a direct method to experimentally measure and determine the properties and geometrical characteristics (thickness, length, etc.) of such an interphase zone not only for (BNNS)-polymer, but also for the recently widespread nanocomposites of other 2D materials (graphene, MoS<sub>2</sub>, WS<sub>2</sub>, Mxenes, etc.) and different substrates [4-6]. There are several theoretical developments that attempt to fill this lack of information about the interphase zone. In the dissertation of Kochetov [7], the Lewis-Nielsen model was used with a third phase (interface) added to the other two – spherical/platelet nanoparticles of BN and an epoxy matrix, to explain the Kapitza's resistance of an interphase boundary phenomenon and its influence on thermal conductivity. Kochetov has proved that such a phase must exist, since accounting for it yields realistic thermal conductivity values compared to experimental data, unlike the

\* To whom all correspondence should be sent:  
E-mail: [t.petrova@iche.bas.bg](mailto:t.petrova@iche.bas.bg)

case of only two phases in the model. Kochetov's model yielded the following values for the width of the interface zone:  $1.6 \div 2.5$  nm. This author also mentioned that for a polymer/nanoclay the width of this zone is  $5 \div 15$  nm and for PVA/Si nanocomposites it is  $5 \div 10$  nm.

Later, the scientists' interest to hBN/polymer or other nanocomposites, as well as to the interface zone between them, increased: hBN/epoxy [8], hBN/Si [9], hBN/PDMS [10], BNNT/PMMA [11], hBN/PMMA [12], hBN/PVA [13], and hBN/sapphire [14]. But only in [8], [9] and [11], the interface area has also been considered and studied. In [11], the load transfer characteristics of boron nitride nanotube (BNNT)/PMMA interfaces by using a micromechanic shear-lag model that takes into account the elastoplastic properties of polymer matrices, have been investigated. Closed-form analytical solutions of the interfacial shear stress distribution profile are derived. The failure of the nanotube-polymer interface and the pull-out force are analyzed using this strain-hardening model based on recently reported nanomechanical single-nanotube pull-out experiments. The BNNT/PMMA interface is found to possess a maximum interface shear strength (IFSS) of  $71 \pm 2$  MPa that is predicted using the strain-hardening model, as compared to  $236 \pm 11$  MPa that is predicted using the elastic model. The thickness of interface matrix layer is fixed in this model as 8.05 nm. In the paper of Yi *et al.* [9] on hBN/Si, the maximum IFSS is 1.25 GPa, unlike much lower values of IFSS in the literature for BNNT/PMMA – 219 MPa and for BNNT/epoxy – 323 MPa. In [9] the thickness of interface layer is 8.1 nm, which is very close to the value in [11]. In contrast to the latter one, in [9] the authors have obtained the interphase thickness of hBN/epoxy to be 0.6 Å (0.06 nm) and IFSS 9.5 MPa. When the surface of hBN is functionalized with additional groups (4 and 8), the IFSS increased from 13.9 to 17.7 MPa. Their results indicate that the interface region of BNNS/EP is composed of three regions, namely, compact region, buffer region, and normal region. As a conclusion, one might say that there are no papers, which discussed the influence of geometry and material properties of interface layer (zone) on the value of ISS in the available literature. Also, there are no studies, in which an optimization of the hBN/polymer nanocomposite geometry is

done, in order to obtain the best stress transfer without failure /delamination. Our contribution to the researches on the above topic has been reported recently [15]. The most important parameters, which influenced the value of ISS, have been theoretically determined by parametric analysis: the magnitude of external load, the thicknesses of the layers and the length of nanocomposite structure hBN/Interface/PMMA. The analytical model results for strain in hBN and ISS are validated successfully in the elastic zone of external loads with experimental data of [12]. After this short literature analysis, it is well established that the reinforcement of polymers by hBN nanofillers is controlled by stress transfer from the matrix to the reinforcement. Also, it is obvious that the existence and consideration of the interface is essential to the stress transfer between the two other phases. One of the most important requirements from the industry applications of the nanostructures is to assure their safe design and loading.

The aim of this work is to find the optimal values of geometry (length and thicknesses of all three layers), as well as the maximal value of external load at the example of hBN/Interface/PMMA nanocomposite under mechanical loading, without delamination in it. Combining 2D stress-function model predictions for interface shear stress [16] and Genetic Algorithm optimization procedure [17], different optimal sets of geometry configurations of the layers (length and thicknesses of all three layers) and maximal load in the considered nanocomposite structure, have been obtained. The objective function in GA multi-parameter problem is the criterion for “no delamination” in the structure, requiring ISS to be less or equal to ultimate shear stress at the interface layer. The novelty of the present work is to find all optimal values of geometry and load parameters simultaneously, which becomes possible by the metaheuristic GA approach used.

#### MATHEMATICAL MODEL

The formulation and derivation of analytical solutions for stresses (and strains) in a 3-layer nanocomposite structure (Fig. 1) by 2D stress-function method were already published in detail in [16]. Here only the most important formulas will be given.

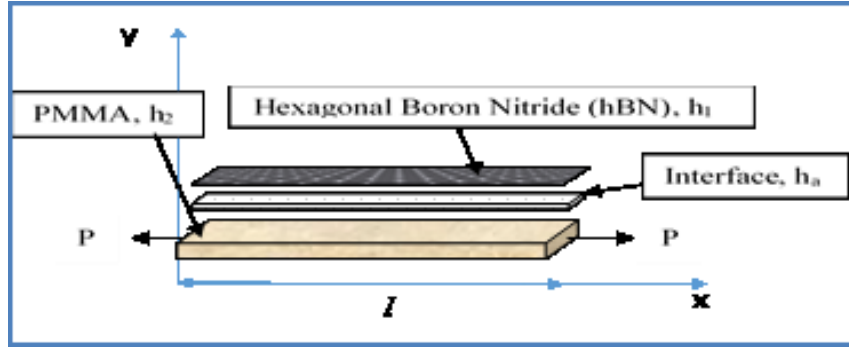


Fig. 1. Representative volume element (RVE) of a 3-layer hBN/Interface/PMMA nanocomposite structure.

According to the model assumptions, all axial stresses in the layers are functions of axial coordinate  $x$  only. Also, the axial stress in the interface layer is set negligible in respect to the same ones in the other two layers. Applying the 2D stress-function method, one can obtain a 4th order differential equation (ODE) with constant coefficients, with respect to the unknown axial stress function  $\sigma_1$  in the first layer (nanolayer). Two types of analytical model solutions for the axial stress  $\sigma_1$  in the nanolayer are derived, with coefficients depending from the geometry of the three-layer nanocomposite, its material properties and external load:

$$\sigma_1(x) = C_1 \exp(\lambda_1 x) + C_2 \exp(\lambda_2 x) + C_3 \exp(\lambda_3 x) + C_4 \exp(\lambda_4 x) - A \quad (1)$$

$$\sigma_1(x) = \exp(-ax)[M_1 \cos(\beta x) + M_2 \sin(\beta x)] + \exp(ax)[M_3 \cos(\beta x) + M_4 \sin(\beta x)] - A \quad (2)$$

In eqs. (1) and (2) the constant  $A$  is the solution for non-homogeneous ODE and depends on the external static load ( $\sigma_0 = P/h_2$ ), and  $C_i$  and  $M_i$  are the integration constants in the model solutions, determined from the respective boundary conditions [16]. All other stresses in the layers, including the interface shear stress (ISS), are expressed by eqs. (1) or (2) and its derivatives. Eq. (2) is the solution for a case of 4 complex roots  $\pm(\alpha \pm i\beta)$ , while eq. (1) corresponds to the case of 4 real roots  $\lambda_i$ . It is worth noting [16] that the type of roots depends on the chosen geometry of the nanocomposite structure (layers' thickness and length).

The model criterion for no interface delamination in the nanostructure was defined, where USS is the ultimate shear stress of interface (adhesive) layer:

$$\sigma_{xy}^{(a)}(x) = h_1 \sigma_1' \leq \sigma_{USS}^{(a)} \quad (3)$$

Graphically, if exists, the delamination starts at both ends of the nanostructure and represents the intersection of the ISS model curve with the straight horizontal line corresponding to the USS.

## MULTI-PARAMETER OPTIMIZATION

## PROBLEM

The genetic algorithm (GA) known as BASIC GA [17] was employed to tackle the formulated below multi-parameter optimization problems. Here, only a short overview on the working steps for GA application is presented.

In the initial iteration called "a generation" in terms of the genetic algorithms, BASIC GA initializes a "population" (set) comprising randomly generated solutions (vectors of values for the control variables), called "chromosomes" or "individuals". The GA operates with a constant, predefined population size that remains unchanged within the searching process. The solutions are represented by their genotype and the search is performed in the continuous space. Through the application of so called "morphogenesis" functions, solutions are transformed (coded) from their genotype to their "phenotype". The latter is needed to compute the values of both the objective functions (OF) of the chromosomes and their "fitness" functions. The fitness function represents a normalized objective function. Following this, genetic operators are applied to the individuals from the population. These operators are "selection for reproduction (crossover)", "reproduction (crossover)", "mutation," and finally, "selection to replacement" as in which the old individuals (from the previous generation) are replaced with the newly created "offspring" (for details see [17]).

At first, a selection for reproduction is carried out. Subsequently, the mutation operator is applied. In the final stage, selection for replacement is carried out to generate a new population for the next generation. A morphogenesis function is applied to the offspring to derive the solutions in their phenotype. Then, the objective functions of all solutions in the pool are computed. The best-value solution for the OF is selected to pass into the new generation. The replacement selection applied is unbiased, meaning the next generation of solutions is augmented to the specified number with solutions randomly selected from the pool. At the conclusion

of this final stage, the number of generations increases. As a criterion for stopping the search, BASIC GA uses reaching a predefined number of generations.

The BASIC GA encompasses various types of genetic selection operators for reproduction, crossover, and mutation, offering users the flexibility to choose among them to address a specific optimization problem. Moreover, the BASIC GA is designed to handle constrained optimization problems by employing penalty functions.

For the considered nanocomposite hBN/Interface/PMMA structure, the goal is to find simultaneously the optimal values of the control variables (length, thicknesses of layers  $h_1$ ,  $h_a$ ,  $h_2$  and external load  $\sigma_0$ ), at which the OF – eq. (3) has the minimum value, less or equal to USS. The control variables are in preliminary defined boundaries (upper and lower) which are physically and technologically correct. The so formulated multi-parameter optimization problem (MPOP) is solved by GA approach for various combinations of selections methods, type of recombination and mutation used. Also, the number of populations, samples and generations are varied too during the optimization procedure. The results can be seen in

Table 1. As a stop criterion the number of generations (iterations) is used.

Meanwhile, an alternative optimization procedure was developed especially for the case of real roots solution – eq. (1) for ISS in the OF. During the optimization, the GA proved to be more suitable for finding the optimal values of the control variables in the case of OF (or ISS) calculated for complex roots - eq. (2). For real roots case for ISS (eq. (1)), the strong requirement for equality in minimization of OF (eq. (3)) makes finding of optimal values of variables in some cases yet impossible or needs too many efforts and computing time. That's why the alternative optimization procedure in Wolfram Mathematica 13.0.1 has been developed (Fig. 2(a)) which offers a solution of the abovementioned problem. Here, different sets of geometry are included in the optimization cycle for the external load, checking if OF is fulfilled or not at the current values of parameters; it's repeated as many times as needed by the user up to reaching close to the optimal solutions. The important model assumption that the axial stress in the interface layer is negligible in respect to the same ones in the other two layers, is additionally checked (Fig. 2(b)). The obtained results are presented in Table 2.

**Table 1.** Optimal values of control variables from GA for hBN/Interface/PMMA (complex roots)

Solution No.	Optimal load $\sigma_0$ , (Pa)	Optimal length $l$ , (m)	Optimal $h_1$ , (m)	Optimal $h_a$ , (m)	Optimal $h_2$ , (m)	GA population, samples, generations numbers	Methods and schemes used in GA*
1	5.52E+09	2.42E-05	2.83E-09	3.31E-08	6.61E-04	300/100/100	TS, AC, NM
2	4.92E+09	2.73E-05	1.95E-09	9.15E-09	7.17E-04	300/100/500	TS, AC, NM
3	4.55E+09	2.13E-05	4.10E-09	1.51E-09	5.44E-04	500/100/500	TS, AC, NM
4	1.73E+09	2.55E-05	1.69E-09	3.17E-08	4.71E-04	500/200/500	RS, AC, NM
5	1.73E+09	2.55E-05	1.69E-09	3.17E-08	4.71E-04	500/200/500	RS, AC, UM
6	3.20E+08	8.31E-05	2.80E-09	4.40E-09	8.62E-04	500/200/500	RWS, TPC, NM
7	3.30E+08	8.31E-05	1.46E-09	3.51E-09	8.62E-04	500/200/500	RWS, UC, BMD
8	3.25E+08	8.31E-05	1.46E-09	4.16E-09	8.57E-04	500/200/500	RWS, BC, PBMD
9	5.57E+09	2.25E-05	5.00E-09	1.00E-09	6.14E-04	500/200/500	RWS, OPC, NM
10	3.29E+08	8.31E-05	1.46E-09	4.27E-09	8.61E-04	500/200/500	RWS, UC, PBMD
11	2.07E+09	3.18E-05	5.57E-10	9.66E-08	7.87E-04	500/200/500	RWS, UC, PBMD
12	1.60E+09	2.04E-05	3.03E-09	3.18E-08	4.22E-04	500/200/500	RWS, UC, PBMD
13	1.71E+09	2.13E-05	1.54E-09	3.21E-08	4.32E-04	500/200/500	TS, AC, NM

\* Tournament selection, Arithmetical crossover, Nonuniform mutation (TS, AC, NM);

Rank selection, Arithmetical crossover, Nonuniform mutation (RS, AC, NM);

Rank selection, Arithmetical crossover, Uniform mutation (RS, AC, UM);

Roulette wheel selection, Two-points crossover, Nonuniform mutation (RWS, TPC, NM);

Roulette wheel selection, Uniform crossover, Parameter based mutation Deb (RWS, UC, PBMD);

Roulette wheel selection, Blend crossover, Parameter based mutation Deb (RWS, BC, PBMD);

Roulette wheel selection, One-point crossover, Nonuniform (RWS, OPC, NM);

Roulette wheel selection, Uniform crossover, Parameter based mutation Deb (RWS, UC, PBMD).

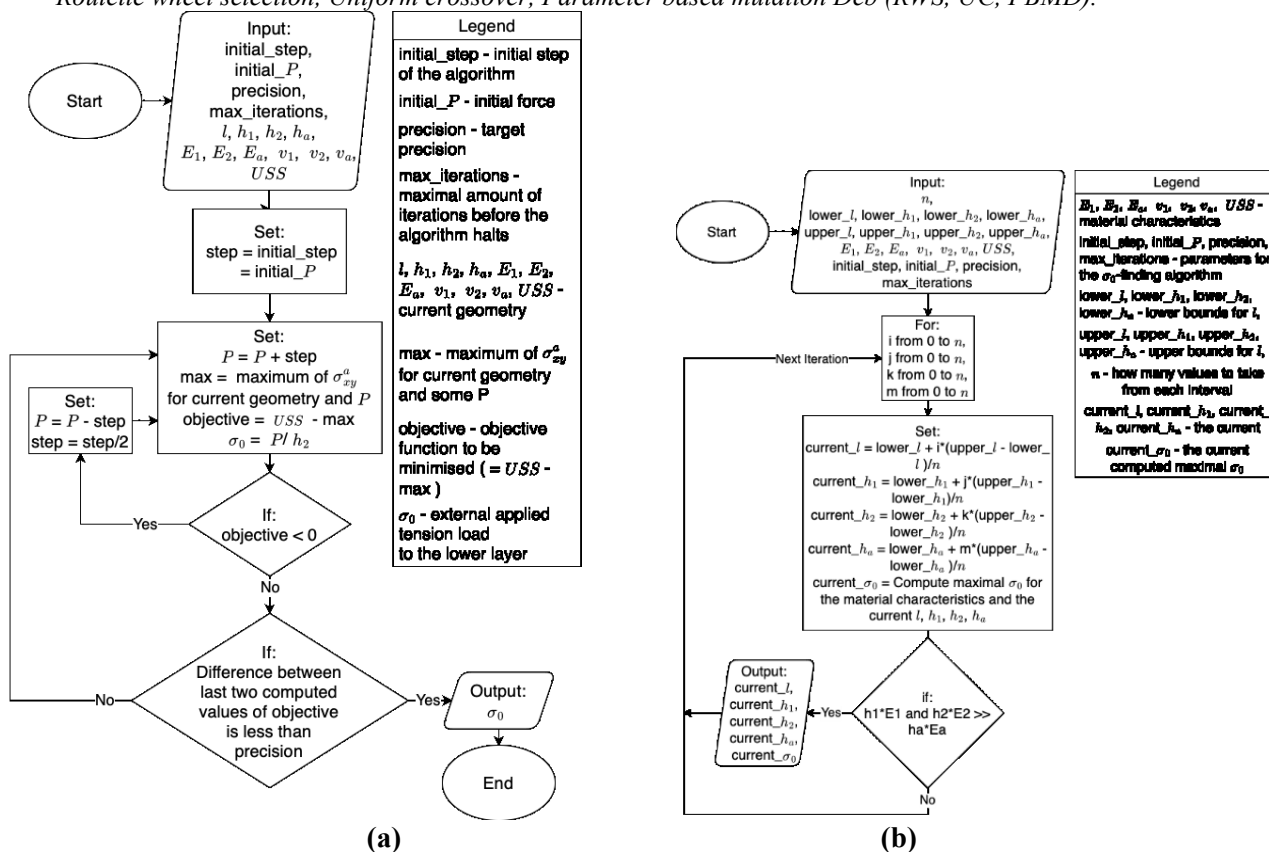


Fig. 2. Schemes of optimization algorithm - (a), and checking of model assumptions for the axial stress in the interface layer - (b).

Table 2. Optimal values of parameters from Mathematica optimization procedure for hBN/Interface/PMMA (real roots)

Solution** No.	M2	M6	M10	M14
Optimal load $\sigma_0$ , MPa	209	113	209	113
Optimal $l$ , m	1e-05	1e-05	2e-05	2e-05
Optimal $h_1$ , m	3.5e-10	1e-09	3.5e-10	1e-09
Optimal $h_a$ , m	1e-08	1e-08	1e-08	1e-08
Optimal $h_2$ , m	1e-06	1e-06	1e-06	1e-06

\*\* to differentiate the solutions in graphic results, these from Mathematica are noted with M

## RESULTS AND DISCUSSION

The material properties: Young modulus  $E$ , (Pa) and Poisson ratio  $\nu$ , (-) of the considered nanocomposite structure (Fig. 1) hBN/Interface/PMMA are taken from [12] as:  $E(\text{hBN})=600$  GPa,  $E(\text{Interface}) = 3.5$  (GPa),  $E(\text{PMMA}) = 3.5$  GPa,  $\nu(\text{hBN}) = 0.21$ ,  $\nu(\text{Interface}) = 0.25$ ,  $\nu(\text{PMMA}) = 0.35$ . Each of the control variables

is fixed in preliminary boundaries (intervals) for optimization procedures.

For the model ISS and GA optimization calculations authors' programs in Mathcad Prime v.6.0 (for complex roots case) and in Wolfram Mathematica 13.0.1 (for real roots case), have been created. The figures are prepared in Sigma Plot, v.13.0.

In Fig. 3, the optimal values of the parameters (load, length, thicknesses of the three layers) obtained in the two optimizations carried out with criterion equation (3), are plotted by two distinct colors symbols. It can be seen that along the ordinate each parameter changes within certain limits (intervals) for each of the two types of solutions (1) and (2) for ISS included in criterion (3).

The limits of the changes of the optimal thicknesses of PMMA  $h_2$  and of the interface layer  $h_a$ , for the cases of real and complex roots, are particularly well differentiated (see the ellipses in blue and red in Fig. 3). The intervals of variation of  $h_1$  (triangles down) and  $l$  (circles) are almost similar for both possible solutions (1) and (2). On the abscissa, each different set of 4 geometry data corresponds to a unique mechanical load such that for each group of five parameters criterion (3) is met or the model-predicted ISS at these load and geometry values is equal to or below the critical USS value.

In order to verify the obtained results, the following Figures 4 and 5 present a part of the

distributions of the ISS along the length of the nanocomposite, obtained at the optimal values of the parameters. As can be seen, for each type of solution, model ISS, calculated at the optimal values of the studied parameters actually meet the criterion of not having delamination in the nanocomposite structure. For the case of ISS, calculated by Mathematica for real roots eq. (1) (Fig. 5), it is worth noting that these optimal values assure that ISS is far from USS, e.g., this geometry and load assure more safety design in comparison with the case ISS for complex roots (Fig. 4).

Given the fact that there are no known experimental ISS data to compare with in the available literature, when such data become available in the future, it will be possible to further validate the results obtained here.

The only data which can be compared, is the thickness of interface layer – our common interval of obtained optimal values for  $h_a$  (m) for both cases of model ISS (real and complex) is  $(1e-09 \div 9.6e-08)$ .

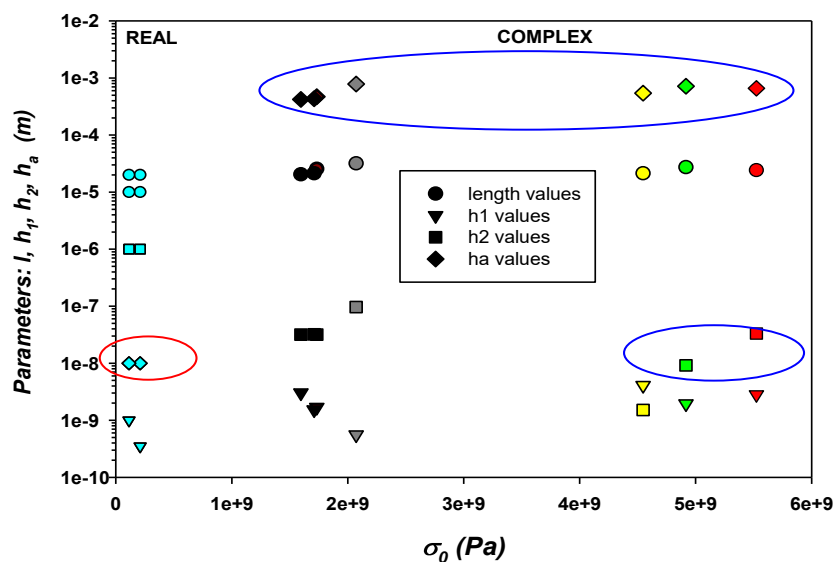


Fig. 3. Optimal solutions for 5 parameters from GA and Mathematica: complex (incrementing) and real roots (Cian)

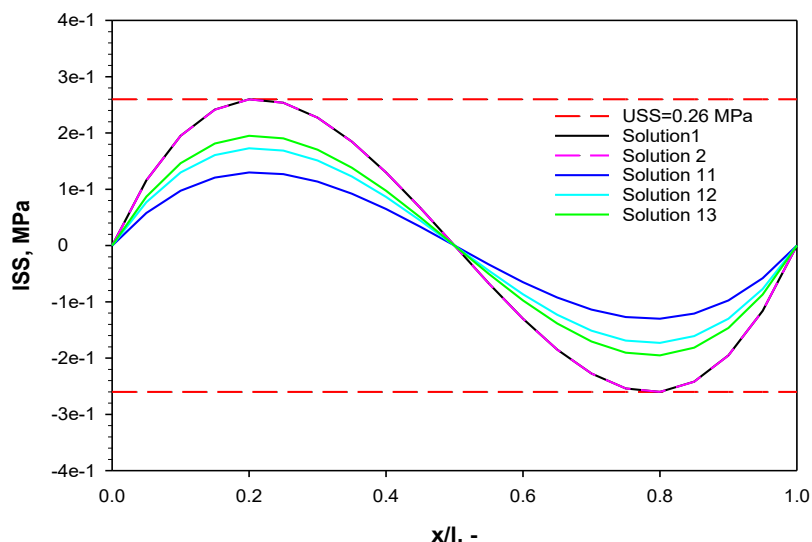


Fig. 4. Model interface shear stress distribution calculated by the optimal values of parameters (complex roots) for considered nanocomposite.

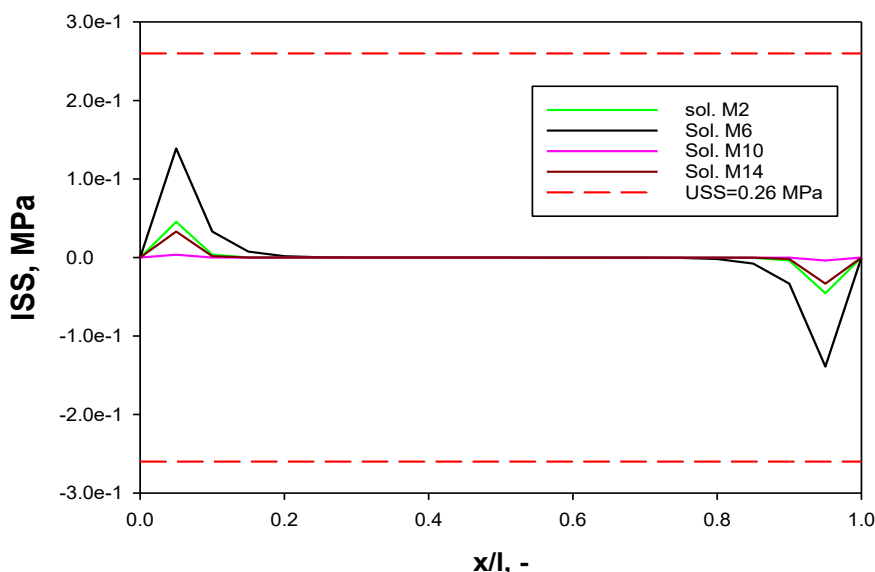


Fig. 5. Model interface shear stress distribution calculated at the optimal values of parameters (real roots) by Mathematica

It is worth noting that the values obtained by Gou *et al.* 2019 [11] (8.05 nm) and by Yi *et al.*, 2019 [9] (8.01 nm), as well as these of Kochetov [7] (1.6÷2.5 nm), are all within the range of the obtained here optimal results for interface thickness  $h_a$ , no matter that different substrates are used in combination with hBN.

### CONCLUSIONS

Here, the 2D stress-function model, combined with GA approach, was successfully applied for the first time to find, optimize and predict the safety load and geometry design of hBN/Interface/PMMA nanocomposite subjected to a static extension load.

The analytical model criterion without delamination in the considered nanocomposite, was

used as an objective function in two formulated multi-parameter optimization procedures for 5 parameters – 4 geometrical and 1 for mechanical loading. The five-parameter optimization problem for nanostructure safety work (without delamination) was formulated and solved with GA approach and Mathematica for hBN/Interface/PMMA.

The possible optimal solutions from GA and Mathematica represent sets of different combinations of all 5 parameters, which vary within predefined boundaries, according to physical and technical prescriptions. The results show that at the obtained optimal values of parameters the model ISSs confirmed and graphically fulfilled the model criterion of no delamination in the

hBN/Interface/PMMA nanocomposite. The obtained here results for the interval of optimal thickness for the interface layer  $h_a$  are in very good coincidence with available literature data for interface thickness in hBN/substrate nanocomposites.

The here proposed methodology for determining and predicting the optimal geometry design and load can be applied to any material combinations for three-layer nanocomposite structures, which satisfy the model assumptions [16].

**Acknowledgement:** This study is performed by the financial support under the contract No. KII-06-H57/3/15.11.2021 with Bulgarian National Science Fund for the project „Optimal safe loads and geometry for layered nanocomposites under thermo-mechanical loading “.

#### Nomenclature

$A$	constant, solution of non-homogeneous ODE of 4 <sup>th</sup> order in [16];
$C_i, M_i$	integration constants in the model solutions, determined from the respective boundary conditions [16];
$E$	Young modulus of a layer material, $Pa$ ;
$h_1, h_a, h_2$	thicknesses of the 1 <sup>st</sup> , interface and 2 <sup>nd</sup> layers in the nanocomposite (Fig. 1), $m$ ;
ISS	model interface shear stress, eq. (3), $Pa$ ;
$l$	length of the nanocomposite (Fig. 1), $m$ ;
$P$	applied tension force to the substrate (Fig. 1), $N.m$ ;
$x, y$	coordinate system (Fig.1), $m$ ;
USS	ultimate shear stress of interface layer in nanocomposite, $Pa$ .

#### Greek symbols

$\alpha \pm i\beta$	complex roots of the characteristic equation, corresponding to ODE of 4 <sup>th</sup> order in [16];
$\lambda_i$	real roots of the characteristic equation, corresponding to ODE of 4 <sup>th</sup> order in [16];
$\nu$	Poisson number (ratio), -;
$\sigma_0 = P/h_2$	external loading stress applied to substrate (Fig. 1), $Pa$ ;
$\sigma_1, \sigma_{x,y}^a$	model [16] axial and shear stress in eqs. (1), (2) and (3), $Pa$ .

#### Abbreviations

BN/BNNS Boron nitride/Boron nitride nanosheet;

BNNT	Boron nitride nanotubes;
GA	genetic algorithm;
hBN	hexagonal boron nitride;
ISS/USS	Interface/Ultimate shear stress;
IFSS	Interface shear strength;
$M2, M6,$	optimal solutions from the
$M10, M14$	optimization procedure in Mathematica, (Table 2);
ODE	ordinary differential equation;
OF	objective function [17];
PDMS	Polydimethylsiloxane, silicone polymer;
PMMA	Poly(methyl methacrylate), plexiglas or acrylic;
PVA	Polyvinyl alcohol, synthetic polymer.

#### REFERENCES

1. W. Liu, B. Ullah, Ch.-Ch. Kuo, X. Cai, *Advances in Polymer Technology*, **2019**, Article ID 4294306, (2019). <https://doi.org/10.1155/2019/4294306>
2. J. Joy, E. George, P. Haritha, S. Thomas, S. Anas, *J. Polym. Sci.*, **58**, 3115 (2020). <https://doi.org/10.1002/pol.20200507>
3. M. G. Rasul, A. Kiziltas, B. Arfaei, R. Shahbazian-Yassar, *2D Materials and Applications*, **5**, article No. 56 (2021). <https://doi.org/10.1038/s41699-021-00231-2>
4. K. Bera, D. Chugh, A. Patra, H. H. Tan, C. Jagadish, A. Roy, *ArXiv preprint arXiv:1907.05591*, (2019). <https://doi.org/10.48550/arXiv.1907.05591>
5. S. S. Akhtar, *Polymers*, **13**, 807 (2021). <https://doi.org/10.3390/polym13050807>
6. M. E. P. Tweedie, Y. Sheng, S. G. Sarwat, W. Xu, H. Bhaskaran, J. H. Warner, *ACS Appl. Mater. Interfaces*, **10**(45), 39177 (2018). <https://doi.org/10.1021/acsami.8b12707>
7. R. Kochetov, PhD thesis, Technische Universiteit Delft, The Netherlands, 2012. [https://www.researchgate.net/publication/241862538\\_Thermal\\_and\\_Electrical\\_Properties\\_of\\_Nanocomposites\\_Including\\_Material\\_Properties](https://www.researchgate.net/publication/241862538_Thermal_and_Electrical_Properties_of_Nanocomposites_Including_Material_Properties)
8. J. Li, J. Chen, M. Zhu, H. Song, H. Zhang, *Appl. Sci.*, **9**, 2832 (2019). <https://doi.org/10.3390/app9142832>
9. C. Yi, S. Bagchi, F. Gou, C. M. Dmuchowski, C. Park, C. C. Fay, H. B. Chew, Ch. Ke, *Nanotechnology*, **30**, 025706 (2019). <https://doi.org/10.1088/1361-6528/aae874>
10. H. Shen, C. Cai, J. Guo, Z. Qian, N. Zhao, J. Xu, *RSC Adv.*, **6**, 16489 (2016). <https://doi.org/10.1039/c6ra00980h>
11. F. Gou, C. Ke, *Multiscale Science and Engineering*, **1**, 236 (2019). <https://doi.org/10.1007/s42493-019-00021-5>
12. W. Wang, PhD thesis, Department of Materials, Faculty of Science and Engineering, The University of Manchester, UK, 2021.
13. W. Wang, Z. Li, A. J. Marsden, M. A. Bissett, R. J.

- Young, *Composites Science and Technology*, **218**, 109131 (2022).  
<https://doi.org/10.1016/j.compscitech.2021.109131>
14. P. Tatarczak, J. Iwański, A. K. Dąbrowska, M. Tokarczyk, J. Binder, R. Stępniewski, A. Wymolek, *Nanotechnology*, **35**, 175703 (2024).  
<https://doi.org/10.1088/1361-6528/ad18e6>
15. T. Petrova, E. Kirilova, A. Apostolov, R. Vladova, B. Boyadjiev, Analytical modelling of axial strain and interface shear stress distributions in hBN/PMMA nanocomposite under mechanical loading, *Book of abstracts of 7<sup>th</sup> International Scientific Conference "MATHEMATICAL MODELING"*, December 6-9, 2023, Borovets, Bulgaria.  
<https://mathmodel.eu/sbornik/2023.pdf>
16. T. St. Petrova, *Bulg. Chem. Commun.*, **55**(3), 349 (2023). <https://doi.org/10.34049/bcc.55.3.SIMNS05>
17. E. Shopova, N. Vaklieva-Bancheva, BASIC-A genetic algorithm for engineering problems solution, *Computers and Chemical Engineering*, **30**, 1293 (2006).  
<https://doi.org/10.1016/j.compchemeng.2006.03.003>

# Development of transdermal cellulose-based patches for Alzheimer's treatment and investigation of penetration behavior

H. Mutlu, E. Akyol\*

*Yildiz Technical University, Department of Chemical Engineering, Istanbul Turkey*

Received June 3, 2024; Accepted: August 17, 2024

Transdermal patch drug delivery systems deliver the drug to the body through the skin and provide a controlled release. The present study aims at developing transdermal patches for Alzheimer's treatment and to improve the penetration characteristics of transdermal patches. Donepezil hydrochloride drug active substance selected in this study is commonly used to treat Alzheimer's disease. HEC (hydroxyethyl cellulose) and CHI (chitosan) were used as polymer-based matrix and natural additives as penetration enhancers for the transdermal patches. The effectiveness of the patches prepared using different plasticizer materials was investigated. Synthesized films under *in vitro* conditions were characterized by UV spectrophotometry, SEM, FTIR and Zetasizer. The drug release kinetics were determined using the zero-order, first-order, Higuchi and Korsmeyer-Peppas kinetic models by analyzing samples taken at certain time intervals using a UV spectrophotometer.

The results in this study confirm that synthesized films can be potential materials for developing treatments for Alzheimer's disease. This project aims to contribute to the healthcare sector by developing unique patch formulations with high stability in order to provide solutions to the problems encountered in the oral treatment of Alzheimer's disease, reducing the negative effects of existing commercial patches and improving their features.

**Keywords:** Drug delivery; Transdermal patch; Donepezil hydrochloride; Penetration; Alzheimer

## INTRODUCTION

Alzheimer's disease is a progressive condition affecting memory, thinking and behavior. Alzheimer's, which affects millions of people worldwide, creates a significant social and economic burden and requires effective treatment strategies [1]. Existing oral medications for Alzheimer's disease have limitations, including issues with adherence, absorption and side effects, highlighting the need for alternative treatment methods and innovative therapeutic approaches, such as transdermal drug delivery systems [2].

Transdermal drug delivery is a method of administering drugs through the skin for systemic distribution [3]. The drug penetrates through the skin layers to reach the systemic circulation, providing a controlled release of the drug [4]. Transdermal patch systems are designed to deliver therapeutically effective amounts of drugs, providing controlled and sustained drug release [5]. Transdermal drug delivery system types are reservoir, matrix and microneedle patch systems. Reservoir systems consist of a drug reservoir that is surrounded by a rate-controlling membrane. The drug is released from the reservoir through the membrane at a controlled rate, ensuring consistent delivery over time. Advancements in nanotechnology, microneedle patches, and transdermal systems hold

promise for further enhancing Alzheimer's treatment options. The non-invasive nature of transdermal patches enhances patient compliance and comfort, particularly in the context of chronic conditions like Alzheimer's [6].

Donepezil is a cholinesterase inhibitor that works by increasing the levels of acetylcholine in the brain, a neurotransmitter that is crucial for memory and learning. The traditional oral formulation of donepezil presents challenges such as gastrointestinal side effects and consistent dosing difficulties, which may impact treatment efficacy [7]. The development of a transdermal patch for delivering donepezil addresses the limitations of the oral formulation and offers a new approach to enhancing treatment outcomes for individuals with Alzheimer's disease.

Challenges in transdermal drug delivery require the use of penetration enhancers. Penetration enhancers play a significant role in improving drug permeation through the skin, minimizing the limitations posed by the skin's natural barriers, and thus increasing the efficiency of transdermal drug delivery [8-11]. Penetration enhancers work with disrupting the skin's barrier function, facilitating drug permeation through mechanisms such as lipid extraction, protein denaturation and alteration of intercellular lipids. Penetration enhancers should

\* To whom all correspondence should be sent:

E-mail: eakyol@yildiz.edu.tr

increase drug permeation by biocompatible and sustainable substances that minimize skin irritation and adverse effects [12].

The present study aims at improving the penetration properties of the synthesized transdermal patches by developing a transdermal formulation for the controlled release of donepezil, one of the important active ingredients in the treatment of Alzheimer's disease.

## MATERIALS AND METHOD

### Materials

The list of purchased chemicals used in this study is given in Table 1. In films prepared based on HEC and CHI polymer, propylene glycol and glycerine are used as plasticizers; natural oils as a penetration enhancer and donepezil HCl which is widely used in Alzheimer's patients, as a drug.

### Transdermal patch preparation

Transdermal patches were prepared by the solvent casting method. All chemicals in the formulation, penetration enhancers and donepezil HCl were dissolved in distilled water and mixed by a magnetic stirrer until they became homogeneous to ensure proper dissolution and uniformity. The formulation of the transdermal patches is summarized in Table 2. To obtain patches, the solution was poured onto Petri dishes and left to dry at room temperature.

### Drug permeation studies using the Franz diffusion cell

Franz diffusion cell consists of a donor and a

receptor chamber separated by a membrane mimicking the biological barrier, enabling the measurement of drug permeation.

*Experimental setup:* The cell is designed to maintain physiological conditions, including temperature, pH and ionic strength to simulate the *in vivo* environment. This ensures that the drug release behavior closely resembles its performance in real-life applications.

*Membrane selection:* The choice of membrane in the Franz diffusion cell is critical, as it determines the relevance of the *in vitro* results to *in vivo* scenarios. Factors such as permeability, selectivity, and compatibility with the drug are essential considerations in membrane selection.

After the patches dried, drug release studies were started in the Franz diffusion cell. Transdermal patch samples were placed on the lid of the Franz cell. Cellulose acetate membrane filters, with a diameter of 47 mm and a pore size of 0.45  $\mu\text{m}$ , were prepared and placed in pH 7.4 buffer solution to mimic the skin. The prepared patches were placed on the cellulose acetate membrane filter in the section between the diffusion cell cover and the receiver chamber. The top of the Franz cell was covered with parafilm to prevent evaporation and foreign objects. The Franz diffusion cell, shaking at 110 rpm, was kept at 37°C to represent body temperature. Drug release was achieved in the Franz cell for 24 h. Samples were collected at specific time intervals and analyzed using a UV-vis spectrophotometer. SEM, FT-IR and zeta potential analyzes were performed for the selected patch.

**Table 1.** Materials and supplier companies

Materials	Supplier
Hydroxyethyl cellulose	Dafimed Company
Propylene glycol	Genesis Company
Glycerine	Tekkim Chemical Company
Donepezil HCl	Abdi İbrahim Medicine Company

**Table 2.** Formulation of the transdermal patches

Film No	HEC (g)	CHI (g)	Propylene Glycol (g)	Glycerine (g)	Gelatine (g)	CaCl <sub>2</sub> (g)	Dimethyl Sulfoxide (g)	Arlasolve (g)	Lysofix (g)	St. John's Wort Oil (g)	Rosehip Oil (g)	Argan Oil (g)	Avocado Oil (g)	Sesame Oil (g)	Grape Seed Oil (g)	Donepezil HCl (g)
1	0.5	-	0.6	0.02	0.02	-	0.5	0.1	-	0.3	-	-	-	-	-	0.1
2	0.4	0.1	0.5	-	0.02	0.03	0.6	-	0.1	-	0.3	-	-	-	-	0.1
3	0.4	0.1	0.5	-	0.02	0.03	0.6	-	0.1	-	-	0.3	-	-	-	0.1
4	0.4	0.1	0.5	-	0.02	0.03	0.6	-	0.1	-	-	-	0.3	-	-	0.1
5	0.4	0.1	0.5	-	0.02	0.03	0.6	-	0.1	-	-	-	-	0.3	-	0.1
6	0.5	0.1	0.5	0.02	0.02	-	0.5	-	-	-	-	-	-	-	0.4	0.1

RESULTS AND DISCUSSION

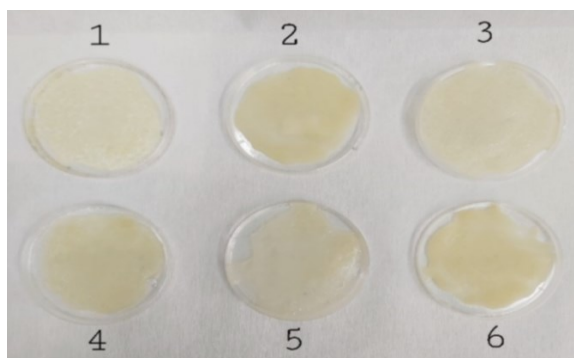


Fig. 1. Images of the transdermal patches

*Kinetic behavior of drug release*

Images of the transdermal patches are shown in Fig. 1. Drug release kinetic behavior graphs provide information about the drug release mechanism and kinetics. Understanding drug release kinetics is significant in predicting the *in vivo* behavior of the formulated drug. Different kinetic models can be used to fit experimental data and interpret drug release kinetics. The choice of carrier material significantly influences drug release kinetics. Factors such as porosity, surface area and degradation rate of the carrier material play a crucial role in determining the release profile of the drug. The morphology of the carrier, including its shape, size and internal structure can impact the diffusion and release of the drug. The kinetics of donepezil HCl drug release were determined using the zero-order, first-order, Higuchi equation and Korsmeyer-Peppas equation. The equations of the kinetic models are given in Table 3.

Table 3. Release kinetic models

Release Kinetics Modeling	
Zero-order Model	$Q=Q_0+k*t$
First-order Model	$Q/Q_0 = 1 - e^{-(k*t)}$
Higuchi Model	$Q=k*t^{1/2}$
Korsmeyer-Peppas Model	$Q/Q_0 = k*t^n$

Q is the amount of drug dissolved over time,  $Q_0$  is the initial amount of drug in solution, k is the zero-order release constant expressed in units of concentration/time.  $R^2$  regression coefficient values were found using kinetic model equations.

The highest  $R^2$  regression coefficient values were observed in Korsmeyer-Peppas and Higuchi release kinetics. In conclusion, it was determined the patches fit the Korsmeyer-Peppas model and the release mechanism was examined through this model. The results are shown in Table 4.

Table 4. Regression coefficient values

Film No	Zero-order Kinetic Model	First-order Kinetic Model	Higuchi Kinetic Model	Korsmeyer – Peppas Kinetic Model
1	0.9833	0.8388	0.9454	0.991
2	0.9887	0.8179	0.9861	0.988
3	0.9827	0.8016	0.9787	0.9778
4	0.9754	0.7835	0.9834	0.9834
5	0.9724	0.7715	0.9899	0.9843
6	0.9908	0.8129	0.9875	0.9946

The controlled release behavior of donepezil was characterized by the Korsmeyer-Peppas equation. The emission exponent (n) values obtained from the slope of the log % emission plot against log t show that the release mechanism is working. Table 5 presents the (n and k) values of the films obtained using the Korsmeyer-Peppas model equation.

Table 5. Korsmeyer-Peppas release kinetic values

Film No	n	k
1	0.5841	0.0079
2	0.6313	-0.1787
3	0.5956	-0.0546
4	0.587	-0.0463
5	0.657	-0.2535
6	0.6723	-0.2984

The graphs are shown in Figs. 2, 3, 4 and 5. Film formulations exhibit a non-Fickian mechanism, as indicated by their n release exponent values falling within the range of  $0.45 < n < 0.89$ .

Non-Fickian release kinetics are characterized by a release rate that is not solely dependent on the concentration gradient, as observed in Fickian diffusion. Instead, the release mechanism may be influenced by factors such as swelling, erosion, or other complex drug release processes. Non-Fickian release kinetics enable the development of controlled release formulations that can modulate the drug release rate over an extended period. This has implications for improving patient compliance and therapeutic efficacy.

*Zeta potential analysis*

Zeta potential analysis indicates the stability of the dispersion and the potential for interactions with other particles or surfaces. Changes in pH and ionic strength can significantly impact the zeta potential of nanoparticles, influencing their stability and drug release properties. Among six films, film 1 has the highest drug release percentage. The zeta potential analysis result for film 1 is shown in Figure 6.

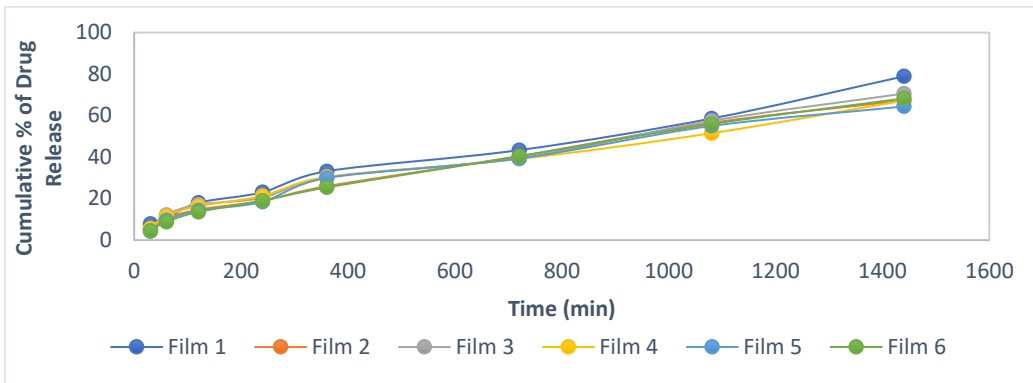


Fig. 2. Zero-order kinetic model

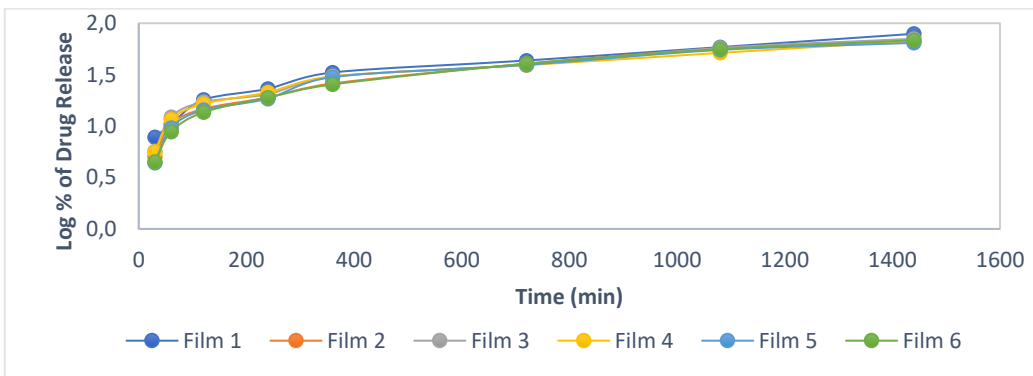


Fig. 3. First-order kinetic model

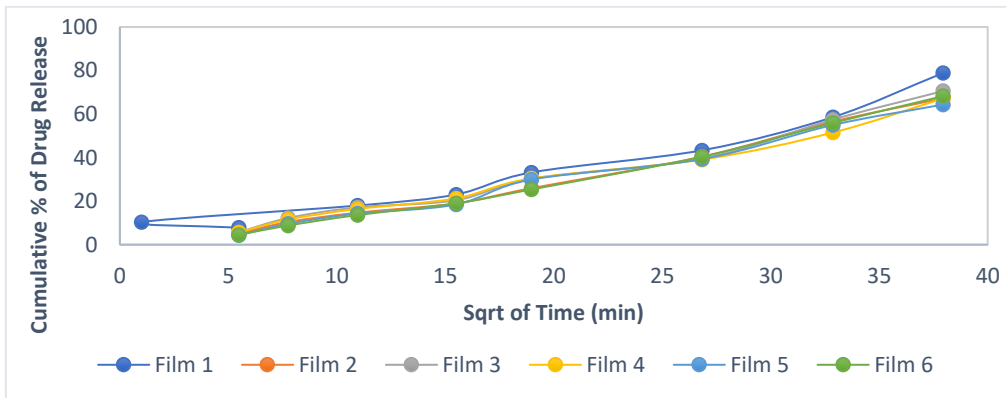


Fig. 4. Higuchi kinetic model

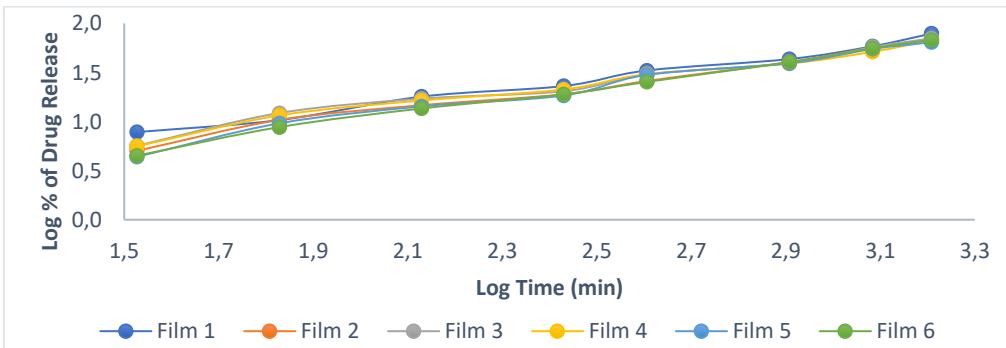


Fig. 5. Korsmeyer-Peppas kinetic model

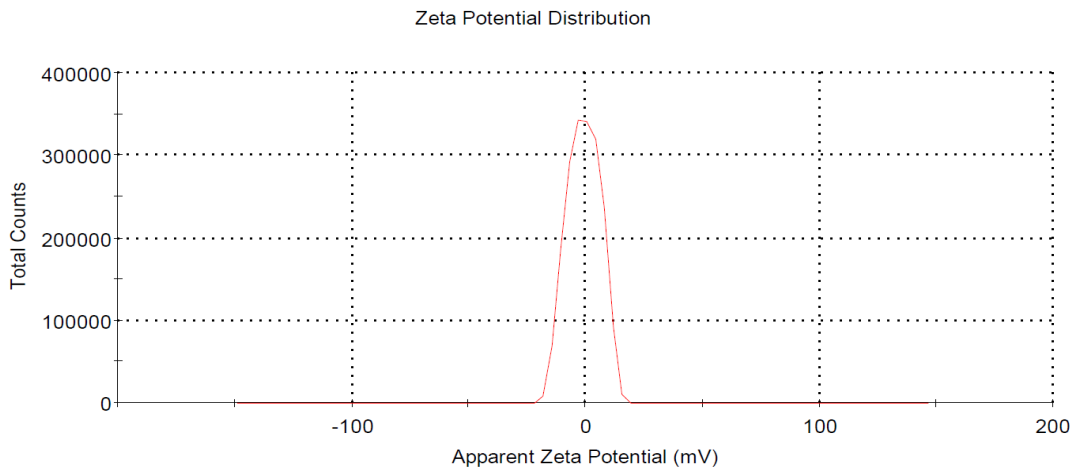


Fig. 6. Zero potential graph for film 1

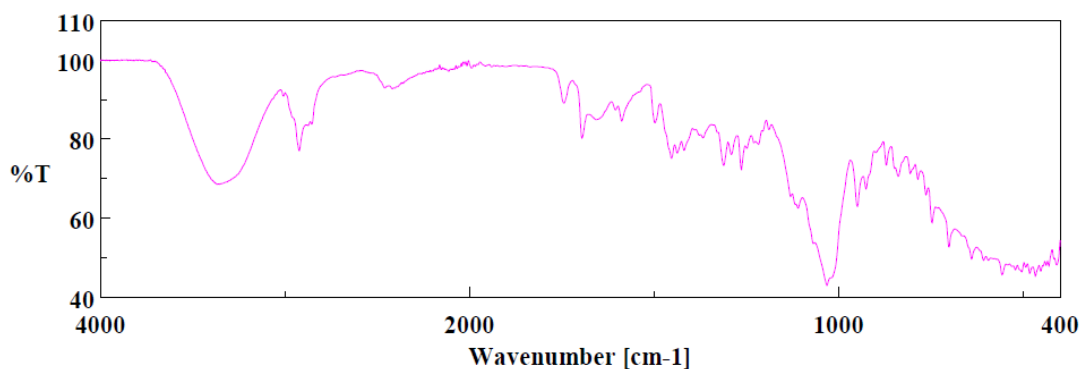


Fig. 7. FTIR analysis for film 1

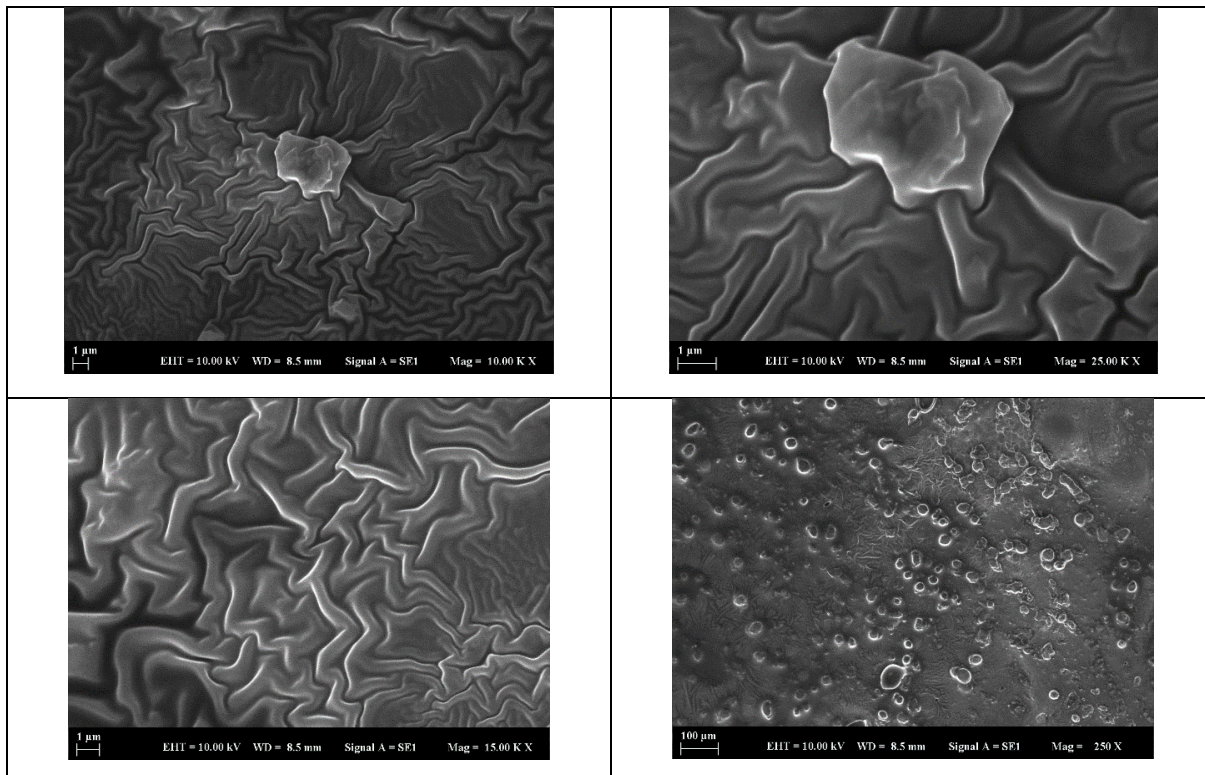


Fig. 8. FTIR analysis for film 1

#### FTIR (Fourier transform infrared) spectroscopy analysis

FTIR analysis provides information on drug-polymer interactions, diffusion processes, and the influence of environmental factors on drug release, aiding in the design of optimized drug delivery systems and this technique allows real-time monitoring of drug release. The FTIR analysis for film 1 is shown in Figure 7.

#### SEM (scanning electron microscopy) analysis

Scanning electron microscopy (SEM) is a powerful imaging technique that uses a focused beam of electrons to generate high-resolution images of the surface of a sample. It provides detailed information about the topography, morphology, and composition of materials at the nanoscale (Fig. 8).

#### CONCLUSION

In this thesis study, six different transdermal patches were successfully synthesized by adding different types and amounts of plasticizers, substances and penetration enhancers in varying ratios. Different release rates were achieved with the added plasticizers, flexibility and pore structure were observed to be different and the characterization results confirmed these. Drug release rates of all patches were examined in a pH 7.4 environment for 24 h. As a result of analyses using UV spectroscopy; the film with the highest release rate is film number 1 with 78.89%. In general, it can be said that the amount of drug release increases due to the increase in the amount of plasticizer in the patch. The drug release rates for other patches are 67.24% for film 2, 70.58% for film 3, 67.18% for film 4, 64.38% for film 5 and 68.25% for film 6. These findings establish a correlation between the substances in varying ratios and the resulting drug release rates, emphasizing the importance of formulation optimization for transdermal patches.

Scanning electron microscopy (SEM) analyses were also carried out at different magnification rates and scales. Accordingly, the most homogeneous

structure of the films and the pore structure in the films containing St. John's wort oil were clearly seen.

Stability studies performed with the Zetasizer device showed that there was no significant change in films kept at room temperature.

According to the analysis results obtained with the FTIR device, the polymers in the films accurately meet the wavelengths specified in the literature. This reveals that the synthesized patches are mostly homogeneously distributed which is confirmed by analysis.

**Acknowledgement:** This study was supported by the Research Fund of the Yildiz Technical University (Project No: FDK-2023-5572).

#### REFERENCES

1. L. Huang, T. Su, X. Li, *Curr. Top Med. Chem.*, **13** (15),1864 (2013).
2. P. Anand, B. Singh, *Arch. Pharm. Res.*, **36**(4), 375 (2013).
3. S. Sadab, S. Sahu, S. Patel, R. Khan, B. Khare, B. Thakur, S. P. K. Jain, *Asian Journal of Dent. and Health Sci.*, **2**(4), 40 (2022).
4. D. Ramadan, M. T. McCrudden, A. J. Courtenay, R. F. Donnelly, *Drug Delivery and Translational Research*, 1-34 (2021).
5. X. Wang, in: *SHS Web of Conferences, EDP Sciences*, **144**, 01006 (2022).
6. A. Hanbali, O.A. Khan, H.M.S. Sarfraz, M. Arafat, M. Ijaz, A. Hameed, *Acta Pharm.*, **69**(2). 197 (2019).
7. Y. Acar, E. Akyol, *The Online Journal of Sci. and Tech.*, **11**(1), 31 (2021).
8. L. Chen, L. Ma, S. Yang, X. Wu, X. Dai, S. Wang, X. Shi, *Journal of Trad. Chinese Med. Sci.*, **6** (4), 347 (2019).
9. S. Chakraborty, N. Gupta, K. T. Sastri, M. Sharadha, P. Chand, H. Kumar, V. Jain, *Journal of Drug Del. Sci. and Tech.*, **73**(1), (2022).
10. L. Bartosova, J. Bajgar, *Curr Med Chem*, **19**(1), (2012).
11. K. Purushotham, K. A. Vijetha, *GSC Biological and Pharmaceutical Sciences*, **22**(2), 245 (2023).
12. D. Ekşi, E. Akyol, I. Küçük, *Bulg. Chem. Commun.*, **55** (3), 289 (2023).

# The effect of pigment on the properties of black automotive enamel

S. Öztürk, İ. Küçük\*

Chemical Engineering Department, Yıldız Technical University, İstanbul, Turkey

Received May 24, 2024; Accepted: August 17, 2024

Lamination process of automotive glasses can be created through either sag bending or press bending. Especially front windshield glasses that are manufactured by sag bending process, must maintain low melting degrees, possess strong chemical and physical properties, and exhibit low UV transmittance, indicating high optical density. Automotive glass enamels meeting these criteria are composed of low-melting bismuth ingredient-based frit,  $\text{CuCr}_2\text{O}_4$  black inorganic pigment, and an organic vehicle. All those components affect the final properties of cured glass paint characteristics. This study examines how different brands of black  $\text{CuCr}_2\text{O}_4$  pigments, used in glass enamel paint, impact physical properties such as color, gloss, optical density and chemical properties.

**Keywords:** Laminated glass, enamel, paint glass-ceramics, pigment

## INTRODUCTION

Owing to increasing mobility and individual vehicle usage rates in recent years, vehicle sales have shown significant increases on both global and domestic markets. Consequently, there has been an acceleration in the demand for glass and processed glass used in vehicles. Especially in the automotive sector, laminated and tempered glasses are processed through sag bending or press bending processes and used on different surfaces of the vehicle [1, 2].

Front glasses, referred to as the 4th surface, use black enamel paints with high opacity, high chemical and mechanical resistance. The tempering temperatures, durations, and final customer test methods for these paints vary depending on the usage location and production processes. Black automotive glass paints consist of three main components [3-5]: a frit containing bismuth,  $\text{CuCr}_2\text{O}_4$  black pigment, and an organic medium (vehicle) (Figure 1).

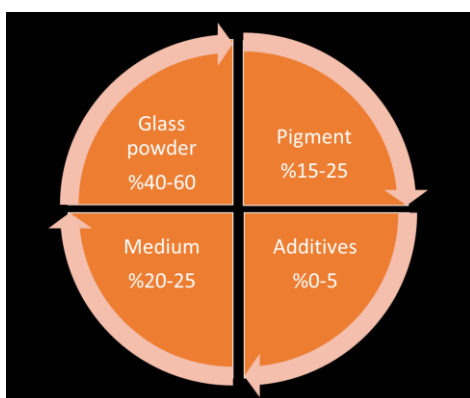


**Figure 1.** Automotive black glass enamel paint composition

The types of these components significantly affect the final paint properties. All these factors affect the color, gloss, optical density, chemical resistance, surface abrasion, and rheological properties that need to be controlled from both surfaces of the glass [6].

In this study, the effects of pigment on the paint properties of glass enamel applied on 10 cm×10 cm×4 mm glass substrate by using the screen-printing method were examined. The most suitable pigment option for the recipe and process were determined by characterizing it through XRF, XRD, PSD, BET, color measurement (L, a, b), gloss measurement, optical transmittance measurement, and chemical analysis tests. It was observed that when the pigment type, crystal structures in the pigment and particle size distribution changed, the color properties get greyish and acid resistance was negatively affected.

## EXPERIMENTAL AND MATERIALS

Automotive glass enamel paints contain 4 main constituents: a bismuth-based frit (Akcoat, Turkey), PBK-28 group  $\text{CuCr}_2\text{O}_4$  inorganic black spinel pigment of 3 different brands (Shepherd, Belgium, solvent- and water-based organic media (Akcoat, Turkey), additives and surface modifiers (Evonik, Germany).

Glass frit was produced in a rotary kiln. The standard procedure can be outlined as follows. Glass frit was melted to 1200 °C in a rotary kiln as bismuth has high density and settles down in a continuous kiln. It is quenched in cold water (25-35 °C) to ensure amorphous structure. The frit is dried and ball-milled up to particle size of D90 value 75 μm. Fine milling was done in bed type high air speed

\* To whom all correspondence should be sent:

E-mail: [kucuk@yildiz.edu.tr](mailto:kucuk@yildiz.edu.tr)

pressured pilot type jet mill. Final particle sizes were adjusted to a D90 value of 6-8  $\mu\text{m}$ . Schematic presentation of bismuth glass frit powder production approach is seen in Figure 2. Frit glass powder should have a melting zone of 640-660  $^{\circ}\text{C}$  defined by hot-stage measurement. Pigment was added to the medium in a high-speed mixer; glass powder, additives were added in the last stages of the recipe process to make an efficient dispersion of all dense materials. All samples were roll-milled three times before silk screen printing (Figure 3).

### RESULTS AND DISCUSSION

XRF, PSD (Malvern Mastersizer 3000) and BET surface area (Quantachrome TouchWin) results of three different brand pigments are shown in Table 1. XRF provides insight into the chemical components of pigment recipe. The analysis by PSD and BET, as seen in Table 1, reveals differences in particle size distribution and surface total area. The acceptance limits of  $\text{Cr}_2\text{O}_3$  should be as high as possible for less

contamination. The higher the D90, the bigger are the pigment particles. BET analysis confirms that the particles are smaller, with larger surface which can easily and effectively be covered and coated by the medium.

XRD (Bruker D8 Advance Eco) tests were made to characterize the crystal phases of similar pigments.

**Table 1.** XRF, PSD comparisons of pigment samples

Oxides	Pigment A	Pigment B	Pigment C
$\text{Cr}_2\text{O}_3$	65	69.3	70
$\text{CuO}$	35	30.5	29.6
$\text{Fe}_2\text{O}_3$	0.2	0.05	0.12
$\text{Al}_2\text{O}_3$	0.1	-	0.08
D (10) $\mu\text{m}$	0.158	0.053	0.02
D (50) $\mu\text{m}$	1.88	1.57	0.06
D (90) $\mu\text{m}$	4.32	4.46	0.29
Surface area ( $\text{m}^2/\text{g}$ )	2.13	2.24	2.62

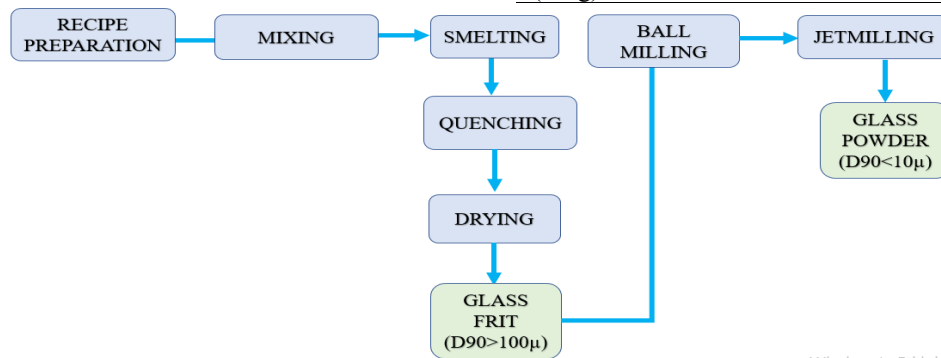


**Figure 2.** Flow diagram of the bismuth glass frit powder production



**Figure 3.** Schematic presentation of the glass enamel preparation and firing method

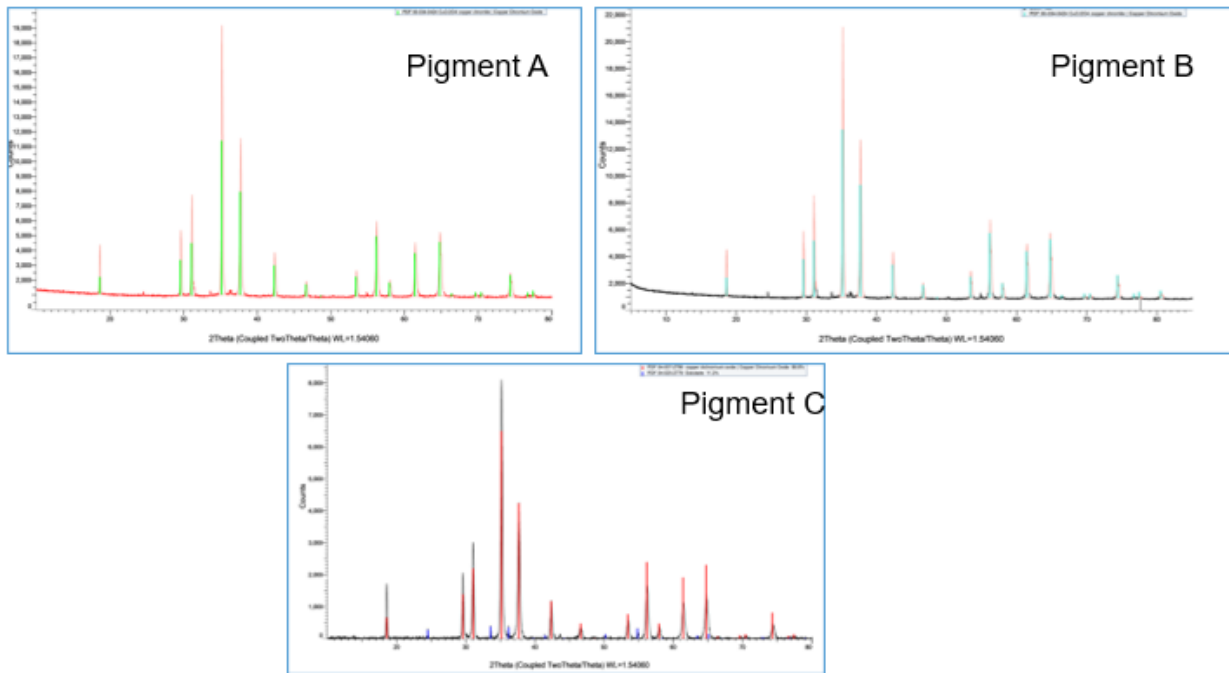


Figure 4. XRD analysis of pigments A, B, C

Table 2. Physical color, gloss and optical density measurements, ΔE values

Experiment	L	a	b	Gloss	O.D	ΔL	Δa	Δb	ΔE
Reference	21.75	-0.02	-1.86	32	0.74	*	*	*	*
Pigment A	21.50	-0.12	-1.86	37	0.73	-0.25	-0.10	0	0.27
Pigment B	21.62	-0.20	-2.04	39	0.70	-0.13	-0.18	-0.18	0.29
Pigment C	23.81	0.01	-1.58	31	0.66	2.06	0.03	0.28	2.08

As seen in Fig. 4, pigments A and B consist of 100%  $Cu_2CrO_4$  while pigment C also contains 11.2 % eskolaite phase.

Color L, a, b values were measured according to ASTM E-1164 standard with colorimetric instrument (Konica Minolta CM-700 D); gloss values were measured with glossmeter (TQC-Sheen GL0030-20°/60°/85°) and 60° values were recorded, optical density results were obtained by optic densitometer (X-rite 361 T) and ΔE values of the test samples were calculated by the equation given below.

$$\Delta E^* = \sqrt{(L_2 - L_1)^2 + \sqrt{(a_2 - a_1)^2 + (b_2 - b_1)^2}} \quad (1)$$

Optical density deviation from standard D: ± 0.2D and gloss values G: ± 5 from the reference values are in the range of acceptance. Experimental results can be seen in Table 2.

When the pigment ratio is constant depending on the pigment XRF results itself, the brightness value increases from 21.5 to 23.81, indicating higher L values. However, color with a ΔE value of 2.08 indicates less firing, which causes a greyish surface

color. Also pigment C causes lower gloss which means higher matness of the surface and supports that there is less firing on the glass enamel paint. Pigment B gives a higher gloss value of 39 compared to the reference glass paint. ΔE lower than 0.5 can be acceptable. Pigment C lowers the optical density the most which is unwanted condition for the UV protective automotive front glass enamels.

Chemical durability tests of samples were done according to ASTM C724-91. A drop of acid was applied to the enamel area of the fired glass and the stained area was covered with watch glass. The sample was washed with distilled water after 15 min and detection range was determined between 1-6. In this range, 1 indicates high acid resistance quality without leaving stains, while 6 indicates complete removal of glass enamel from the surface. Chemical stability of samples is given in Table 3.

Table 3. Chemical stability of samples

	STD	D1	D2	D3
Chemical stability	1	1	1	2

Chemical stability results show that the different types of pigments display different chemical resistance. Pigment C has the lowest result with 2. When melting level is lower, chemicals attack the open pores on the glass enamel and react with pigment particles causing them to deform and change the color to the greyish side.

#### CONCLUSION

The glass ceramic coating composition consists of glass frit, a complex inorganic pigment and organic medium. The current study was designed by keeping frit type, medium and additive type and % ratio, pigment % ratio as constants and changing only the pigment type.

The study shows that the composition, particle size distribution and crystal structure of the pigment and its derivatives have an impact on the physical properties such as color, gloss, and optical density.

Pigments A and B can be chosen as an alternative depending on color properties, gloss and optical density with the help of BET and PSD analysis. Chemical durability can be affected by pigment type. As a result, we believe that the suggested methods show a good result in the production of black automotive glass enamel depending on the material choice upon recipe contents. All components' ratios

and types should be studied thoroughly by controlling all critical methods and factors.

**Acknowledgement:** In this study, all experimental works were conducted in Akcoat Advanced Coatings, Glass Coating Research and Development Laboratory. The authors would like to thank all members of the Glass Coating Department and supporters for their precious contributions.

#### REFERENCES

1. L. Tu, H. Wang, X. Liu, J. Guan, F. Cai, US20230211587A1, 1 (2023).
2. G. Akoshe, E. Maloney, J. Gleason, C. Sridharan, Srinivasan, International Application Published Under The Patent Cooperation Treaty, WO2017/127788A1, 37 (2017).
3. S. Sing, K. Sakoshe, E. George, D. A. Klimas, WO2013/126369A1, 1 (2013).
4. R. Prunchak, M. Sgriccia, WO2008/130747A1, 1 (2008).
5. H.-W. Lin, Ch.-P. Chang, W.-H. Hwu, M.-D. Ger, *Journal of Materials Processing Technology*, **197**, 284 (2008).
6. S. Öztürk, İ. Küçük, B. Çiçek, 2nd International Karatekin Science and Technology Conference (IKSTC 2nd), Çankırı, Türkiye, 2023.

## Improved packaging performance of olive tree-based biochar-loaded poly(lactic acid) films

F. Uğur Nigiz\*, Z. İ. Özyörü, S. Balci

*Faculty of Engineering, Department of Chemical Engineering, Çanakkale Onsekiz Mart University, Turkey*

Received June 5, 2024; Accepted: August 17, 2024

Petroleum-containing packaging materials have created serious ecological problems for the environment due to their resistance to biological degradation. In this context, the use of biodegradable films as alternative to packaging materials is gaining importance. Among various biopolymers, poly(lactide) (PLA) is an effective and durable material. However, the mechanical strength of PLA polymer is low. In addition, its vapor permeability is high, which limits the use of this material. Biochar (BC) is an additive that can be produced from many wastes and acts as a fertilizer in the soil. Adding it to the PLA material makes the packaging film completely compostable and improves its properties. In this study, biochar was synthesized from olive pruning waste by the slow pyrolysis method. Biochar was added to the PLA films in different ratios (5, 10, 15, 20 wt.%). The packaging properties of the films were investigated. Specific surface area (BET), biochar yield, and ash content, as well as tensile strength, swelling, water vapor permeability, and opacity of the films were determined. Owing to the high lignin rate and low volatile matter in the olive branch, biochar was produced with a yield of 29.75%. When the BC concentrations of the films increased, the water vapor permeability capacity gradually decreased from 4.43% to 1.36%. The maximum tensile strength value was obtained as 14.91 MPa for 5 wt.% biochar-loaded PLA films.

**Keywords:** polylactic acid packaging, biochar, composite films

### INTRODUCTION

The increasing environmental problems and depletion of petroleum resources have led to an increase in the usage of renewable resources in the manufacture of biodegradable food packaging materials [1]. Traditionally used plastics are obtained by processing raw materials obtained from fossil resources such as oil, natural gas, and coal. The non-degradability of plastics in the environment has significantly increased waste accumulation. Disposal and recycling of waste have become the primary problems for waste management [2].

In recent years, the general trend in food packaging has been towards the use and development of biodegradable packaging. Biodegradable plastics are environmentally friendly plastics that can be used instead of traditional ones [3]. Biopolymers, also known as green polymers, are naturally occurring polymers derived from biomass, that can be broken down into their constituent parts by ambient microbes [4]. In nature, there are many different polymers in the structure of various plant and animal resources (trees, leaves, fruits, seeds, animal skin and bones, etc.). Although these polymers are environmentally friendly materials, the high water solubility of most of them is a significant disadvantage for applications that require long-term use. The most widely used resources in the

production of biodegradable packaging materials are cellulose and starch [5].

An aliphatic polymer belonging to the poly( $\alpha$ -hydroxy acid) family, polylactic acid (PLA) is derived from sustainable and natural sources such as sugar cane, corn, and starch [4]. Lactic acid (LA) and ring-opening polymerization are the two processes used in industry to produce PLA [6]. PLA films are suitable for injection molding and vacuum forming and have low moisture permeability. When used as a food packaging material, PLA films have a high barrier property in preventing the loss of the aroma of the product. The disadvantage of unmodified PLA packaging is its fragility and limited use in hot product applications due to its degradation temperature of around 60 °C [4]. The advantages of PLA include strong sealing properties, low-temperature adhesion, heat sealability to paper or cardboard, stability, transparency, thermoplasticity, and easy processing. It has been reported that PLA packaging is used in products such as beverage cups, fresh pasta, bread and salad bags, thermoformed containers for bakery products, agricultural covers and boxes [4]. In addition, PLA is preferred in bread and bakery products because it does not fog [7].

Biochar is a black coal-like substance formed by the thermochemical conversion of various biomasses in an inert atmosphere [8]. Biomass loses its volatile matter content at high temperatures (400-500°C) and biochar remains [9]. Biochar is a porous,

\* To whom all correspondence should be sent:

E-mail: [filiz.ugur@comu.edu.tr](mailto:filiz.ugur@comu.edu.tr)

carbon-rich material with large specific surface area, containing a lot of aromatic carbon and functional groups (-OH, -COOH, C=O, and C-O) [10] and has unique physical, chemical, and biological properties [11].

In recent years, biochar applications have received considerable attention in the fields of environment, agriculture, and industry. Biochar acts as a carbon sink in the soil, slowing down the chemical oxidation and reduction of biomass and preventing the release of carbon into the atmosphere [12]. Biochar-doped polymer composites take advantage of the porous structure of biochar. The polymer fills the pores in the biochar by flowing into them, thus creating a mechanical bond between the polymer and biochar. In addition, the large surface area of biochar aids particle dispersion within the polymer matrix. By imparting mechanical properties to polymer composites, biochar provides flame resistance to the composite due to its natural carbon content, stable C-C covalent bonds, and aromatic ring content [9]. There are several studies using biochar as an additive in different polymers such as polyamide, polycarbonate, polyvinyl alcohol, polyethylene, polypropylene, and epoxy [13]. In the literature, there are limited studies on the use of different source-based BC in the PLA matrix. Aup Negoen *et al.* [14] prepared carbon-rich biochar (CRB) samples of cassava rhizome, durian peel, pineapple peel, and corn cob BC by using a simple pyrolysis method. They used PLA as the matrix, added biochars in different proportions and examined the thermal and mechanical properties. They found that the cassava root composite, which has a higher carbon content, has a better elastic modulus and impact resistance. Huang *et al.* studied the physical and chemical properties of biochar produced from vine leaves by adding it to the PLA matrix. The strength and stress were found to be much higher in samples with biochar added, and their strength increased [15]. Kane *et al.* prepared biochar at 900 °C and added it into PLA and recycled high-density polyethylene (HDPE) in different ratios. The addition of biochar affected the properties of HDPE and PLA differently, but the key finding of the study was that food waste-derived biochar suffered almost twice a mass loss after 40 days in the subsoil in high biochar-loaded samples compared to pure PLA. In other words, the biodegradation of the film increased with the addition of biochar [16].

In this study, biochar-incorporated PLA films were produced and their potential for use as packaging was investigated. BC was produced from olive tree branches by the slow pyrolysis method.

The surface area, efficiency, and ash content were measured. Characterization tests of PLA films with 5-20% BC loading were carried out and water and moisture retention, opacity, and mechanical strength were tested.

## EXPERIMENTAL

### Materials

Olive branches were collected from Çanakkale, Türkiye. Hydrochloric acid (HCl) and K<sub>2</sub>CO<sub>3</sub> were obtained from Sigma Aldrich. PLA polymer (2003D) was purchased from NatureWork. Chloroform and N,N- dimethyl formamide (DMF) were obtained from Merck Chemicals, Türkiye.

### Methods

- *BC preparation.* Olive tree branches were cut to ≈5 mm and dried in an oven at 60°C for 24 h. The dried olive branches were converted into biochar in a pyrolysis furnace. For this, dried olive branches, potassium carbonate (K<sub>2</sub>CO<sub>3</sub>), and pure water were mixed in a ratio of 1:2:4 and kept at room temperature for 24 h. Olive branches were removed by filtration and dried overnight in an oven at 105°C. The dried olive branches were pyrolyzed in a tube furnace at 650°C in N<sub>2</sub> atmosphere with a flow rate of 5 L/min at a temperature of 650°C, a temperature rise rate of 10°C/min, and a cooking time of 2 h. The product was washed with 10% HCl solution by mass and washed with distilled water until the pH value was about 7. The washed product was dried in the oven at 105°C for 24 h and kept in a desiccator. The BC yield and ash content were calculated as shown in Equation 1 and Equation 2, respectively [17]:

$$\text{BC Yield (\%)} = \frac{M_f(\text{g})}{M_i(\text{g})} * 100 \quad (1)$$

$$\text{Ash content (\%)} = \frac{M_r(\text{g})}{M_f(\text{g})} \times 100 \quad (2)$$

where M<sub>i</sub> and M<sub>f</sub> are the weights of biomass and biochar before and after pyrolysis, respectively. M<sub>r</sub> is the ash content of BC after it was kept at 850 C in an ash oven for 4 h.

JEOL JSM-7100-F scanning electron microscope (SEM) was used to study the BC's structure. 30 kV was used for the SEM analysis. The pore characterization of BC was performed with the Quadrasorb SI Brunauer-Emmett-Teller (BET) equipment. The samples were vacuum-sealed and degassed for an hour at 200 °C. Nitrogen gas adsorption was used.

- *Film preparation.* The polymer solution containing 10% PLA by mass, 90% chloroform and 10% DMF by volume was stirred at 40 °C until completely dissolved. Separately, 0-20% biochar (by mass of polymer) was dissolved in 5 ml of DMF

and dispersed by mixing with a homogenizer for 30 min. Then it was added to the PLA-DMF-chloroform solution and mixed at room temperature for 2 h, the mixture was poured into a glass Petri dish and the films were immersed in a water bath to complete the phase separation. Then, the films were removed and dried at 60 °C in the oven.

- **Film characterization.** The swelling test is used to determine the water resistance of films or the porosity of films, i.e. how much water they can trap in water. To test the swelling properties of the films, each sample was soaked in 25 mL of deionized water for 24 h and the values before ( $W_i$ ) and after ( $W_s$ ) water retention were recorded. The swelling degree calculation is given as Equation 3:

$$SD (\%) = \frac{W_i - W_s (g)}{W_i (g)} * 100 \quad (3)$$

Water vapor uptake values (WVU) of the film samples were determined by the ASTM E96-95 standard method. Using permeation cups, the obtained films were exposed to pure water vapor without contact for 24 h at 25°C. The vapor uptake values of the films were determined by weighing the final ( $W_f$ ) and initial ( $W_i$ ) of the films, respectively.

$$WVU (\%) = \frac{W_f - W_i (g)}{W_i (g)} * 100 \quad (4)$$

The opacity, i.e. light transmittance, of the films was determined using a UV-Vis spectrophotometer (Shimadzu-1280). After being prepared, the films were cut into rectangular strips and put on the spectrophotometer cell's two outer surfaces. A wavelength of 600 nm was used to measure the absorbance (A) value. The opacity was calculated per thickness of film (l) as shown in Equation 5:

$$\text{Opacity} = \frac{A}{l} \quad (5)$$

Tensile strength and elongation at break values of the films were determined by a Universal Testing Machine (Ankarin) with ASTM D882 standard. After the width and thickness of the prepared films were measured, they were placed between two clamps, and the distance was measured. The test started and the strength values were measured.

## RESULTS AND DISCUSSION

In this study, biochar was synthesized by the slow pyrolysis method and then added to the PLA matrix at different rates, and its film properties were examined. When the efficiency of the produced biochars was analyzed, its value was found to be 29.75%. It has been observed that this value generally varies between 20-35% depending on the lignin and cellulose structure in the biomass content [10, 11, 17-19]. Efficiency also decreases, especially

at high pyrolysis temperatures. However, in this study, although the temperature was 650 °C, nearly 30% efficiency was achieved. In this case, highly efficient BC can be obtained from olive pruning waste. The ash content was found to be 3.37%. This value is similar to that in the literature [20, 21].

One of the most important characteristics in BC synthesis is the porous and morphological structure of BC. In this way, the film properties of PLA can be improved. When SEM images are examined for BC, it is seen that BC has a uniform pore structure. The activation process contributes to enhancing the homogeneous pore structure as shown in Figure 1. It can be said that  $K_2CO_3$  is distributed in the cellulosic structure on the surface and inside of the olive branch. The resulting metallic potassium increases porosity through intercalation through carbon layers [21].

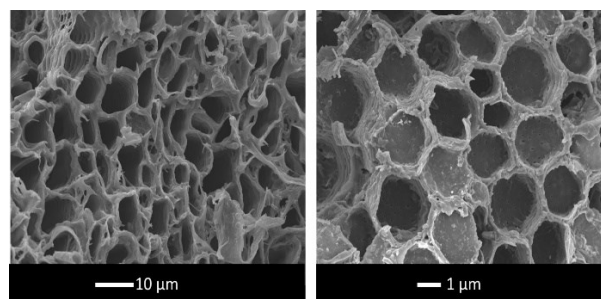


**Fig. 1.** SEM analysis of the BC

The increase in surface area provides many advantages depending on the usage area of BC. Increasing surface area increases the performance of BC, especially in important experimental studies such as moisture retention, water retention, and gas permeability. Therefore, a high surface area is an expected and desired result. In this study, the activation process was applied to increase the surface area of BC. The surface areas of non-activated BC and  $K_2CO_3$ -activated BC were obtained as 1.44 m<sup>2</sup>/g and 659,255 m<sup>2</sup>/g, respectively. Activation increases the specific surface area of biochar by increasing the number of mesopores.

Another important factor for preparing composites is the homogeneous distribution of fillers in the polymer matrix. This depends on both the size of the particles and the polymer-particle compatibility. The BC used in this study has a meso-structure. For this reason, especially in cast-film preparation, it can provide a more durable structure by allowing the polymers to fill the pores. However, on the other hand, the inhomogeneity of the particle size may cause a decrease in mechanical strength. BC distribution in PLA was observed by an optical

microscope (SOIF-BK5000) (Figure 2). At a low loading rate (wt. 5% and 10 %), a homogenous distribution can be clearly seen. As the biochar concentration increased, agglomeration increased, as seen from the microscope images. Although biochars were distributed in an ultrasonic mixer and stirred in a magnetic stirrer, a heterogeneous appearance was obtained at the high loading rate [22]. According to these results, it was predicted that mechanical strength may also decrease, especially at high additive rates.

Additionally, it was observed that biochar particles had a circular shape. As a result of the distance measurements of the particles, the highest distance was measured as 4.8  $\mu\text{m}$  in the 5% BC-PLA packaging film, while this value was measured as

17.0  $\mu\text{m}$  for the PLA packaging film containing 20% BC. This situation is due to the concentration difference [23].

The efficiency of packaging as a barrier against food deterioration, nutrient loss, and flavor degradation when exposed to visible and ultraviolet light depends on its optical qualities. Foods are long-lasting and shielded from light in this way. The opacity results of the films are given in Figure 3. It is observed that as the BC ratio in PLA films increases, their opacity increases. This result is attributed to the light absorption capacity of BC. The reason for this is higher than that of PLA films. Depending on the increasing particle size, this increase is normal, although not very regular [24].

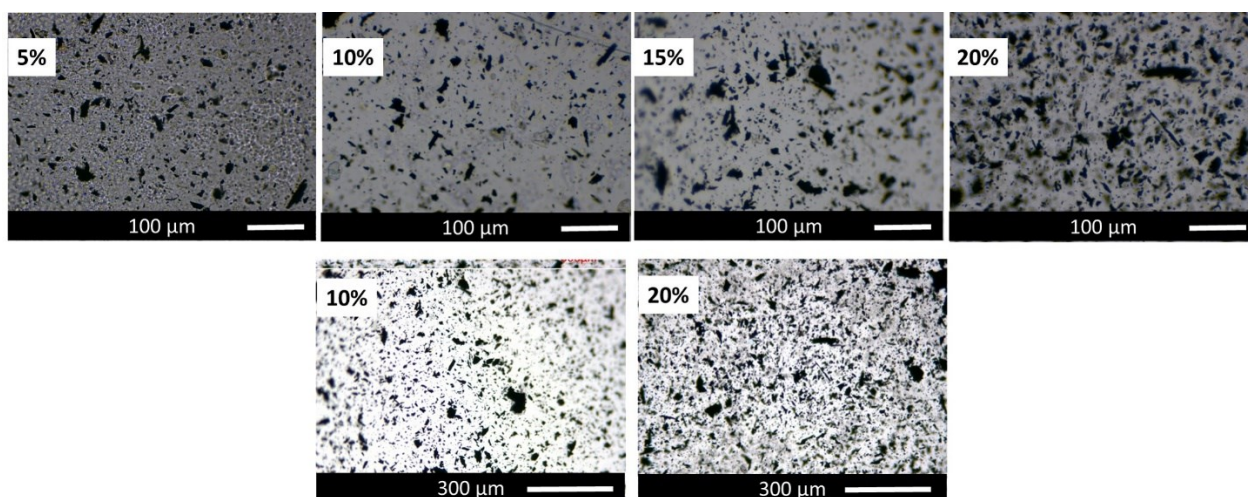


Fig. 2. Optical microscopy analysis of the BC loaded PLA films

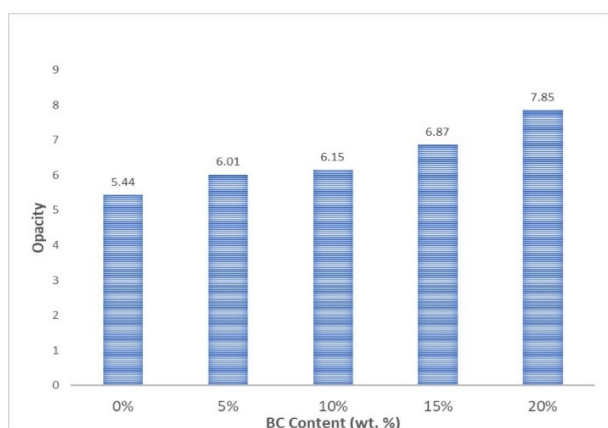


Fig. 3. Opacity results of BC-PLA films

The swelling test provides information about the water solubility of the film. However, it is not desired that this value be too high. Otherwise, they will lose their properties in contact with water during use. In this study, PLA was used as the matrix and

this polymer is quite rigid and has high water resistance. It has no solubility in water. However, in this case, it takes a long time for it to become biodegradable after use. For this reason, BC additive increases its affinity for water and provides a structure that is durable in use and easily degradable after use. Biochar is a hydrophilic material due to the presence of hydrophilic groups [24]. Therefore, it has the ability to absorb water. It is expected that the swelling ratios of the formed PLA films increase as the BC concentrations increase. Figure 4 indicates the swelling degree of the films. According to the swelling test results, it was observed that the swelling ratio increased as the BC concentration increased. It was found that the swelling rate of the PLA packaging film containing 0% BC was 1.29%, while it was 10.10% in the film containing 20% BC. According to the results, it is clear that the water solubility of packaging films in the soil is improved

by BC addition [25]. This shows that the films are biodegradable in nature and will decompose faster than other petroleum-derived plastics [26].

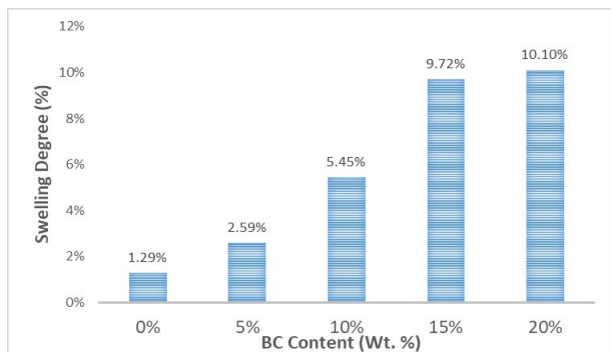


Fig. 4. Swelling degree results of BC-PLA films

Another important feature of the packaging film is the water vapor permeability or water vapor uptake. The water vapor barrier properties of a physically or chemically biodegradable packaged product are related to moisture balance and are of great importance in preserving or extending its shelf life [27]. The movement of water between food goods and their surroundings has a direct impact on how long they last on the shelf. For the packaging to have greater durability, the films' water transfer capacity should be minimal [28]. Vapor permeability is an undesirable feature in the case of vapor transport from outside to inside because it causes deterioration of food inside the package. On the other hand, vapor permeability from inside to outside is desired because it ensures that the food remains dry in the package. Therefore, it is quite difficult to characterize these two features. In this study, water vapor uptake (WVU) was calculated instead of permeability. During this test, the films were naturally exposed to water vapor at room temperature. Figure 5 shows the WVU values of the films with and without BC. According to the test results, the water vapor permeability capacity of the films gradually decreases as BC concentrations increase. The reason for this is that the biochar in the films absorbs water and restricts the passage of water vapor through the film. This is a desired result [24]. It was also related to the fact that the biochar slows down the diffusion of water vapor and makes pores in composite films more tortuous [29].

Another important feature desired in a packaging film, regardless of the purpose it is used for, is its mechanical strength. Mechanical strength preserves the shape and rigidity of films during transportation and packaging.

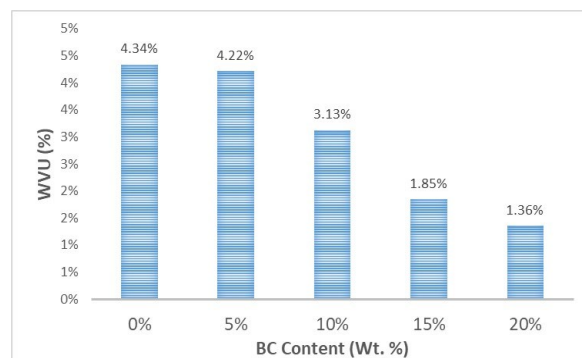


Fig. 5. Water vapor uptake results of BC-PLA films

However, if a polymer film is used for transport purposes, this value becomes more important. For use only for packaging purposes, lower mechanical strength is acceptable. Food packaging can typically take the shape of an elastic film for various uses or a non-deformable material to guarantee structural integrity or reinforce the food structure [27]. Tensile strength depends on film content, film thickness, moisture content, and additives. Figure 6 shows the mechanical test results of films with and without BC.

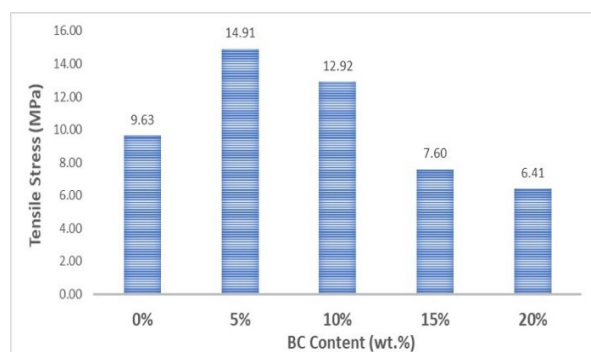


Fig. 6. Mechanical test results of BC-PLA films

As seen in the figure, mechanical strength increased compared to pure film at 5% loading rate. This result is attributed to the equal load transfer between the PLA and BC. During the film preparation, PLA solution fills the BC pores. According to the rule of mixture phenomena, the strength of PLA increased. However, after this loading rate, the mechanical strength began to gradually decrease. Although the strength achieved at 10 wt.% loading rate is lower than that at 5 wt.%, it is higher compared to the pure PLA. It may be acceptable to use. However, the strength obtained at 15 wt.% and 20 wt.% loading rates is lower than that of pure PLA film, which indicates that the material structure is deteriorated. As confirmed from microscopic analysis, particle distributions and sizes were not homogeneous at high loading rates. This shows that the load transfer within the film was not distributed properly and adhesion problems occurred

between the polymer and BC [14, 22]. Therefore, no matter how much the other properties improve, it is not appropriate to use these ratios in the PLA matrix.

### CONCLUSION

In this study, biochar was obtained from olive branch waste, characterized, and added to PLA to obtain a natural packaging material. The usability of the composite material obtained was investigated by performing some of the tests required for packaging. According to the swelling test results, it was observed that the swelling ratio increased from 1.29% to 10.10% when the BC enhanced from 0 wt% to 20 wt.%. This result allows to conclude that the BC additive increases the solubility of the composite material in nature. It was observed that the BC improves the vapor resistance. The increased ratio decreased the water vapor uptake from 4.43% to 1.36%. BC also significantly increased the mechanical strength of the films. However, the strengths decreased, especially after 10 wt.% loading. This shows that BC loading above 10% is not suitable for packaging. Based on all these results, it may be concluded that converting olive branches into biochar enables the acquisition of a very important additive material, and the use of this material in packaging is very beneficial.

**Acknowledgement:** The current study was supported by the Scientific Research Project Coordination Center of Çanakkale Onsekiz Mart University (Project No: FBA-2023-4345).

### REFERENCES

- H. Namazi, M. Mosadegh, *Journal of Polymers and the Environment*, **19**, 980 (2011).
- S. Nanda, B. R. Patra, R. Patel, J. Bakos, A. K. Dalai, *Environmental Chemistry Letters*, **20** (1), 379 (2022).
- Y. Tokiwa, B. P. Calabia, C. U. Ugwu, S. Aiba, *International Journal of Molecular Sciences*, **10** (9), 3722 (2009).
- A. B. H. Yoruç, V. Uğraşkan, *Afyon Kocatepe Üniversitesi Fen ve Mühendislik Bilimleri Dergisi*, **17** (1), 318 (2017).
- .. B. Gümüşderelioğlu, T. G. Biyomalzemeler Bilim ve Teknik Dergisi. *TÜBİTAK, Temmuz Özel Sayısı* (2016)..
- M. Murariu, P. Dubois, *Advanced Drug Delivery Reviews*, **107**, 17 (2002).
- Z. Ayhan, Ed. *Baysal T, İçier F, Nobel Yayınları*, **43** (2012).
- M. U. Jamal, A. J. Fletcher, *BioEnergy Research*, **1** (2023).
- O. Das, N. K. Kim, M. S. Hedenqvist, R. J. Lin, A. K. Sarmah, D. Bhattacharyya, *Environmental Management*, **62**, 403 (2018).
- P. Tu, G. Zhang, G. Wei, J. Li, Y. Li, L. Deng, H. Yuan, *Bioresources and Bioprocessing*, **9** (1), 131 (2022).
- S. S. Sahoo, V. K. Vijay, R. Chandra, H. Kumar, *Cleaner Engineering and Technology*, **3**, 100101 (2021).
- C. Zhang, G. Zeng, D. Huang, C. Lai, M. Chen, M. Cheng, ... R. Wang, *Chemical Engineering Journal*, **373**, 902 (2019).
- Q. Zhang, H. Lei, H. Cai, X. Han, X. Lin, M. Qian, ... W. Mateo, *Journal of Cleaner Production*, **252**, 119898 (2020).
- K. Aup-Ngoen, M. Noipitak, *Sustainable Chemistry and Pharmacy*, **15**, 100204 (2020).
- S. Kane, C. Ryan, *Composites Part C: Open Access*, **8**, 100274 (2022).
- J. A. Allen, A. E. Downie, *Energy & Fuels*, **34** (11), 14223 (2020).
- F. R. Vieira, C. M. R. Luna, G. L. Arce., I. Ávila, *Biomass and Bioenergy*, **132**, 105412 (2020).
- M. S. Jesus, A. Napoli, P. F. Trugilho, Á. A. Abreu Júnior, C. L. M. Martinez, T. P. Freitas, *Cerne*, **24**, 288 (2018).
- L. Wang, M. N. Olsen, C. Moni, A. Dieguez-Alonso, J. M. de la Rosa, M. Stenrød, ... L. Mao, *Applications in Energy and Combustion Science*, **12**, 100090 (2022).
- A. Herath, C. A. Layne, F. Perez, E. B. Hassan, C. U. Pittman Jr, T. E. Mlsna, *Chemosphere*, **269**, 128409 (2021).
- L. Zhu, N. Zhao, L. Tong, Y. Lv, *RSC Advances*, **8** (37), 21012 (2018).
- L. Lisuzzo, M. R. Caruso, G. Cavallaro, S. Milioto, G. Lazzara, *Industrial & Engineering Chemistry Research*, **60** (4), 1656 (2021).
- E. Kavas, P. Terzioğlu, M. Taş, F. N. Parm, Ç. Kuş, S. Küçükaydın, M. E. Duru, *Eurasian Journal of Biological and Chemical Sciences*, **3** (2), 121 (2020).
- M. S. G. Edward, A. C. F. Louis, H. Srinivasan, S. Venkatachalam, *Iranian Polymer Journal*, **31** (12), 1523 (2022).
- T. de Moraes Crizel, A. de Oliveira Rios, V. D. Alves, N. Bandarra, M. Moldão-Martins, S. H. Flôres, *Food Hydrocolloids*, **74**, 139 (2018).
- S. Dursun, N. Erkan, M. Yesiltas, *Journal of Fisheries Sciences*, **4** (1), 50 (2010).
- N. Gürler, S. Paşa, H. Emel, *Journal of the Taiwan Institute of Chemical Engineers*, **123**, 261 (2021).
- S. F. Hosseini, M. Rezaei, M. Zandi, F. Farahmandghavi, *Food Chemistry*, **194**, 1266 (2016).
- D. She, J. Dong, J. Zhang, L. Liu, Q. Sun, Z. Geng, P. Peng, *Composites Science and Technology*, **175**, 1 (2019).

## Determination of trace and major elements in commercial propolis samples by ICP-OES after microwave digestion

G. Arda, A. Karasakal\*

*Tekirdağ Namık Kemal University, Science and Letters Faculty, Department of Chemistry, Tekirdağ, Turkey.*

Received May 7, 2024; Accepted: August 15, 2024

Propolis is a resinous product collected by bees from specific plant sources. There are more than 300 compounds in the structure of propolis. The main ones are phenolic compounds (flavonoids and phenolic acids), benzoic acid and its derivatives, cinnamic alcohol, cinnamic acid and its derivatives, monoterpenes, diterpenes, triterpenes and sesquiterpenes and their alcohol and benzaldehyde derivatives, other phenolic acids and derivatives, alcohols, sugars, ketones, heteroaromatic compounds, aliphatic hydrocarbons, minerals, steroid hydrocarbons and amino acids. Studies have reported that propolis has anti-inflammatory, antihepatotoxic, anticancer, antiviral and antibacterial activities. The concentrations of Na, Mg, K, Ca, P, Fe, Cu, B, Mn, Zn and Al were determined in commercial propolis drop products by ICP-OES. For microwave digestion method, 1 mL of propolis samples in reaction vessels directly, added to each flask 9 mL concentrated HNO<sub>3</sub>. The method was validated according to the parameters of accuracy, precision, linearity, recovery, LOD and LOQ. The recovery percentages were obtained to be between 69.67 to 104.05% in propolis samples.

**Keywords:** Propolis; Microwave digestion; ICP-OES, Food supplement, Spectroscopy

### INTRODUCTION

Bee products such as honey, pollen, royal jelly and propolis have been used since the early ages of mankind for nutrition, health protection and treatment of diseases. Propolis is a sticky substance collected by honey bees from bark, leaves and plant secretions [1]. Propolis, which contains many phenolic compounds such as phenolic acids, esters and flavonoids, is also rich in biological and pharmacological properties. These compounds in the chemical structure of propolis give propolis many biological activities such as antibacteriyel, antiviral, antifungal, antitumor, anti-inflammatory and antiulcer. Propolis, which has many different effects, was first discovered and widely used by the Greeks as a natural antibiotic due to these properties [2]. In addition to this, it is nowadays used versatile in the food sector, apitherapy centers, dermatological and cosmetic applications as well as medicine. In recent years, especially during the coronavirus (covid-19) pandemic, interest in propolis, which is a unique mineral, has increased considerably since it is known to strengthen the immune system and increase body resistance.

Raw propolis contains many different structures and has a mixed composition. Propolis contains resin, vegetable balsam, wax, essential and aromatic oils, pollen, other organic compounds and minerals [3]. Other components consist of other compounds such as vitamins, minerals and elements [4-5]. Deficiency can cause health problems and excessive amounts can have toxic effects [6-8]. Determination

of elemental amounts is important for human survival and ecological cycle. Therefore, it is important to make chemical measurements of the elements in dietary supplements.

Macro and micro (trace) elements play a role in many important functions of the organism. Regulation of biological functions of vitamins, enzymes and hormones, oxygen transport, elimination of free radicals, and their use as building and support materials are examples of these functions [6]. In our country and in the world, there are studies on the quantitative analysis of some phenolic compounds and elements in propolis, but there is no study on the quantitative determination of commercial propolis elemental content by ICP-OES. ICP-OES is one of the most frequently used techniques in metal determinations due to its wider working range compared to AAS (Atomic absorption spectroscopy), its ability to determine many elements at the same time (even if their concentrations are very low and different), and its more sensitive results in the determination of refractory elements [9].

In this study, we investigated the multielement contents in commercial propolis drop products by ICP-OES. For elemental analysis, samples were solubilized by microwave and then analyzed by ICP-OES.

### EXPERIMENTAL

#### *Instrumentation*

ICP-OES (Spectro/ Spectroblue) and MarsXpress (CEM) were used for measurements and microwave digestion. Rf power was 1.4 kW, nebulizer gas flow

\* To whom all correspondence should be sent:

E-mail: akarasakal@nku.edu.tr

was 1.0 L min<sup>-1</sup>, plasma-Ar flow was 12 L min<sup>-1</sup> and auxiliary gas flow was 1.0 L min<sup>-1</sup>.

#### Reagents and standards

Nitric acid (65%) and Hydrogen peroxide (35%) were supplied from Sigma-Aldrich, Steinheim, Germany. and Nitric acid and Hydrogen peroxide were used for digestion procedure. Concentration ranges of standard solutions prepared by dilution from 1000 µg/mL stock solution 1.25 - 25 µg/mL for Na, 5-100 µg/mL for Mg, 15-300 µg/mL for Ca, 15-300 µg/mL for K, 25-1000 ng/mL for P, Fe, Cu and B, respectively. Standard stock solutions were supplied from the Merck (Darmstadt, Germany). The stock solution and working standards were diluted in HNO<sub>3</sub>.

#### Preparation of samples

Commercial propolis samples were purchased in Turkey. The brand names of the propolis drop samples were labeled to A, B and C. A, B and C brands were used water, ethyl alcohol and glycol-water mixture as solvent, respectively.

#### Microwave digestion procedure

1 mL of commercial propolis drop samples and 9 mL of HNO<sub>3</sub> was added in digestion vessels. For microwave digestion, commercial propolis samples were kept at 200°C for 45 minutes. After cooling processes, 3 mL of digested samples were took and were diluted to 20.0 mL with ultrapure water. Analyzes were repeated 3 times.

#### Recovery

Percentage recovery values were calculated with the standard addition method. Percent recovery value was calculated using the formula  $C_s - C_k / C_k \times 100$ , where  $C_s$  is element concentration of the spiked sample,  $C_t$  is element concentration of the blank target sample,  $C_k$  is known spike concentration.

### RESULTS AND DISCUSSION

The elemental contents of commercial propolis drop samples dissolved in three different solvents were investigated. Microwave digestion procedure was used because solubilization using a closed system microwave oven for solubilization of samples process is fully realized and evaporation losses are eliminated. Na, Ca, Mg, K, Al, B, Cu, Fe, Mn, P, and Zn were investigated in propolis samples. Analytical parameters are presented in Table 1.

LOD and LOQ were analysed according to  $3\sigma$  and  $10\sigma$ . %RSD values were below 5%. All experiments were performed in triplicate and the

results expressed as mean  $\pm$  SD. The concentrations (µg/mL) of Na, Ca, Mg, K, Al, B, Cu, Fe, Mn, P, and Zn in commercial propolis samples are given in Table 2.

**Table 1.** Values of LOD and LOQ

Element	LOD, ng/mL	LOQ, ng/mL
Na	159.1	530
Ca	19.3	64
Mg	28.7	96
K	129.2	431
Al	0,4838	1,613
B	2,949	9,830
Cu	0,0619	0,206
Fe	0,6769	2,253
Mn	0,6791	2,264
P	7,937	26,457
Zn	0,6433	2,144

**Table 2.** Element concentrations of commercial propolis samples

	A, µg/mL	B, µg/mL	C, µg/mL
<b>Na</b>	68.40±1.77	57.28±3.34	3144.02±35.76
<b>Ca</b>	391.15±2.70	9.28±0.08	5.53±0.20
<b>Mg</b>	40.40±1.54	10.08±0.05	2.40±0.07
<b>K</b>	670.03±4.67	209.92±4.45	131.0±2.22
<b>Al</b>	24.11±0.77	16.15±0.10	1.19±0.03
<b>B</b>	5.51±0.12	0.70±0.03	0.00±0.00
<b>Cu</b>	0.79±0.04	0.00±0.00	0.00±0.00
<b>Fe</b>	19.45±0.33	48.14±0.18	4.36±0.19
<b>Mn</b>	4.71±0.05	0.76±0.02	0.14±0.01
<b>P</b>	127.57±1.30	29.59±0.37	2.40±0.25
<b>Zn</b>	8.86±0.16	2.09±0.01	0.12±0.01

The order of the element levels after application of microwave digestion procedure was determined to be C>A>B for Na, A>B>C for Ca, A>B>C for Mg, A>B>C for K, A>B>C for Al, A>B>C for B, A>B=C for Cu, B>A>C for Fe, A>B>C for Mn, A>B>C for P and Zn. The highest mean concentrations were obtained for A, and the lowest concentration was obtained for C in commercial propolis samples. Na was found as the highest element concentration (3144.02 µg/mL) in C

sample. K was observed as the second highest element concentration (670.03 µg/mL) in A sample. Ca was found as the third highest element concentration in A sample. Cu and B were found as the lowest element concentration (0 µg/mL) in C sample. Zn was observed as the second lowest element concentration (0.12 µg/mL) in C sample. Zn was found as the third lowest element

concentration (0.12 µg/mL) in C sample. The highest element concentration (24.11 µg/mL) of Al was found in A sample. All Al concentrations are acceptable levels by Turkish Food Codex. Recovery results of commercial propolis samples are given in Table 3. Currently, in analytical procedures, recovery percentages in the range from 69.67 to 101.94%.

**Table 3.** Recovery results of commercial propolis samples

Element	A,%	B,%	C,%
Na	95.6	97.7	100.9
Ca	87.75	89.44	89.31
Mg	102.3	104.05	94.06
K	69.67	97.39	92.61
Al	91.61	91.41	88.24
B	101.94	101.84	102.2
Cu	101.22	101.92	97.52
Fe	94.15	98.6	90.99
Mn	96.05	95.23	89.65
P	96.36	100.1	98.8
Zn	98.78	97.52	91.44

Korn and et al. found Zn, Fe, Mn and Cu concentrations in natural propolis samples by ICP-OES. Zn, Mn Fe and Cu concentrations were higher than our results for all propolis samples [10]. Ferreira et al. analyzed the elemental content of geopropolis after microwave solubilization method by ICP-OES. Zn, Mg, K, Mn and Cu concentrations were higher than our results for all samples and Na concentrations were lower than our C samples and Fe values were lower than our A and B samples. [11]. Tomic and et al. were investigated macro and microelements in Serbian propolis samples by ICP-OES. Cu, B, Mn and Fe values were higher than our results for all samples [12]. Matuszewska and et al were analyzed bee pollen, propolis, and royaljelly collected in west-central Poland by ICP-OES. Cu, P and Fe were higher than our results for all samples [13]. Liben and et al. were investigated elemental contents in honey and propolis samples in Ethiopia. Total phenolic and flavonoid contents were analysed in propolis but element contents of propolis weren't investigated [14].

When we consider the results of the analysis of commercial propolis drop samples in general, it was observed that all the elements (Ca, Mg, K, Al, B, Cu, Mn, P and Zn) except Fe and Na were more abundant in A samples. The elemental concentrations found in studies on natural propolis samples in the literature are very similar to the analysis results of propolis samples with water as solvent in our study. The results obtained as a result of the study show that water is a better solvent for commercial propolis

samples, as it was found that the elemental contents of commercial propolis drop samples using water as a solvent are closer to the elemental contents of natural propolis samples in the literature. Calcium is an essential element for enzyme activation and bone development. Sodium plays an important role in the functioning of muscle and nerve cells in our body. Potassium is involved in the functioning of enzymes, cell division and growth, and the regulation of blood pressure. Potassium deficiency can cause heart problems. High doses of copper damage the liver and kidneys, while deficiency causes fatigue and anemia. Iron is found in red blood cells called hemoglobin, which is responsible for blood production and transports oxygen from the blood to the tissues. The most important functions of manganese in our body are to contribute to the formation of carbohydrate and fat metabolism and to regulate blood sugar. Zinc is an important trace element involved in protein and DNA synthesis. Daily intake doses for calcium, magnesium, sodium and potassium are 1000-1200 ppm; 320-420 ppm; 1300-1500 ppm; 2000-2300 ppm, respectively [15].

### CONCLUSION

The concentrations of sodium (Na), magnesium (Mg), potassium (K), calcium (Ca), phosphorus (P), iron (Fe), copper (Cu), boron (B), manganese (Mn), zinc (Zn) and aluminum (Al) in commercial propolis samples were investigated. This the first study in propolis samples using microwave digestion by ICP-OES. Ca, Mg and K values were below RDA levels

so the findings indicate all propolis samples are not good source of essential elements but Na were above RDA in propolis drop samples dissolved in ethyl alcohol. Fe and Mn values in all propolis samples were above RfD and TDI values but Cu and Zn values in propolis samples dissolved in water were above for RfD and TDI values.

#### REFERENCES

1. S. Castaldo F. Capasso. *Fitoterapia*, **73**(1), S1 (2002).
2. A. Papachristoforou, E. Koutouvela, I. Mourtzinou, *Chem. & Diversity*, **16**(7), e1900146 (2019).
3. V.S. Bankova, S.L. De Castro, M.C. Marcucci. *Apidologie*, **31**, 3 (2000).
4. R. Christov, B. Trusheva, M. Popova, V.S. Bankova, M. Bertrand, *Natural Product Research* **20**(6), 531 (2006).
5. W. Yang, Z. Wu, Z.Y. Huang, X. Miao. *J. Food Sci. Technol.*, **54**(11), 3375 (2017).
6. Parsons PJ, Barbosa F. Atomic spectrometry and trends in clinical laboratory medicine. *Spectrochim. Acta Part B, Atomic Spect.*, **62**(9), 992v(2007).
7. Y. Zheng, X.K. Li, Y. Wang, I. Cai. *Hemoglobin*, **32**(1–2), 135 (2008).
8. M.L. Carvalho, T. Magalhães, M. Becker, A. von Bohlen. *Spectrochim. Acta Part B Atomic Spect.*, **62**(9), 1004 (2007).
9. C. Douvris, T. Vaughan, D. Bussan, G. Bartzas, R. Thomas, Review of the global application landscape. *Science of The Total Environ.*, **905**, 167242 (2023).
10. M.G.A. Korn, M.A.P. Guida, J.T.P. Barbosa, E.A. Torres, A.P. Fernandes, J.C.C. Santos, K.G.F. Dantas, J.A. Nóbrega, *Food Anal. Methods*, **6**, 872 (2013).
11. R.C. Ferreira, F.S. Dias, C.A. Tannus, F.B. Santana, D.C.B.M. Santos, F.S. Dias, M.S. Castro, H.N. Brandão, A.F.S. Júnior, L.C.R.C. Silva, F.A. Chinalia, Essential and Potentially Toxic Elements from. *Biol. Trace Element Research*, **199**, 3527 (2021).
12. S. Tosic, G. Stojanovic, S. Mitic, A. Pavlovic, S. Alagic. *J. Apic. Sci.*, **61**(1), 5 (2017).
13. E. Matuszewska, A. Klupczynska, K. Maciołek, Z.J. Kokot, J. Matysiak, *Molecules*, **26**, 2415 (2021).
14. T. Liben M, Atlabachew A. Abebe, *Cogent Food & Agri.*, **4**, 1475925 (2018).
15. A. Karasakal, *Biological Trace Element Research*, **197** (2), 683 (2020).

### Instructions about Preparation of Manuscripts

**General remarks:** Manuscripts are submitted in English by e-mail. The text must be prepared in A4 format sheets using Times New Roman font size 11, normal character spacing. The manuscript should not exceed 15 pages (about 3500 words), including photographs, tables, drawings, formulae, etc. Authors are requested to use margins of 2 cm on all sides.

Manuscripts should be subdivided into labelled sections, e.g. INTRODUCTION, EXPERIMENTAL, RESULTS AND DISCUSSION, etc. **The title page** comprises headline, author(s)' names and affiliations, abstract and key words. Attention is drawn to the following:

a) **The title** of the manuscript should reflect concisely the purpose and findings of the work. Abbreviations, symbols, chemical formulae, references and footnotes should be avoided. If indispensable, abbreviations and formulae should be given in parentheses immediately after the respective full form.

b) **The author(s)**' first and middle name initials and family name in full should be given, followed by the address (or addresses) of the contributing laboratory (laboratories). **The affiliation** of the author(s) should be listed in detail (no abbreviations!). The author to whom correspondence and/or inquiries should be sent should be indicated by an asterisk (\*) with e-mail address.

**The abstract** should be self-explanatory and intelligible without any references to the text and containing up to 250 words. It should be followed by keywords (up to six).

**References** should be numbered sequentially in the order, in which they are cited in the text. The numbers in the text should be enclosed in brackets [2], [5, 6], [9–12], etc., set on the text line. References are to be listed in numerical order on a separate sheet. All references are to be given in Latin letters. The names of the authors are given without inversion. Titles of journals must be abbreviated according to Chemical Abstracts and given in italics, the volume is typed in bold, the initial page is given and the year in parentheses. Attention is drawn to the following conventions: a) The names of all authors of a certain publications should be given. The use of "et al." in the list of references is not acceptable; b) Only the initials of the first and middle names should be given. In the manuscripts, the reference to author(s) of cited works should be made without giving initials, e.g. "Bush and Smith [7] pioneered...". If the reference carries the names of three or more authors it should be quoted as "Bush et al. [7]", if Bush is the first author, or as "Bush and co-workers [7]", if Bush is the senior author.

**Footnotes** should be reduced to a minimum. Each footnote should be typed double-spaced at the bottom of the page, on which its subject is first mentioned. **Tables** are numbered with Arabic numerals on the left-hand top. Each table should be referred to in the text. Column headings should be as short as possible but they must define units unambiguously. The units are to be separated from the preceding symbols by a comma or brackets. Note: The following format should be used when figures, equations, etc. are referred to the text (followed by the respective numbers): Fig., Eqns., Table, Scheme.

**Schemes and figures.** Each manuscript should contain or be accompanied by the respective illustrative material, as well as by the respective figure captions in a separate file. As far as presentation of units is concerned, SI units are to be used. However, some non-SI units are also acceptable, such as °C, ml, l, etc. Avoid using more than 6 (12 for review articles) figures in the manuscript. Since most of the illustrative materials are to be presented as 8-cm wide pictures, attention should be paid that all axis titles, numerals, legend(s) and texts are legible.

**The authors are required to submit the text with a list of three individuals and their e-mail addresses that can be considered by the Editors as potential reviewers. Please note that the reviewers should be outside the authors' own institution or organization. The Editorial Board of the journal is not obliged to accept these proposals.**

The authors are asked to submit **the** final text (after the manuscript has been accepted for publication) in electronic form by e-mail. The main text, list of references, tables and figure captions should be saved in separate files (as \*.rtf or \*.doc) with clearly identifiable file names. It is essential that the name and version of the word-processing program and the format of the text files is clearly indicated. It is recommended that the pictures are presented in \*.tif, \*.jpg, \*.cdr or \*.bmp format. The equations are written using "Equation Editor" and chemical reaction schemes are written using ISIS Draw or ChemDraw programme.

## EXAMPLES FOR PRESENTATION OF REFERENCES

### REFERENCES

1. D. S. Newsome, Catal. Rev.–Sci. Eng., 21, 275 (1980).
2. C.-H. Lin, C.-Y. Hsu, J. Chem. Soc. Chem. Commun., 1479 (1992).
3. R. G. Parr, W. Yang, Density Functional Theory of Atoms and Molecules, Oxford Univ. Press, New York, 1989.
4. V. Ponec, G. C. Bond, Catalysis by Metals and Alloys (Stud. Surf. Sci. Catal., vol. 95), Elsevier, Amsterdam, 1995.
5. G. Kadinov, S. Todorova, A. Palazov, in: New Frontiers in Catalysis (Proc. 10th Int. Congr. Catal., Budapest (1992), L. Guzzi, F. Solymosi, P. Tetenyi (eds.), Akademiai Kiado, Budapest, 1993, Part C, p. 2817.
6. G. L. C. Maire, F. Garin, in: Catalysis. Science and Technology, J. R. Anderson, M. Boudart (eds.), vol. 6, Springer Verlag, Berlin, 1984, p. 161.
7. D. Pocknell, GB Patent 2 207 355 (1949).
8. G. Angelov, PhD Thesis, UCTM, Sofia, 2001, pp. 121-126.
9. JCPDS International Center for Diffraction Data, Power Diffraction File, Swarthmore, PA, 1991.
10. CA 127, 184 762q (1998).
11. P. Hou, H. Wise, J. Catal., in press.
12. M. Sinev, private communication.
13. <http://www.chemweb.com/alchem/articles/1051611477211.html>.

***Texts with references which do not match these requirements will not be considered for publication!!!***

## CONTENTS

<i>D. Duranoğlu, I. Küçük, Ü. Beker</i> , Continuous flow chromium (VI) adsorption onto peach stone- and acrylonitrile-divinylbenzene copolymer-based activated carbons.....	203
<i>E. Neziri, D. Duranoğlu</i> , Modeling of continuous-flow phenol adsorption onto acrylonitrile-divinylbenzene copolymer .....	208
<i>B. Hazar, D. Şakar</i> , Kinetic investigation of methyl violet dye adsorption on agar-agar impregnated activated carbon.....	215
<i>Z. O. Ozyalcin, A. S. Kipcak</i> , Drying kinetics, mathematical modeling and color analysis of <i>Solen marginatus</i> : A comparative study of oven, infrared, and microwave drying methods.....	221
<i>O. T. A. Alshamhazi, I. Küçük, I. Doymaz</i> , Investigation of mass transfer in infrared drying of Ahlat pears: experimental and modeling approaches.....	228
<i>B. Gök, E. Kıpçak</i> , The effect of chemical pretreatment on the drying behavior of blueberries.....	233
<i>B. Eren, Y. Yalcin Gurkan</i> , Theoretical study of possible reaction pathways with the OH radical of the Apranax (AP) molecule with naproxen sodium (NS) as an active ingredient.....	242
<i>G. Serdaroğlu</i> , Carvacrol and 4-IP-2-MeO-1-MB derivatives: DFT computations and drug-likeness studies.....	247
<i>N. Guven, B. Gurkan, Y. Yalcin Gurkan</i> , Removal of penicillin group antibiotics azlocillin, cloxacillin, methicillin from wastewater by DFT method.....	255
<i>N. Tokatli Demirok, A. Karasakal</i> , Determination of macro- and microelement contents in thyme oil and rosemary oil by ICP-OES.....	260
<i>E. Kirilova, R. Fridmans, A. Puckins, J. Oreha, S. Osipovs</i> , Photophysical study of benzanthrone 3-isothiocyanate as novel fluorescent label.....	265
<i>F. T. Tuğcu</i> , Synthesis of substituted 4-methylphenyl-2-iminothiazolidinone compounds <i>via</i> one-pot method.....	270
<i>S. Meral, A. Alaman Ağar</i> , Synthesis, characterization and effects to cholesteric lyotropic liquid crystal media of -ONNO- type Schiff bases and metal complexes.....	274
<i>E. Akyol, M. Danisman</i> , Evaluating the efficacy of cherry stem extracts against calcium oxalate monohydrate crystallization in kidney stone treatment.....	282
<i>E. G. Reis, G. S. Pozan Soylu</i> , Investigation of <i>in vitro</i> digestive process in optimization of ultrasound-assisted extraction with citric acid anhydride for antioxidant production from red beet, Swiss chard, and dragon fruit.....	288
<i>D. Unlu</i> , Dehydration of industrial isopropanol wastewater by pervaporation using carboxy methyl cellulose and graphene oxide hybrid membranes.....	296
<i>K. Turhan</i> , Optimization of ozonation in the removal of Basic Blue 41 in aqueous solution.....	302
<i>Z. Kadioğlu, D. Şakar</i> , Methyl violet dye removal investigation on submicron particle size rubber powder obtained from scrap tyre functionalized with agar-agar.....	309
<i>Ö. Yolaçan, S. Deniz</i> , Effects of additives on mechanical and barrier properties of polyhydroxyalkanoate-derived bio-nanocomposite films by solution casting.....	314
<i>B. Boyadjiev, T. Petrova, R. Vladova, E. Kirilova, A. Apostolov, A. Moravski</i> , Optimization and determination of the factors influencing the delamination in graphene/MoS <sub>2</sub> /PET nanocomposite under mechanical loading.....	321
<i>Z. B. Al-Ruqeishi, O. K. Abou-Zied</i> , The influence of gold nanorods' aspect ratio on the structure and spectroscopic properties of TiO <sub>2</sub> nanoparticles for solar cell utilization.....	328
<i>T. Petrova, E. Kirilova, R. Vladova, A. Apostolov, B. Boyadjiev, A. Moravski</i> , Multi-parameter optimization of layered hBN/PMMA nanocomposite under mechanical loading.....	333
<i>H. Mutlu, E. Akyol</i> , Development of transdermal cellulose-based patches for Alzheimer's treatment and investigation of penetration behavior.....	342
<i>S. Öztürk, İ. Küçük</i> , The effect of pigment on the properties of black automotive enamel.....	348
<i>F. Uğur Nigiz, Z. İ. Özyörü, S. Balci</i> , Improved packaging performance of olive tree-based biochar-loaded poly(lactic acid) films.....	352
<i>G. Arda, A. Karasakal</i> , Determination of trace and major elements in commercial propolis samples by ICP-OES after microwave digestion.....	358
<b>INSTRUCTIONS TO AUTHORS</b> .....	362